

# On the role of C<sub>4</sub> and C<sub>5</sub> products in electrochemical CO<sub>2</sub> reduction

Simon D. Rihm<sup>1,2,3</sup>, Mikhail Kovalev<sup>2</sup>,  
Alexei A. Lapkin<sup>1,2</sup>, Joel W. Ager<sup>4,5,6</sup>, Markus Kraft<sup>1,2,7,8</sup>

released: November 24, 2022

<sup>1</sup> Department of Chemical Engineering  
and Biotechnology  
University of Cambridge  
Philippa Fawcett Drive  
Cambridge, CB3 0AS  
United Kingdom

<sup>2</sup> CARES  
Cambridge Centre for Advanced  
Research and Education in Singapore  
1 Create Way  
CREATE Tower, #05-05  
Singapore, 138602

<sup>3</sup> Department of Chemical &  
Biomolecular Engineering  
National University of Singapore  
4 Engineering Drive 4  
Singapore, 117585

<sup>4</sup> Department of Materials Science  
and Engineering  
University of California at Berkeley  
Berkeley, CA 94720  
USA

<sup>5</sup> BEARS  
Berkeley Educational Alliance  
for Research in Singapore Center  
1 Create Way  
CREATE Tower, #11-01  
Singapore 138602

<sup>6</sup> Lawrence Berkeley National Laboratory  
Berkeley, CA 94720  
USA

<sup>7</sup> School of Chemical  
and Biomedical Engineering  
Nanyang Technological University  
62 Nanyang Drive  
Singapore, 637459

<sup>8</sup> The Alan Turing Institute  
London  
United Kingdom

Preprint No. 299



---

*Keywords:* CO<sub>2</sub> reduction reaction, gas-chromatography mass-spectrometry, gas-diffusion electrode, electrocatalysis, carbon dioxide electrolysis, electrochemical reduction, reaction mechanism analysis, proton-transfer reaction mass-spectrometry

**Edited by**

Computational Modelling Group  
Department of Chemical Engineering and Biotechnology  
University of Cambridge  
Philippa Fawcett Drive  
Cambridge, CB3 0AS  
United Kingdom

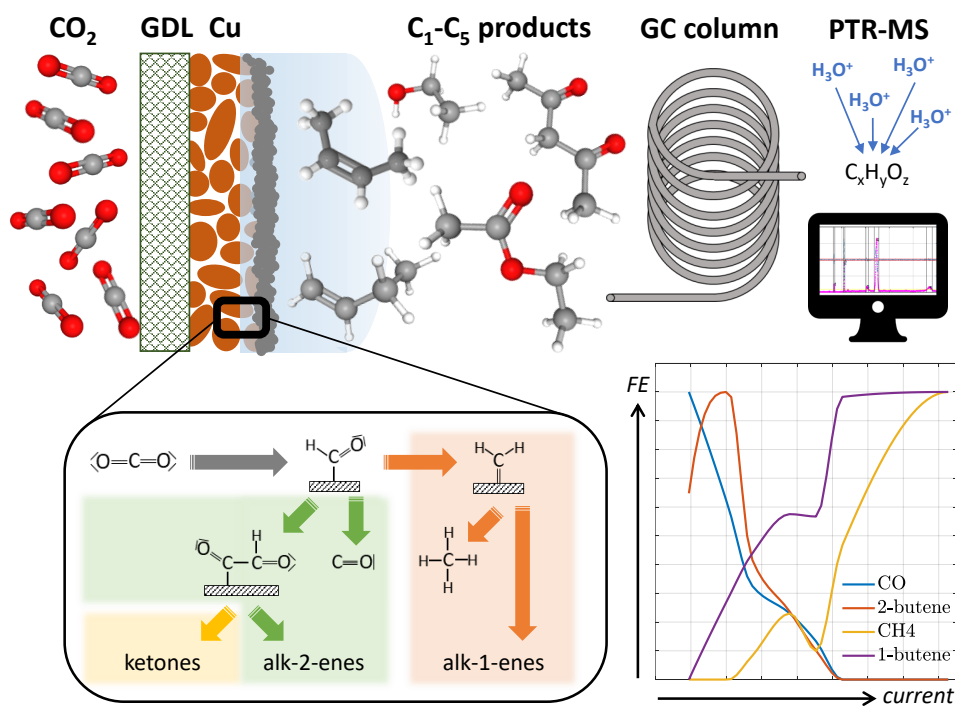
**E-Mail:** [mk306@cam.ac.uk](mailto:mk306@cam.ac.uk)

**World Wide Web:** <https://como.ceb.cam.ac.uk/>



## Abstract

Utilising carbon dioxide by synthesising commodity chemicals via electrocatalysis shows potential for long-term energy storage and industry decarbonisation. The latest copper-based gas-diffusion electrodes can operate at high currents, enabling large conversion rates. However, our incomplete understanding of active reaction paths in this system hinders us from designing catalysts with improved selectivities and reduced poisoning. Here, we identify and analyse ten previously unknown minor products of electrochemical CO<sub>2</sub> reduction. Using an ultra-sensitive GC-MS setup, we report more than 20 products, including C<sub>5</sub> species for the first time. From the trends in selectivity, we hypothesise two distinct reaction paths: while the coupling of oxygenated intermediates begins at very small potentials and favours double bond formation in the middle of carbon chains, coupling of highly-reduced methane precursors requires a large potential and leads to double bond formation at the chain end. This contribution represents a significant step towards the holistic comprehension of the mechanism for electrocatalytic CO<sub>2</sub> reduction and calls for further mechanistic exploration via minor products and investigation of favourable reaction conditions.



## Highlights

- Comprehensive GC-MS study of high-performance eCO<sub>2</sub>R GDE products
- Identification of over 20 different products, including four- and five-carbon species reported for the first time
- Trends for different isotopes and isomers over applied potential analysed
- Mechanism analysis revealing reduction state before coupling as driving factor for double bond locations and resulting selectivity trends

# Contents

<b>1</b>	<b>Introduction</b>	<b>3</b>
<b>2</b>	<b>Methods</b>	<b>4</b>
2.1	GC-PTR-TOF-MS . . . . .	4
2.2	Electrochemical Flow-Cell . . . . .	5
2.3	Experimental setup and measurements . . . . .	5
2.4	Product identification and quantification . . . . .	6
<b>3</b>	<b>Results and discussion</b>	<b>7</b>
3.1	Identified products . . . . .	7
3.2	Functional groups and isomers . . . . .	8
3.3	Relative Faradaic Efficiencies . . . . .	10
3.4	Mechanistic implications . . . . .	13
3.5	Full mechanism schema . . . . .	17
<b>4</b>	<b>Conclusions</b>	<b>20</b>
	<b>Nomenclature</b>	<b>23</b>
<b>A</b>	<b>Electrochemistry measurements</b>	<b>24</b>
<b>B</b>	<b>Gas Chromatography</b>	<b>26</b>
<b>C</b>	<b>Methodology</b>	<b>30</b>
<b>D</b>	<b>Single species discussion</b>	<b>37</b>
<b>E</b>	<b>Proton-Transfer Reaction Mechanisms</b>	<b>82</b>
<b>F</b>	<b>C13 verification of specific traces</b>	<b>98</b>
<b>G</b>	<b>Quantification of abundance</b>	<b>104</b>
<b>H</b>	<b>Kinetic Isotope Effect</b>	<b>106</b>
	<b>References</b>	<b>108</b>

# 1 Introduction

The development of true negative emission technologies is mission-critical for mitigating climate change [1]. Electrochemical reduction of CO<sub>2</sub> (eCO<sub>2</sub>R) to hydrocarbons is a promising way to convert emissions into fuels and commodity chemicals. Copper-based electrodes are particularly promising because they can produce C<sub>2+</sub> species, including a variety of valuable products [2, 3]. Researchers in the field have intensely studied these electrodes [4–6], particularly to produce ethylene [7] as they can reach large Faradaic Efficiencies of up to 75% with some setups [8]. Recently, gas-diffusion electrodes (GDE) operated under alkaline conditions have been in the spotlight [9–11] as they allow for large current densities and could enable economically viable applications in the long term [12]. As of now, the chemical industry is hard-to-decarbonise; eCO<sub>2</sub>R could not only help to decarbonise this sector, but also ultimately make it a negative emissions sector.

However, a key issue remains. Increasing and maintaining selectivities toward one or more specific products is still challenging because the products are formed in a multi-step mechanism. Synthesising ethylene via electrocatalysis requires 12 reduction steps, and C<sub>3</sub> products require even more. These reduction steps are thought to appear as elementary proton-coupled electron-transfer (PCET) reactions with similar energetics and scaling relationships that depend on active surface facets of the metal catalyst [13–15]. Understanding the mechanism is crucial for two reasons: first, it shows what products are possible and whether they can be scaled up, and second it shows what reaction paths are responsible for these products so we can engineer systems to favour or disfavour them.

Many research studies have investigated the mechanism computationally via *ab initio* studies [14, 16–18] and experimentally by identifying intermediates either via surface spectroscopy [19, 20] or by injecting supposed common intermediates as reactants into the system [21]. However, most major advancements in understanding have occurred by detecting minor products because any complete reaction mechanism must account for them [3, 4, 22]. Kuhl et al.’s study [2] from 2012 is exemplary in this respect. It introduced NMR for sensitive detection of liquid products (detecting 16 different species) and derived the influential hypothesis of enol-like intermediates as main contributors in the mechanism [4, 23].

Minor products can be indicative of common intermediates towards major products. Many mechanism studies describe the desorption of an intermediate on the path towards a major product [24, 25]. These “intermediates” have a lower reduction state than the major product they relate to. Moreover, minor products, even in very small amounts, can lead to catalyst poisoning in different ways. For example, they can accumulate on top of the catalyst and inactivate parts of the surface, as Kovalev et al. observed for polymerising acrolein [26]. But these minor products can also indicate a surface species that is a “dead end” which will not react any further, so its coverage rises to the point where it hinders eCO<sub>2</sub>R [27].

Therefore, analysing minor products can help derive practical information for the design of future reactors and catalysts. Understanding the eCO<sub>2</sub>R mechanism can help steering the reaction in the desired direction (e.g. by stabilising certain intermediates via surface ligands [28]) and avoid catalyst poisoning. While analytical methods for eCO<sub>2</sub>R

products have improved, advances have mostly focused on time efficiency and *operando* capabilities [29, 30]. Introduced mass spectrometry methods are mostly based on “hard” ionisation that leads to a wide range of fragments and therefore have limitations in identifying unexpected products [31], but a few methods based on “soft” ionisation were used [32].

In recent studies, Löffler et al. established proton-transfer reaction mass spectrometry (PTR-MS) with a time-of-flight (TOF) analyser as a way to precisely analyse the liquid products in real-time [32, 33]. In previous work, present authors applied PTR-TOF-MS to the gas outlet of a state-of-the-art flow cell to achieve accuracies so high that naturally occurring  $^{13}\text{C}$  isotopes could be measured confidently, and a Kinetic Isotope Effect was described and quantified for the first time in such a system [34]. For unambiguous product identification before the *operando* measurements, a gas-chromatography mass-spectrometry (GC-MS) setup was used. This experiment indicated the existence of a  $\text{C}_4$  species which warranted further investigation.

Applying GC-PTR-TOF-MS to a collected sample of eCO<sub>2</sub>R products allows product identification at unprecedented sensitivity. Using the gas outlet flow of a high-current GDE operating under high pH allows us to investigate the mechanism under commercially relevant conditions, as prevalent reaction paths might substantially differ from those active in previously studied systems [35]. This study aims to observe and identify as many eCO<sub>2</sub>R products from the reduction of CO<sub>2</sub> via electrolysis as possible. By analysing selectivity trends across products’ functional groups as well as the applied potential, we derive implications for the respective reaction paths. Finally, we discuss existing hypotheses regarding the eCO<sub>2</sub>R mechanism to confirm or reject them based on our observations and formulate new ones.

## 2 Methods

### 2.1 GC-PTR-TOF-MS

PTR-MS is a well-established method for monitoring volatile organic compounds in atmospheric samples [36]. A PTR-MS instrument connects an ion source to a drift tube in which the primary ion (e.g.,  $\text{H}_3\text{O}^+$ ) reacts with an analyte based on its proton affinity (PA). The analyser then detects the ions formed. This method achieves a high mass resolution (particularly in combination with a TOF detector) [37], but a high concentration of analytes can deplete the primary ion resulting in clusters and fragments that lower the sensitivity and complicate identification [38]. Hence, detecting low-concentration species in eCO<sub>2</sub>R product mixtures is challenging, as using strong dilution to mitigate depletion might lower concentrations under the detection limit. The combination with gas chromatography solves this, as analytes are separated and eluted one at a time. This effectively creates an ultra-sensitive GC-MS with “soft” ionisation in contrast to the typical “hard” electron impact ionisation with a less-accurate quadrupole sensor previously used for eCO<sub>2</sub>R product analysis [39].

## 2.2 Electrochemical Flow-Cell

Our GDE is based on nanostructured copper deposited on carbon paper. Its preparation as well as the anode and electrochemical flow-cell setup has been described in detail in a previous article [26]. For the gas inlet, CO<sub>2</sub> of 99% purity was used with the flow-rate set to 50 sccm. An additional experiment was done with an additional experiment of <sup>13</sup>CO<sub>2</sub> (99% isotope content) for confirmation purposes at the same inlet flow-rate. For each experiment (except a run with <sup>13</sup>CO<sub>2</sub>), electrolysis was performed at a constant potential applied vs a Hg/HgO reference electrode. Seven runs were carried out with a controlled cell voltage with steps of 0.5 V from  $U_{\text{Hg/HgO}} = -2.0\text{ V}$  to  $-5.0\text{ V}$ . Each time, we ran the cell for 5 min before collecting a gas sample at the outlet and directing it to the measurement setup.

## 2.3 Experimental setup and measurements

Fig. 1 shows the experimental setup of this work. We directed the cell's outlet into a sampling loop of 1 ml followed by a gas chromatograph Agilent 7890 equipped with Hayesep D packed column (length of 6'). Nitrogen was used as a gas carrier. The outlet of the GC was connected to the inlet line of the PTR-TOF-MS, and the analyte was diluted with an additional 200 sccm of pure N<sub>2</sub> before the drift chamber. The dilution prevented the MS detector from becoming saturated as some species were produced at high concentrations. We heated the MS inlet line at 80 °C to decrease the memory effect that we observed in our previous work [34].

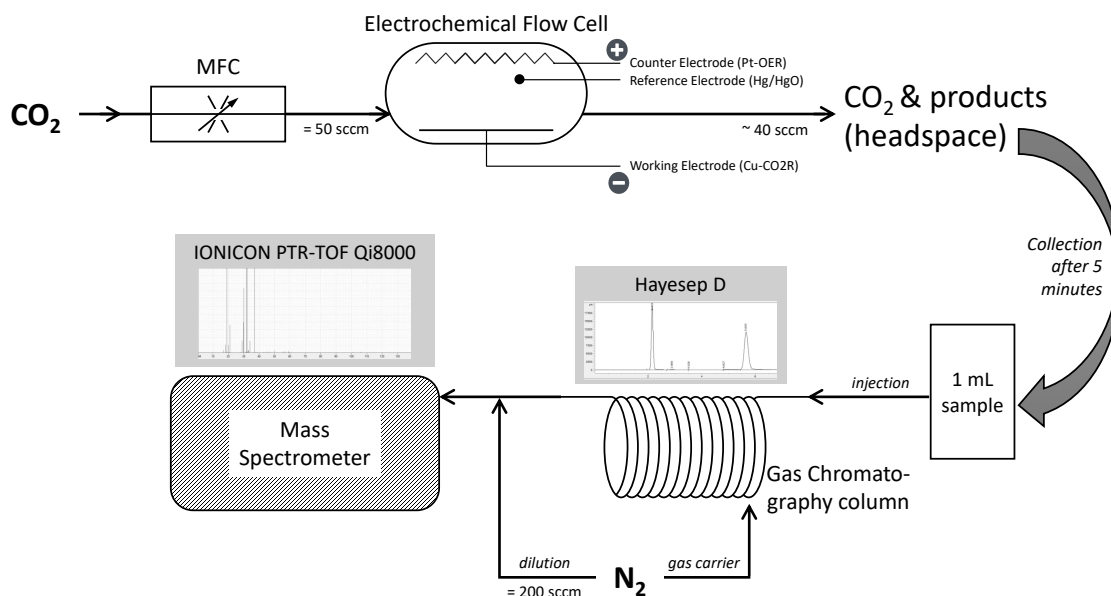


**Figure 1:** Schematic of electrochemical cell and GC-MS setup.

We selected the GC conditions to maximise the potential for species to separate on the selected column. We programmed the GC oven to separate light gases at a lower temper-

ature of 80 °C, medium gaseous products at 130 °C, and the remaining species at 200 °C. The overall run was completed at  $t = 45$  min after the injection of the sample. We utilising a PTR-TOF-MS Qi8000 from IONICON Inc (Austria) with multiple supply reactive ions tube, using  $\text{H}_3\text{O}^+$  ions to ionise separated product species. We found the drift tube settings were optimal at 114 Td to achieve a good sensitivity and resolution of 3500 to 4100m/ $\Delta$ m.

## 2.4 Product identification and quantification

We identified eCO<sub>2</sub>R products based on retention times and ionisation spectra as shown in Fig. 2. To confirm the electrolysis of carbon dioxide as the species' origin, we compared the ion chromatograms to an additional experiment with <sup>13</sup>CO<sub>2</sub>. We computed the peak area for all resulting ions as a measure of signal strength. Further product confirmation and especially discrimination between positional and stereoisomers was achieved by tracking the ratios of these signals across cell voltages.

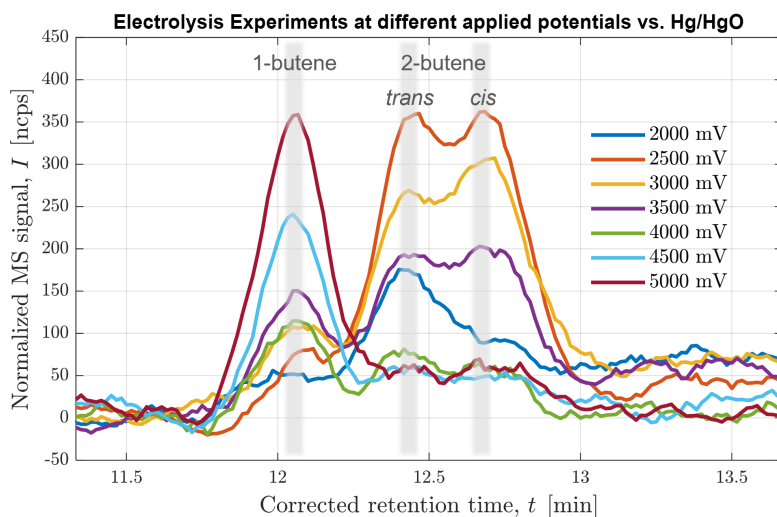


**Figure 2:** Extracted ion chromatogram for  $m/z = 57.070$  Da ( $\text{C}_4\text{H}_9^+$  ion)

There is a lack of data on the precise reaction rate coefficients for proton transfer reactions with small organic compounds. As such, absolute quantification is bound to be flawed. However, as our study is focused on the mechanistic implications of minor products and their trends, and not cell performance assessments, we only need a relative measure for selectivity. Therefore, we introduce the concept of a relative Faradaic Efficiency as

$$\eta_{rf}(U_k) = \frac{\int_i I_j(U_k)}{J(U_k)} / \max_k \left( \frac{\int_i I_j(U)}{J(U)} \right), \quad (1)$$

where  $\int_i I_j$  is the integrated peak area of ion  $j$  at the retention time of species  $i$  and  $J$  is the average current density measured during electrolysis at cell voltage  $U_k$ .

Using the relative Faradaic Efficiency (rFE) has many advantages. First, the qualitative trend across cell voltages is precise because we compare the rFE of all resulting ions to verify a certain species. We can pick the species with the least uncertainty to represent

that product. Second, we can more effectively compare the curve shapes of different products as they all peak at 100%. This is especially helpful for these high-current cells as all species production declines at a certain potential, making analysis of Tafel slopes less effective.

## 3 Results and discussion

### 3.1 Identified products

Tab. 1 lists the 23 different products of electrocatalytic CO<sub>2</sub> reduction we identified. At least ten of the products have never been reported before to the best of our knowledge.

**Table 1:** Overview of all detected products, the ones shown in blue are reported for the first time. Information on species makeup is given as the number of electrons transferred and the number of carbon and oxygen atoms.

species	# e <sup>-</sup>	# C	# O	species	# e <sup>-</sup>	# C	# O	species	# e <sup>-</sup>	# C	# O
carbon monoxide 	2	1	1	propylene 	18	3	0	1-butene 	24	4	0
formaldehyde 	4	1	1	propanol 	18	3	1	2-cis-butene 	24	4	0
methanol 	6	1	1	butanedione 	18	4	2	2-trans-butene 	24	4	0
methane CH <sub>4</sub>	8	1	0	ethyl acetate 	20	4	2	2,3-pentanedione 	24	5	2
acetaldehyde 	10	2	1	butadiene 	22	4	0	2,4-pentanedione 	24	5	2
ethylene 	12	2	0	butanal 	22	4	1	1-pentene 	30	5	0
ethanol 	12	2	1	butanone 	22	4	1				
propanal 	16	3	1								
acetone 	16	3	1								
allyl alcohol 	16	3	1								

C<sub>1</sub> and C<sub>2</sub> products have been measured and described at length for eCO<sub>2</sub>R on copper-based catalysts. We detected no additional products of one or two carbon lengths in these experiments. Interestingly, we did not expect to observe methane as its proton affinity is much smaller than water's. However, the primary ion H<sub>3</sub>O<sup>+</sup> in the drift chamber is not completely pure, and a small percentage of residual O<sub>2</sub><sup>+</sup> ions led to significant ionisation. The proton affinities of carbon monoxide and ethylene are also smaller than water's, but the large concentrations led to some detectable protonation.

Despite Mandahl et al. previously identifying propylene as a minor product of eCO<sub>2</sub>R [40], it has only recently been reported as a product with a potentially significant production rate [10]. In this study, we detected a relatively large signal of propylene, indicating absolute Faradaic Efficiencies about one order of magnitude below ethylene. Propanol has been extensively described before, as have the three detected C<sub>3</sub>H<sub>6</sub>O isomers: propionaldehyde (propanal), acetone, and allyl alcohol.

Interestingly, we identified C<sub>4</sub> and C<sub>5</sub> products. While Calvinho et al. have previously formed a complex C<sub>4</sub> product with catalysts based on transition metal phosphides [41], the mechanism for copper-based catalysts is very different and heavily favours C<sub>1</sub> and C<sub>2</sub> products. Apart from a small signal indicating the existence of butene in a former work of the present authors [34], none of these products have ever been reported to the best of our knowledge. The distinction of stereoisomers for butene and pentanedione is particularly novel.

Apart from butene isomers shown in Fig. 2, we identified several oxygenated C<sub>4</sub> species: The signals indicating C<sub>4</sub>H<sub>8</sub>O showed similar trends as the C<sub>3</sub>H<sub>6</sub>O species mentioned above. Partially based on analogy, we identified butanal and butanone. Interestingly, we also observed two double-oxygenated species: butanedione and ethyl acetate, which is the only ester found so far.

For the first time, we report evidence of a C<sub>5</sub> species as a product of electrocatalytic CO<sub>2</sub> reduction. First, we identified pentene. In analogy to butene, we found a second peak, most likely representing the isomer 2-pentene. However, no quantifiable distinction of (stereo-)isomers was possible due to low concentrations. Moreover, we identified pentanedione with two well-separated and very distinct peaks differing only in intensity and fragmentation. The two isomers are thought to be 2,3- and 2,4-pentanedione respectively.

As interesting as the products identified are the ones absent in this study. Apart from methane, we detected no other hydrocarbons. This is easily explained by their very small proton affinities, which makes them detectable only at substantial concentrations by PTR-MS. In a previous study [34], Ren et al. detected ethane and propane by classic GC, and we expect them to be present also here at small concentrations. We could not detect carboxylic acids due to the large pH in the electrolyte, which causes them to be present as their conjugate base without entering the vapour phase. Nonetheless, we expect the presence of formate and acetate, as they have been detected in a previous study after electrolyte neutralisation [34]. In contrast to the study by Kuhl et al. [2], we found no double-oxygenated C<sub>2</sub> and C<sub>3</sub> species. One might attribute this to the small vapour pressure of liquid products and the focus of this study on the gas phase, but two facts speak against this: first, they were neither detected by HPLC in the previous study [34]; and second, glyoxal has a sufficient vapour pressure (similar to well-observed propanal) to be detected in the gas phase.

### 3.2 Functional groups and isomers

The minor products we observed are mostly analogous species to more common products but with a longer carbon chain. Tab. 2 shows products sorted according to functional groups and thereby illustrates this for alkenes, ketones, and aldehydes. More interesting

are the products that defy this trend in some way. One example is the diones (butanedione and pentanedione), which only exist for  $C_{\geq 4}$ , while most of the former studies have been focused on  $C_{\leq 3}$ . There seems to be a shift away from ketones and aldehydes towards diones with growing carbon chains. This observation gives grounds for hypotheses regarding the reaction path: for example, the dimerisation of multi-carbon intermediates via preferable coupling between oxygenated carbon atoms is a sensible explanation. Butadiene falls into a similar category as the diones: it is the smallest conjugated diene possible. Since it is also the only diene reported so far, no trend can be observed - only the absence of a trend away from alkenes towards alkadienes with longer carbon chains.

**Table 2:** Possible CO<sub>2</sub>R products of most common functional groups for C<sub>1</sub>-C<sub>5</sub> are listed. The colour indicates whether it has been detected in eCO<sub>2</sub>R reactors with Cu-based electrodes. Green species were detected in this study, blue and purple species were not detected here but by Kuhl et al. [2] or Ren et al. [34] respectively.

# C	alkane	alkene	alcohol	ketone	aldehyde
1	methane	-	methanol	-	formaldehyde
2	ethane	ethylene	ethanol	-	acetaldehyde
		-	vinyl alcohol ethylene glycol	-	glyoxal
3	propane	propylene	propanol	acetone	propanal
		-	allyl alcohol hydroxyacetone allene propylene glycol	-	propanedial
4	butane	butylene	butanol	butanone	butanal
		-	crotyl alcohol hydroxybutanone butadiene butanediol butanedione	-	butanediol butanedial
5	pentane	pentylene	pentanol	pentanone	pentanal
		-	pentenol hydroxypentanone pentadiene pentanediol pentanedione	-	pentanediol pentanedial

The formation of alcohols also becomes less likely for longer carbon chains. This may be because alcohols are usually produced towards larger applied potentials compared to their ketone and aldehyde counterparts, while most products with longer carbon chains are favoured at smaller applied potentials. It also should be noted that we observe fewer species containing alcohol groups than in previous similar studies: we have not identified glycolaldehyde, hydroxyacetone, and butanol; we have not found glycols for any carbon chain length. The latter is not surprising as neither postulated double-oxygenated C<sub>2</sub> species (glyoxal, ethylene glycol [2]) could be reproduced in our work. Since these products are the main reason to hypothesise enol-like intermediates as critical, this may have mechanistic implications for high-current GDEs. If we assume the initial dimerisation takes place between two oxygenated intermediates, at least one of the carbon-oxygen bonds seems to break very easily under these conditions - potentially, this is driven by the alkaline environment as key steps have been shown to be pH-dependent [15, 42], causing our unique product distribution.

We will not discuss the carboxylic acids in much detail as they are not quantifiably detectable and seem to follow a different mechanistic logic that permits two oxygen atoms to bind to the same carbon. The simplest explanation is that there is a dimerisation before the breaking of the first C-O bond, as suggested by Shah et al. [23]. Alternatively, Garza et al. have proposed a ring closure mechanism that transfers oxygen between carbon atoms [4], even though it seems energetically unlikely [27]. Any species where one carbon atom is connected to two oxygen atoms faces a challenge of mechanistic explanation as either coupling occurred before the first dissociation of water (or related), external oxygen was incorporated as suggested before [43], or oxygen moved between carbon atoms via aforementioned ring closure mechanism.

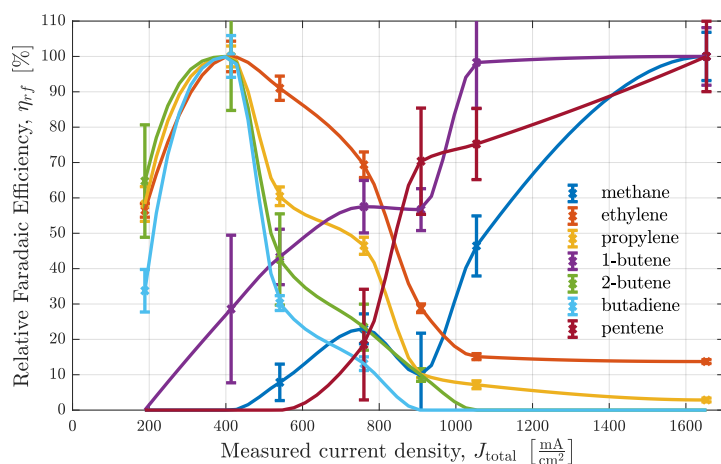
The ethyl acetate detected in this study seems to also face this challenge but can be more readily explained by a coupling step of two oxygenated intermediates. The possibility of ethyl acetate production via secondary bulk reactions of eCO<sub>2</sub>R products still remains: the esterification of acetic acid and ethanol seems unlikely since it is generally catalysed by acids, but a disproportionation of acetaldehyde is possible since it is catalysed by alkoxides and acetaldehyde is abundant. All these double-oxygenated functional groups were left out of Tab. 2 for the sake of simplicity. Furthermore, glycolaldehyde, as reported by Kuhl et al. [2], and acrolein, as reported by Kovalev et al. [26], are also missing.

### 3.3 Relative Faradaic Efficiencies

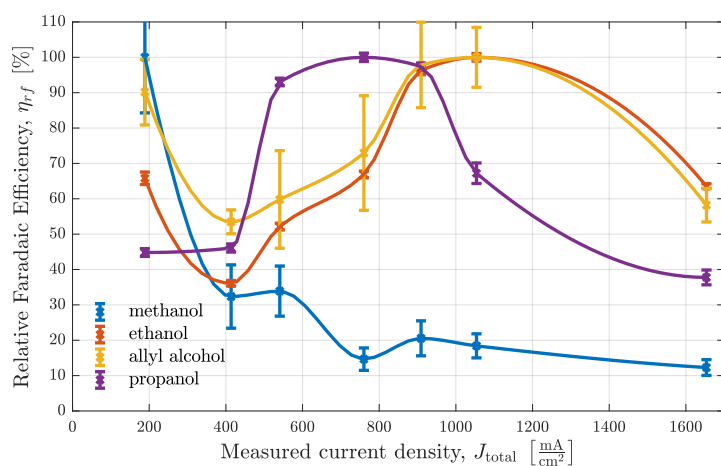
Fig. 3 shows the relative Faradaic Efficiencies of all products detected over the measured current density. Each measured point is indicated by a cross. Its error bar shows the empirical standard deviation based on the uncertainty of calculated peak areas used in Eq. (1). A piecewise cubic interpolation is shown as a solid line going through the points. For data points with a signal-to-noise ratio so large, it cannot be considered a peak with confidence, no measurement data is shown. Instead, the interpolation assumes zero.

Uncertainties for some of the data points are considerably larger than for others. There are two reasons for this: Firstly, all integrated signals are shown relative to their maximum value of 100%, which amplifies the uncertainties of signals with smaller absolute intensities. Secondly, to calculate a measure of relative Faradaic Efficiency, all data were normalized by current density, which pronounces uncertainties at smaller applied potentials. These effects lead to specifically large standard deviations for species detected with small absolute signals at small applied potentials, as can be seen in Fig. 3(c).

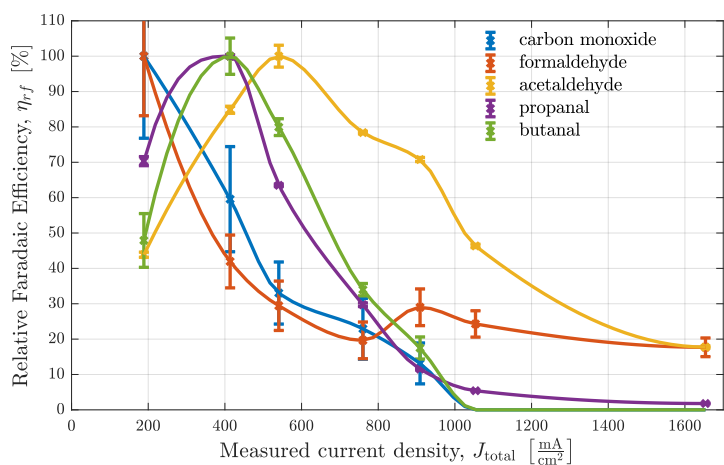
Species were clustered into four different groups based on their functional groups. This makes it easier to track the large number of species. It also serves as a starting point for a mechanism discussion, as similar or complementary selectivity trends can indicate common reaction paths, intermediates, and rate- or selectivity-determining steps.



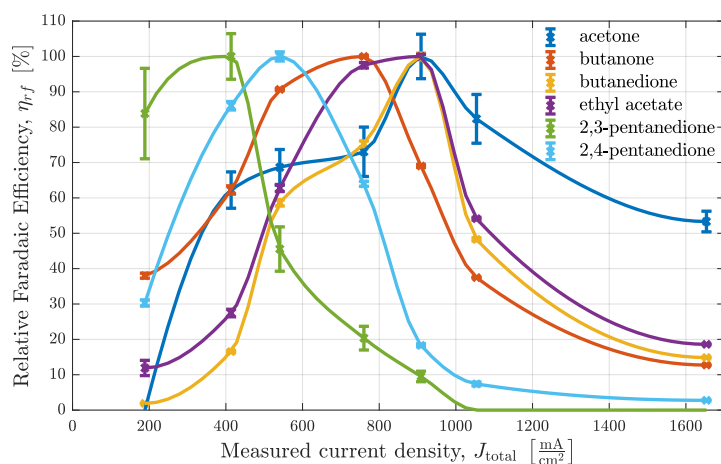
(a) Selectivity trends of all pure hydrocarbon products detected



(b) Selectivity trends of all detected products containing alcohol groups.



(c) Selectivity trends of all detected products containing carbonyl groups at the end of the carbon chain (mostly aldehydes).



(d) Selectivity trends of all detected products containing carbonyl groups in the middle of the carbon chain (mostly ketones and diketones).

**Figure 3:** *Relative Faradaic Efficiencies and empirical standard deviations of selected traces representing all detected products across the range of applied potential.*

Some of the trends the products exhibit are unexpected: For example, the butene isomers 1-butene and 2-butene show trends almost opposite of each other. The differences in selectivity trends between alcohols, aldehydes, and ketones are also much larger than expected, as current efficiencies reported by Kuhl et al. [2] showed very similar trends and peak efficiencies across all products apart from propanal and  $C_1$  species. Another unexpected finding is the large rFE level of some products at high currents well beyond  $1 \text{ A cm}^{-2}$ , implying ongoing competition between  $\text{CO}_2$  reduction and hydrogen evolution (HER). Some products seem to have two local maxima of Faradaic Efficiency for different applied potentials - this can be seen most prominently for ethanol. Moreover, a general trend exhibited by many of the products is noteworthy: similar products with different lengths of the carbon chain always show peak selectivities at smaller applied potentials for the longer chains than the shorter chains. This is especially apparent comparing aldehydes, ketones, and diketones of  $C_3$  and  $C_4$  type. It implies a larger coverage of intermediates that are responsible for coupling at smaller applied potentials, suggesting less-reduced intermediates for coupling steps. The widely accepted hypothesis of either  $\ast\text{CO}$  or  $\ast\text{CHO}$  [16, 17, 44] intermediates as  $C_1$  coupling intermediates is in agreement with this observation. This trend is consistently observed for  $C_{2+}$  products.

In Fig. 3(a), it becomes apparent how different the behaviours of pure hydrocarbons (mostly alkenes) are - even between positional isomers, as mentioned before. It further indicates that alkenes can be put into one of two categories for the most part regarding their trend curve of rFE. The stark differences between those two categories indicate a fundamental difference in the governing reaction mechanism - most likely already on the level of initial coupling. For the production of ethylene, the existence of two independent reaction paths has been established before [18, 21] - one at lower applied potentials via the coupling of an oxygenated intermediate and one at larger applied potentials sharing an intermediate with methane. The curve of ethylene's rFE hints at this behaviour by exhibiting a peak stretched from small to medium currents and still showing significant production

(especially in absolute terms) for large currents. Propylene shows a qualitatively similar behaviour with less pronounced selectivity for larger currents, indicating a smaller likelihood of production via the second pathway. Meanwhile, 2-butene does not show any indication of a second high-potential pathway as its rFE curve is similar to that of carbon monoxide in Fig. 3(c). In contrast, 1-butene and 1-pentene only show behaviour coinciding with methane production, therefore indicating the high-potential pathway as the exclusively governing mechanism.

Taking a closer look at Fig. 3(b) and Fig. 3(c), methanol behaves similarly to formaldehyde, indicating a common reaction path. This is expected, as Schouten et al. showed feeding  $\text{CH}_2\text{O}$  produces  $\text{CH}_3\text{OH}$  [21]. This reaction path could also explain the small amounts of methane produced for small to medium applied potentials which is supported by formaldehyde production continuing at larger currents and methane showing a first local maximum at medium currents. Aldehydes have been suggested as precursors for alcohol (sharing a reaction path) for  $\text{C}_{2+}$  as well, but in Fig. 3(c) acetaldehyde, propanal and butanal behave quite differently than their alcohol counterparts, while the behaviour of methanol does not indicate a large activation barrier for the reduction of a carbonyl group. However, this does not disprove the aforementioned hypothesis, as this might depend on neighbouring carbon atoms and functional groups present in  $\text{C}_{2+}$  species.

### 3.4 Mechanistic implications

Based on the identified products and analysed selectivity trends, we can derive implications for the reaction paths. Combining these with the findings regarding intermediates and common pathways reported in other publications [3, 21, 23], we can postulate reaction mechanisms based on experimental findings alone. In this work, we limit our discussion of the mechanism to a few very clear trends of products' rFE. General trends of maximum Faradaic Efficiency reached at small or large applied potentials point towards major differences on the level of coupling. The more intricate variations point towards splitting pathways at a later stage.

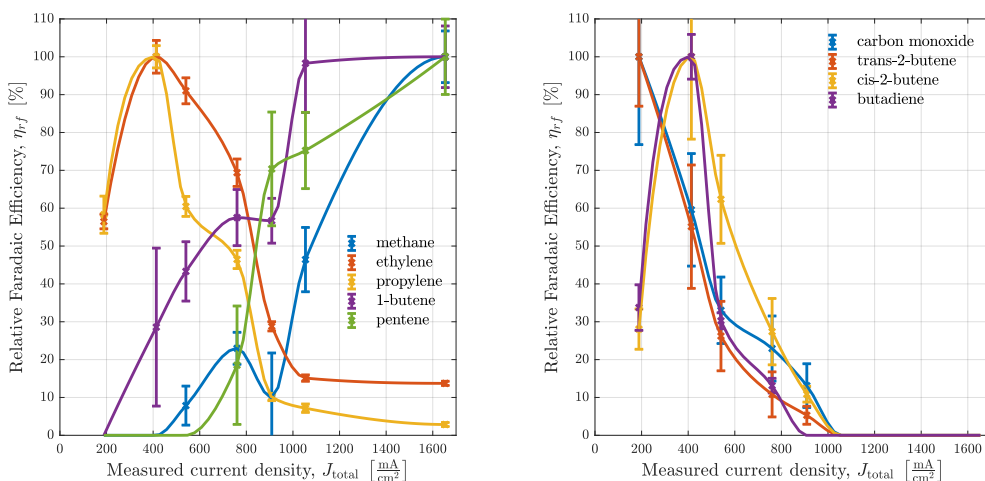
When discussing mechanism implications, we must remember that while shared markers (e.g. similar rFE curve) between two products can point towards a shared reaction path, it is not imperative. It is also worth noting that the failure to detect a certain product which is hypothesised to be a key intermediate in its adsorbed form does not necessarily disprove the hypothesis. For example, we did not find any glyoxal, but this does not mean that  $**\text{CHOCHO}$  is not an intermediate on the main reaction path, as the desorption equilibrium might be fully on the side of the adsorbed state or the subsequent reduction step is so fast that almost no  $**\text{CHOCHO}$  exists on the surface.

Based on the general trends in functional groups and rFE stated previously, we derive our first hypothesis. As we do not observe any double-oxygenated species for  $\text{C}_{<4}$  and generally no more than two oxygen atoms in a single species, we assume at least one C-O bond is rapidly broken after the first coupling, assuming the coupling happens between two single-oxygenated  $\text{C}_1$  intermediates. For  $\text{C}_{\geq 4}$  products, double-oxygenated products are present, and we observe a trend from single- to double-oxygenated products of which different isomers share the same selectivity trends. Therefore, we speculate that

these are formed via the coupling of the same single-oxygenated  $C_2$ – $C_3$  intermediates, where position and direction determine the eventual isomer. The general trend of rFE peaks for longer carbon chains moving towards smaller voltages strengthens this hypothesis because we would expect these peaks to coincide if chain growth was driven by the continuous addition of a single  $C_1$  intermediate. Following this logic, the coverages of  $C_2$  and  $C_3$  coupling intermediates seem to peak at smaller applied potentials than that of the  $C_1$  coupling intermediate. After the coupling of these to double-oxygenated  $C_4$  or  $C_5$  intermediates, the breaking of the C-O bond seems to be less promoted than its  $C_2$  and  $C_3$  counterparts.

Tab. 2 indicates the most common functional groups in the products are the double bonds in alkenes, hydroxy groups in single primary alcohols, and carbonyl groups in ketones and aldehydes. Therefore, understanding the commonalities and differences in the reaction paths leading up to these products is particularly important.

As mentioned before, butene isomers seem to rely on different mechanisms. Fig. 4 elucidates the selectivity behaviour of 1-butene as similar to methane and 1-pentene, whereas 2-butene behaves similarly to butadiene and carbon monoxide. This points to different modes of achieving double bonds: via the coupling reaction of a highly-reduced intermediate (1-butene, 1-pentene) and via water dissociation after coupling of oxygenated intermediates (2-butene, butadiene). Moreover, the existence of diones and esters suggests that at least some coupling reactions take place between two oxygenated monomers. Purely based on their structure, ethylene and propylene could be produced via either of these modes; this actually seems to be the case as their rFE curves exhibit a hybrid behaviour: peak selectivity is reached at small currents similar to the curves in Fig. 4(b), but does not decline as rapidly. Instead, we can see a plateau around  $J \approx 0.8 \text{ A cm}^{-2}$  coinciding with the first increase of methane and 1-butene, before decreasing to a constant value even for large currents.



(a) rFE of all identified alk-1-enes and methane. (b) rFE of  $C_4$  species and carbon monoxide.

**Figure 4:** Comparing selectivity trends of different alkenes with  $C_1$  products that might share common intermediates.

This hypothesis corresponds with the two-pathway theory put forward by Luo et al. [18] and recently assessed within a microkinetic model [27] for Cu(100) surfaces: towards ethylene production,  $*\text{CHO}-*\text{CHO}$  coupling is dominant for smaller applied potentials (leading to aldehydes as well as alk-2-enes), while  $*\text{CH}_2-*\text{CH}_2$  coupling is dominant for larger applied potentials (leading to alk-1-enes). We extend this theory to include all produced alkenes discriminate between positional isomers: while a low-potential pathway of successive coupling of oxygenated intermediates leads to the formation of alk-2-enes, a high-potential pathway leads to alk-1-enes by addition of a highly-reduced intermediate.

Within 2-butene, we can distinguish the cis and trans form, and the selectivity trends even differ slightly, as shown in Fig. 4(b), yet not as fundamentally as the positional isomers. This could be the result of very similar reaction paths that only branch at the very end, as shown in Fig. 5. Based on the homogeneous coupling of a  $\text{C}_2$  intermediate that might be an acetaldehyde or ethylene precursor, the two stereoisomers are produced based on the order the carbon atoms are hydrogenated. Based on the respective selectivity trends, the initial hydrogenation of a  $\text{CH}_2$  group seems to be preferred over hydrogenation of less-reduced mid-chain carbon atoms only at an increased voltage (leading to cis-2-butene).

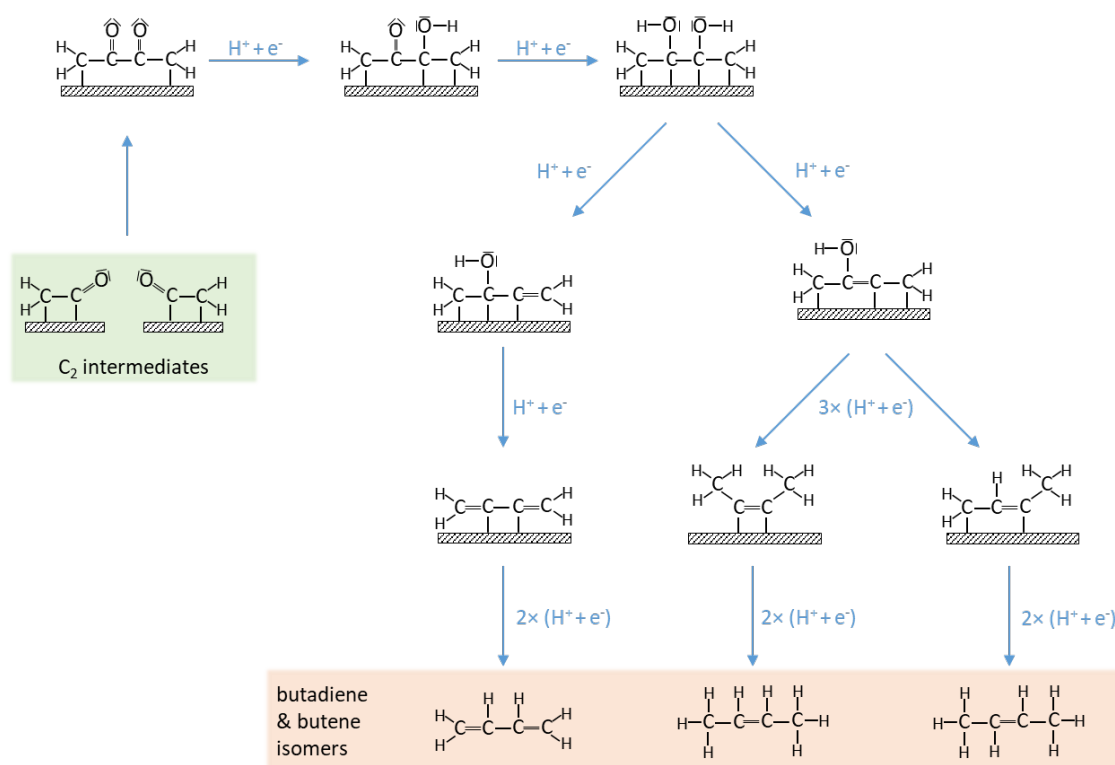


**Figure 5:** Suggested mechanism from common intermediate towards butadiene and 2-butene stereoisomers.

This 2-butene pathway relies on the prior hydrogenation of a carbonyl group to a hydroxy group and finally dissociates water in such a fashion that the freed electron initiates a double bond with the neighbouring carbon atom towards the middle. Even if this neighbouring carbon atom is also oxygenated, its hydrogenation will most likely not lead to a second double bond as allenes are unstable. This could also explain the relative Faradaic

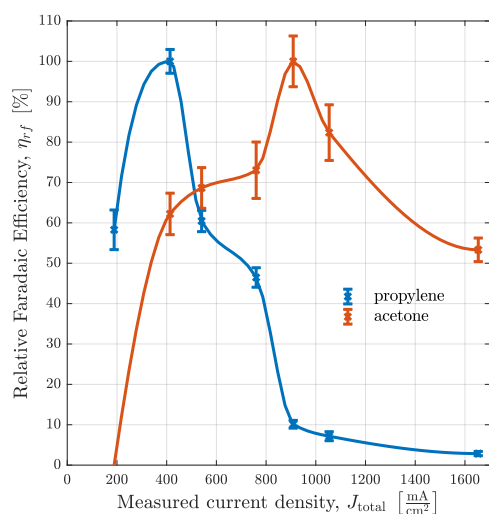
Efficiency curve of butanedione, which is shifted to significantly higher currents as it would require  $\text{CH}_2$  hydrogenation at both ends of the first intermediate after the coupling step shown in Fig. 4(b). Similar subsequent hydrogenation steps would be necessary to form ethyl acetate if the coupling occurs between carbon and oxygen rather than carbon and carbon. This would explain the similar selectivity trends of ethyl acetate and butanedione shown in Fig. 3(d) and is a much more likely mechanistic explanation than the disproportionation of acetaldehyde as peak rFE would be expected at much smaller currents.

Butadiene behaves similarly to 2-butene, seemingly contradicting the hypothesis around the formation of mid-chain and end-chain double bonds. It can be explained along similar lines: if the reduction of a double-oxygenated  $\text{C}_4$  intermediate leads to the formation of a double bond towards the end rather than the middle of the chain, the second oxygen splitting is free to also lead to a double bond at the other end of the chain. This is not possible if the first oxygen splitting leads to double bond formation in the middle of the chain, as allenes are sterically improbable. While the order of hydrogenation matters for the 2-butene stereoisomers, the butadiene structure does not depend on it.

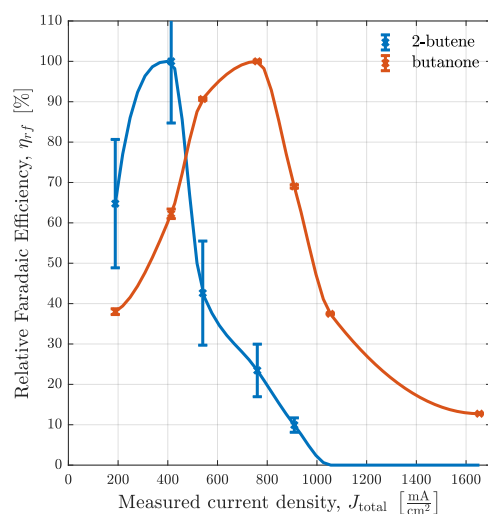
This analysis now provides further insights into the coupling mechanism for the production of all alkenes - including ethylene and propylene. For smaller applied potentials, symmetrical coupling of oxygenated intermediates leads to the formation of double bonds in the middle of the carbon chain. The trends of aldehyde's Faradaic Efficiencies largely coincide with those of the formerly discussed alk-2-enes which supports this hypothesis. For larger applied potentials, asymmetrical coupling of a highly-reduced intermediate forms a double bond at the end of a carbon chain. Based on the experimental findings of Schouten et al. [7] on single-crystal electrodes, the coupling of oxygenated intermediates takes place on (100) and (111) facets while the addition of a highly-reduced intermediate is almost exclusive to (100). This means that catalyst nanomaterials could be engineered to prefer either alk-1-enes or alk-2-enes based on the ratios of active facets.

According to the hypothesis for alk-2-ene production illustrated in Fig. 5, we suspect double bonds in alk-2-enes form via mid-chain carbonyl groups. If the intermediate preceding the splitting of reaction paths would be hydrogenated at one of the  $\text{CH}_2$  groups instead of the carbonyl group first, it would form a ketone. As mentioned before, we suspect these hydrogenation steps to be preferred at more elevated voltages. Indeed, relative Faradaic Efficiencies of ketones (and diketones) appear generally shifted towards larger currents in Fig. 6(a) and 6(b). Note that the selectivity trends shown are not just two different curves with deviating peaks, they appear complimentary as a decrease of the alk-2-ene's rFE coincides with an increase of ketone's rFE and a plateau coincides with a plateau.

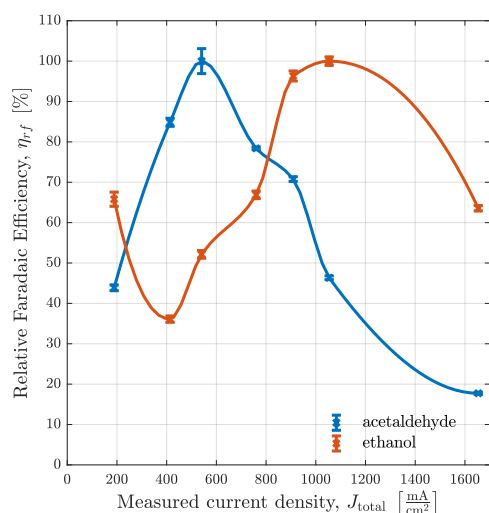
A similar observation can be made for aldehydes and primary alcohols, which we suspect share a common reaction path as well. This is a common hypothesis for  $\text{C}_2$  (acetaldehyde and ethanol respectively), confirmed by multiple observations [21, 24, 33]. As relative Faradaic Efficiencies for alcohols appear generally more shifted towards larger currents, we speculate it follows a pathway with a larger reaction barrier starting at the same intermediate. This makes logical sense as alcohols need additional reduction steps before desorbing - mainly the hydrogenation of the end-chain carbonyl group.



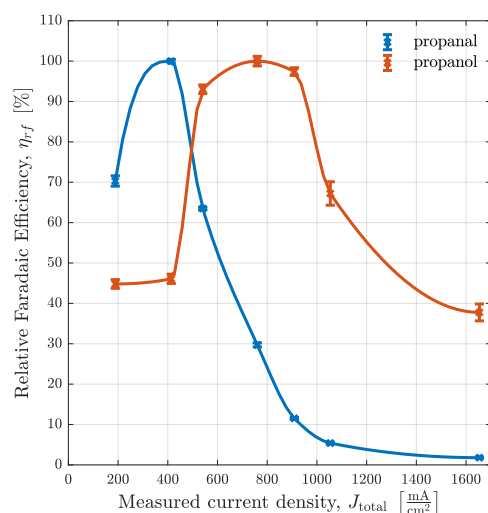
(a) C<sub>3</sub> alk-2-enes and ketones.



(b) C<sub>4</sub> alk-2-enes and ketones.



(c) C<sub>2</sub> aldehydes and alcohols.



(d) C<sub>3</sub> aldehydes and alcohols.

**Figure 6:** *Relative Faradaic Efficiencies of corresponding products in comparison. The upper figures show selectivity trends of alk-2-enes and ketones while the lower figures show those aldehydes and primary alcohols.*

### 3.5 Full mechanism schema

We formulated different hypotheses to account for the identified products and synthesized them to form a coherent reaction schema which is illustrated in Fig. 7. Products are ordered by their level of reduction because coupling must occur “before” the least-reduced product of a common path. Furthermore, we expect coupling after the first oxygen dissociation [3] - for this, no incorporation of outside oxygen needs to be assumed, notwithstanding recent challenges to that notion [43].

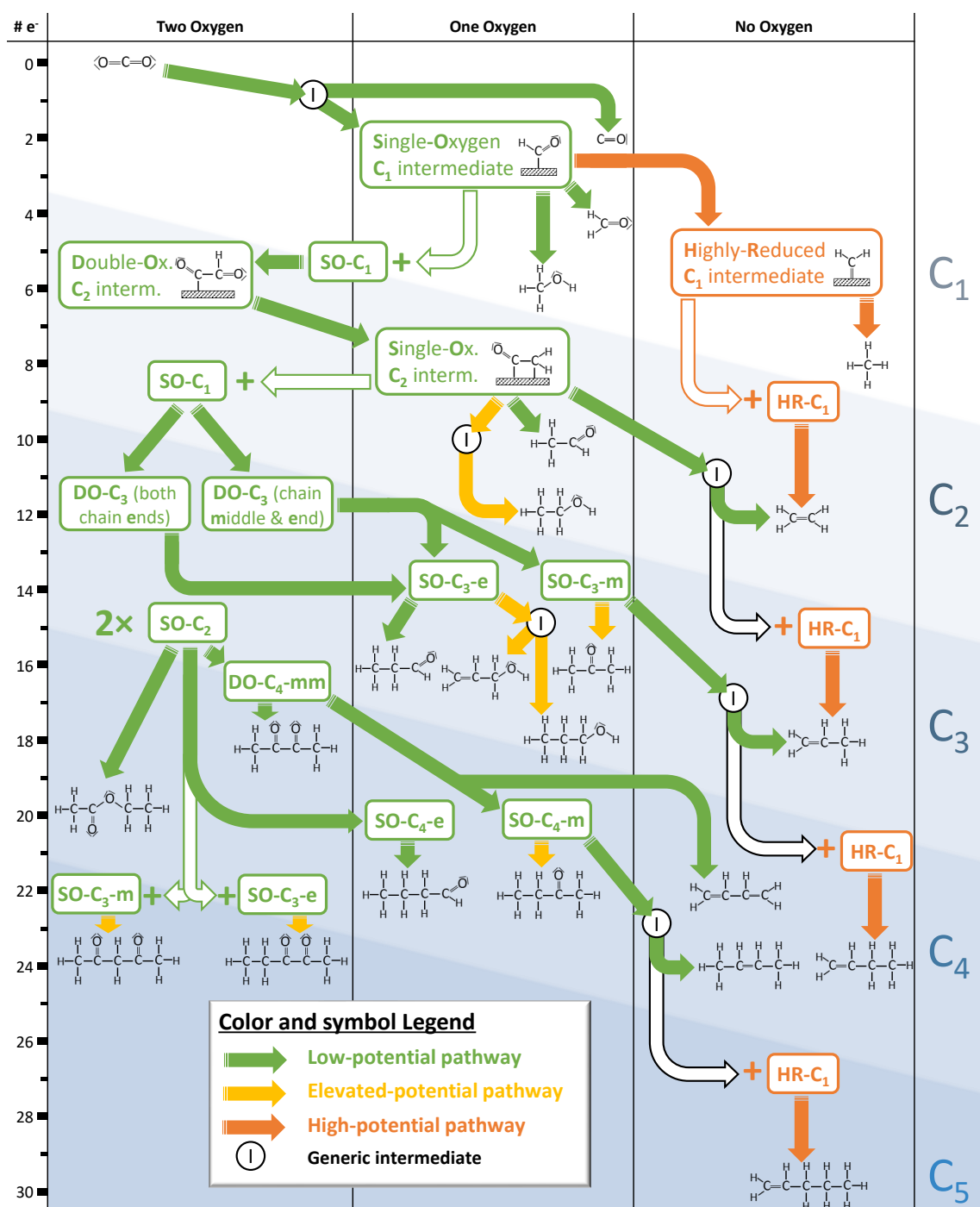


**Figure 7:** Overview of identified electrocatalytic CO<sub>2</sub> reduction products, supplemented by the reaction mechanism hypothesized in this study and likely key intermediates. The separation by number of carbon and oxygen as well as number of electrons transferred makes this graph a useful template for further mechanism discussion in the form established by Nitopi et al. [3].

Most of the proposed eCO<sub>2</sub>R mechanisms rely on the assumption of coupling steps being rate- and selectivity-determining [4, 17, 22, 45] as do the hypotheses formulated in this study. We find the degree of reduction of C<sub>1</sub> intermediates before coupling to be key. While there is an ongoing discussion around the C<sub>1</sub> intermediate responsible for dimerisation at small applied potentials [42, 46, 47], our proposed reaction paths are satisfied by postulating any single-oxygenated C<sub>1</sub> intermediate. As a second main contributor for larger applied potentials, we also postulate a non-oxygenated, highly-reduced C<sub>1</sub> intermediate (most likely \*CH<sub>2</sub>) in agreement with recent studies [18, 27].

We hypothesise most products are formed by initial coupling via the low-potential pathway. We believe the double-oxygenated C<sub>2</sub> intermediate resulting from the coupling is quickly reduced to break at least one of the C-O bonds as no double-oxygenated products for C<sub><4</sub> are detected. The resulting single-oxygenated C<sub>2</sub> intermediate can couple again with other single-oxygenated intermediates or be further reduced via respective paths with different activation barriers. This way, a pattern emerges for ever-longer carbon chains. For C<sub>4+</sub> formation, we speculate the coupling takes place between two of these single-oxygenated multi-carbon intermediates followed by less immediate C-O bond breaking and concurrent production of double-oxygenated species. We speculate the coupling reactions are driven by interactions between more oxidised carbon atoms, explaining the higher prevalence of mid-chain oxygen for C<sub>4</sub> and C<sub>5</sub>.

According to our hypothesis, further reduction of single-oxygenated intermediates depends mostly on the position of the oxygen: While mid-chain oxygen leads to the formation of alk-2-enes or alkadienes as illustrated in Fig. 5, end-chain oxygen leads to aldehydes if the electrochemical cell is operated at low currents. Increasing potentials favour different reaction paths of these single-oxygenated intermediates, further reduction of end-chain oxygen leading to alcohols and a different sequence of hydrogenating mid-chain oxygen leading to ketones.

Chain-end oxygen generally seems to lead to a wider variety of less-reduced products. For example, the double-oxygenated C<sub>3</sub> intermediate with oxygen on both chain ends can be assumed a precursor also to acrolein, following the established framework. Polymerizing acrolein has been demonstrated as a failure mechanism of copper-based GDEs [26] so stabilizing mid-chain oxygen over end-chain oxygen could be a way to increase longevity of GDEs. This might be achieved by topological engineering as selectivities and overall activity of eCO<sub>2</sub>R are significantly determined by surface facets and respective binding energies [39, 48].

If the applied potential is increased beyond a certain point, the coverage of oxygenated intermediates declines as highly-reduced intermediates begin to dominate. The coupling of abundant highly-reduced C<sub>1</sub> intermediates with another multi-carbon intermediate explains the increased production of alk-1-enes. At this point, HER is expected to start dominating eCO<sub>2</sub>R.

## 4 Conclusions

In summary, we analysed the hydrocarbons produced via electrocatalytic CO<sub>2</sub> reduction within a gas-diffusion electrode using a GC-MS with a high-resolution PTR-TOF-MS. We identified more than 20 distinct products - confirming 10 hitherto unknown ones, including multiple C<sub>5</sub> species. The product separation in the GC column allowed us to identify minor products and closely related isomers that are hard to distinguish with conventional mass spectrometry. Meanwhile, the proton-transfer reactions led to a large number of different secondary ions and fragments that could be analysed by the high-resolution time-of-flight sensor with high accuracy. This helped us to identify and quantify products

By carefully post-processing and integrating the measured intensities, we were able to compare signals across different experiments within the same ion and species. We established a relative measure for Faradaic Efficiency and verified the trends between different secondary ions of the same species. Developing these relative Faradaic Efficiencies across different applied potentials revealed selectivity trends of the different species that can be grouped by the shape of their curves. This helped investigate the complex eCO<sub>2</sub>R mechanism that accounts for the map of identified products, considering reduction levels and the number of carbon as well as oxygen atoms.

We derived three key hypotheses based on careful observations and a few largely accepted assumptions. These extend our partial understanding of the eCO<sub>2</sub>R mechanism for high-current GDEs at high pH as constructed in Fig. 7. In addition, Fig. 8 summarises and illustrates the main hypotheses in a more abstract manner.

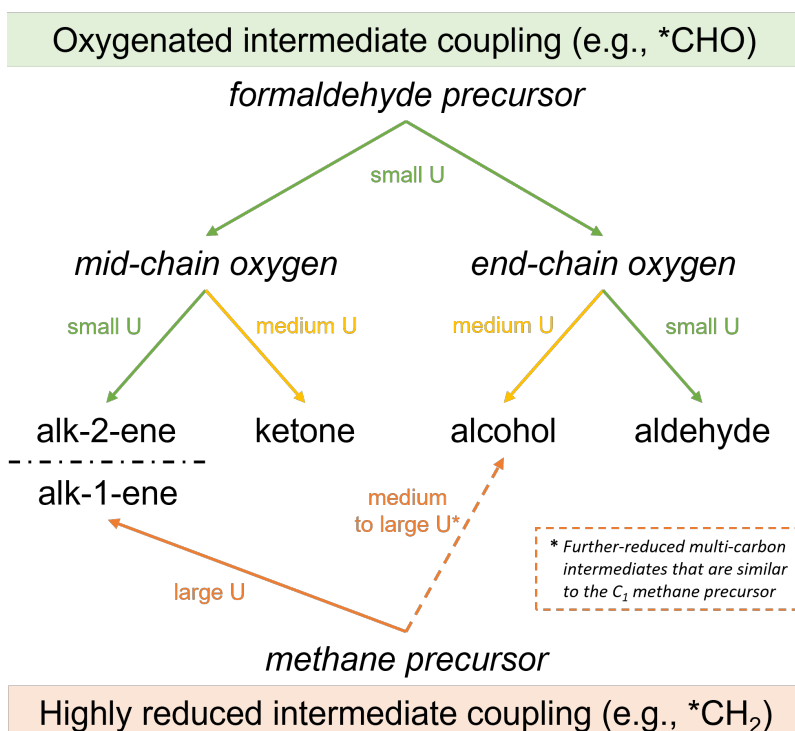


**Figure 8:** General hypotheses regarding the eCO<sub>2</sub>R mechanism.

The first and most important hypothesis details the mechanism of the two distinct pathways towards ethylene which have been acknowledged in many previous studies. We postulate reaction steps for forming double bonds either on the ends or the middle of the carbon chain depending on applied potentials. The low-potential pathway is based on the coupling reaction between oxygenated intermediates (e.g., \*CHO) and the subsequent formation of double bonds towards the centre of the molecule via the dissociation of water. The high-potential pathway is based on the addition of a highly-reduced, non-oxygenated intermediate (e.g., \*CH<sub>2</sub>) to the end of a molecule, immediately forming a double bond. This hypothesis is firstly supported by selectivity trends of 1-butene and 1-pentene coinciding with that of methane, as the highly-reduced intermediate would be its precursor, and only C<sub>4+</sub> species develop pure alk-1-enes. Secondly, the selectivity trend of trans-2-butene coincides with that of carbon monoxide and formaldehyde, as the initial oxygenated intermediate would be its precursor. The selectivity trends of the well-known products ethylene and propylene exhibit a mixture of both trends as they can form by either of the two mechanisms - reaching peak Faradaic Efficiency at small applied potentials that are not decreasing sharply with larger potentials but rather converging to a constant production level even for large currents.

The second hypothesis states that all other oxygen-containing products likely form by a similar mechanism of initial coupling via an oxygenated C<sub>1</sub> intermediate but are not fully reduced to pure hydrocarbons. The dissociation of the first oxygen is rapid for the C<sub>2</sub> and C<sub>3</sub> intermediate, which is thought to be formed by iterative coupling with the same oxygenated C<sub>1</sub> intermediate. These single-oxygenated intermediates can now couple again, forming C<sub>4</sub> and C<sub>5</sub> products. The orientation of coupling intermediates and the sequence of subsequent reduction steps are critical as they decide the position of oxygen. Based on mid- or end-chain oxygen intermediates, ketones, aldehydes, and alcohols are produced. The third hypothesis concerns the potential-dependence of different product types with a common oxygenated multi-carbon intermediate. While mid-chain oxygen leads to the formation of mostly alk-2-enes at very small voltages, as stated in the first hypothesis, elevated potentials lead to increased ketone production. This is most likely caused by a different sequence of hydrogenation steps. Intermediates with end-chain oxygen mostly form aldehydes at small voltages, but the further reduction to primary alcohols becomes more prevalent with elevated potentials. It is unclear if further-reduced multi-carbon intermediates similar to the methane precursor play a role in forming these (especially unsaturated) alcohols.

In conclusion, we monitored minor C<sub>3</sub>-C<sub>5</sub> products to reveal significant and generalisable insights into the eCO<sub>2</sub>R mechanism. We found that positional isomerism in intermediates is particularly important for product selectivity. This is most apparent for alkenes but also for aldehydes and ketones. As most of consequential product isomerisms only start to exist for C<sub>3-4</sub> species, longer-chain products play a critical role as mechanistic indicators.

The presented data is by no means exhausted with the discussion in this work. Further utilisation of the results by other researchers is possible and encouraged. Especially the mechanism discussion, which is an ongoing and disputable subject, can be complemented by the comprehensive map provided in Fig. 7. Further studies investigating some of the more obscure species and trends found in this work are needed. Understanding the underlying mechanism of eCO<sub>2</sub>R on a first-principle basis is critical for the design and

optimisation of CO<sub>2</sub> utilisation processes. These processes are in turn essential to mitigate climate change as negative emission technologies will be necessary to achieve the goals set out in the Paris climate agreement [1]. Moreover, they could convert the hard-to-decarbonise sector of chemicals into a negative emissions sector, because CO<sub>2</sub> would be captured and effectively stored in a variety of products that are at present produced from fossil resources.

## **Research data**

Research data supporting this publication is available in the University of Cambridge data repository ([doi:10.17863/CAM.91052](https://doi.org/10.17863/CAM.91052)).

## **Conflicts of interest**

There are no conflicts to declare.

## **Acknowledgements**

This work was supported by the National Research Foundation (NRF), Prime Minister's Office, Singapore under its Campus for Research Excellence and Technological Enterprise (CREATE) programme through the eCO<sub>2</sub>EP project operated by Cambridge Centre for Advanced Research and Education in Singapore (CARES) and the Berkeley Education Alliance for Research in Singapore (BEARS). art of this work was supported by Towards Turing 2.0 under the EPSRC Grant EP/W037211/1 and The Alan Turing Institute. S. D. Rihm acknowledges financial support from Fitzwilliam College, Cambridge, and the Cambridge Trust. M. Kraft gratefully acknowledges the support of the Alexander von Humboldt Foundation.

For the purpose of open access, the author has applied a Creative Commons Attribution (CC BY) licence to any Author Accepted Manuscript version arising.

# Nomenclature

## Upper-case Roman

- I* Signal intensity (counts per second)
- J* Electric current
- U* Applied potential

## Lower-case Greek

- $\delta$  Shift of isotope ratio of a product in relation to expected natural abundance
- $\eta$  Efficiency measure (for example Faradaic Efficiency or relative FE)

## Abbreviations

- eCO<sub>2</sub>R Electrochemical CO<sub>2</sub> Reduction
- GC-MS Gas-chromatography mass-spectrometry
- ET Elution time
- rFE Relative Faradaic Efficiency
- GDE Gas-diffusion electrode
- HER Hydrogen Evolution Reaction
- IIP Intermediate-indicating product
- MS Mass Spectrometry
- PA Proton Affinity
- PCET Proton-coupled Electron Transfer
- PI Primary Ion
- PTR Proton-transfer reaction
- RHE Reversible Hydrogen Electrode
- RRC Reaction rate constant
- SNR Signal-to-noise ratio
- SIFT Selected Ion Flow Tube
- TOF Time of flight

## A Electrochemistry measurements

During the experiments, the potential applied against the Hg/HgO the reference electrode was controlled and current measured. For better comparison, we convert all voltages to reference other standards: First we convert to Standard Hydrogen Electrode (SHE) and then to the pH-independent Reversible Hydrogen Electrode (RHE) as follows:

$$U_{\text{SHE}} = U_{\text{Hg/HgO}} + 0.098 \text{ V} \quad (\text{A.1})$$

$$U_{\text{RHE}} = U_{\text{SHE}} + 0.828 \text{ V} \quad (\text{A.2})$$

Before the GC-MS measurements were conducted, a Frequency Response Analysis (FRA) was carried out to determine the internal resistance for iR compensation, see Fig. 9. At high frequencies, the Faradaic resistance of the electrode-electrolyte interface drops to zero because of the double-layer capacitance. At this point, the imaginary part of the impedance is gone and we get  $R_i = \Re(Z_0)$  with  $\Im(Z_0) \approx 0$ .

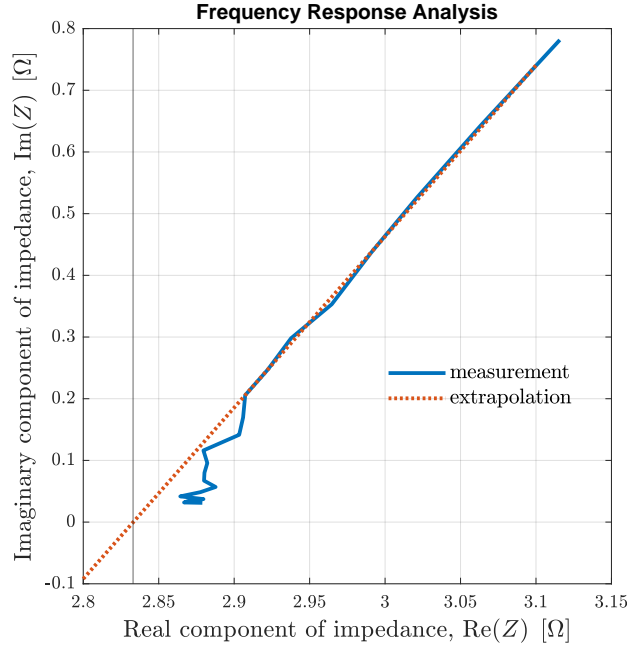


**Figure 9:** Complex impedance measured in FRA.

It is best practice to multiply with a correction factor of 0.7 [49], so we get

$$R_i = \Re(Z_0) \cdot 0.7 = 1.981 \Omega \quad (\text{A.3})$$

The final iR compensation is then applied via

$$U_{\text{RHE}}^{\text{corr}} = U_{\text{RHE}} - I_{\text{cell}} \cdot R_i + \frac{RT}{F} \ln(10) \cdot \text{pH} \quad (\text{A.4})$$

with the assumption of  $\text{pH} = 14$ . Relevant values are given in Tab. 3.

**Table 3:** Conversion and compensation of applied potential during the measurements.

	time	Applied potential [mV]						
		2000	2500	3000	3500	4000	4500	5000
$U_{\text{Hg/HgO}}$	5 min	-2000	-2500	-3001	-3501	-4000	-4500	-4999
	30 min	-2000	-2501	-3001	-3500	-4000	-4500	-4998
	average	-2000	-2501	-3001	-3500	-4000	-4500	-4999
Current	5 min	-188	-405	-523	-762	-922	-1003	-1624
	30 min	-190	-417	-554	-786	-901	-1049	-1702
	average	-189	-414	-541	-760	-909	-1054	-1654
$U_{\text{SHE}}$	5 min	-1902	-2402	-2903	-3403	-3902	-4402	-4901
	30 min	-1902	-2403	-2903	-3402	-3902	-4402	-4900
	average	-1902	-2403	-2903	-3402	-3902	-4402	-4901
$U_{\text{RHE}}$	5 min	-1073	-1574	-2075	-2575	-3074	-3573	-4073
	30 min	-1074	-1575	-2075	-2574	-3074	-3573	-4072
	average	-1074	-1574	-2075	-2574	-3074	-3573	-4073
$U_{\text{RHE}}^{\text{corr}}$	5 min	-701	-772	-1038	-1065	-1247	-1586	-855
	30 min	-697	-749	-979	-1016	-1289	-1494	-701
	average	-700	-755	-1004	-1069	-1273	-1486	-797

As we can see in Fig. 10, the absolute compensated applied potential vs. RHE seems to decrease while the uncorrected applied potential is increased. The reasons are probably that internal surface area has increased by wetting/restructuring and/or decrease of  $iR$ . This is supported stark by drop in  $\text{CO}_2$  and  $\text{H}_2\text{CO}_3$  registered for the largest current which indicates a high  $\text{CO}_2\text{R}$  rate. There is probably also lots of hydrogen being produced.

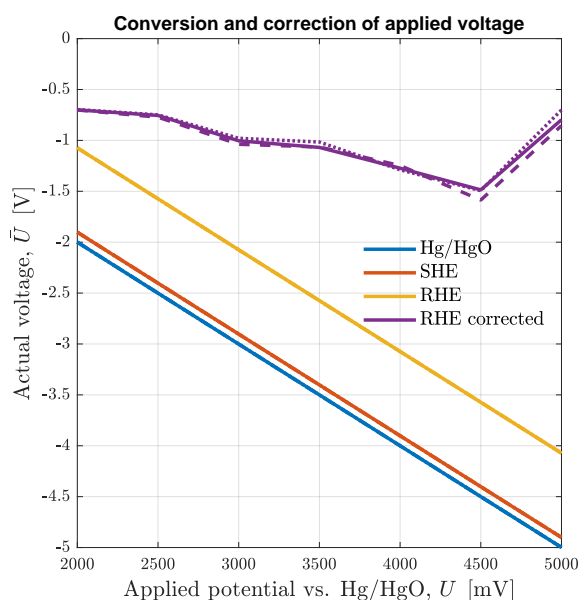


**Figure 10:** Converted and compensated applied potential values.

## B Gas Chromatography

The exhaust of flow cell was directed into the sampling loop of an Agilent 7890 gas chromatograph (GC). Packed column Hayesep D was used to separate products. In order to extract also products that would take an impractical large amount of time to elute from the column, it was heated up in two steps, see appendix B.1. For the species identification, we rely on some well-known (relative) retention times for this specific column, see B.2. These can be put into absolutes and compared to species found.

### B.1 Heating procedure

The heating protocol of the column started off at  $T_1 = 70^\circ\text{C}$  which was held for 3 min. A first heating ramped followed with a rate of  $40^\circ\text{Cmin}^{-1}$  until  $T_2 = 125^\circ\text{C}$  was reached and held again for 2 min. A final rate with the same rate of  $40^\circ\text{Cmin}^{-1}$  brought the temperature up to a final  $T_3 = 200^\circ\text{C}$  which was held for 40 min until the end of the experiment.

Fig. 11 shows the temperature curve. The first heating ramp starts after  $t_{1A} = 180\text{ s} = 3\text{ min}$  and ends after  $t_{1B} = 262.5\text{ s} = 4.375\text{ min}$ . The second heating ramp starts after  $t_{2A} = 382.5\text{ s} = 6.375\text{ min}$  and ends after  $t_{2B} = 495\text{ s} = 8.25\text{ min}$ . Heating ends after  $t_3 = 2895\text{ s} = 48.25\text{ min}$ .

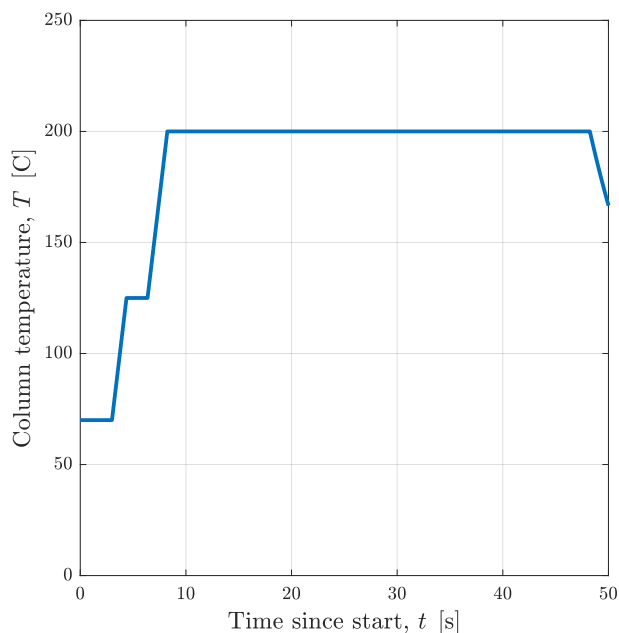


**Figure 11:** Heating protocol of the GC column used in the experiment.

The heating causes some of the polymers that make up the stationary phase to disintegrate so they are detected by the PTR-MS. This happens continuously it only leads to a shift of the signals' baselines that needs to be accounted for. This is shown exemplary for the

$C_3H_7O^+$  trace which exhibits a clear two-step-plateau. Start and end are marked with vertical lines at  $t_1 = 3.4$  min,  $t_2 = 6.8$  min, and  $t_3 = 48$  min. This shows that - as expected - the heating leads to an increase in detected counts per second with a slight delay of a few seconds.

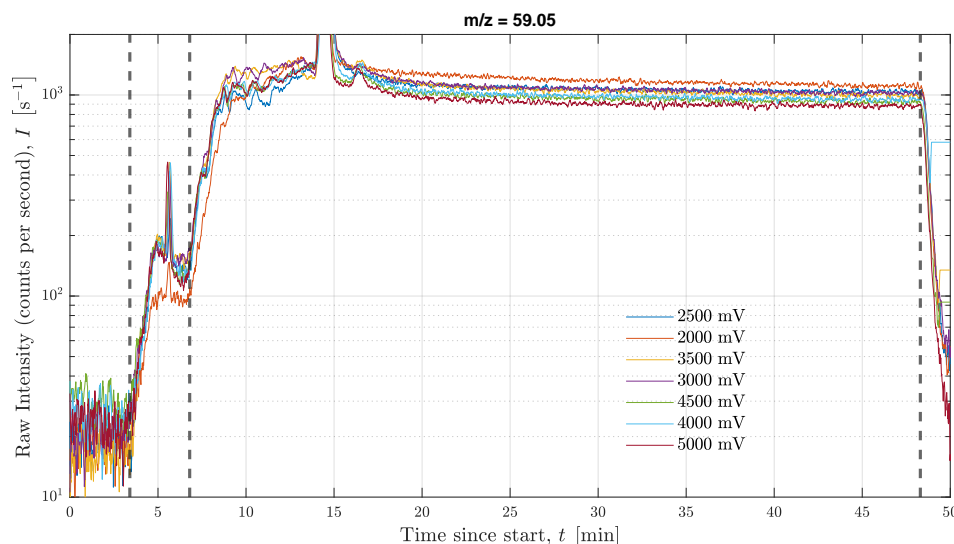


**Figure 12:** Signals for  $C_3H_7O^+$  trace ( $m/z = 59.05$  Da).

## B.2 Documented retention times

Estimated (relative) retention times for the Hayesep D column are based on manufacturer information and published chromatograms listed below.

1. <https://www.vici.com/columns/r-index-d.php> [50]
2. <https://www.vici.com/hayesep/rettimes.php> [51]
3. [https://www.vici.com/hayesep/hsd\\_c11.php](https://www.vici.com/hayesep/hsd_c11.php) [52]
4. <https://www.vici.com/columns/d-mix.php> [53]

The first listed reference contains the most data and is used as a reference for all the others. In order to compare retention times across different sources (therefore experimental conditions like temperature and carrier gas), a calibration is necessary. Data from the three other sources was adjusted by picking two respective species that are also part of the first (or another already adjusted) data set and making sure their values match without violating relative retention times within a data set. Tab. 4 shows documented (i.e. value read from table or diagram) and adjusted values.

**Table 4:** *Relative retention times of different hydrocarbons for Hayesep D column compiled and adjusted from different sources, all given in seconds for better distinction. Documented values (“doc.”) are taken from tables or read from diagrams in respective sources listed above. For the adjusted values (“adj.”), two species highlighted in yellow are chosen for which adjusted values from another source are available and all values from this source are linearly adjusted (first species used to fix intersection, the second for the slope).*

compound	Source 1	Source 2		Source 3		Source 4		result
	doc.	doc.	adj.	doc.	adj.	doc.	adj.	
hydrogen						95	89	89
methane	100	102	100			107	100	100
air		54	88					88
acetylene	180			101	154			154 to 180
ethylene	184	366	166	113	166			166 to 184
carbon dioxide		186	121			132	122	121 to 122
acetylene		348	161					161
ethane	200	504	200					200
methanol	284							284
propylene	290			235	290			290
propane	300							300
propadiene								
propyne	304							304
acetaldehyde	335							335
isobutane	381							381
1-butene	389			347	404			389 to 404
1,3-butadiene	390							390
butane	400							400
trans-2-butene	400							400
acetonitrile	403							403
cis-2-butene	404							404
acetone	441							441
methylene chloride	451							451
isopentane	485							485
carbon monoxide						99	93	93
pentane	500							500
water		516	203					203
1-pentene				518	578			578
1-hexene				836	901			901
chloroform	543							543
ethyl acetate	560							560

### B.3 Absolute retention times

To help with species identification, the relative retention times compiled in appendix B.2 need to be adjusted to fit the experimental conditions at hand. This is done for the three different temperatures of the heating protocol discussed in appendix B.1. For each, a reference species is chosen the existence of which is certain: methane, ethylene, propylene. In Tab. 5 the adjusted values are shown for each regime and compared to the retention times measured in our experiment - in reality of course these values have partially helped to actually identify these species as discussed in appendix D.

**Table 5:** Documented, adjusted, and measured retention times of relevant hydrocarbons, all given in seconds for better distinction. For each section of the heating protocol, a calibration was made to fit a reference species highlighted in yellow.

compound	documented see Tab. 4	adjusted to temperature			experiment $U_{\text{Hg}/\text{HgO}} = 3 \text{ V}$
		$T_1$	$T_2$	$T_3$	
air	88	152	179	166	
hydrogen	89	155	182	169	
carbon monoxide	93	160	188	175	132
methane	99	172	202	188	173
carbon dioxide	121	209	246	228	231
acetylene	154	267	314	291	
acetylene	159	275	324	301	
ethylene	166	287	304	313	338
ethane	200	346	407	378	
water	203	351	413	384	
methanol	284	491	578	536	425
propylene	290	502	591	548	548
propane	300	519	611	567	
propyne	304	526	619	574	
acetaldehyde	335	580	682	633	628
propadiene	354	612	720	668	
isobutane	381	659	776	720	
1-butene	389	673	792	735	720
1,3-butadiene	390	675	794	737	730
butane	400	692	814	756	
trans-2-butene	400	692	814	756	744
cis-2-butene	404	699	823	764	761
acetone	441	763	898	833	918
isopentane	485	839	987	916	
pentane	500	865	1018	945	
ethyl acetate	560	969	1141	1059	1397
1-pentene	578	1000	1177	1092	1026
1-hexene	901	1559	1835	1703	

## C Methodology

Large amounts of data are generated during the experiment by the PTR-MS: Every second of the experiment, counts for specific masses are registered and saved. These need to be assigned to traces that can be then used for species identification and analysis. In total, three main steps are necessary to identify species, isolate data associated with them and calculate indicative measures for these species that can be displayed for the different applied potentials:

1. Separation and export of traces
2. Assignment of traces and identification of species
3. Deconvolution of species' traces and data analysis

The workflow is illustrated in Fig. 13: A 3-dimensional data set (for each measurement) is first broken down into a number of discrete 2-dimensional data sets, see appendix C.1. These are then split into smaller 2-dimensional data sets (along the time dimension) and assigned to groups (species), see appendix C.3. Some post-processing is done to each data set of each group to produce some measure of concentration or isotope fraction that can be compared to the same measure from other experiments (or even other groups), see appendix C.3.

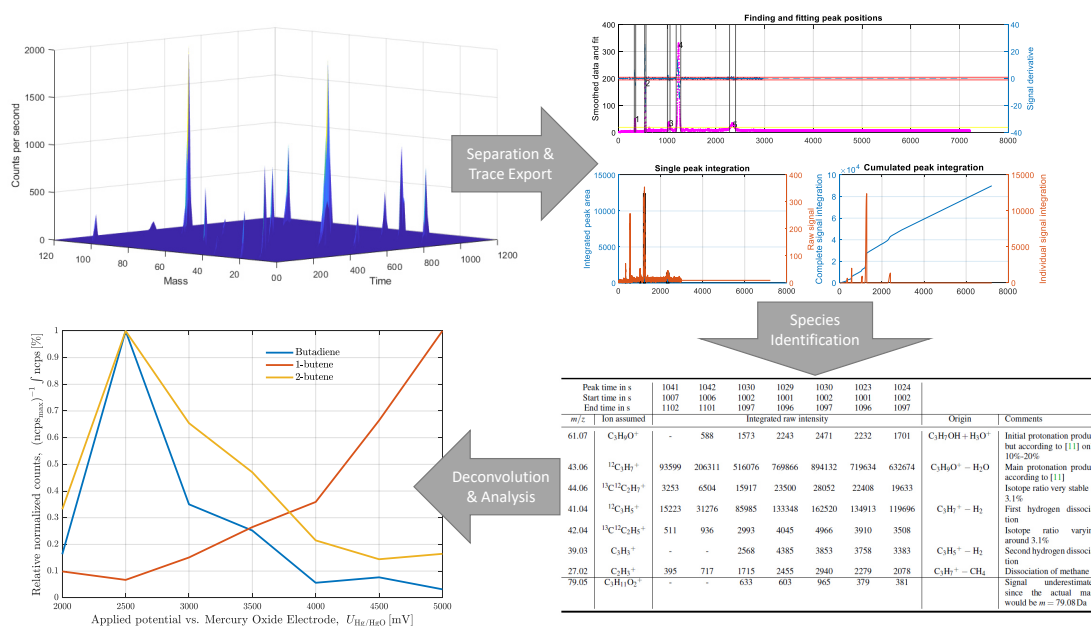


**Figure 13:** General workflow of data analysis for GC-MS experiments conducted.

## C.1 Separation and Export

Original PTR-TOF-MS data was collected in cycles of 1 s where detector signal was averaged for each cycle period and recorded into a file. Consecutive collection of cycles was further evaluated with the PTRMS Viewer software [54] in order to extract intensities of each trace over time. Peaks were fitted with Pseudo-Vougt function as it found to be most accurate in simulating its areas. For the 7 main measurements conducted, 75 traces were exported for further analysis. They are listed in Tab. 6 with their masses and the ion the trace was based on. Each of them was selected for at least one of the following reasons:

- Clear peak was detected
- Known ionization product of common hydrocarbon
- Isotope of trace with large signal
- Keeping track of primary ions and water clusters

**Table 6:** List of all exported traces with their mass-to-charge ratio and the composition of the ion this export was based on. Formulas refer to the most common isotopes if not specified otherwise - then the exception applies to one of the atoms. All traces with signal plateaus due to GC heating are highlighted, minor baseline shifts in green and major ones in yellow.

$m/z$ [Da]	trace	$m/z$ [Da]	trace	$m/z$ [Da]	trace
21.022	H <sub>3</sub> O <sup>+</sup> (O <sub>18</sub> )	46.037	C <sub>2</sub> H <sub>5</sub> O <sup>+</sup> (C <sub>13</sub> )	73.028	C <sub>3</sub> H <sub>5</sub> O <sub>2</sub> <sup>+</sup>
26.016	C <sub>2</sub> H <sub>2</sub> <sup>+</sup>	47.013	CH <sub>3</sub> O <sub>2</sub> <sup>+</sup>	73.066	C <sub>4</sub> H <sub>9</sub> O <sup>+</sup>
27.023	C <sub>2</sub> H <sub>3</sub> <sup>+</sup>	47.049	C <sub>2</sub> H <sub>7</sub> O <sup>+</sup>	77.060	C <sub>3</sub> H <sub>9</sub> O <sub>2</sub> <sup>+</sup>
28.032	C <sub>2</sub> H <sub>4</sub> <sup>+</sup>	48.052	C <sub>2</sub> H <sub>7</sub> O <sup>+</sup> (C <sub>13</sub> )	78.063	C <sub>3</sub> H <sub>9</sub> O <sub>2</sub> <sup>+</sup> (C <sub>13</sub> )
29.039	C <sub>2</sub> H <sub>5</sub> <sup>+</sup>	53.040	C <sub>4</sub> H <sub>5</sub> <sup>+</sup>	79.039	C <sub>2</sub> H <sub>7</sub> O <sub>3</sub> <sup>+</sup>
31.018	C <sub>2</sub> H <sub>6</sub> <sup>+</sup>	55.038	H <sub>7</sub> O <sub>3</sub> <sup>+</sup>	79.056	C <sub>6</sub> H <sub>7</sub> <sup>+</sup>
31.019	C <sub>2</sub> H <sub>3</sub> O <sup>+</sup>	55.055	C <sub>4</sub> H <sub>7</sub> <sup>+</sup>	79.075	C <sub>3</sub> H <sub>11</sub> O <sub>2</sub> <sup>+</sup>
33.033	C <sub>2</sub> H <sub>5</sub> O <sup>+</sup>	57.070	C <sub>4</sub> H <sub>9</sub> <sup>+</sup>	83.049	C <sub>5</sub> H <sub>7</sub> O <sup>+</sup>
33.994	O <sub>2</sub> <sup>+</sup> (O <sub>18</sub> )	58.041	C <sub>3</sub> H <sub>6</sub> O <sup>+</sup>	83.086	C <sub>6</sub> H <sub>11</sub> <sup>+</sup>
34.037	CH <sub>5</sub> O <sup>+</sup> (C <sub>13</sub> )	59.050	C <sub>3</sub> H <sub>7</sub> O <sup>+</sup>	85.028	C <sub>4</sub> H <sub>5</sub> O <sub>2</sub> <sup>+</sup>
37.028	H <sub>5</sub> O <sub>2</sub> <sup>+</sup>	60.052	C <sub>3</sub> H <sub>7</sub> O <sup>+</sup> (C <sub>13</sub> )	86.036	C <sub>4</sub> H <sub>6</sub> O <sub>2</sub> <sup>+</sup>
39.025	C <sub>3</sub> H <sub>3</sub> <sup>+</sup>	61.029	C <sub>2</sub> H <sub>5</sub> O <sub>2</sub> <sup>+</sup>	87.045	C <sub>4</sub> H <sub>7</sub> O <sub>2</sub> <sup>+</sup>
40.031	C <sub>3</sub> H <sub>4</sub> <sup>+</sup>	61.065	C <sub>3</sub> H <sub>9</sub> O <sup>+</sup>	89.058	C <sub>4</sub> H <sub>9</sub> O <sub>2</sub> <sup>+</sup>
41.039	C <sub>3</sub> H <sub>5</sub> <sup>+</sup>	63.044	C <sub>2</sub> H <sub>7</sub> O <sub>2</sub> <sup>+</sup>	91.083	C <sub>4</sub> H <sub>11</sub> O <sub>2</sub> <sup>+</sup>
42.042	C <sub>3</sub> H <sub>6</sub> <sup>+</sup>	63.008	CH <sub>3</sub> O <sub>3</sub> <sup>+</sup>	93.070	C <sub>7</sub> H <sub>9</sub> <sup>+</sup>
43.018	C <sub>2</sub> H <sub>3</sub> O <sup>+</sup>	64.047	C <sub>2</sub> H <sub>7</sub> O <sub>2</sub> <sup>+</sup> (C <sub>13</sub> )	97.101	C <sub>7</sub> H <sub>13</sub> <sup>+</sup>
43.055	C <sub>3</sub> H <sub>7</sub> <sup>+</sup>	64.011	CH <sub>3</sub> O <sub>3</sub> <sup>+</sup> (C <sub>13</sub> )	101.060	C <sub>5</sub> H <sub>9</sub> O <sub>2</sub> <sup>+</sup>
43.989	CO <sub>2</sub> <sup>+</sup>	65.061	C <sub>2</sub> H <sub>9</sub> O <sub>2</sub> <sup>+</sup>	103.075	C <sub>5</sub> H <sub>11</sub> O <sub>2</sub> <sup>+</sup>
44.021	C <sub>2</sub> H <sub>3</sub> O <sup>+</sup> (C <sub>13</sub> )	66.063	C <sub>2</sub> H <sub>9</sub> O <sub>2</sub> <sup>+</sup> (C <sub>13</sub> )	105.091	C <sub>5</sub> H <sub>13</sub> O <sub>2</sub> <sup>+</sup>
44.058	C <sub>3</sub> H <sub>7</sub> <sup>+</sup> (C <sub>13</sub> )	67.054	C <sub>4</sub> H <sub>3</sub> O <sup>+</sup>	107.070	C <sub>4</sub> H <sub>11</sub> O <sub>3</sub> <sup>+</sup>
44.998	CO <sub>2</sub> H <sup>+</sup>	69.069	C <sub>5</sub> H <sub>9</sub> <sup>+</sup>	107.088	C <sub>8</sub> H <sub>11</sub> <sup>+</sup>
45.033	C <sub>2</sub> H <sub>5</sub> O <sup>+</sup>	71.049	C <sub>4</sub> H <sub>7</sub> O <sup>+</sup>	119.086	C <sub>9</sub> H <sub>11</sub> <sup>+</sup>
46.000	CO <sub>2</sub> H <sup>+</sup> (C <sub>13</sub> )	71.086	C <sub>5</sub> H <sub>11</sub> <sup>+</sup>		

It is important to keep in mind that the traces will inevitably also include signals of other ions with very similar masses. For example, the difference in mass between an additional hydrogen atom and an additional neutron in one of the carbon atoms is  $\approx 0.002$  Da and therefore beyond the resolution of our PTR-MS. Furthermore, shifting baseline signals due to GC heating (see appendix B.1) were observed for a majority of traces.

This is related to the reason why we did not use an available software tool such as AMDIS for signal deconvolution and product identification. First of all, there is no extensive PTR-TOF-MS database available. Furthermore, deconvolution needs to be done differently as overlaps are observed on the mass as well as the time axis and while the TOF sensor can actually discriminate between ions of very similar atomic mass units. Deconvolution of different traces at similar times is not the main issue here but rather that of the same or similar (overlapping) traces at similar times. Lastly, the subtraction of complex rising and falling baselines due to GC heating other systemic effects needed to be done manually.

## C.2 Species Identification

After exporting the traces, their signals were analysed and peaks detected in an automated fashion. For this, the signal data was smoothed by a moving average with a window length of  $\Delta t = 10$  s. The derivative of the smoothed signal was then approximated by the difference quotient. Based on detected baseline noise levels (via median signal values and derivatives), different thresholds for smoothed signal and derivative were set as shown in Fig. 14. When certain conditions were met, a peak was identified. For peak location the time with the maximum smoothed signal value was chosen, peak boundaries were set at the times signal and derivative fell below defined thresholds again.

The example trace in Fig. 14 exhibits two plateaus due to GC heating as described in B.1. For the peaks on different baselines, the signals can be separated into different temperature regimes and re-processed separately if peak detection is unclear - which is not the case here. Location of peaks and plateaus can be double-checked manually by looking at cumulated signal counts - jumps constitute peaks and constant slopes constitute plateaus.

All detected peaks of all recorded traces were then clustered according to the time of peak signal. A few notable time ranges emerged where for many traces peaks were recorded for all applied potentials. For some other time ranges, only few peaks were recorded at only some of the applied potentials. After elimination of some measurement artifacts, all these time ranges correspond with one or more detected species.

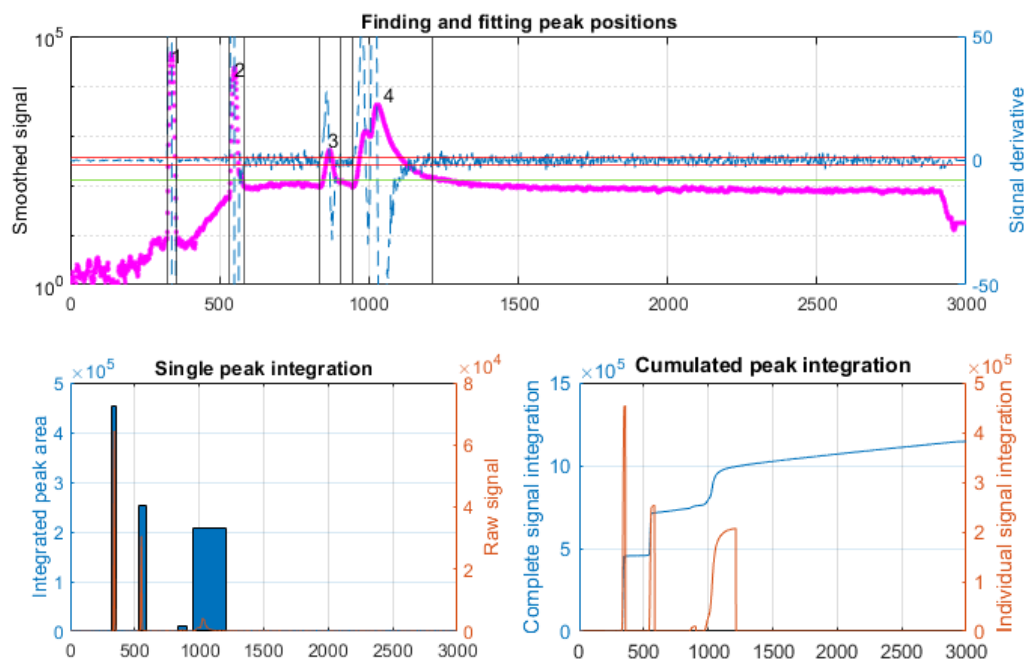


**Figure 14:** Exemplary peak detection for  $C_3H_5^+$  trace at  $U_{Hg/HgO} = 3500\text{mV}$ , all figures show experimental time in seconds on the x-axis. The top figure shows the smoothed signal data in pink and its derivative in blue. The left y-axis refers to the signal data and the green horizontal indicates the detected baseline signal. The right y-axis refers to the derivative and the red horizontal lines indicate expected noise boundaries. The detected peaks are numbered from 1-4 and their detected boundaries are indicated by black vertical lines. The bottom left figure shows raw signals and their values from integration over the detected boundaries. The bottom right figure shows the cumulated signal sum compared to individual peak contributions.

These species are most likely products of the electrocatalytic reduction of carbon dioxide and were identified (see appendix D) via one or multiple of these three benchmarks:

1. Comparison of the time at which a peak was detected to GC retention times given by the manufacturer (compiled and adjusted, see appendix B.3) or verified by us with pure substances
2. Comparison of traces peaking at the same time and their signal ratios with expected ions and fragments according to SIFT studies (see appendix E.1.2) or from analogy to similar species
3. Relative intensities of traces across applied potentials (compared to known species in existing literature, e.g. [2])

### C.3 Species Analysis

After assigning all peaks of all traces to certain species (or times), the signals are integrated within the determined boundaries of their peak. This integration is partially done already as part of the species identification process described in C.2 but re-done for the quantitative analysis. For a better separation of peaks as well as precise determination of peak time, signals are first smoothed via moving average as described before. The detected baseline is subtracted from the signal subsequently, which not only helps remove systematic errors (e.g. polymer disintegration from GC heating) but also separation of overlapping signals of species with similar elution times. For this reason, the underlying baseline was assumed to be a quadratic function from the boundary with the smaller signal value to the boundary with the larger signal value which results in the subtraction of  $2/3 \min(\overline{I(t_1)}, \overline{I(t_2)}) + 1/3 \max(\overline{I(t_1)}, \overline{I(t_2)})$  from the signal within the defined boundaries  $t_1$  and  $t_2$ . This is a suitable assumption since it removes a plateau efficiently (subtracted value will be close to linear average) as well as it deconvolutes overlapping peaks as the arm of a Gaussian function close to the peak is approximated well by a quadratic function. In a next step the signal is integrated within these boundaries by summing up the counts recorded for every second:  $\int_{t_1}^{t_2} I(t) = \sum_{j=x(t_1)}^{x(t_2)} I(x)$ .

For the absolute values (counts) listed in D, we use a moving average of window length  $\Delta t = 8$  s for the initial smoothing of the signal and an additional length  $t_b = 5$  s for the lower and upper boundaries to compute the baseline from mean values  $\overline{I(t_1)} = 1/t_b \sum_{j=x(t_1-t_b)}^{t_1} I(x)$  and  $\overline{I(t_2)} = 1/t_b \sum_{j=x(t_2)}^{t_2+t_b} I(x)$ . For an in-depth analysis of the data, additional post-processing is necessary to satisfy the following requirements: First of all, some measure of accuracy is needed (like standard deviation) which requires data sampling. Furthermore we need relative values so data points can be compared with one another - for this, two slightly different workflows have been established: the first in C.3.1 to calculate a relative Faradaic Efficiency for “internal” comparison (same trace or at least species across different applied potentials) and the second in C.3.2 to calculate trace fractions for “external” comparison (same applied potential across different traces or even species) and finally to compute a measure of the Kinetic Isotope Effect.

#### C.3.1 Measure for Faradaic efficiency

For FE we want to capture the full signal also in its width because for large concentrations peaks do not only get more intense but also broader due to the GC column. The tabulated signal integration values in D depend on the chosen parameters for post-processing, so these need to be sampled calculating a measure of accuracy. As is shown in Fig. 15, the post-processing of the signal is done many times for all possible combinations of window length for moving average, exact boundary location in relation to the detected ranges, and window length for baseline calculation at the boundaries. With over 1,000 data points generated, statistical operations can be carried out with confidence on the distribution at hand - specifically, mean and standard deviations are calculated.

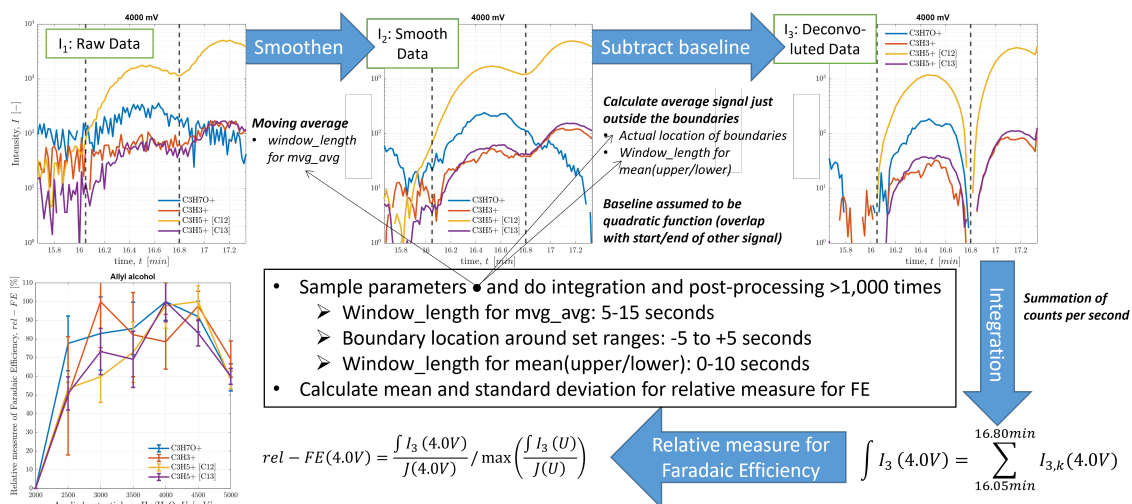


**Figure 15:** Data analysis workflow for obtaining relative intensities across applied potentials and specifically a (relative) measure for Faradaic Efficiencies.

Since exact rate constants for the PTR reactions are unavailable (see appendix E), we cannot calculate species concentrations and therefore Faradaic Efficiencies. A few steps can be taken though to come up with at least a relative measure for Faradaic Efficiencies (*rel - FE*): First, the integrated intensities are divided by the average current density measured at the corresponding applied potential. This way, the effect of larger currents leading to larger concentrations despite sinking (or stagnant) Faradaic Efficiencies is removed and we have a measure for CO<sub>2</sub>R selectivity. In a second step, all these values are normalized by dividing through the largest  $\int I/J$  as shown in Fig. 15. The resulting relative Faradaic Efficiencies now range from 0% to 100% (which is always the maximum) can now be compared between ions originating from the same species where they should exhibit similar values. The curves of different species (CO<sub>2</sub>R products) can also be compared to one another in a qualitative fashion.

### C.3.2 Measure for trace ratios

In order to quantify KIE but also the product ratios of proton transfer reactions in the PTR-MS (see appendix E), fractions of trace signals need to be calculated. In this case, using the full integrated signal between the detected boundaries would introduce a larger error due to the small signal of some minor traces and related higher noise levels further away from the peak. Since the calculation of fractions within the same experiment does not depend on the full range of the signal, we can use smaller ranges by sampling boundaries close to the actual peak location as shown in Fig. 16. While the window length for moving average smoothing is set constant ( $\Delta t = 8$  s, the baseline values at the boundaries used for deconvolution and noise subtraction are mean values from sampling close to the detected signal boundaries. With 1,000 integration ranges close to the peak location then being sampled and fractions of integrated signal calculated, statistical operations can be carried out with confidence on the distribution at hand - specifically, mean and standard deviations are calculated.

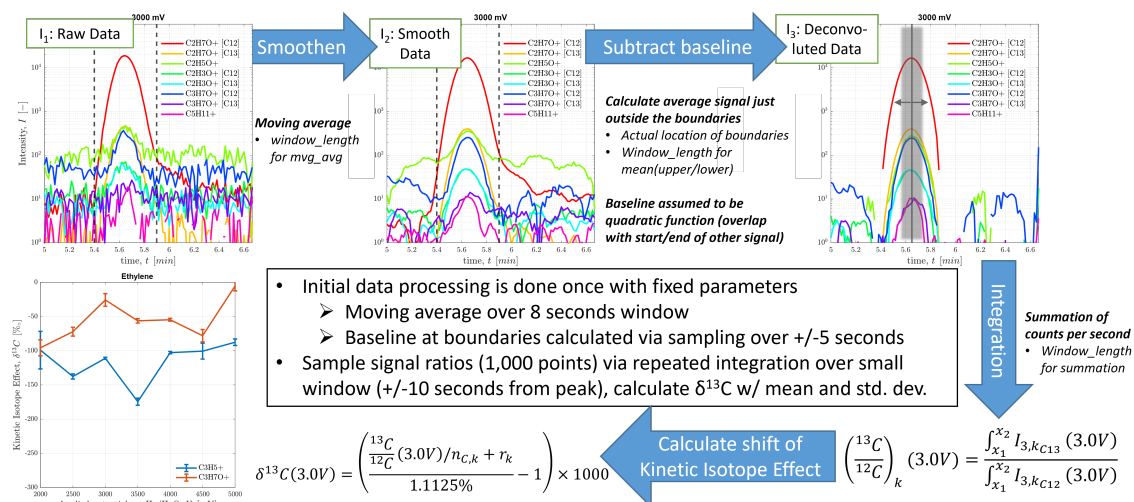


**Figure 16:** Data analysis workflow for obtaining signal ratios between fragments or isotopes and specifically a measure for the Kinetic Isotope Effect.

The Kinetic Isotope Effect can now be quantified by calculating the fraction of signal from a  $^{13}\text{C}$  isotope in relation to its corresponding  $^{12}\text{C}$  trace and comparing this fraction to the natural  $^{13}\text{C}$  abundance of 1.1125% [55]. In above Fig. 16,  $n_{\text{C},k}$  is the number of carbon atoms in the species and  $r_k$  a correction for calculating the shift caused by KIE. Details and results are give in appendix H.

## D Single species discussion

In this section the identification and analysis of individual species is discussed in detail.

An overview of all peak clusters (traces with signal peaks detected at the same times) and the corresponding species (CO<sub>2</sub>R products which were subsequently identified) is given in Tab. 7. The methodology deployed for clustering and identification is described in C.2.

**Table 7:** All detected peak clusters of specific retention times of the GC.

Retention time [s]	Species detected	Comment	
129 to 135	CO	Some protonation even though proton affinity is technically too small, see appendix D.1	
168 to 177	CH <sub>4</sub>	Proton affinity too small for protonation, see appendix D.2	
234 to 242	CO <sub>2</sub> /H <sub>2</sub> CO <sub>3</sub>	Some separation of carbonic acid into water and carbon dioxide components observable, see appendix D.3	
331 to 342	C <sub>2</sub> H <sub>4</sub>	Additional effects and reactions observed due to large concentration, see appendix D.4	
427 to 461	CH <sub>2</sub> O/CH <sub>3</sub> OH	Some dissolved methanol apparently not separable, see appendix D.5	
542 to 551	C <sub>3</sub> H <sub>6</sub>	Additional effects and reactions observed due to large concentration, see appendix D.6	
622 to 631	CH <sub>3</sub> CHO	Additional effects and reactions observed due to large concentration, see appendix D.7	
709 to 722	CH <sub>3</sub> CH <sub>2</sub> OH	Additional effects and reactions observed due to large concentration, see appendix D.8	
716 to 754	C <sub>4</sub> H <sub>8</sub> /C <sub>4</sub> H <sub>6</sub>	But(adi)ene isomers distinguishable, see appendix D.9	
770 to 788	c-C <sub>3</sub> H <sub>6</sub> ?	apparently cyclo-propane, see appendix D.10	
862 to 875	1-C <sub>3</sub> H <sub>6</sub> O	propanal	Constitutional isomers of C <sub>3</sub> H <sub>6</sub> O separated by GC, see appendix D.11
903 to 925	2-C <sub>3</sub> H <sub>6</sub> O	acetone	
985 to 993	CH <sub>2</sub> CHCH <sub>2</sub> OH	allyl alcohol	
1011 to 1029	C <sub>5</sub> H <sub>10</sub>	Pentene isomers distinguishable?	Peaks are quite close to each other, hard to distinguish; see appendix D.12
1027 to 1048	CH <sub>3</sub> CH <sub>2</sub> CH <sub>2</sub> OH	n- or i-propanol?	
1225 to 1234	(CH <sub>3</sub> CO) <sub>2</sub>	Most likely butanedione, see appendix D.13	
1310 to 1320	C <sub>4</sub> H <sub>8</sub> O	C <sub>4</sub> H <sub>8</sub> O isomers distinguishable, see appendix D.14	
1319 to 1414	CH <sub>3</sub> COOC <sub>2</sub> H <sub>5</sub>	Actual acetate detected, see appendix D.15	
2196 to 2222	C <sub>5</sub> H <sub>8</sub> O <sub>2</sub>	2,3-pentanedione	Constitutional isomers of C <sub>5</sub> H <sub>8</sub> O <sub>2</sub> separated by GC, see appendix D.16
2320 to 2389	C <sub>5</sub> H <sub>8</sub> O <sub>2</sub>	2,4-pentanedione	

Hereafter, details for each of the listed species are given. This includes a table of all detected peaks across applied potentials, their retention times and integrated signal values. The upper part of these tables gives retention times of maximum signal as well as detected boundaries of the signal as described in C.2. In the lower part, all traces with detected peaks for these retention times are listed with their integrated signal values. For these, the raw signal has been smoothed and detected baseline was already subtracted as described in C.3. If for none of the listed traces a peak was registered for a specific applied potential, no retention times are given and the integration yields zero for all traces as there are no boundaries for summation. If for only one or multiple of the traces no peak (with reasonable SNR) was detected at a specific potential, the result from integration within the defined boundaries is given but highlighted in red since the value is not meaningful.

Detected retention times are discussed in comparison to documented and expected (relative) retention times as mentioned in appendix B.2 and B.3. The discussions around species identification also include arguments regarding different species' proton affinities that are listed in appendix E.1.3 since this value indicates if we expect (substantial) protonation of a potential CO<sub>2</sub>R product or not. Furthermore, all species were verified within the <sup>13</sup>C experiment described in appendix F.

A few types of figures and graphs are deployed to support identification and analysis discussion. The three most prominent ones are the following: The first shows smoothed intensities of a specific trace signal around the relevant time scales. The second shows smoothed intensities for all relevant traces at a specific applied potential around the relevant time scales. The third shows relative Faradaic Efficiencies (see appendix C.3.1) calculated with relevant traces across all applied potentials. The fourth shows the share of integrated signal (see appendix C.3.2) from relevant traces across all applied potentials.

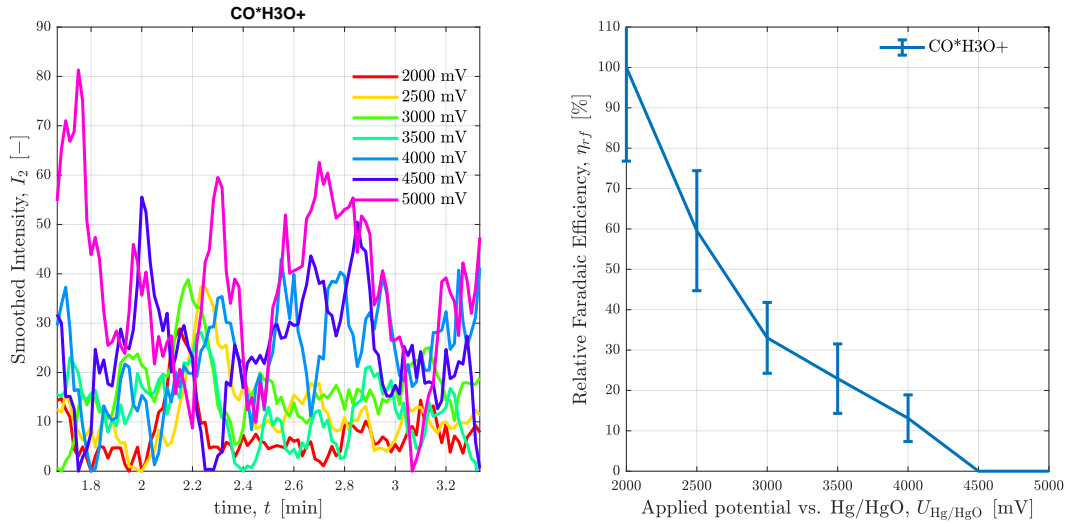
## D.1 Carbon monoxide

After 129s to 134s we detect a peak of mass  $m = 47.013$  Da. We do not expect to see carbon monoxide via the PTR-MS since its proton affinity is smaller than that of water but multiple indicators point towards it. First of all, it lines up with the expected retention time of CO for this column. Second, it seems to be the trace of a cluster with H<sub>3</sub>O<sup>+</sup> (rather than proton being completely transferred). Third, it follows the trend observed for carbon monoxide with other methods: it can only be detected for small to medium applied potentials and production peaks at a relatively small applied potential.

**Table 8:** All detected traces that are peaking with carbon monoxide.

Retention time		Applied potential vs. Hg/HgO in mV							
		2000	2500	3000	3500	4000	4500		5000
Peak time in s		129	134	131	134	-	-	-	
Start time in s		123	129	123	127	133	-	-	
End time in s		142	148	142	146	146	-	-	
$m/z$	Ion assumed	Integrated smoothed intensity (Normalized counts)						Origin	Comments
47.01	CO·H <sub>3</sub> O <sup>+</sup>	264	340	292	246	191	0	0	CO + H <sub>3</sub> O <sup>+</sup> Proton affinity too small, but due to large concentration at small U <sub>Hg/HgO</sub> , some clusters are forming.

These results were not be reproduced with  $^{13}\text{C}$  because this experiment was only conducted at larger applied potentials.



(a) Smoothed Intensities of  $\text{CO}\cdot\text{H}_3\text{O}^+$  trace

(b) Relative Faradaic Efficiencies of  $\text{CO}$  traces

**Figure 17:** Analysis of traces and Integrated smoothed intensities within  $\text{CO}$  peak.

## D.2 Methane

At this retention time (168 s to 177 s) we expect to find methane but it also has a proton affinity much smaller than water so that it cannot be protonated by  $\text{H}_3\text{O}^+$ . The small contamination of  $\text{O}_2^+$  can ionize the methane though, leading to  $\text{CH}_3\cdot\text{O}_2^+$  according to [56]. But since only a small fraction of the produced methane will get ionized, there are clustering reactions with the few ionized methane molecules.

**Table 9:** All detected traces that are peaking with methane.

Retention time	Ion assumed	Applied potential vs. Hg/HgO in mV						Origin	Comments	
		2000	2500	3000	3500	4000	4500			5000
Peak time in s	-	-	174	174	177	170	169			
Start time in s	-	-	165	165	169	160	160			
End time in s	-	-	184	184	188	179	179			
$m/z$	Ion assumed	Integrated smoothed intensity (Normalized counts)						Origin	Comments	
47.01	$\text{CH}_3\cdot\text{O}_2^+$	0	0	12	142	5	451	1349	$\text{CH}_4 + \text{O}_2^+$	Ionization by residual $\text{O}_2^+$ [57]
63.04	$\text{C}_2\text{H}_7\text{O}_2^+$	0	0	-5	6	6	8	8	$\text{CH}_3\cdot\text{O}_2^+ + \text{CH}_4$	Just hypothetical
33.03	$^{12}\text{CH}_5\text{O}^+$	0	0	1787	4646	8251	8134	7939	$\text{C}_2\text{H}_7\text{O}_2^+ - \text{CH}_2\text{O}$	Isotope ratio around 1.5%
34.04	$^{13}\text{CH}_5\text{O}^+$	0	0	25	86	99	80	96		
43.02	$\text{C}_2\text{H}_3\text{O}^+$	0	0	194	290	421	407	475	$\text{C}_2\text{H}_7\text{O}_2^+ - \text{H}_2 - \text{H}_2\text{O}$	
31.02	$\text{CH}_3\text{O}^+$	0	0	440	450	2349	3104	2567	$\text{C}_2\text{H}_7\text{O}_2^+ - \text{CH}_3\text{OH}$	Alternatively $\text{CH}_3\text{O}_2^+ - \text{O}$

Due to the large concentration, almost all  $\text{CH}_3\cdot\text{O}_2^+$  ions cluster with unionized methane which seems to immediate fragment mostly to  $\text{CH}_5\text{O}^+$  which is detected as main signal

(see Fig. 18(a)). For the supposed PTR reaction mechanism based on the findings, see appendix E.3.1. Even though the  $^{13}\text{C}$  experiment was conducted at an applied potential that would allow for considerable methane production, only a signal of  $\text{CH}_5\text{O}^+$  with small SNR was detected. This is probably due to the fact that the electrode used was from a different batch and has therefore slightly different selectivities. The Faradaic Efficiency of methane peaked at a fairly large applied potential (see Fig. 18(b)) which is expected when considering the general trends observed in methane production. [3]

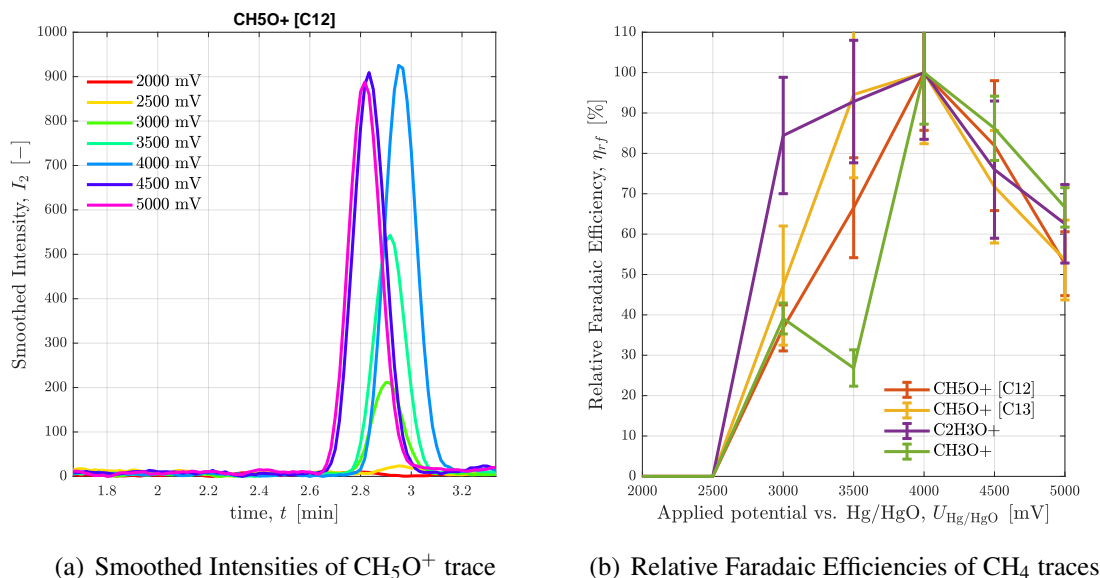


**Figure 18:** Analysis of traces and Integrated smoothed intensities within  $\text{CH}_4$  peak.

### D.3 Carbon Dioxide

For this retention time (234 s to 242 s) we expect to find unconverted carbon dioxide but it should not react in a significant way with any of the ionic precursors [58]. It has the lowest proton affinity of all species analysed yet but next to the  $\text{CO}_2^+$  ionized by residual  $\text{O}_2^+$  we actually find protonated carbon dioxide  $\text{CO}_2\text{H}^+$ . This could be caused by the sheer number of  $\text{CO}_2$  molecules in its large concentration, so we still see some occasional protonation. Furthermore, we detect carbonic acid which usually immediately decomposes in the gas phase. This seeming contradiction can be explained by the good solubility of carbon dioxide in water which seems to cause some of the gas phase humidity to recombine with  $\text{CO}_2$  in the GC column. One piece of evidence indicating that detected  $\text{H}_3\text{CO}_3^+$  signals are not only caused by ionization of  $\text{CO}_2$  via a  $\text{H}_5\text{O}_2^+$  is the fact that signals of water-related traces are detected as documented in Tab. 10. If we accept the existence of carbonic acid, the  $\text{CO}_2\text{H}^+$  signal could also be caused by water dissociation from protonated carbonic acid, see Tab. 10. Signals and isotope ratios of these are quite similar (and also hard to explain if only caused by carbon dioxide) so they might be connected in this way and carbon dioxide is not directly protonated after all.

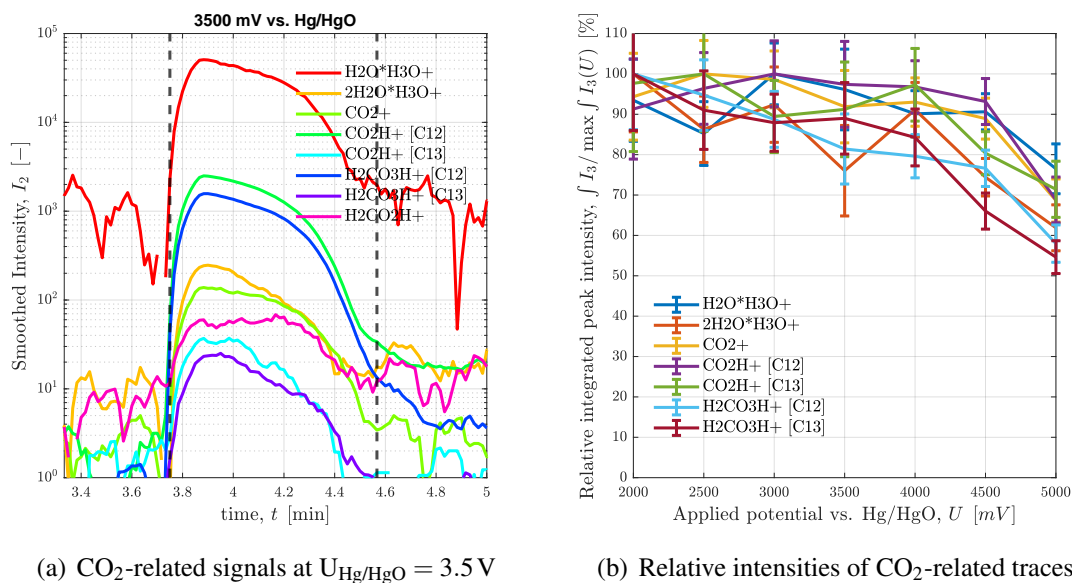
**Table 10:** All detected traces that are peaking with carbon dioxide.

Retention time		Applied potential vs. Hg/HgO in mV								
		2000	2500	3000	3500	4000	4500			
Peak time in s		228	233	231	232	235	228	23		
Start time in s		222	226	223	225	227	220	223		
End time in s		271	275	272	274	276	269	272		

$m/z$	Ion assumed	Integrated smoothed intensity (Normalized counts)							Origin	Comments
37.03	$\text{H}_2\text{O} \cdot \text{H}_3\text{O}^+$	1264804	1150109	1300788	1302750	1145293	1146872	995620	$\text{H}_2\text{O} + \text{H}_3\text{O}^+$	
55.04	$2\text{H}_2\text{O} \cdot \text{H}_3\text{O}^+$	6345	4920	5636	4661	5415	4268	3598	$2\text{H}_2\text{O} + \text{H}_3\text{O}^+$	signal $\approx$ 5% of above
43.99	$\text{CO}_2^+$	3605	3741	3681	3502	3421	3248	2517	$\text{CO}_2 + \text{O}_2^+$	
45.00	$^{12}\text{CO}_2\text{H}^+$	54962	56098	57828	57437	55161	52793	39338	$\text{CO}_2 + \text{H}_3\text{O}^+$	Or from $\text{H}_2\text{CO}_3\text{H}^+ - \text{H}_2\text{O}$
46.00	$^{13}\text{CO}_2\text{H}^+$	853	859	737	747	767	630	580		Isotope ratio around 1.4%
63.01	$\text{H}_2^{12}\text{CO}_3\text{H}^+$	46005	41957	38971	36527	34585	33026	25217	$\text{H}_2\text{CO}_3 + \text{H}_3\text{O}^+$	
64.01	$\text{H}_2^{13}\text{CO}_3\text{H}^+$	608	532	506	519	486	368	312		Isotope ratio around 1.5%
47.01	$\text{H}_2\text{CO}_2\text{H}^+$	1089	1037	1360	1520	1744	1494	2422	$\text{H}_2\text{CO}_3\text{H}^+ - \text{O}$	small SNR

When looking at the trace peaks, retention times of  $\text{H}_2\text{O}$ - and  $\text{CO}_2$ -related traces seem slightly shifted which indicates some separation by the GC column. This shift is not significant enough (see Fig. 19(a)) and trends not consistent to draw any conclusions from it. All main signals of the three components were verified within the  $^{13}\text{C}$  experiment where the shift is a bit more pronounced and the order of elution ( $\text{CO}_2$ , then  $\text{H}_2\text{CO}_3$ , then  $\text{H}_2\text{O}$ ) meets expectations since water should exhibit a much longer retention time than carbon dioxide.



**Figure 19:** Analysis of traces and Integrated smoothed intensities within  $\text{CO}_2$  peak.

As can be seen in Fig. 19(b), the relative signal (integrated counts or intensities) of all related traces with good SNR decreases consistently with larger applied potentials. This is indicating that  $\text{CO}_2\text{RR}$  is actually increasing with applied potential (and not just HER or other factors that could increase total current density, see appendix A) which means that there is less  $\text{CO}_2$  left after the reaction.

## D.4 Ethylene

At this retention time we expect to find ethylene. Technically, its proton affinity is also smaller than water and thus should not be protonated by hydronium ions. But since the proton affinities are very similar, protonation is actually expected and corresponding reactions are documented in the literature as well as ionization via residual  $O_2^+$ . [57]

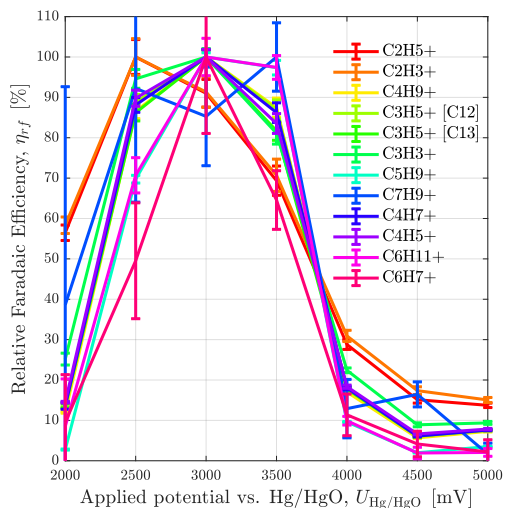
**Table 11:** All detected traces that are peaking with ethylene.

Retention time	Applied potential vs. Hg/HgO in mV								
	2000	2500	3000	3500	4000	4500			
Peak time in s	337	341	339	339	342	335	333		
Start time in s	322	326	324	324	327	319	318		
End time in s	352	356	354	354	357	349	348		
$m/z$	Ion assumed	Integrated smoothed intensity (Normalized counts)						Origin	Comments
28.03	$C_2H_4^+$	4475	8655	8494	8331	7050	5280	6406	$C_2H_4 + O_2^+$ Ionization of ethylene via $O_2^+$ [57]; reaction rate constant seems similar to $H_3O^+$ ionization since signal ratio around 2%, same as primary ion contamination
26.02	$C_2H_2^+$	1464	2010	1821	1811	1837	1610	1818	$C_2H_4^+ - H_2$ Dissociation of hydrogen
29.04	$C_2H_5^+$	168077	655239	777461	838673	414534	253757	358452	$C_2H_4^+ + H_3O^+$ Protonation via primary ion, very large signal; main $H_3O^+$ product according to [57]
27.02	$C_2H_3^+$	8078	30459	36317	39799	20703	13519	18260	$C_2H_5^+ - H_2$ Dissociation of hydrogen
57.07	$C_4H_9^+$	7208	114452	172559	212993	49352	19208	38482	$C_2H_3^+ \cdot C_2H_4$ Cluster forming
55.06	$C_4H_7^+$	1093	16993	25145	30563	7697	3029	5907	$C_4H_9^+ - H_2$ alternatively via $C_2H_3^+ \cdot C_2H_4$
53.04	$C_4H_5^+$	390	5350	7778	9176	2402	1009	1863	$C_4H_7^+ - H_2$ Dissociation of hydrogen
41.04	$^{12}C_3H_5^+$	16896	251220	369133	453209	110184	43613	84667	$C_4H_9^+ - CH_4$ Dissociation of methane
42.04	$^{13}C^{12}C_2H_5^+$	555	7696	11643	13412	3482	1416	2752	Isotope ratio stable around 3.1%
69.07	$C_5H_9^+$	458	24685	46218	63421	7477	1795	4974	$C_3H_5^+ \cdot C_2H_4$ Cluster forming
93.07	$C_7H_{13}^+$	34	22	60	9	24	29	-9	Only hypothetical
93.07	$C_7H_9^+$	-2	29	51	67	13	20	-9	not confirmed, might also be $C_4H_{13}O_2^+$ signal via $C_2H_9O_2^+ \cdot C_2H_4$
39.03	$C_3H_3^+$	1097	8724	12038	13767	4550	2217	3428	$C_3H_5^+ - H_2$ Dissociation of hydrogen
83.09	$C_6H_{11}^+$	6	121	211	293	37	10	18	$C_4H_7^+ \cdot C_2H_4$ Cluster forming
79.05	$C_6H_7^+$	5	42	127	121	34	6	0	$C_6H_9^+ - H_2$ Dissociation of hydrogen
47.05	$^{12}C_2H_7O^+$	40962	156512	187021	204251	100532	62137	86747	$C_2H_4 \cdot H_3O^+$ Second $H_3O^+$ product according to [57], signal 20% confirmed
48.05	$^{13}C^{12}C_7H_7O^+$	929	3619	4497	4733	2344	1458	2142	Isotope ratio reliably around 2.4%
59.05	$^{12}C_3H_7O^+$	536	1019	2669	3185	3437	2220	3422	$C_4H_{11}O^+ - CH_4$ Dissociation of methane
60.05	$^{13}C^{12}C_2H_7O^+$	-55	121	137	138	139	184	189	Ratio too large for isotope, confirming $C_2H_4 \cdot O_2^+$
71.09	$C_5H_{11}^+$	0	23	96	91	10	-4	-10	$C_4H_{11}O^+ \cdot C_2H_4 - CH_3OH$ Cluster forming
45.03	$C_2H_5O^+$	876	3228	3712	3928	1953	1486	1898	$C_2H_7O^+ - H_2$ Dissociation of hydrogen
43.02	$^{12}C_2H_3O^+$	195	531	547	655	324	293	388	$C_2H_5O^+ - H_2$ Dissociation of hydrogen
44.02	$^{13}C^{12}CH_3O^+$	195	492	571	629	406	259	279	Isotope ratio incalculable due to $CO_2^+$ overlap
65.06	$^{12}C_2H_9O_2^+$	795	3155	3453	4119	1892	1160	1656	$C_2H_4 + H_5O_2^+$ coincides with visible drop in $H_5O_2^+$
66.06	$^{13}C^{12}CH_9O_2^+$	18	88	89	128	52	24	38	Isotope ratio stable around 2.9%
91.08	$C_4H_{11}O_2^+$	-1	2	32	61	8	-5	10	not confirmed
43.99	$CO_2^+$	241	573	632	680	497	271	330	$C_2H_4 \cdot O_2^+ - CH_4$ most likely explanation since $C_2H_4 \cdot O_2^+$ confirmed even though not documented
67.054	$C_5H_7^+$	22	1318	2523	3193	505	126	305	$C_5H_9^+ - H_2$
105.09	unknown	37	297	473	666	300	167	297	origin unclear

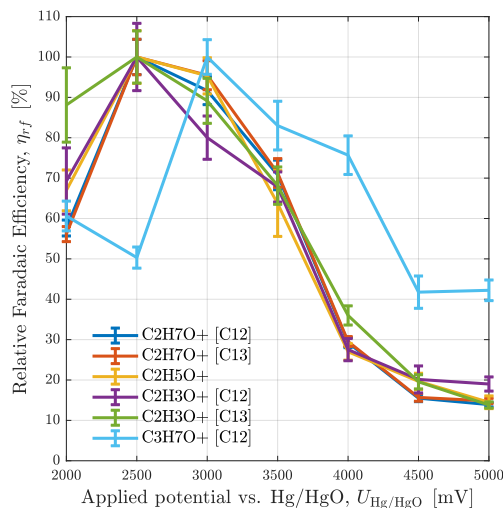
Due to the large ethylene concentration, additional effects were observed: Clustering of ionized ethylene with unionized ethylene, dissociation of different small molecules to create a wide range of fragments, and detectable protonation by  $H_5O_2^+$  cluster ion. For the full PTR reaction mechanism based on these findings, see appendix E.3.2. Key species were also verified within the  $^{13}C$  experiment. Isotope ratios of the different fragments are quite different, which can be partially explained by the different numbers of  $^{13}C$  in these ions but also seem to be caused by signal overlaps with other traces such as  $C_2H_4O_2^+$  and  $CO_2^+$ , pointing towards a  $C_2H_4 \cdot O_2^+$  cluster forming. Furthermore, a trace with  $m/z = 105$  Da has been consistently detected but couldn't be ascribed to a specific fragment.

In Fig. 20 the relative Faradaic Efficiencies computed by different traces are sorted by the

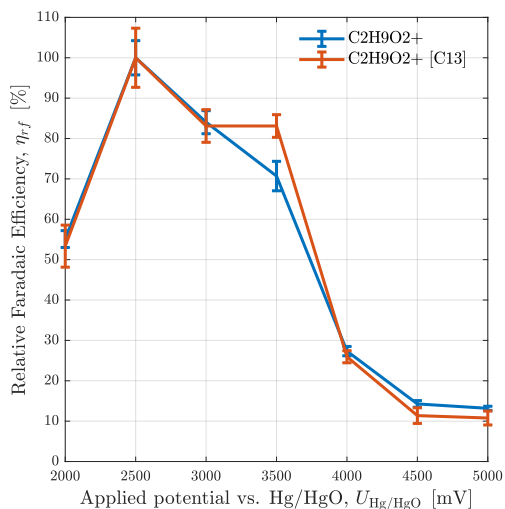
supposed initial ionization reaction. Traces based on  $\text{H}_3\text{O}^+$  ionization consistently show the same trend of increasing ethylene production while ramping up from small applied potentials, peaking at small to medium potential before declining again. Meanwhile, traces based on  $\text{O}_2^+$  ionization seem to peak much earlier.



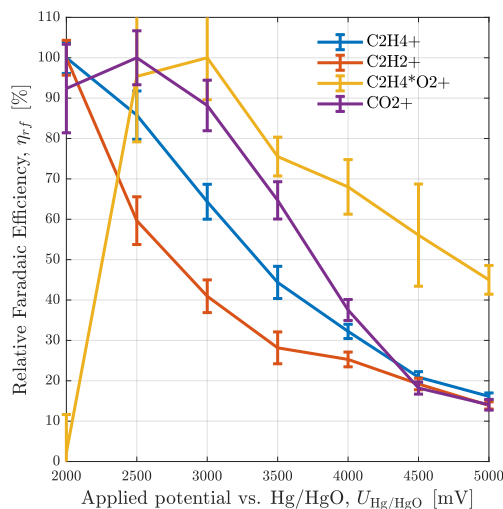
(a) Traces related to  $\text{C}_2\text{H}_5^+$  ion



(b) Traces related to  $\text{C}_2\text{H}_4 \cdot \text{H}_3\text{O}^+$  ion



(c) Traces related to  $\text{C}_2\text{H}_4 \cdot \text{H}_5\text{O}_2^+$  ion

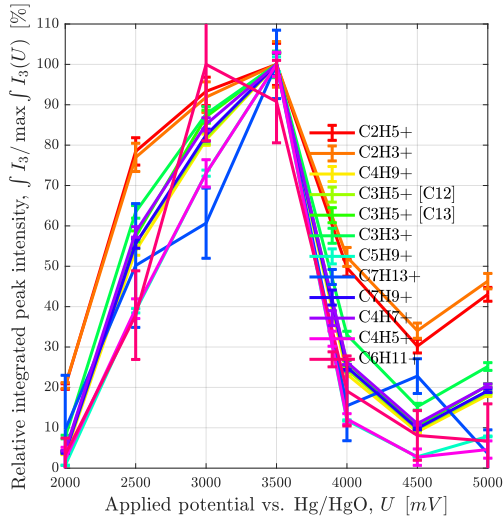


(d) Traces related to  $\text{O}_2^+$  ionization

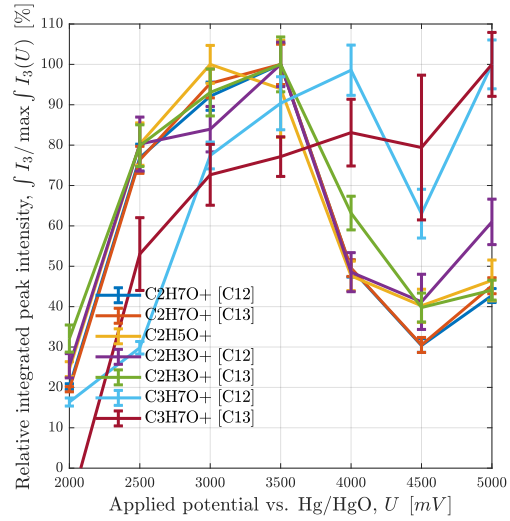
**Figure 20:** Relative Faradaic Efficiencies of different  $\text{C}_2\text{H}_4$ -related traces and fragments.

The reason for this is the complete depletion of  $\text{O}_2^+$  ions reacting with ethylene in concentrations as large as produced at most of the applied potentials used. The ion depletion is discussed in E.2.1 and when looking at relative signals not normalized by current in Fig. 21, most  $\text{O}_2^+$ -related traces in Fig. 21(d) can be seen at a similar level of intensity for all  $U_{\text{Hg}/\text{HgO}} \leq 2.5$  V. The relative Faradaic Efficiencies in Fig. 20(a) exhibit a relatively flat peak for a similar reason: There is a partial depletion of  $\text{H}_3\text{O}^+$  for medium applied

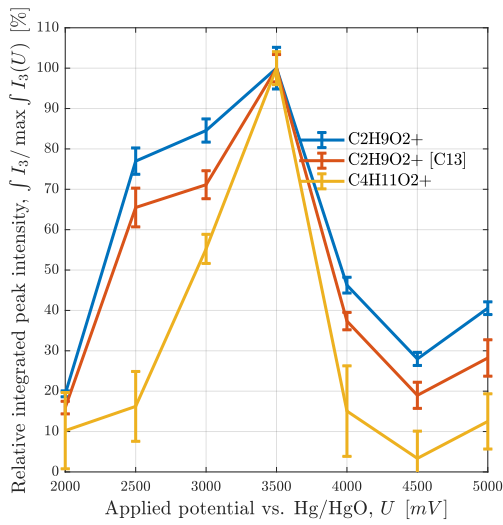
potentials as discussed in E.2.1: Fig. 21(a) shows a similar level of intensities at these applied potentials, the signal at  $U_{\text{Hg}/\text{HgO}} = 3.5\text{V}$  probably not peaking as high as it could have with sufficient  $\text{H}_3\text{O}^+$  available.



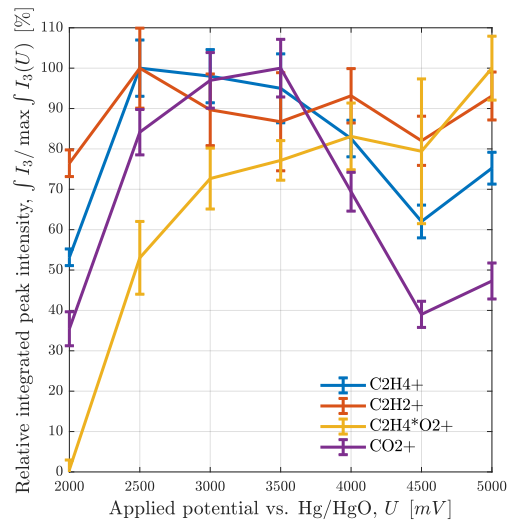
(a) Traces related to  $\text{C}_2\text{H}_5^+$  ion



(b) Traces related to  $\text{C}_2\text{H}_4 \cdot \text{H}_3\text{O}^+$  ion



(c) Traces related to  $\text{C}_2\text{H}_4 \cdot \text{H}_5\text{O}_2^+$  ion



(d) Traces related to  $\text{O}_2^+$  ionization

**Figure 21:** Integrated smoothed intensities of different  $\text{C}_2\text{H}_4$ -related traces and fragments.

A few exceptions are observed: Traces representing clusters show smaller relative intensities since they require two or more ethylene molecules and thereby depend on concentration with a larger exponent, see E.2.1. This is specifically obvious in Fig. 21(a) when comparing  $\text{C}_2$ -products to  $\text{C}_3$ - and  $\text{C}_4$ -products. The same applies to  $\text{C}_3\text{H}_7\text{O}^+$  in Fig. 21(d) for small applied potentials. At larger applied potentials, it shows larger relative intensities than  $\text{C}_2$  traces though. For the  $^{13}\text{C}$  isotope this can be explained by signal overlap

from  $\text{C}_2\text{H}_4 \cdot \text{O}_2^+$ . In fact, the behaviour shown seems to be a mixture of  $\text{H}_3\text{O}^+$  and  $\text{O}_2^+$  origin. This does not explain why the  $^{12}\text{C}$  version shows a similar behaviour - even though it is not as pronounced. The reason could be signal overlap with another fragment of  $\text{O}_2^+$  ionization origin: for example  $\text{C}_2\text{H}_3 \cdot \text{O}_2^+$  via H abstraction.

## D.5 Formalin

For this retention time window (413 s to 446 s), some convoluted traces are observed. Trace analysis and experience point towards formaldehyde in addition to water and small amounts of methanol, see Fig. 22. This mixture is known as formalin and since the column used is not designed to separate these components in particular, we observe them here even though methanol and water are documented with longer retention times.

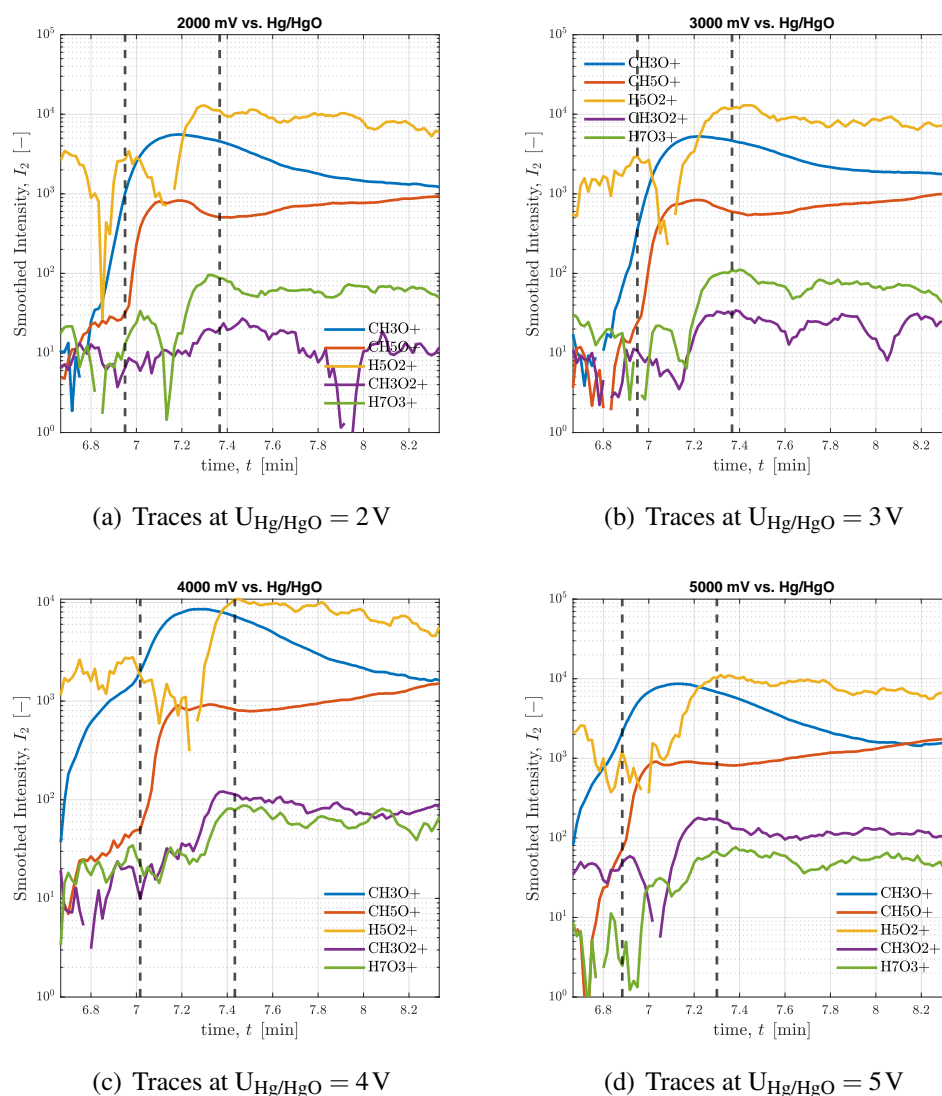


**Figure 22:** Analysis of formalin-related signals at different applied potentials.

There seems to be some separation at least - a distinct shift of peaks is visible, see Fig. 23. We first detect a  $\text{CH}_5\text{O}^+$  peak which is the main protonation product of methanol. [59] After this, a second  $\text{CH}_5\text{O}^+$  peak is detected, coinciding with a  $\text{CH}_3\text{O}^+$  peak. This could be also originate from methanol as it is one of the two documented  $\text{O}_2^+$  products. The signal is way larger though so it points rather towards formaldehyde.[59] It seems to be mixed with methanol which is only partially separated by the GC column. Note that this sequence is contrary to usual observation of methanol taking longer than formaldehyde as per their boiling points. The last hydrocarbon peak detected is  $\text{CH}_3\text{O}_2^+$ , which is ascribed to formaldehyde even though it is not documented in the literature. This can be explained by water molecules interfering with the pure protonation of formaldehyde.

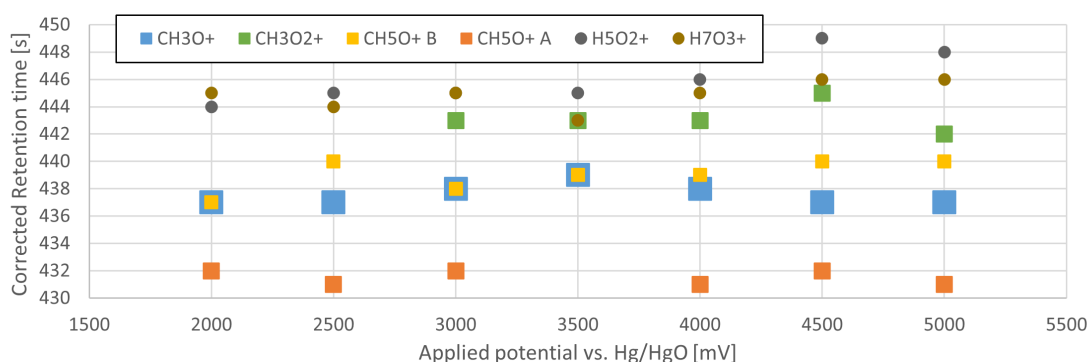


**Figure 23:** Overview of adjusted retention times of formalin-related traces peaking.

There seems to be some separation at least, a slight shift of peaks is visible. We first detect methanol, then formaldehyde and then water - see Fig. 23. Note that this sequence is contrary to usual observation of methanol taking longer than formaldehyde in most gas chromatographs.  $\text{CH}_3\text{O}_2^+$  is ascribed to formaldehyde even though it is not documented in the literature [59] [56]. It shows a flat, but stretched peak and for some applied potentials even two distinct peaks, where the first one is coinciding with  $\text{CH}_3\text{O}^+$  and the latter one with the water-related traces. This can be explained by water molecules interfering with the pure protonation of formaldehyde, details below.

**Methanol** appears first. Two peaks of  $\text{CH}_5\text{O}^+$  can be distinguished for most potentials: One earlier than  $\text{CH}_3\text{O}^+$  (almost coinciding with  $\text{CH}_2\text{O}$ -related traces) and one coinciding with  $\text{CH}_3\text{O}^+$  peak, indicating a partial separation from formaldehyde.

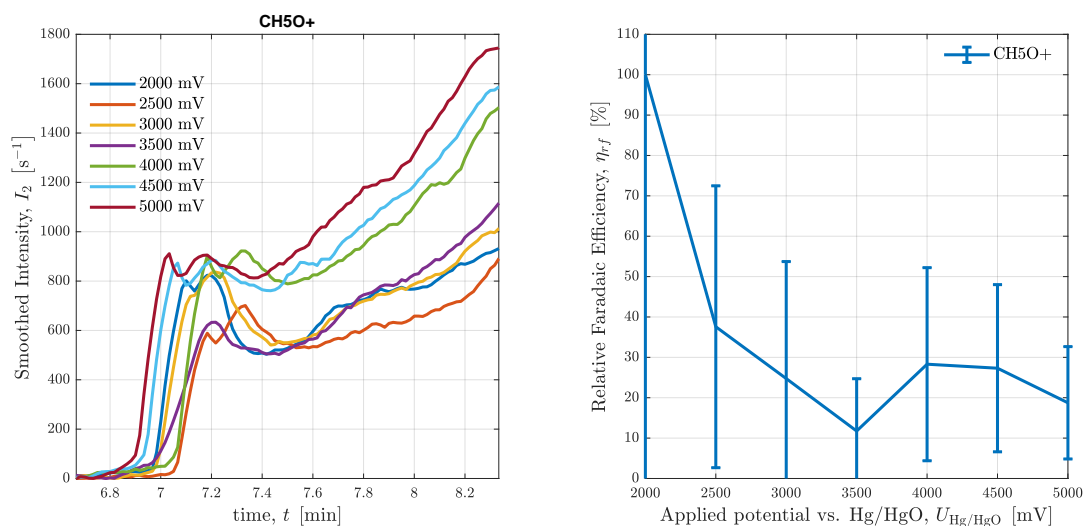
**Table 12:** All detected traces that are peaking with  $\text{CH}_3\text{OH}$ .

Retention time	Applied potential vs. Hg/HgO in mV						
	2000	2500	3000	3500	4000	4500	5000
Peak time in s	424	429	425	426	429	421	419
Start time in s	418	424	417	418	423	417	413
End time in s	429	435	428	429	434	428	424

$m/z$	Ion assumed	Integrated smoothed intensity (Normalized counts)						Origin	Comments	
33.03	$\text{CH}_5\text{O}^+$	1013	1144	330	155	2191	2588	2920	$\text{CH}_3\text{OH} + \text{H}_3\text{O}^+$	Only protonation product of methanol according to [59]

As can be seen in Fig. 24(a), for applied potentials of  $U_{\text{Hg}/\text{HgO}} = 3.0\text{V}$  to  $3.5\text{V}$  the two  $\text{CH}_5\text{O}^+$  are barely separated and can hardly be deconvoluted. The corresponding integrated signal values in Tab. 24 are therefore marked in yellow. Moreover, Fig. 24(b) shows a clear trend of decreasing Faradaic Efficiencies with increasing applied potentials - the decrease is monotonous if the mentioned outliers are removed. The trace was verified in the  $^{13}\text{C}$  experiment.



(a) Smoothed Intensities of  $\text{CH}_5\text{O}^+$  trace

(b) Relative Faradaic Efficiencies of pure  $\text{CH}_3\text{OH}$  trace

**Figure 24:** Analysis of traces and Integrated smoothed intensities within  $\text{CH}_3\text{OH}$  peak.

**Formaldehyde** appears second. The main signal is of directly protonated formaldehyde as its proton affinity is larger than water. A second peak of methanol coincides, see Tab. 13.

**Table 13:** All detected traces that are peaking with formaldehyde.

Retention time	Ion assumed	Applied potential vs. Hg/HgO in mV							Origin	Comments
		2000	2500	3000	3500	4000	4500	5000		
Peak time in s		431	437	431	431	436	429	428	$\text{CH}_2\text{O} + \text{H}_3\text{O}^+$	Only protonation product according to [56] see Tab. 12
Start time in s		413	419	413	415	420	411	412		
End time in s		464	470	464	466	471	462	463		
$m/z$		Integrated smoothed intensity (Normalized counts)							$\text{CH}_3\text{OH} + \text{H}_3\text{O}^+$	Isotope ratio of both peaks $\approx 1\%$
31.02	$\text{CH}_3\text{O}^+$	207000	20103	25575	30742	33735	31164	36007		
33.03	$^{12}\text{CH}_5\text{O}^+$	2682	2311	3675	3860	2011	1796	1777		
34.04	$^{13}\text{CH}_5\text{O}^+$	34	18	43	50	32	11	12		

As seen in Fig. 25(a) the amount of formaldehyde detected decreases steadily with applied potential as does methanol. Due to incomplete separation these signals are dependent on each other but the pure methanol signal shown in Fig. 24(b) shows a similar trend.

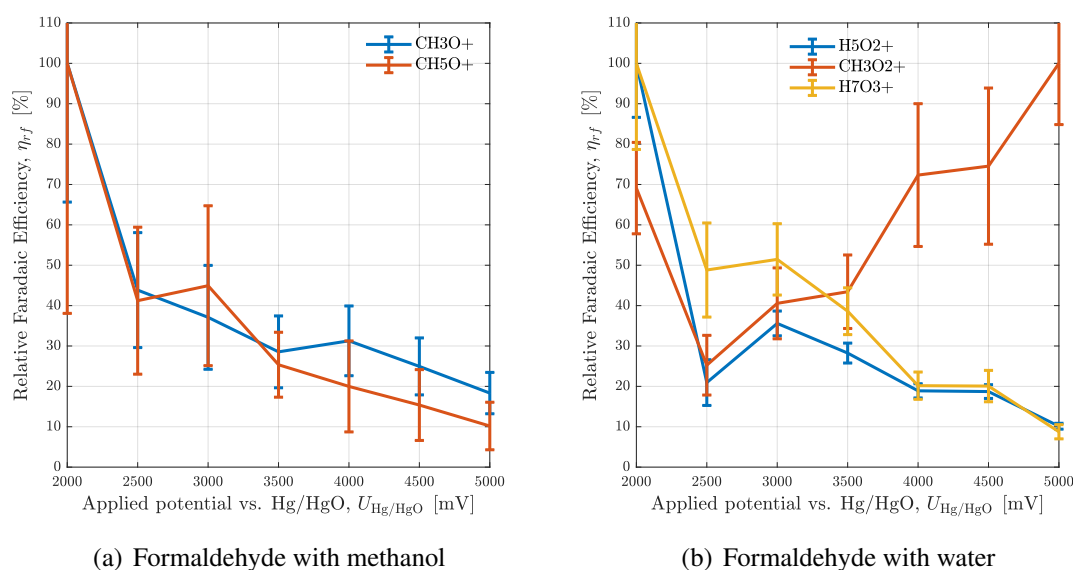


**Figure 25:** *Relative Faradaic Efficiencies of traces related to formaldehyde.*

Because the retention time of formaldehyde coincides with the second heating phase of the GC column, intensity baselines appear quite large. For this reason - and also due to difficult signal deconvolution - all standard deviations shown are quite large.

**Water** appears last. With it, a  $\text{CH}_3\text{O}_2^+$  signal appears - probably due to incomplete separation from formaldehyde. The shift towards later retention times makes sense when comparing literature values and boiling points, see Tab. 14.

**Table 14:** *All detected traces that are peaking with formaldehyde-related water.*

Retention time	Applied potential vs. Hg/HgO in mV							Origin	Comments	
	2000	2500	3000	3500	4000	4500	5000			
Peak time in s	438	445	438	439	448	436	436	$\text{H}_2\text{O} \cdot \text{H}_3\text{O}^+$ $\text{CH}_3\text{O}^+ \cdot \text{H}_2\text{O} - \text{H}_2$ $2\text{H}_2\text{O} \cdot \text{H}_3\text{O}^+$		
Start time in s	432	435	431	429	438	430	427			
End time in s	457	460	456	454	463	455	452			
$m/z$	Ion assumed	Integrated smoothed intensity (Normalized counts)								
37.03	$\text{H}_5\text{O}_2^+$	288236	116841	264798	287558	241115	276788	223423		
47.01	$\text{CH}_3\text{O}_2^+$	193	231	473	629	1340	1475	3230		
55.04	$\text{H}_7\text{O}_3^+$	992	908	1411	1429	915	1033	511		

In Fig. 25(b) the relative Faradaic Efficiencies of water-related traces of formaldehyde show a similar trend than the methanol-related ones. In contrast, however, the  $\text{CH}_3\text{O}_2^+$  trace exhibits an opposite trend of increasing Faradaic Efficiencies with applied potential. This might be caused by small SNR of this trace but could also point towards the actual trend for formaldehyde since all other traces analysed either show some overlap with methanol (and therefore are influenced by its trend of large Faradaic Efficiencies at small applied potentials [3]) or are water- (resp.  $\text{H}_3\text{O}^+$ -) related and largely influenced by column heating.

## D.6 Propylene

At this retention time (542s to 551s) we expect to find propylene. We expect mostly protonation by  $\text{H}_3\text{O}^+$  as well as some ionization via residual  $\text{O}_2^+$  [57].

**Table 15:** All detected traces that are peaking with propylene.

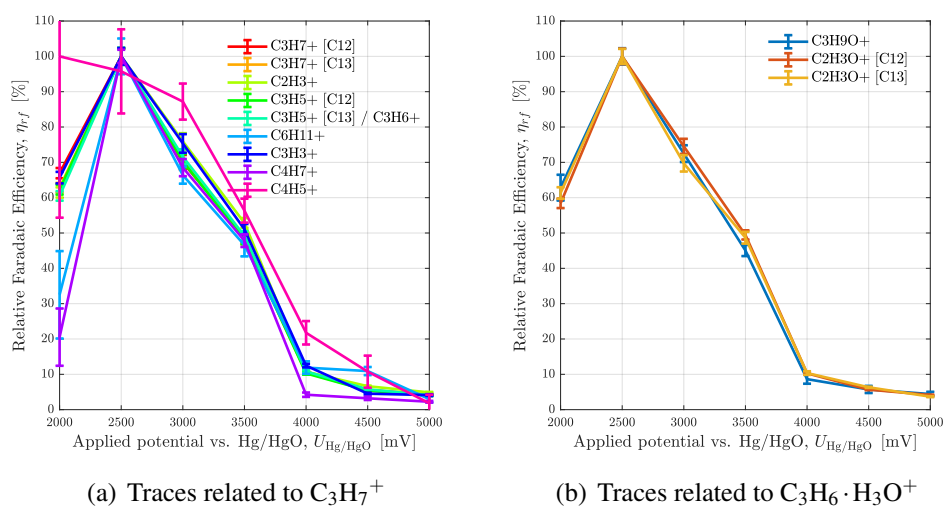
Retention time	Applied potential vs. Hg/HgO in mV								Origin	Comments
	2000	2500	3000	3500	4000	4500	5000			
Peak time in s	547	550	549	550	552	544	542			
Start time in s	532	537	536	535	539	530	528			
End time in s	562	567	566	565	569	560	558			

$m/z$	Ion assumed	Integrated smoothed intensity (Normalized counts)							Origin	Comments
43.06	$^{12}\text{C}_3\text{H}_7^+$	435480	1427939	1309573	1284908	339875	204422	239703		
44.06	$^{13}\text{C}^{12}\text{C}_2\text{H}_7^+$	12630	44081	40767	39083	10186	6154	7435		Very stable isotope ratio at 3.0%
27.02	$\text{C}_2\text{H}_3^+$	1257	4502	4473	4352	1069	768	872	$\text{C}_3\text{H}_7^+ - \text{CH}_4$	Dissociation of methane
41.04	$^{12}\text{C}_3\text{H}_5^+$	80488	283117	261040	250610	64201	38970	44468	$\text{C}_3\text{H}_7^+ - \text{H}_2$	Dissociation of ethylene
42.04	$^{13}\text{C}^{12}\text{C}_2\text{H}_5^+$	2451	9043	8463	8164	2157	1315	1474		Isotope ratio $\approx 3.2\%$ indicates that $\approx 5\%$ are $\text{C}_3\text{H}_6^+$ via $\text{O}_2^+$ [57]
83.09	$\text{C}_6\text{H}_{11}^+$	86	661	634	550	108	77	21	$\text{C}_3\text{H}_5^+ \cdot \text{C}_3\text{H}_6$	Cluster forming
39.03	$\text{C}_3\text{H}_3^+$	2049	6889	6947	6523	1855	721	1054	$\text{C}_3\text{H}_5^+ - \text{H}_2$	Alternatively $\text{C}_6\text{H}_{11}^+ - \text{C}_3\text{H}_8$
55.06	$\text{C}_4\text{H}_7^+$	196	2075	1844	1815	192	197	154	$\text{C}_6\text{H}_{11}^+ - \text{C}_2\text{H}_4$	Dissociation of ethylene
53.04	$\text{C}_4\text{H}_5^+$	14	28	35	34	17	7	2	$\text{C}_4\text{H}_7^+ - \text{H}_2$	Dissociation of hydrogen
61.07	$\text{C}_3\text{H}_9\text{O}^+$	216	706	686	580	145	94	132	$\text{C}_3\text{H}_6 \cdot \text{H}_3\text{O}^+$	Second $\text{H}_3\text{O}^+$ product, not documented by [57]
43.02	$^{12}\text{C}_2\text{H}_3\text{O}^+$	17156	64481	62911	58542	14615	9224	10682	$\text{C}_3\text{H}_9\text{O}^+ - \text{CH}_4 - \text{H}_2$	Sequence of dissociation unclear
44.02	$^{13}\text{C}^{12}\text{CH}_3\text{O}^+$	601	2159	1999	1936	506	344	317		Isotope ratio varying around 3.3%
26.02	$\text{C}_2\text{H}_2^+$	43	138	134	167	12	35	33	$\text{C}_3\text{H}_6^+ - \text{CH}_4$	Dissociation of methane
40.06	$\text{C}_3\text{H}_4^+$	66	240	192	209	59	46	30	$\text{C}_3\text{H}_6^+ - \text{H}_2$	Dissociation of hydrogen

The detection of  $\text{C}_3\text{H}_5^+$  first points in towards propyne or allene which form the same ionization products according to [57] but the column used should separate these from propylene. For this reason, we conclude the dissociation of hydrogen to an unusually high degree (around 20% of the  $\text{C}_3\text{H}_7^+$  signal) at our specific conditions, see appendix E.

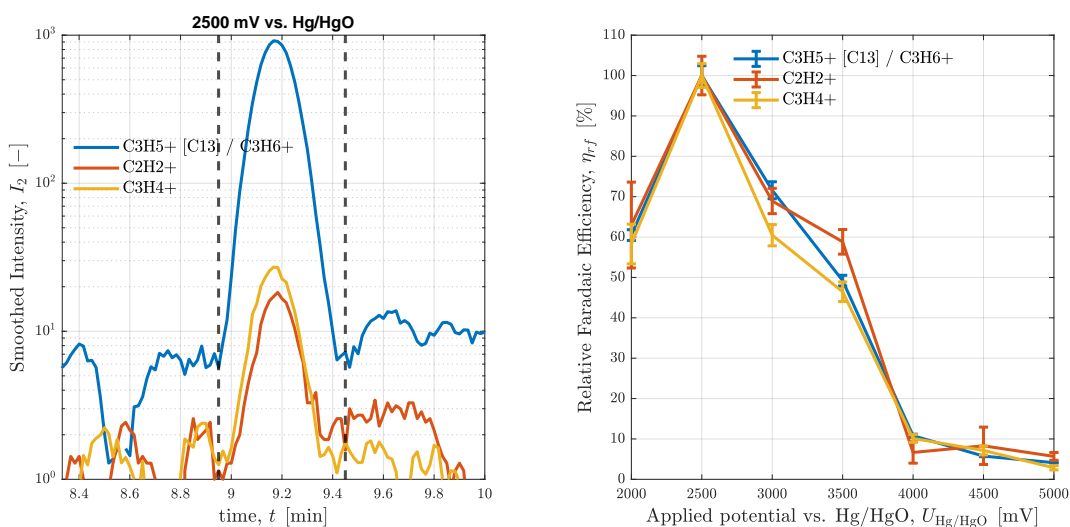
Looking at the relative Faradaic Efficiencies of protonated propylene in Fig. 26, it consistently shows an initial stark increase with applied potential, peaking at  $U_{\text{Hg}/\text{HgO}} = 2500$  mV before dropping off sharply. This behaviour is similar to the one observed for ethylene (see appendix D.4) where  $\eta_{rf}$  peaks even earlier.



**Figure 26:** Relative Faradaic Efficiencies of  $\text{C}_3\text{H}_6 + \text{H}_3\text{O}^+$ -related traces and fragments.

Apart from the ionization products of hydronium, we can also detect species that are clearly ionized by  $O_2^+$ . The initial ion,  $C_3H_6^+$  cannot be feasibly separated from the C-13 isotope of  $C_3H_5^+$  since the masses are almost identical and the expected intensities of the former are much smaller based on two observations: First, the intensities of the following product,  $C_2H_2^+$ , are extremely small and second, the isotope ratio of  $C_3H_5^+$  is only very slightly above expected levels. This means, that fraction of  $O_2^+$  ionization is smaller than its concentration and therefore has a smaller reaction rate constant than  $H_3O^+$ .

In contrast to ethylene, the trends of Faradaic Efficiencies shown in Fig. 27(b) look the same as the ones in Fig. 26. Even though we see many of the same effects regarding cluster-forming (see 60) and  $H_3O^+$  depletion (see E.2.1), the relative Faradaic Efficiencies appear largely undistorted. The key difference is the fact that we do not see  $O_2^+$  depletion which was probably responsible for the differences discussed in D.4.



(a)  $C_3H_6^+$ -related signals at  $U_{Hg/HgO} = 2.5V$

(b) Relative Faradaic Efficiencies of  $C_3H_6^+$ -related traces

**Figure 27:** Analysis of traces and relative Faradaic Efficiencies within  $C_3H_6$  peak.

**A notable irregularity** is the  $C_2H_5O^+$  trace that we analysed in some detail as a potential candidate to close the mechanistic gap between  $C_3H_9O^+$  and  $C_2H_3O^+$  via dissociation of methane first and then hydrogen. As can be seen in Fig. 28, there are peaks close to propylene's retention time, but the main signal does not seem to be caused by propylene. They also cannot be ascribed to formalin or acetaldehyde as the former has a much smaller retention time and the latter leads to a distinctive  $C_2H_5O^+$  peak shortly after the times shown in the graph.

This behaviour could not be verified within the  $^{13}C$  experiment and instead a distinct peak at propylene retention time appears. The  $^{13}C_2H_3O^+$  trace shows a second peak though which mass coincides with  $^{12}C_2H_3O^+$ . The shift to slightly larger times looks similar to the larger applied potentials in Fig. 28 which suggests a non-electrocatalytic yet systemic reason.

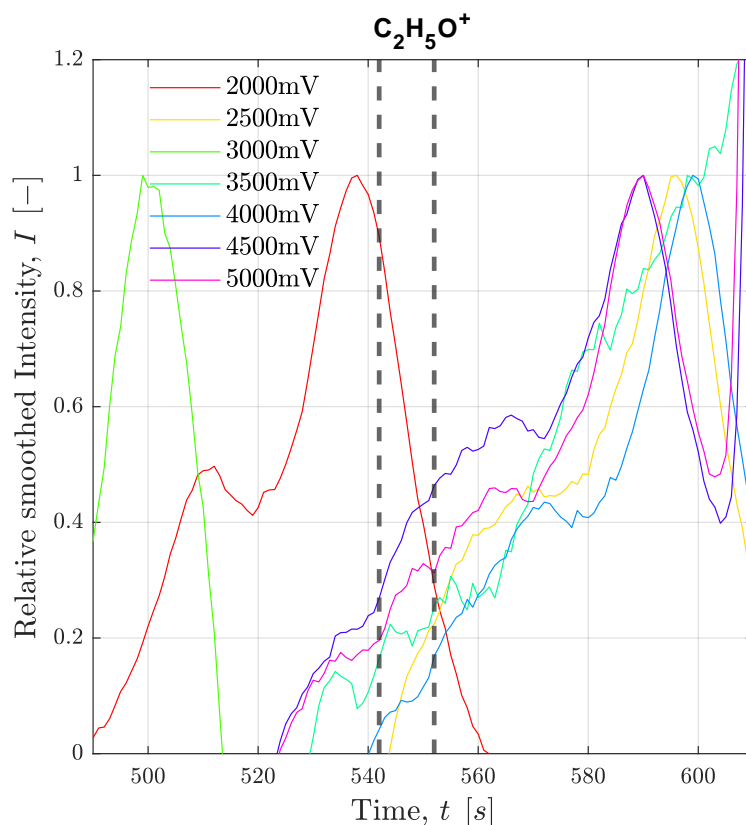


**Figure 28:** Intensity of  $\text{C}_2\text{H}_5\text{O}^+$  trace over different applied potentials vs.  $\text{Hg}/\text{HgO}$ . A dashed line indicates the location of all other traces peaking with propylene.

All other main species could be verified which lends credibility to the presumed PTR reactions. Even within the  $^{12}\text{C}$  measurement results, smaller overlapping peaks can be located within the relevant boundaries in Fig. 28. Intensities are comparatively very small though so they cannot be properly deconvoluted.

## D.7 Acetaldehyde

At this retention time we expect to find acetaldehyde. We expect mostly protonation by  $\text{H}_3\text{O}^+$  as well as some ionization via residual  $\text{O}_2^+$  [56]. Some additional minor secondary and tertiary ions were recorded in a single compound PTR-MS verification experiment.

The  $^{13}\text{C}^{12}\text{CH}_3\text{O}^+$  trace cannot be separated from the  $\text{C}_2\text{H}_4\text{O}^+$  signal since they are both at  $m \approx 44.02\text{Da}$ , which leads to the large isotope ratio, see Tab. 16. According to [56], both  $\text{O}_2^+$  products ( $\text{C}_2\text{H}_4\text{O}^+$  and  $\text{C}_2\text{H}_3\text{O}^+$ ) should appear in similar concentrations but this is definitely not the case here as the signals detected are an order of magnitude smaller. We only see the  $^{13}\text{C}^{12}\text{CH}_3\text{O}^+$  increased by a few percent compared to what is expected.

For an overview of the hypothesized PTR reactions, see appendix E.3.4. For  $\text{C}_2\text{H}_7\text{O}^+$  the mechanism is not entirely clear and the isotope ratio is extremely large (consistently between 4% and 5%) which begs the question if either the dissociation of oxygen is not

**Table 16:** All detected traces that are peaking with acetaldehyde.

Retention time	2000		2500		Applied potential vs. Hg/HgO in mV		5000		Origin	Comments
	Peak time in s	Start time in s	End time in s	3000	3500	4000	4500	5000		
45.033	626	609	654	628	630	632	625	623	$\text{CH}_3\text{CHO} + \text{H}_3\text{O}^+$	Extremely large signal: Main product of $\text{C}_3\text{H}_6$ protonation with $\text{H}_3\text{O}^+$ according to [56]; Detector probably saturated
46.037	631	614	659	83469	91014	99063	78236	47491		Isotope ratio going up from 2.1% to more than 5% at medium potentials due to saturation
89.058	614	614	659	658	841	935	600	220	$\text{C}_2\text{H}_5\text{O}^+ + \text{CH}_3\text{CHO}$	Cluster forming
61.029	614	614	659	658	841	935	600	220	$\text{C}_4\text{H}_9\text{O}_2^+ - \text{C}_2\text{H}_4$	See discussion below
63.044	628	2896	3714	22406	24264	18402	11124		$\text{CH}_3\text{CHO} \cdot \text{H}_3\text{O}^+$	Second $\text{H}_3\text{O}^+$ product due to large concentration (around 1%), not documented by [56]
64.047	306	581	616	579	485	281				Isotope ratio varying from 2.0% to 2.5%
47.013	220	368	761	721	647	276	1015		$\text{C}_2\text{H}_7\text{O}_2^+ - \text{CH}_4$	Dissociation of methane
47.049	728	2896	3714	4104	4517	3427	2337		$\text{C}_2\text{H}_7\text{O}_2^+ - \text{O}$	Dissociation of oxygen atom?
48.052	-3	132	188	209	202	199	112			Isotope ratio varying between 4% and 5%
43.018	604	1427	2411	2787	2876	2344	1603		$\text{CH}_3\text{CHO} + \text{O}_2^+$	One of two ionization products according to [56]
44.021	2	84	166	191	143	111	142		$\text{CH}_3\text{CHO} + \text{O}_2^+$	Isotope ratio (up to 10%) indicates influence of $\text{C}_2\text{H}_4\text{O}^+$ as second $\text{O}_2^+$ product [56]
26.016	10	134	143	173	167	96	81		$\text{C}_2\text{H}_4\text{O}^+ - \text{H}_2\text{O}$	Dissociation of water

the correct mechanism or if we are observing the influence of  $^{18}\text{O}$  oxygen isotopes and related selectivities.

For the main protonation product  $\text{C}_2\text{H}_5\text{O}^+$  we calculate an even larger isotope ratio but in this case is a symptom of detector saturation as described in E.2.3. This is exemplified in Fig. 29(b) where the total fraction of  $^{13}\text{C}$  signal is increasing and  $^{12}\text{C}$  is decreasing to the point of maximum acetaldehyde production. Fig. 29(a) shows the actual signal of  $\text{C}_2\text{H}_5\text{O}^+$  exhibiting double peaks for most applied potentials.

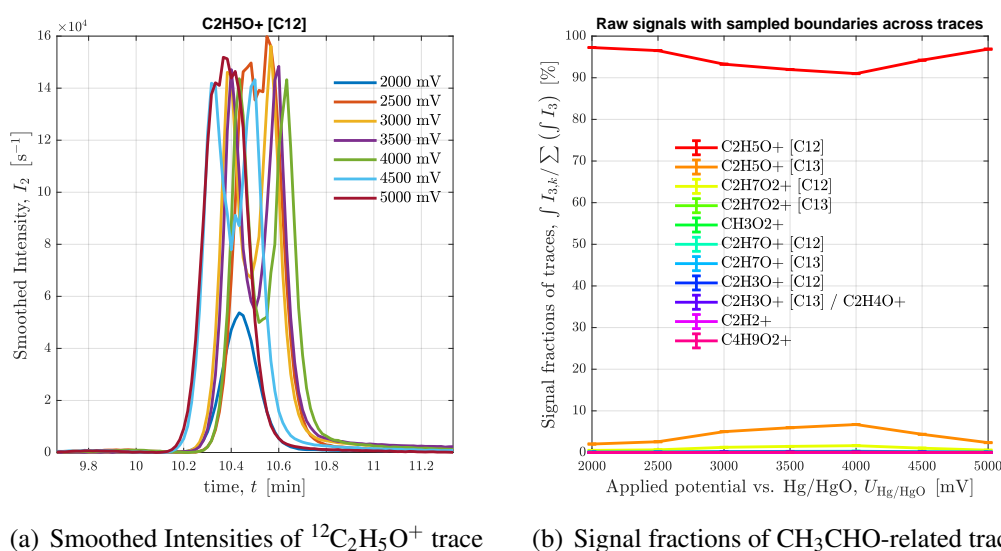


**Figure 29:** Illustration of detector saturation experienced for acetaldehyde analysis.

Most likely, the measurement at lowest applied potential  $U_{\text{Hg}/\text{HgO}} = 2000\text{ mV}$  yields the actual  $^{13}\text{C}$  isotope ratio (2.1%) as it does not exhibit the characteristic double peak. For a coherent qualitative analysis of the main protonation product the  $^{13}\text{C}$  isotope is more suitable in this case though as signals are significantly large for all applied potentials and no detector saturation occurs, see Fig. 30(a). As seen in Fig. 30(b), relative Faradaic Efficiencies are peaking at medium applied potentials which is in line with trends reported in the literature [3]. The key traces  $^{13}\text{C } ^{12}\text{CH}_5\text{O}^+$  and  $^{12}\text{C}_2\text{H}_7\text{O}_2^+$  show a very coherent trend while  $^{12}\text{C}_2\text{H}_7\text{O}^+$  and  $\text{C}_4\text{H}_9\text{O}_2^+$  are in line with expectations of tertiary ions via fragmentation and clustering under conditions of PI depletion discussed in E.2.2.

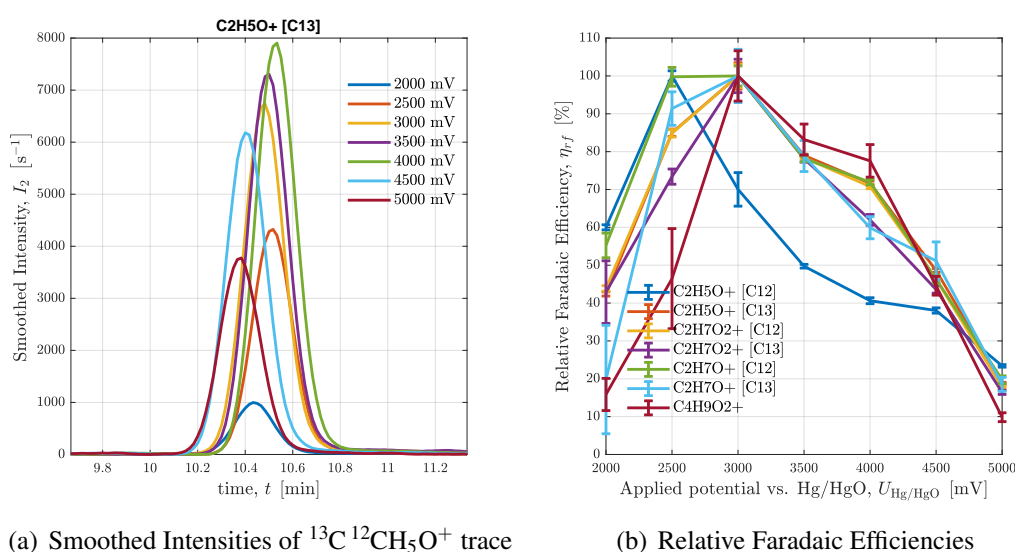


**Figure 30:** Analysis of traces related to  $\text{H}_3\text{O}^+$  ionization of acetaldehyde.

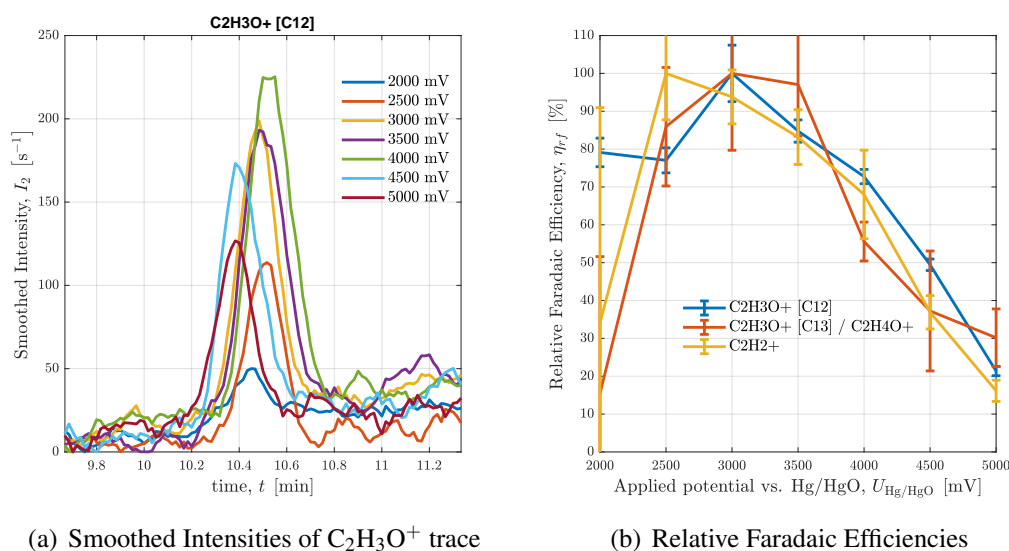


**Figure 31:** Analysis of traces related to  $\text{O}_2^+$  ionization of acetaldehyde.

As residual  $\text{O}_2^+$  does not suffer PI depletion for acetaldehyde (see E.2.1), it is illuminating to study the traces connected to its secondary ions in Fig. 31: The shape of relative FE curve in Fig. 31(b) is very similar of that in Fig. 30(b) but only  $\text{C}_2\text{H}_3\text{O}^+$  has a large enough SNR to warrant acceptable uncertainties. The comparatively large value at  $U_{\text{Hg}/\text{HgO}} = 2\text{V}$  is probably still caused by noise level for the most part as seen in Fig. 31(a).

**A notable irregularity** is the  $\text{C}_2\text{H}_5\text{O}_2^+$  trace that we analysed in some detail as it shows peaks close to acetaldehyde retention time and could be explained mechanistically by dissociation of ethylene from  $\text{C}_4\text{H}_9\text{O}_2^+$  or hydrogen from  $\text{C}_2\text{H}_7\text{O}_2^+$ . As can be seen in Fig. 32, there are peaks close to acetaldehyde's retention time, but none of them seem to actually caused by acetaldehyde. They also cannot be ascribed to propylene or ethanol as the former has a much smaller retention time and the latter a much larger retention time.

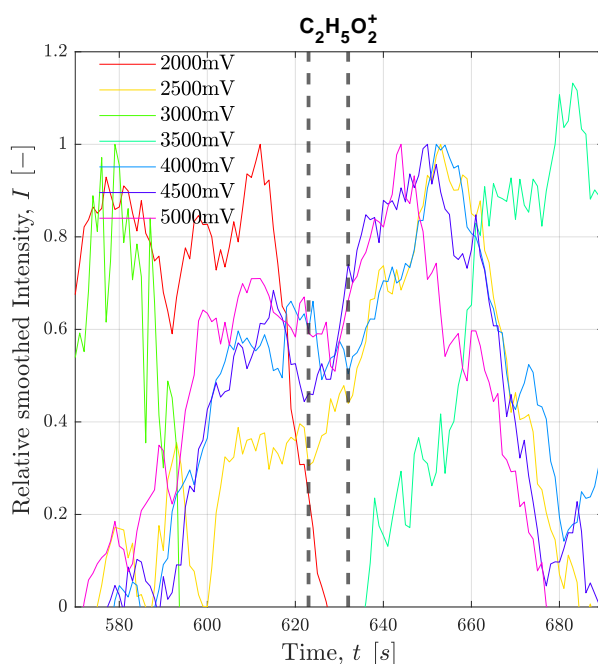


**Figure 32:** Intensity of  $\text{C}_2\text{H}_5\text{O}_2^+$  trace over different applied potentials. A dashed line indicates the location of all other traces peaking with acetaldehyde.

This behaviour could not be verified within the  $^{13}\text{C}$  experiment and instead a distinct peak at acetaldehyde retention time appears. The  $^{13}\text{C}_2\text{H}_5\text{O}_2^+$  has a somewhat small SNR and appears slightly shifted. Moreover, a verification experiment with acetaldehyde as single compound also shows a small signal along with most other traces listed in 16. This lends credibility to the presumed PTR reactions.

## D.8 Ethanol

Based on the identified peaks shown in Tab. 17, this is ethanol. Retention times have not been reported for this compound yet, though it fits into the picture with the highest boiling

point of the C<sub>2</sub> compounds.

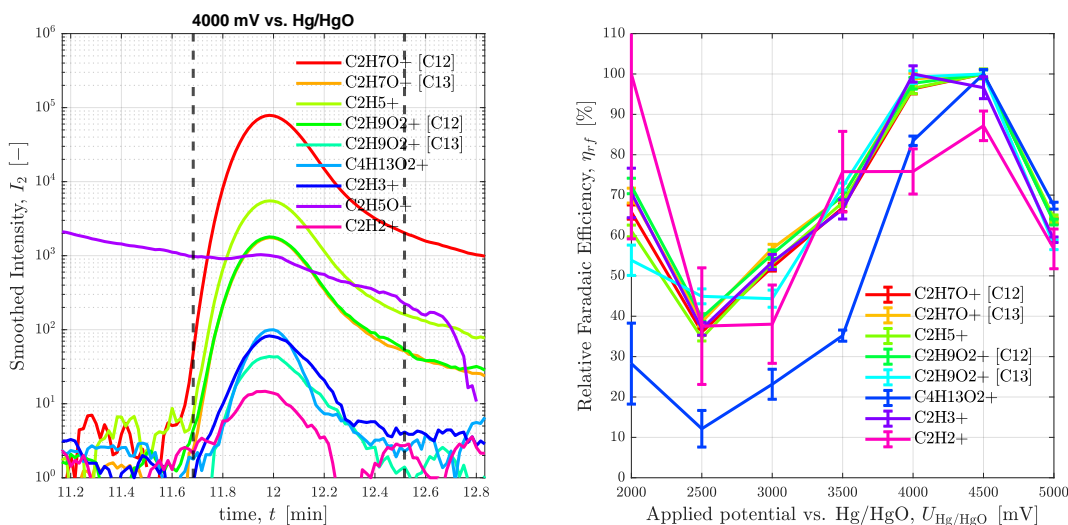
**Table 17:** All detected traces that are peaking with ethanol.

Retention time		Applied potential vs. Hg/HgO in mV							
		2000	2500	3000	3500	4000	4500		
Peak time in s		717	720	717	718	719	712	710	
Start time in s		700	703	700	699	701	692	690	
End time in s		750	753	750	749	751	742	740	

<i>m/z</i>	Ion assumed	Integrated smoothed intensity (Normalized counts)						Origin	Comments	
47.05	<sup>12</sup> C <sub>2</sub> H <sub>7</sub> O <sup>+</sup>	172549	205754	388661	698355	1204265	1445112	1440198	C <sub>2</sub> H <sub>5</sub> OH + H <sub>3</sub> O <sup>+</sup>	Main product of ethanol protonation with H <sub>3</sub> O <sup>+</sup> according to [59]
48.05	<sup>13</sup> C <sup>12</sup> CH <sub>7</sub> O <sup>+</sup>	4072	4905	9388	16133	27371	32007	32057		Isotope ratio stable around 2.3%
29.04	C <sub>2</sub> H <sub>5</sub> <sup>+</sup>	11543	14333	28598	51301	87134	104305	105251	C <sub>2</sub> H <sub>7</sub> O <sup>+</sup> - H <sub>2</sub> O	Dissociation of water
27.02	C <sub>2</sub> H <sub>3</sub> <sup>+</sup>	175	200	404	667	1277	1396	1348	C <sub>2</sub> H <sub>5</sub> <sup>+</sup> - H <sub>2</sub>	Dissociation of hydrogen
93.07	C <sub>4</sub> H <sub>13</sub> O <sub>2</sub> <sup>+</sup>	128	88	197	409	1184	1601	1732	C <sub>2</sub> H <sub>7</sub> O <sup>+</sup> · C <sub>2</sub> H <sub>5</sub> OH	Signal very small but somewhat underestimated since the actual mass would be <i>m</i> = 93.12 Da
45.03	C <sub>2</sub> H <sub>5</sub> O <sup>+</sup>	3876	5129	8869	11083	13240	12788	10023	C <sub>2</sub> H <sub>7</sub> O <sup>+</sup> - H <sub>2</sub>	Hard to separate from descending arm of acetaldehyde peak; possibly O <sub>2</sub> <sup>+</sup> product
65.06	<sup>12</sup> C <sub>2</sub> H <sub>9</sub> O <sub>2</sub> <sup>+</sup>	4391	5286	9568	16874	28405	33578	33321	C <sub>2</sub> H <sub>5</sub> OH · H <sub>3</sub> O <sup>+</sup>	Second H <sub>3</sub> O <sup>+</sup> product due to large concentration (around 2%), not documented by [59]
66.06	<sup>13</sup> C <sup>12</sup> CH <sub>9</sub> O <sub>2</sub> <sup>+</sup>	76	143	197	426	713	825	743		Isotope ratio varies around 2.4%
26.02	C <sub>2</sub> H <sub>2</sub> <sup>+</sup>	69	47	36	181	181	255	257	C <sub>2</sub> H <sub>6</sub> O <sup>+</sup> - H <sub>2</sub> O - H <sub>2</sub>	Possibly dissociations from second O <sub>2</sub> <sup>+</sup> product

This is the last reported species for which cluster formation due to large concentrations was observed, see appendix E.3.5. All main traces were verified within the <sup>13</sup>C experiment.



(a) C<sub>2</sub>H<sub>5</sub>OH signals at U<sub>Hg/HgO</sub> = 2.5 V

(b) Relative Faradaic Efficiencies of C<sub>2</sub>H<sub>5</sub>OH traces

**Figure 33:** Analysis of traces and integrated intensities within C<sub>2</sub>H<sub>5</sub>OH peak.

An interesting case here is the O<sub>2</sub><sup>+</sup> ionization which should be observed as RRC are reported to be similar to H<sub>3</sub>O<sup>+</sup> [59]. C<sub>2</sub>H<sub>5</sub>O<sup>+</sup> should be the main product but is first hard to quantify due to overlaps with the much larger acetaldehyde signal as seen in Fig. 33(a) - nonetheless its strength is between 1% and 2% of C<sub>2</sub>H<sub>7</sub>O<sup>+</sup> which supports the hypothesis. On the other hand though, no significant signal was detected for C<sub>2</sub>H<sub>6</sub>O<sup>+</sup> which should be the second O<sub>2</sub><sup>+</sup> product - intensities are in an order of magnitude that points towards only

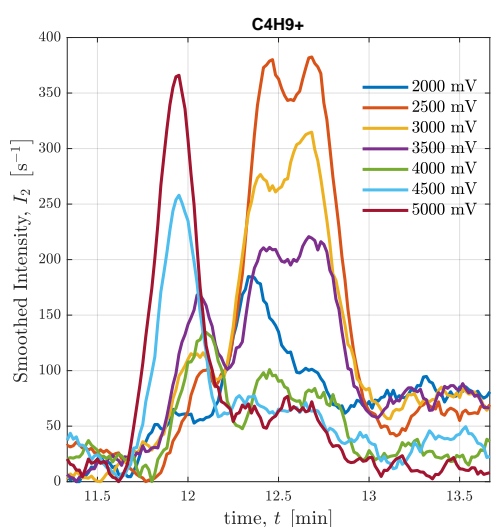
$^{13}\text{C}^{12}\text{CH}_5\text{O}^+$  though. This might be just another instance where reported product ratios from SIFT are not applicable (see appendix E.1.1) as  $\text{C}_2\text{H}_2^+$  could be a corresponding product of rapid hydrogen and water dissociation.

As we can see in Fig. 33(b), relative Faradaic Efficiency keeps decreasing with applied potential at first but then rises again up to  $U_{\text{Hg}/\text{HgO}} = 4000\text{mV}$  in contrast to the literature where a further decrease in specific current density is reported for larger applied potentials [2]. Most traces' trends agree very well with each other except for  $\text{C}_2\text{H}_2^+$  which can be explained by the small SNR. The curve of the cluster trace's ( $\text{C}_4\text{H}_{13}\text{O}_2^+$ ) relative Faradaic Efficiency significantly below the others is expected behaviour as explained in E.2.2.

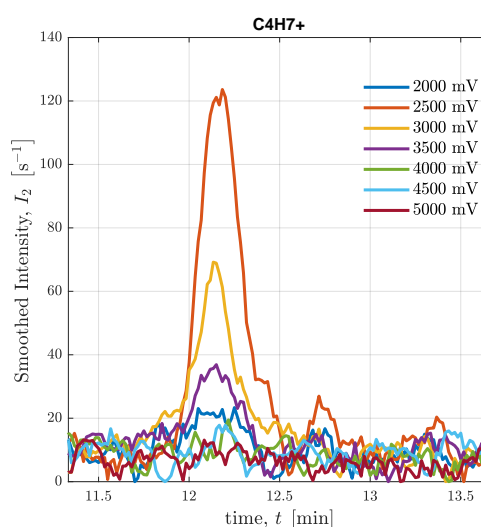
## D.9 But(adi)ene

Based on reported retention times and observed traces peaking, we expect butene and/or butadiene which is confirmed by secondary ions observed as seen in Fig. 34: Direct protonation products  $\text{C}_4\text{H}_9^+$  and  $\text{C}_4\text{H}_7^+$  as well as traces of a tertiary  $\text{C}_3\text{H}_6^+$  ion by fragmentation. We analyse the three traces in some more detail:

- $\text{C}_4\text{H}_9^+$  is reported for protonation of 2-butene [57] and its signal in Fig. 34(a) shows 3 distinct peaks that indicate the presence of 3 different butene isomers. With increasing potential main signal shifts from second third and then first peak - suggesting different selectivities and possibly different reaction paths for butene isomers.
- $\text{C}_4\text{H}_7^+$  peaks in Fig. 34(b) meanwhile do not coincide with any of the  $\text{C}_4\text{H}_9^+$  and are in fact positioned directly between the first and the second. Butadiene is the most likely origin based on similarity of species and reported retention times.
- $\text{C}_3\text{H}_6^+$  trace shown in Fig. 34(c) is interpreted as dissociation of a methyl radical from the protonated butene based on a similar mechanism in the literature suggested



(a) Intensities of  $\text{C}_4\text{H}_9^+$  trace



(b) Intensities of  $\text{C}_4\text{H}_7^+$  trace

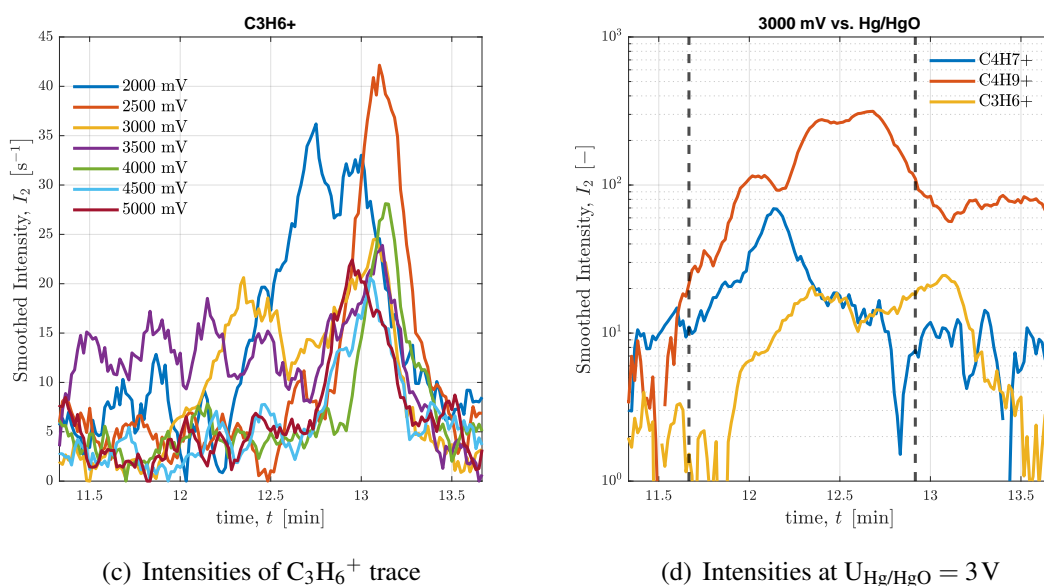


**Figure 34:** Analysis of traces and integrated intensities within butene / butadiene peak.

for  $O_2^+$  ionization of 2-butene [57]. Generally speaking, it seems to point towards 2-butene rather than 1-butene since the double bond can help stabilize the radical. It is notable that the retention time coincides only with one of the two latter peaks of  $C_4H_9^+$  as shown in Fig. 34(d) - switching from one to the other with applied potential. The SNR is quite small though and the peaks are not completely separable from the next eluted species around  $t = 770$  s to 788 s.

Fig. 35 shows the different retention times of detected peaks. The small but significant shifts attest to the fact of different species with similar chemical constitution that are just barely separated by the gas chromatography.

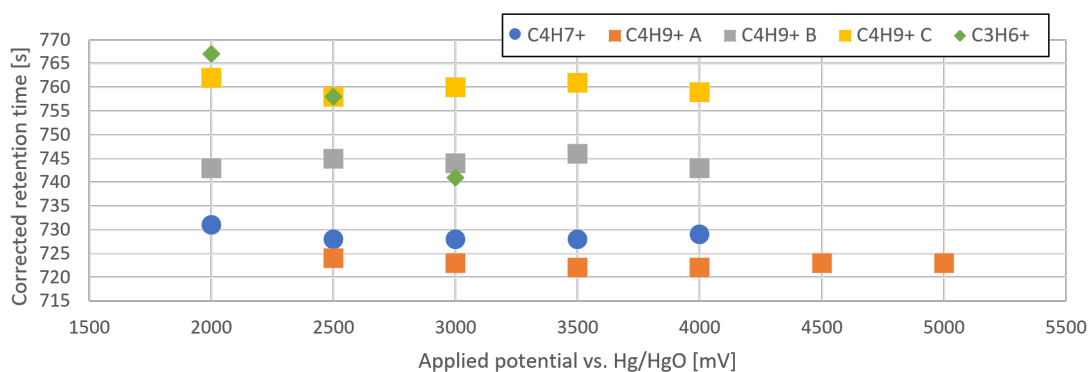


**Figure 35:** Overview of adjusted retention times of but(adi)ene-related traces peaking.

In Fig. 35 we observe 3-4 clusters of peaks throughout all applied potentials. We therefore suggest the following assignments:

1. The peak around  $t = 717$  s to 723 s is probably 1-butene. The documented relative retention times agree with 1-butene eluting first.
2. The peak around  $t = 728$  s to 733 s is probably butadiene. The  $C_4H_9^+$  trace is actually at a minimum at this time so it is unlikely to be a butene isomer. Furthermore, documented retention times point towards butadiene as between 1- and 2-butene.
3. The latter double peak of  $C_4H_9^+$  is probably 2-butene which matches documented retention times and the observation of  $C_3H_6^+$  as a fragment from methyl dissociation as discussed above.
  - (a) Documented retention times suggest peaks at  $t = 740$  s to 747 s to be trans.
  - (b) Documented retention times suggest peaks at  $t = 757$  s to 765 s to be cis.

**1-butene** peak as described above was separated from the other peaks, peak locations and integrated values are shown in Tab. 18.

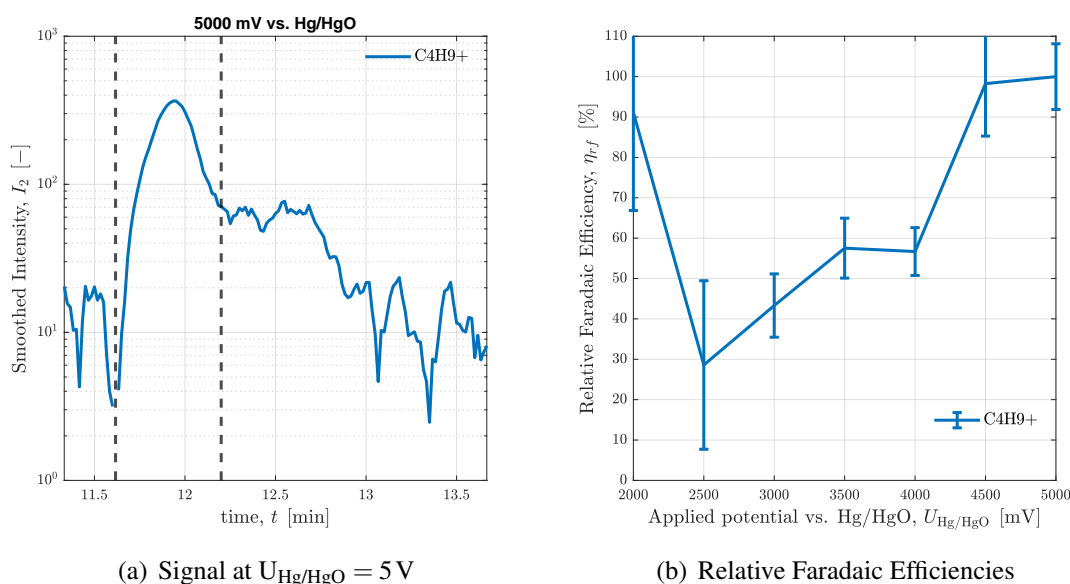
**Table 18:** All detected traces that are peaking with 1-butene.

Retention time	Applied potential vs. Hg/HgO in mV							Origin	Comments
	2000	2500	3000	3500	4000	4500	5000		
Peak time in s	715	725	721	723	726	717	716	C <sub>4</sub> H <sub>8</sub> + H <sub>3</sub> O <sup>+</sup>	
Start time in s	701	707	709	710	709	699	697		
End time in s	722	729	730	733	738	730	732		

$m/z$	Ion assumed	Integrated smoothed intensity (Normalized counts)							Origin	Comments
57.07	C <sub>4</sub> H <sub>9</sub> <sup>+</sup>	663	557	934	1632	1883	3683	5487		

The distinct 1-butene-related peak of  $C_4H_9^+$  was verified by the <sup>13</sup>C experiment.



**Figure 36:** Analysis of traces and integrated intensities within 1-butene peak.

In Fig. 36 it is apparent that 1-butene production rises sharply with applied potential and keeps increasing even at  $U_{\text{Hg}/\text{HgO}} = 5000 \text{ mV}$ . It is the first alkene observed that does not exhibit a selectivity peak at smaller applied potentials, compare to D.4 and D.6. The initial high relative Faradaic Efficiency is caused by the large SNR of a small signal combined with small current densities.

**Butadiene** peak via  $\text{C}_4\text{H}_9^+$  appears separated from the other peaks (via  $\text{C}_4\text{H}_7^+$ ) - peak locations and integrated values are shown in Tab. 19.

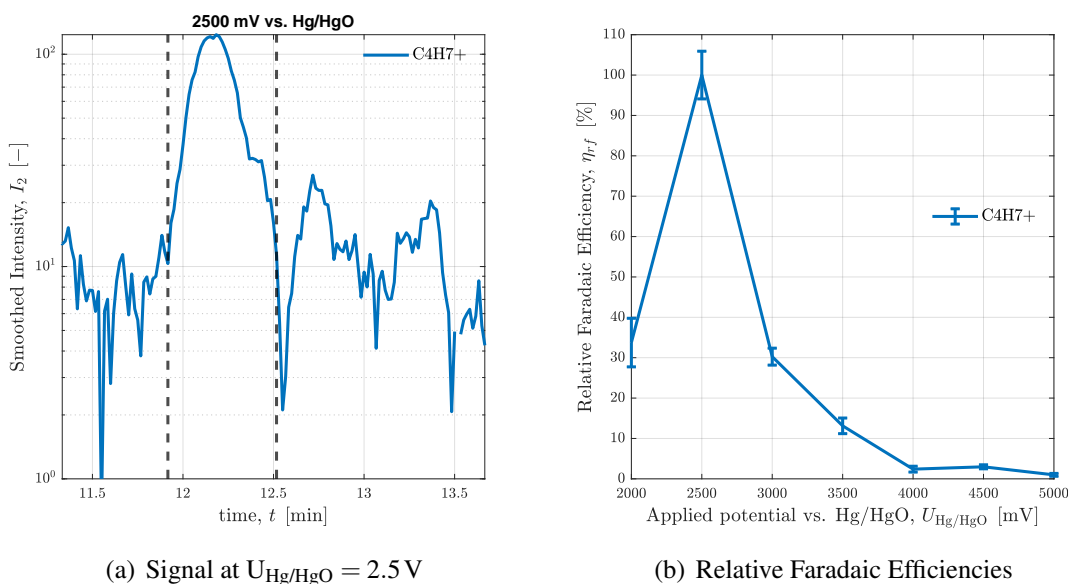
**Table 19:** All detected traces that are peaking with butadiene.

Retention time	Applied potential vs. Hg/HgO in mV						
	2000	2500	3000	3500	4000	4500	5000
Peak time in s	728	731	730	729	733	730	728
Start time in s	719	715	715	718	717	722	718
End time in s	745	751	751	745	738	739	732

$m/z$	Ion assumed	Integrated smoothed intensity (Normalized counts)						Origin	Comments	
55.055	$\text{C}_4\text{H}_7^+$	370	2021	725	558	120	165	68	$\text{C}_4\text{H}_6 + \text{H}_3\text{O}^+$	

The  $\text{C}_4\text{H}_7^+$  peak is only reliably detectable at small applied potentials, the other values are therefore somewhat skewed and could be declared 0 as done for other species. This is also the reason why it could not be verified by the  $^{13}\text{C}$  experiment since that operates with a relatively large applied potential.



**Figure 37:** Analysis of traces and integrated intensities within butadiene peak.

In Fig. 37 it is apparent that butadiene production peaks sharply at  $U_{\text{Hg}/\text{HgO}} = 2500 \text{ mV}$  and is basically non-existent for  $U_{\text{Hg}/\text{HgO}} > 3500 \text{ mV}$ .

**2-trans-butene** peaks as described above was separated from the other peaks, peak locations and integrated values are shown in Tab. 20.

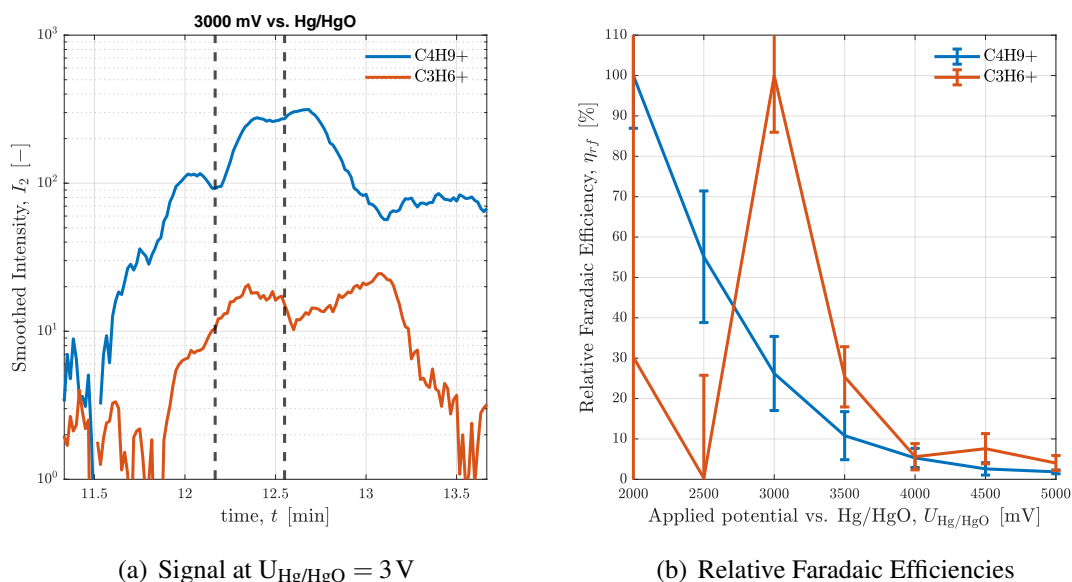
**Table 20:** All detected traces that are peaking with 2-trans-butene.

Retention time	Applied potential vs. Hg/HgO in mV						
	2000	2500	3000	3500	4000	4500	5000
Peak time in s	740	747	744	746	747	741	740
Start time in s	725	729	730	733	738	733	735
End time in s	756	755	753	756	758	749	745

$m/z$	Ion assumed	Integrated smoothed intensity (Normalized counts)						Origin	Comments	
57.07	$C_4H_9^+$	1973	2144	1342	843	583	400	387	$C_4H_8 + H_3O^+$	appears for few applied potentials only
42.04	$C_3H_6^+$	61	-33	177	42	25	9	11	$C_4H_9^+ - CH_3$	

The  $C_3H_6^+$  trace is quite low signal-to-noise and only reliably detected for some of the applied potentials. It could also not be verified by the  $^{13}C$  experiment so is to be taken with some caution. Meanwhile,  $C_4H_9^+$  was verified with  $^{13}C$  as first of a double peak.



**Figure 38:** Analysis of traces and integrated intensities within 2-trans-butene peak.

The  $C_4H_9^+$  peak is very clearly detectable and intensities follow a clear trend of large relative Faradaic Efficiencies at low applied potentials sharply dropping with increased current until at larger applied potentials almost no 2-trans-butene could be detected, see Fig. 38.

**2-cis-butene** peaks as described above was separated from the other peaks, peak locations and integrated values are shown in Tab. 21.

**Table 21:** All detected traces that are peaking with 2-cis-butene.

Retention time		Applied potential vs. Hg/HgO in mV						Origin	Comments
		2000	2500	3000	3500	4000	4500		
Peak time in s		765	763	760	762	765	759	757	
Start time in s		756	755	753	756	758	749	745	
End time in s		772	780	778	782	780	772	774	
$m/z$	Ion assumed	Integrated smoothed intensity (Normalized counts)							
57.07	$C_4H_9^+$	390	3118	2589	1624	744	605	912	$C_4H_8 + H_3O^+$
42.04	$C_3H_6^+$	165	5	-47	-13	-32	-32	-33	$C_4H_9^+ - CH_3$ appears for few applied potentials only

The  $C_3H_6^+$  trace is quite low signal-to-noise and only reliably detected for some of the applied potentials. It could also not be verified by the  $^{13}C$  experiment so is to be taken with some caution. Meanwhile,  $C_4H_9^+$  was verified with  $^{13}C$  as second of a double peak.

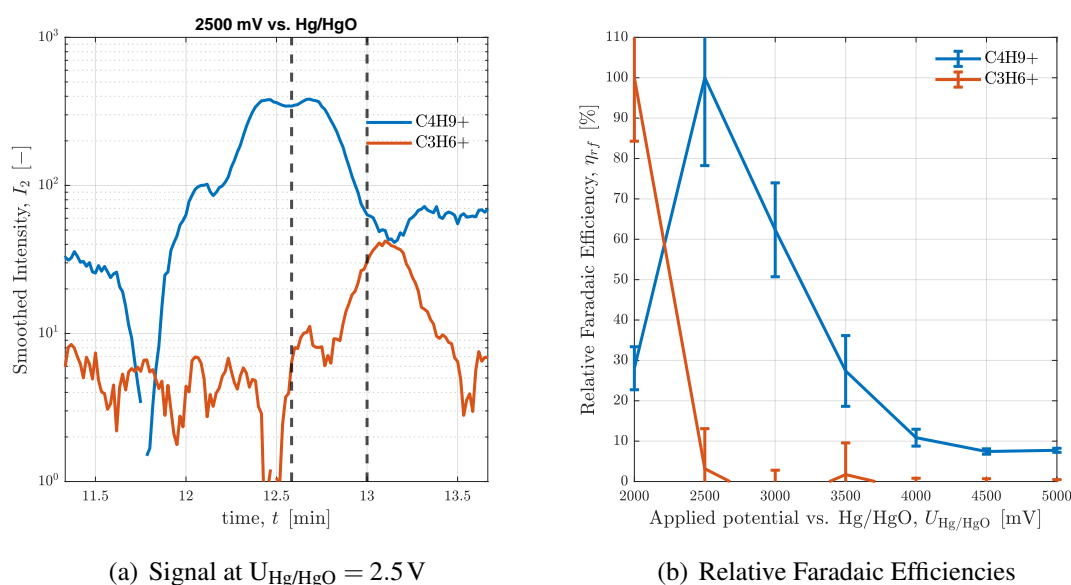


**Figure 39:** Analysis of traces and integrated intensities within 2-cis-butene peak.

The  $C_4H_9^+$  peak is very clearly detectable and intensities follow a clear trend of sharp increase at low applied potentials (peaking at  $U_{Hg/HgO} = 2500$  mV) and then slowly decreasing until at larger applied potentials almost no 2-cis-butene could be detected, see Fig. 39.

## D.10 Cyclopropane

There are no species expected based on documented retention times at this time. But given the consistent finding of  $C_3H_6^+$  and the fact that other non-oxygenated  $C_3$  species were detected much earlier, we have reason to assume that this is actually cyclopropane.

**Table 22:** All detected traces that are peaking with cyclopropane.

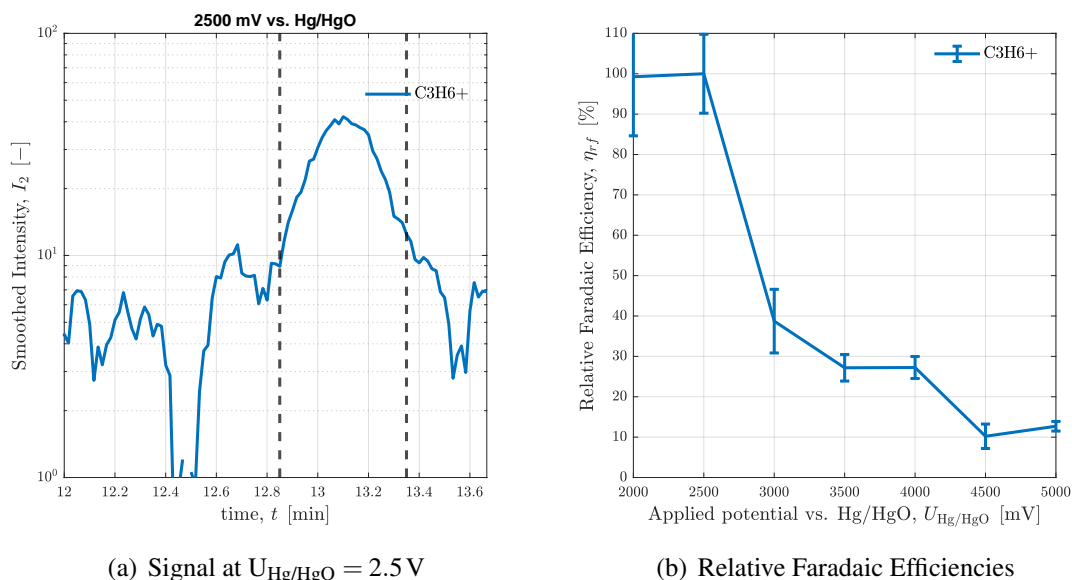
Retention time	Applied potential vs. Hg/HgO in mV								Origin	Comments
	2000	2500	3000	3500	4000	4500	5000			
Peak time in s	778	786	784	787	789	783	777			
Start time in s	773	771	770	772	775	776	764			
End time in s	794	798	795	796	798	796	798			

$m/z$	Ion assumed	Integrated smoothed intensity (Normalized counts)								Origin	Comments
42.042	$C_3H_6^+$	226	589	308	264	342	133	308	$C_3H_6 + O_2^+$	Reported as main $O_2^+$ ionization product by [57]	

For cyclopropane we would usually expect  $C_3H_7^+$  as the main protonation product according to [57] - we do not find peaks at  $m = 41.04$  Da either though. For this reason, we suggest that we see a fairly large amount of cyclopropane that was not protonated due to PTR-MS parameters and therefore ionized by residual  $O_2^+$ .

In Fig. 40(b) we see relative Faradaic Efficiencies peaking early at  $U_{Hg/HgO} = 2500$  mV but then basically trailing off at a constant level up to larger applied potentials. This behaviour is somewhat similar to the one of 2-butene at earlier retention times and attests to the fact that it is somewhat influenced by it - double peaks for some of the applied potentials indeed had to be separated. Within the  $^{13}C$  experiment cyclopropane could not be verified unambiguously - we find a corresponding peak though with low signal-to noise ratio which can be partially attributed to the large peak from ethanol before.

**Figure 40:** Analysis of traces and integrated intensities within 2-cis-butene peak.

## D.11 C<sub>3</sub>H<sub>6</sub>O isomers

Around  $t = 850$  s to  $1000$  s a large signal of  $C_3H_7O^+$  is observed that coincides with documented retention times for acetone. But on closer examination, three distinct peaks can

be identified, indicating three constitutional isomers of  $C_3H_6O$  that were separated by the column. As shown in Fig. 41, these three species lead to different fragments and ion ratios that can help with identification. These have been verified within the  $^{13}C$  experiment.

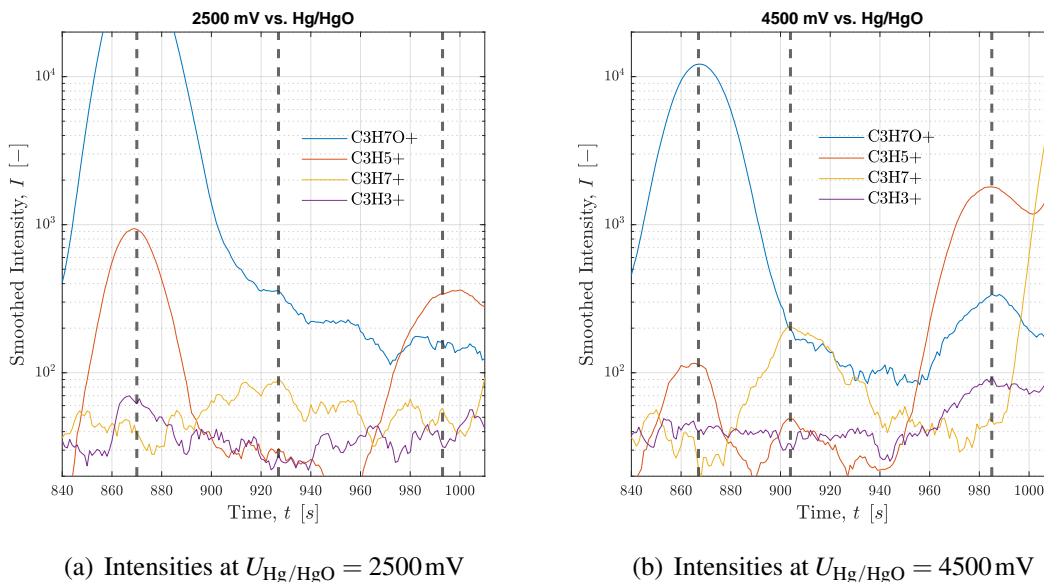


**Figure 41:** Intensities of traces related to  $C_3H_6O$  for different applied potentials.

Based on simple combinatorics, only two  $C_3H_6O$  species besides acetone seem realistic: propionaldehyde and allyl alcohol. Most other possible isomers are either less stable tautomers of the aforementioned or ethers. The only non-cyclical ether is methyl vinyl ether and with a significantly differing boiling point and vapour pressure would be expected to elute much earlier than the other compounds. Cyclical compounds seem unlikely: even though a cyclical product has been observed for the first time in this study, its derivatives are even less stable and production is not expected at this rate if at all. Additionally, these three species (acetone, propanal, allyl alcohol) have been observed as eCO2R products before [2].

We assigned the  $C_3H_6O$  isomers as following based on retention times, recorded fragments, and observed trends:

1. The peak around  $t = 862 \text{ s}$  to  $875 \text{ s}$  is most likely propanal as it has the smallest boiling point of the three and exhibited the largest signal at lower applied potentials as the others which is supported by the literature [2].
2. The peak around  $t = 903 \text{ s}$  to  $925 \text{ s}$  is most likely acetone. Its signal is significantly smaller and peaks barely from the overlapping propanal. This is expected behaviour as its boiling point is only slightly higher and it has been reported as the least-produced of the three isomers [2].
3. The peak around  $t = 985 \text{ s}$  to  $993 \text{ s}$  is most likely allyl alcohol. With a much higher point it elutes significantly later than the first two isomers.

**Propanal** peak as described above was observed with the highest number of fragments and largest overall signals as shown in Tab. 23.

**Table 23:** All detected traces that are peaking with propanal.

Retention time	Applied potential vs. Hg/HgO in mV							Origin	Comments
	2000	2500	3000	3500	4000	4500	5000		
Peak time in s	864	870	868	872	874	867	866		
Start time in s	835	840	837	839	845	837	837		
End time in s	905	910	907	909	915	907	907		

$m/z$	Ion assumed	Integrated smoothed intensity (Normalized counts)							Origin	Comments
59.05	$^{12}\text{C}_3\text{H}_7\text{O}^+$	506760	1546721	1501732	1283260	593135	302796	178824	$\text{CH}_3\text{CH}_2\text{CHO} + \text{H}_3\text{O}^+$	Large signal; Only propanal protonation product according to [56]
60.05	$^{13}\text{C}^{12}\text{C}_2\text{H}_7\text{O}^+$	16529	49233	48808	42080	20053	10282	5774	$\text{C}_3\text{H}_7\text{O}^+ - \text{C}_2\text{H}_4$	Isotope ratio quite stable at 3.3%
31.02	$\text{CH}_3\text{O}^+$	13971	29425	24311	14739	8645	4747	5215		
41.04	$^{12}\text{C}_3\text{H}_5^+$	6926	19974	16663	9516	3770	2291	800	$\text{C}_3\text{H}_7\text{O}^+ - \text{H}_2\text{O}$	Dissociation of ethylene
42.04	$^{13}\text{C}^{12}\text{C}_2\text{H}_5^+$	353	681	529	300	138	148	21		
39.03	$\text{C}_3\text{H}_3^+$	856	688	601	553	425	199	157	$\text{C}_3\text{H}_5^+ - \text{H}_2$	Dissociation of hydrogen
77.06	$^{12}\text{C}_3\text{H}_9\text{O}_2^+$	2652	8244	6863	4523	2098	1130	564	$\text{CH}_3\text{CH}_2\text{CHO} \cdot \text{H}_3\text{O}^+$	Second $\text{H}_3\text{O}^+$ product (around 0.5%), not documented by [56]
78.06	$^{13}\text{C}^{12}\text{C}_2\text{H}_9\text{O}_2^+$	141	343	235	224	93	59	-18		Small signal-to-noise; Isotope ratio varying around 3.3%
61.07	$\text{C}_3\text{H}_9\text{O}^+$	584	1705	1503	1457	533	396	202	$\text{C}_3\text{H}_9\text{O}_2^+ - \text{O}$	Dissociation of oxygen radical
64.05	unknown	1	177	140	111	75	51	-1		Unknown origin

Within the  $^{13}\text{C}$  experiment we were able to verify all the main propanal-related traces. A verification experiment with acetaldehyde as single compound showed all ions found to be contributing more than 0.1% of the overall signal above with their expected ratios. The suggested PTR mechanism can be found in appendix E.3.7. Ratios of all observed isotopes within the original experiment are calculated to be  $\approx 3.3\%$ . Moreover, even though the signal of  $^{12}\text{C}_3\text{H}_7\text{O}^+$  is very large, we do not seem to have detector saturation since the isotope ratio does not drop even at peak intensities. These occur at  $U_{\text{Hg}/\text{HgO}} = 2500\text{ mV}$  before decreasing again with applied potential.

One detected trace peak remains unexplained, at  $m/z \approx 64\text{ Da}$ . This trace was first assigned to the isotope  $^{13}\text{C}^{12}\text{CH}_7\text{O}_2^+$  but since  $^{12}\text{C}_2\text{H}_7\text{O}_2^+$  was not detected at all, this suggestion was discarded. It does not seem to be an artefact it can be detected consistently at all applied potentials where the other propanal traces also show large intensities and follows a similar trend. It could not be verified neither within the  $^{13}\text{C}$  nor the pure compound experiment, which suggests it is some obscure fragmentation like a methylidyne radical  $\text{C}_3\text{H}_9\text{O}_2^+ - \text{CH} \longrightarrow \text{C}_2\text{H}_8\text{O}_2^+$ .

What is interesting to see is that the peaks of the different traces are not exactly coinciding for some of the applied potentials and in fact seem to shift away from each other with increased applied potential, see Fig. 42(a). We see  $\text{C}_3\text{H}_5^+$ ,  $\text{CH}_3\text{O}^+$ , and  $\text{C}_3\text{H}_9\text{O}_2^+$  first, then  $\text{C}_3\text{H}_7\text{O}^+$  and  $\text{C}_3\text{H}_9\text{O}^+$  a few seconds later (up to  $\Delta t = 10\text{ s}$  for  $U_{\text{Hg}/\text{HgO}} > 4000\text{ mV}$ ). These slight shifts illustrated by the red and green dotted lines might be random and seem mostly arbitrary. The main ion ( $\text{C}_3\text{H}_7\text{O}^+$ ) shift towards few seconds later maybe due to overlap of smaller acetone peak and  $\text{C}_3\text{H}_9\text{O}^+$  has very flat peak, the exact location is hard to make out.

As we can see in Fig. 42(b), relative Faradaic Efficiency peaks early at  $U_{\text{Hg}/\text{HgO}} = 2500\text{ mV}$  and decreases with larger applied potentials. Most traces' trends agree very well with each other, the ones with smaller SNR and therefore larger uncertainties deviate somewhat. The ratio of fragments and clusters can be seen to increase for the largest concentrations as expected.

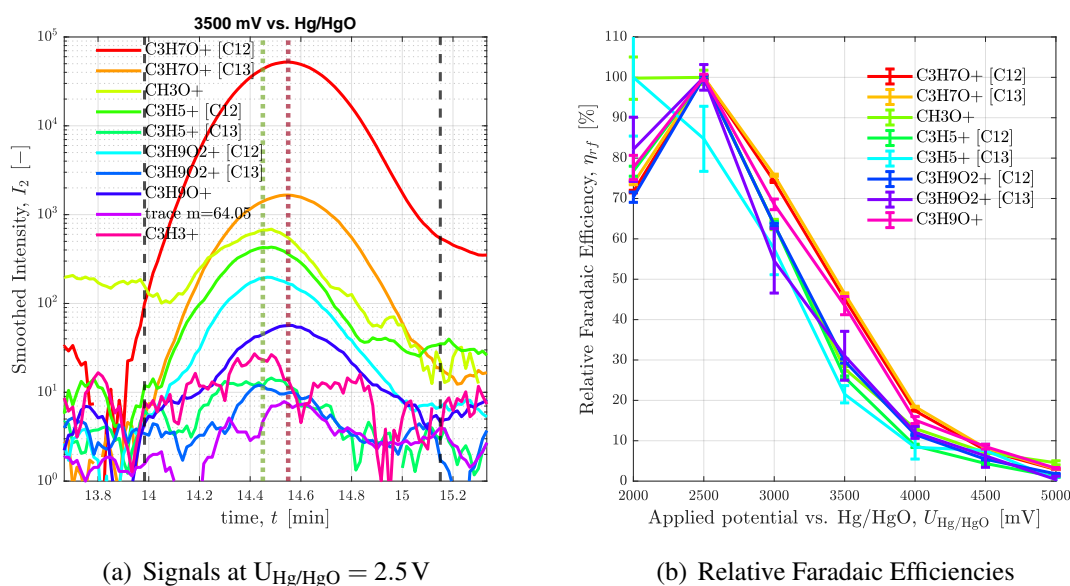


**Figure 42:** Analysis of traces and integrated smoothed intensities within propanal peak.

**Acetone** peak as described above was observed with small signals and massive overlap of propanal's  $C_3H_7O^+$  for applied potentials  $U_{Hg/HgO} > 2.0V$  as seen in Tab. 24.

**Table 24:** All detected traces that are peaking with acetone.

Retention time	Applied potential vs. Hg/HgO in mV							Origin	Comments	
	2000	2500	3000	3500	4000	4500	5000			
Peak time in s	-	927	918	925	917	904	908	$CH_3COCH_3 + H_3O^+$	Propanal peak is so broad that it still covers acetone peak location	
Start time in s	-	893	891	899	895	890	884			
End time in s	-	943	941	949	945	940	934			
$m/z$	Ion assumed	Integrated smoothed intensity (Normalized counts)								
59.05	$C_3H_7O^+$	<i>Cannot quantitatively distinguished from propanal</i>							$CH_3COCH_3 + H_3O^+$	Propanal peak is so broad that it still covers acetone peak location Dissociation of oxygen Isotope ratio varying around 2.5% More likely than $C_3H_7O^+ - H_2O$
43.06	$^{12}C_3H_7^+$	0	1210	1788	2855	4238	4213	4159	$C_3H_7O^+ - O$	
44.06	$^{13}C^{12}C_2H_7^+$	0	63	82	43	106	72	231		
41.04	$C_3H_5^+$	0	-626	-224	263	647	579	838	$C_3H_7^+ - H_2$	

The signals for acetone are very small but sufficient to postulate its existence. The peaks of main traces (or rather main distinguishable traces) were verified within the  $^{13}C$  experiment. The prominent  $C_3H_5^+$  signal first seems to contradict the postulated acetone as water dissociation via  $C_3H_7O^+ - H_2O$  is very unlikely for ketones. Closer analysis reveals an even larger  $C_3H_7^+$  signal, indicating subsequent dissociation of atomic oxygen and hydrogen. These traces were reproduced in a verification experiment with pure compound. The signal ratio of  $C_3H_7^+$  to  $C_3H_5^+$  of 2 to 3 for acetone can be used to unambiguously identify acetone versus propanal with a ratio of  $\approx 0.1$ .

$C_3H_7O^+$  should still be dominant. This is almost impossible to verify for most applied potentials due to the massive overlap of the propanal-attributed peak as propanal's con-

centration seems at least one order of magnitude higher. For larger applied potentials  $C_3H_7O^+$  intensities drop to the level of  $C_3H_5^+$  though as shown in Fig. 43(a). It is possible that oxygen dissociation is more likely for completely dry acetone. Due to humidity effects, the comparability with reported data or verification experiments is limited when it comes to oxygenated ions.

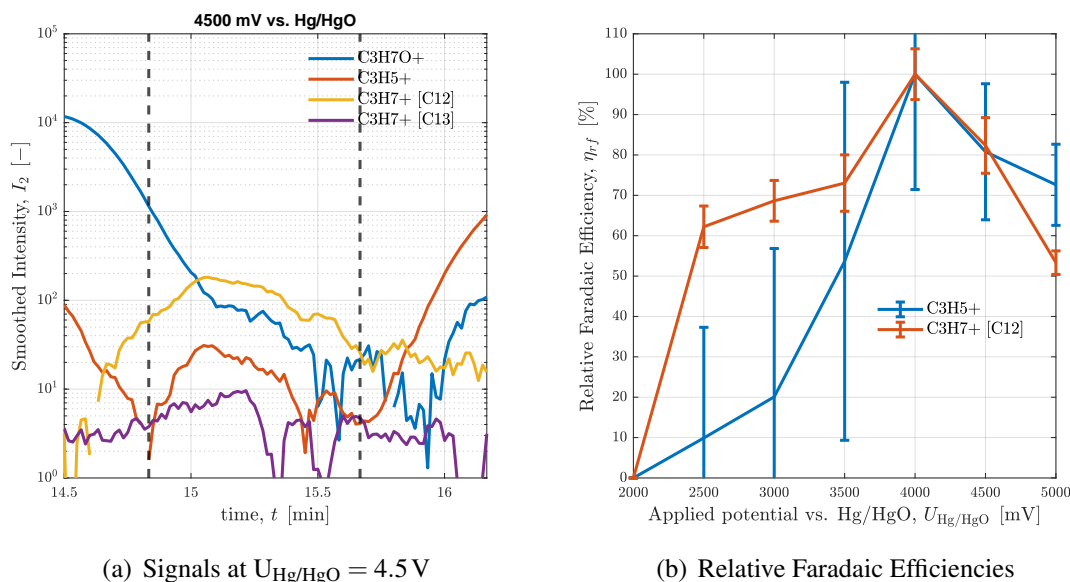


**Figure 43:** Analysis of traces and integrated smoothed intensities within acetone peak.

As shown in Fig. 43(b), acetone exhibits a selectivity trend deviating substantially from the one seen for propanal: although small SNR creates large uncertainties, an increase in relative FE for larger potentials is undeniable with a visible peak at  $U_{Hg/HgO} = 4.5$  V.

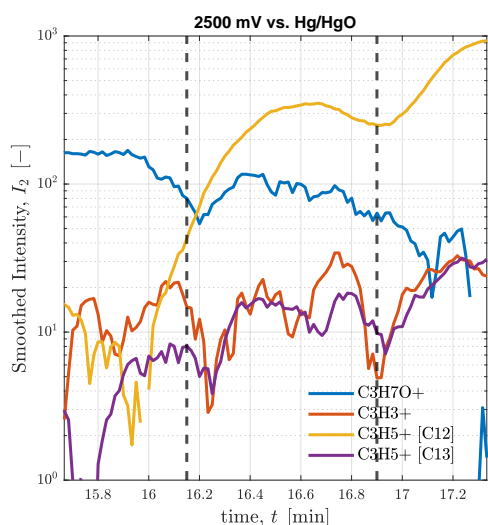
**Allyl alcohol** peak as described above can be clearly distinguished from propanal and acetone, all traces are given in Tab. 24.

**Table 25:** All detected traces that are peaking with allyl alcohol.

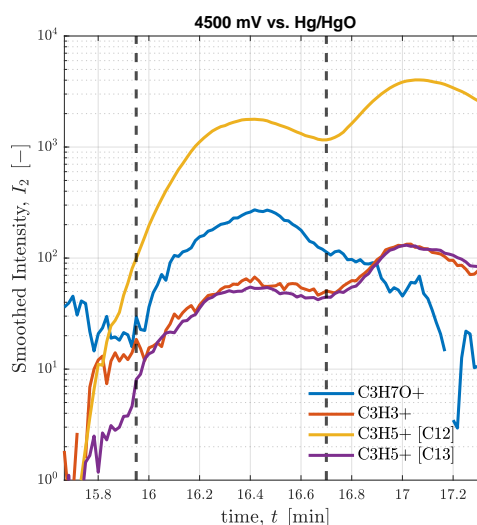
Retention time	Applied potential vs. Hg/HgO in mV							Origin	Comments
	2000	2500	3000	3500	4000	4500	5000		
Peak time in s	991	993	992	990	991	985	984	$CH_2CHCH_2OH + H_3O^+$ $C_3H_7O^+ - H_2O$	Distinguishable peak before larger peak
Start time in s	955	964	963	964	968	957	954		
End time in s	1015	1024	1023	1024	1028	1017	1014		
$m/z$	59.05	41.04	42.04	39.03					
Ion assumed	$C_3H_7O^+$	$^{12}C_3H_5^+$	$^{13}C^{12}C_2H_5^+$	$C_3H_3^+$					
		Integrated smoothed intensity (Normalized counts)							
		2495	1874	2790	4297	5751	6239	6383	
		5026	6635	10644	18128	27787	32257	29084	
		142	228	439	601	959	948	1053	Isotope ratio oscillating around 3%
		265	247	586	641	605	896	1094	Distinguishable peak before larger peak

Main traces were verified within  $^{13}C$  experiment. Even though  $C_3H_5^+$  and  $C_3H_3^+$  peaks

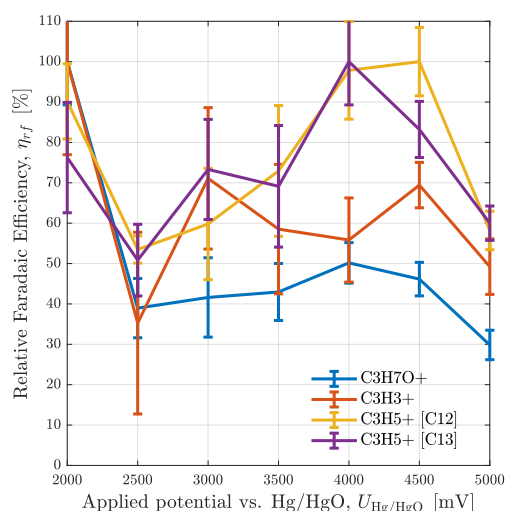
at this time are shortly followed by larger peaks as shown in Fig. 44(b) (mostly pentene), we were able to separate contributions.



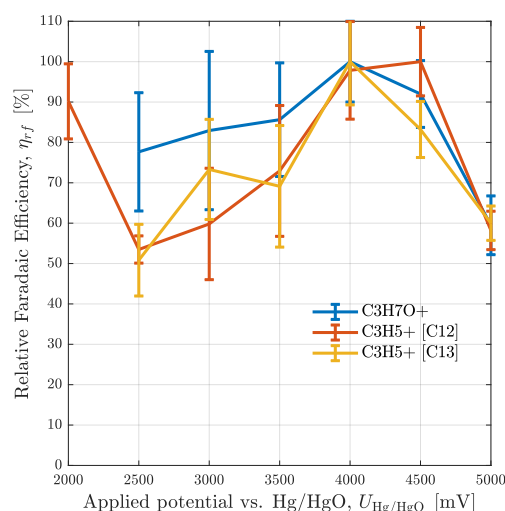
(a) Signals at  $U_{\text{Hg/HgO}} = 2.5 \text{ V}$



(b) Signals at  $U_{\text{Hg/HgO}} = 4.5 \text{ V}$



(c) Relative Faradaic Efficiencies



(d) Adjusted relative FE

**Figure 44:** Analysis of traces and integrated smoothed intensities within acetone peak.

The relative Faradaic Efficiencies shown in Fig. 44(c) show a similar trend but the different curves are not very coherent. This is caused by the very small signals amongst large noise levels for small applied potentials as seen in Fig. 44(a) and the amplification of these when dividing by the small current densities. This is a common occurrence and corrected in our workflow by neglecting the values and traces with too large SNR. To illustrate this, Fig. 44(d) shows corrected relative FE for all traces with sufficient SNR. The values for  $U_{\text{Hg/HgO}} = 2.0 \text{ V}$  have been neglected in accordance with the red highlights in Tab. 25. This shows the  $\text{C}_3\text{H}_5^+$  trace to be in good agreement with the others and there-

fore representative for allyl alcohol. It shows an initial peak of Faradaic Efficiencies for small applied potentials that first decrease and then increase again with larger potentials. It peaks again around 4.0 V to 4.5 V with only slightly larger selectivities than for 2.0 V.

## D.12 Pentene and propanol

Around  $t = 1000$  s to 1100 s we observe peaks of a few  $C_3$  traces. The large  $C_3H_7^+$  signal in combination with the smaller  $C_3H_9O^+$  signal as well as its boiling point close to allyl alcohol strongly suggest propanol as the source. Seemingly contradictory, we also find  $C_5H_{11}^+$ , which hints towards pentene production.

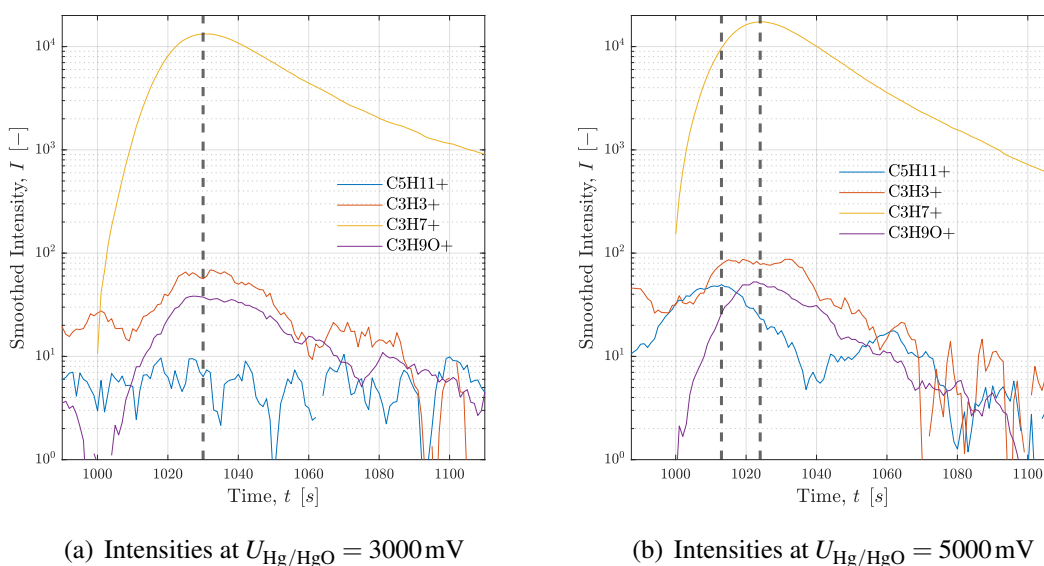


**Figure 45:** Intensities of traces peaking around  $t \approx 1020$  s for different applied potentials.

Upon analysis of precise peak times as shown in Fig. 45, a slight difference between  $C_3$  and  $C_5$  is apparent for larger applied potentials. This is indicated by the two dashed lines in Fig. 45(b). On closer examination, the  $C_3H_3^+$  trace is showing a peak at both times. We therefore hypothesize pentene as well as propanol production which was just barely separated by GC column.

**Pentene** was observed for  $t = 1011$  s to 1029 s which coincides quite well with its expected relative retention time. Detected signals are listed in Tab. 26. While the  $C_3H_3^+$  trace can be unambiguously identified as peaking with pentene as well as propanol for most applied potentials, the overlap is so substantial and overall SNR so low that the separated signal is hardly quantifiable. For this reason, its values are highlighted yellow.

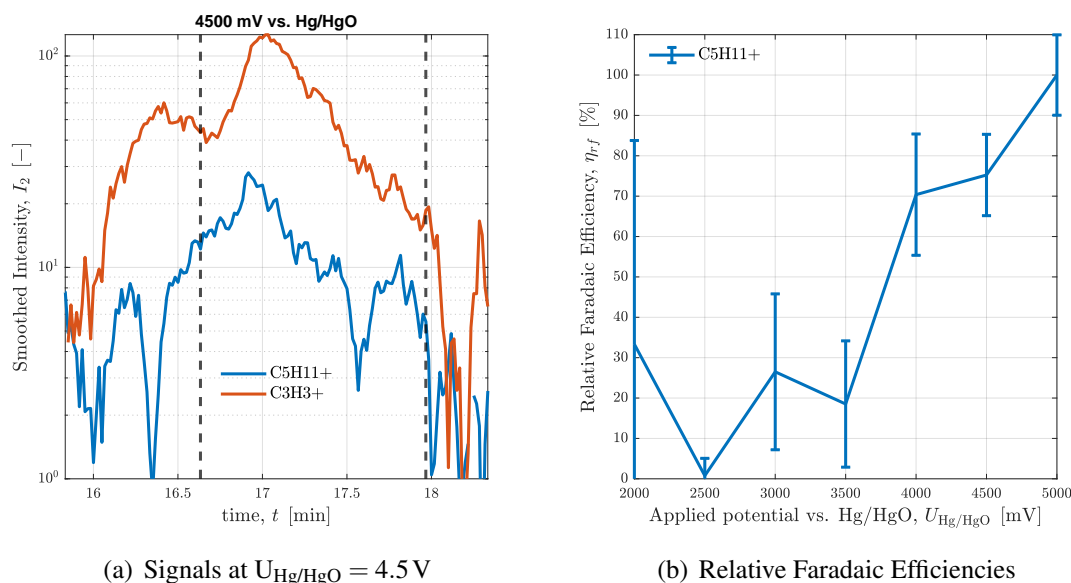
**Table 26:** All detected traces that are peaking with pentene.

Retention time	Applied potential vs. Hg/HgO in mV							Origin	Comments
	2000	2500	3000	3500	4000	4500	5000		
Peak time in s	-	-	-	1027	1026	1019	1013		
Start time in s	-	-	-	1002	1003	998	992		
End time in s	-	-	-	1082	1083	1078	1072		

$m/z$	Ion assumed	Integrated smoothed intensity (Normalized counts)						Origin	Comments	
71.09	$C_5H_{11}^+$	-	-	-	103	486	555	1022	$C_5H_{10} + H_3O^+$	Only documented protonation product of pentene [60]
39.03	$C_3H_3^+$	-	-	-	3376	2853	2585	2400	$C_3H_5^+ - H_2$	Other origins possible, multiple subsequent dissociations necessary
41.04	$C_3H_5^+$	<i>Cannot quantitatively distinguished from propanol</i>						$C_3H_7^+ - H_2$	Possibly other origin	
43.06	$C_3H_7^+$	<i>Cannot quantitatively distinguished from propanol</i>						$C_5H_{11}^+ - C_2H_4$	Ethylene dissociation	

The question remains, which pentene isomer we found. We argue that at least the main portion of it will be 1-pentene for a few reasons. First of all, retention time and PTR products coincide with what is documented in the literature for 1-pentene. But since other isomers are not as well-documented, they might possibly look very similar. Here we can use analogy to the well-observed butene peaks from D.9 as second reason: the relative Faradaic Efficiency increasing with applied potential shown in Fig. 46(b) resemble the trends observed for 1-butene and corresponds well to the mechanism proposed for alk-1-enes in the main text.



**Figure 46:** Analysis of traces and integrated smoothed intensities within pentene peak.

When looking at  $C_5H_{11}^+$  trace closely in Fig. 46(a), we see a slightly stretched peak or even a second peak around 10s to 30s after the main peak which hints towards a very small fraction of 2-butene also being produced. This is more pronounced for the slightly smaller applied potentials which lends additional credibility to this theory in analogy to butene and the proposed mechanism for alk-2-enes. A possible third peak can even be

seen  $\approx 50$ s later, which again hints at the existence of both stereoisomers in analogy to butene.

The large majority of the small amount of pentene produced will still be 1-pentene as 1-butene also dominated the butene production (partially due to larger total current densities at applied potentials where the alk-1-enes exhibit their largest Faradaic Efficiency). The  $C_5H_{11}^+$  peak was verified within the  $^{13}C$  experiment. It even shows the triple peak indicating aforementioned isomers as the current is comparable to the one at  $U_{Hg/HgO} = 4.5$  V in the main experiment.

**Propanol** was observed for 1027s to 1048s with a number of traces listed in Tab. 27. All key species detected were verified by the C13 experiment, our hypothesized PTR mechanism is shown in appendix 63.

**Table 27:** All detected traces that are peaking with propanol.

Retention time	Applied potential vs. Hg/HgO in mV							Origin	Comments
	2000	2500	3000	3500	4000	4500	5000		
Peak time in s	1041	1042	1030	1029	1030	1023	1024		
Start time in s	1007	1006	1002	1001	1002	1001	1002		
End time in s	1102	1101	1097	1096	1097	1096	1097		

$m/z$	Ion assumed	Integrated smoothed intensity (Normalized counts)							Origin	Comments
61.07	$C_3H_9O^+$	262	501	1403	2093	2311	2003	1698	$C_3H_7OH + H_3O^+$	Initial protonation product but according to [59] only 10%-20%
43.06	$^{12}C_3H_7^+$	80428	180829	478402	723575	840705	687309	608056	$C_3H_9O^+ - H_2O$	Main protonation product according to [59]
44.06	$^{13}C^{12}C_2H_7^+$	2727	5714	14735	22028	26232	21358	18789		Isotope ratio very stable at 3.1%
41.04	$^{12}C_3H_5^+$	10904	25896	74688	111755	125898	103751	91558	$C_3H_7^+ - H_2$	First hydrogen dissociation
42.04	$^{13}C^{12}C_2H_5^+$	476	873	2412	3498	3599	2959	2678		Isotope ratio varying around 3.1%
39.03	$C_3H_3^+$	618	307	1902	3468	3000	2650	2495	$C_3H_5^+ - H_2$	Second hydrogen dissociation
27.02	$C_2H_3^+$	341	603	1601	2359	2757	2231	1992	$C_3H_7^+ - CH_4$	Dissociation of methane
79.05	$C_3H_{11}O_2^+$	-16	114	210	256	257	186	270	$C_3H_7OH \cdot H_3O^+$	Signal underestimated since the actual mass would be $m = 79.08$ Da

In this case, identifying the specific isomer is difficult. According to SIFT literature [59], 1-propanol (or n-propanol) and 2-propanol (or i-propanol) lead to slightly different product distributions in  $C_3H_7^+$  and  $C_3H_9O^+$  (90:10 vs. 80:20). Since we observe almost exclusively  $C_3H_7^+$  (more than 99%), this might hint towards 1-propanol or just the fact that in our specific PTR conditions, water dissociation after protonation is dominant. We do not observe any of the  $O_2^+$  ionization products either which is notable given the large intensities for some of the  $H_3O^+$  products and similar rate coefficients according to [59].

As Baasandorj et al. [61] observed a very similar fragmentation pattern (and also the dominance of  $C_3H_7^+$  versus  $C_3H_9O^+$ ) for small humidities and comparable reduced field strength, we decided to carry out additional verification experiments using the pure compounds 1-propanol and 2-propanol. The resulting signal ratios are shown in Tab. 28.

These experiments seem to suggest the presence of 2-propanol rather than 1-propanol as most signal ratios are closer to the reference. This is not definitively conclusive as there are arguments for both: 1-Propanol is the obvious candidate as it is the only isomer so far reported to be produced from CO2R [2]. Its boiling point coincides with that of allyl alcohol and therefore makes sense to elute at almost the same time (see appendix D.11). While the signal ratios of unoxxygenated ions does not coincide with the pure compound this might be caused by overlap with pentene - meanwhile, the signal ratios of oxygenated species are closer to the reference of 1-propanol. On the other hand, substantial pentene

**Table 28:** Signal ratios detected in verification experiments with pure compound compared to the average signal ratios detected at this retention time.

ion signal ratio	1-Propanol	2-Propanol	eCO2R GC-MS
$C_3H_7^+$ / total	57.83%	74.23 %	85.03 %
$C_3H_5^+$ / total	38.40%	23.42 %	14.07 %
$C_3H_3^+$ / total	2.03%	1.01 %	0.35 %
$C_2H_3^+$ / total	1.45%	0.31 %	0.27 %
$C_3H_9O^+$ / total	0.26%	0.82 %	0.24 %
$C_3H_{11}O_2^+$ / total	0.02%	0.21 %	0.03 %
$C_3H_5^+$ / $C_3H_7^+$	66.40%	31.55%	16.55%
$C_3H_3^+$ / $C_3H_5^+$	5.29%	4.31%	2.49%
$C_3H_{11}O_2^+$ / $C_3H_9O^+$	7.69%	25.61 %	12.50 %

overlap does not seem very likely considering its  $C_5$  signal as well as the agreement of selectivity trends for oxygenated and unoxygenated species alike (see Fig. 47(b)). Furthermore,  $C_3H_{11}O_2^+$  signal is underreported so the actual ratio might be also closer to 2-propanol as all the others are.

The main issue with verification is that the eCO2R-GC-MS system cannot be adequately replicated as there are always cross-interactions of species as well as effects of the gas chromatography - most notably the lack of humidity in the drift chamber at most times. We might have a mixture that is not separated. The peaks are quite flat and stretched, some minor fragments like  $C_3H_3^+$  and  $C_2H_3^+$  even indicate a double peak, see Fig. 47(a).

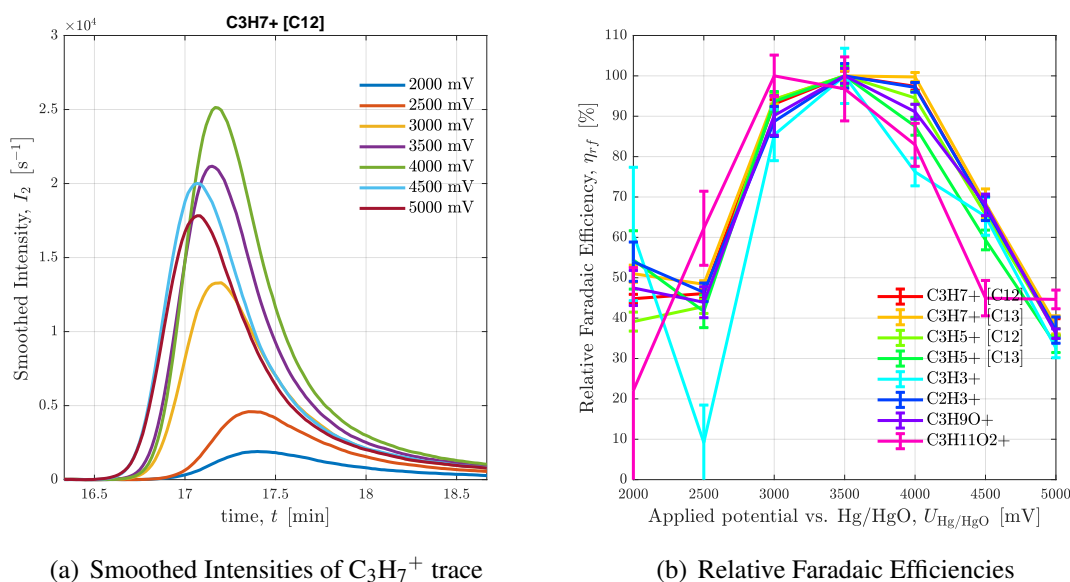


**Figure 47:** Analysis of traces and integrated smoothed intensities within propanol peak.

While substantial propanol production is observed for all applied potentials, Faradaic Efficiency peaks around  $U_{Hg/HgO} = 3.5$  V as shown in Fig. 47(b).

## D.13 Butanedione

Around  $t = 1225$  s to 1234 s a double-oxygenated  $C_4$  species is observed. The signals are listed in Tab. 29 and attributed to butanedione. Based on boiling temperatures, one might expect it to elute shortly after butanone instead of the observed  $\approx 30$  s prior to it, but boiling points are only a rough indicator.

**Table 29:** All detected traces that are peaking with butanedione.

Retention time		Applied potential vs. Hg/HgO in mV							Origin	Comments
		2000	2500	3000	3500	4000	4500	5000		
Peak time in s		1228	1232	1231	1232	1234	1227	1229		
Start time in s		1180	1185	1182	1185	1193	1184	1184		
End time in s		1270	1275	1272	1275	1283	1274	1274		
$m/z$	Ion assumed	Integrated smoothed intensity (Normalized counts)								
87.05	$C_4H_7O_2^+$	237	4018	15217	26670	43015	24220	11523	$C_4H_6O_2 + H_3O^+$	Main protonation product expected butanedione [62]
43.02	$^{12}C_2H_3O^+$	3612	68290	316036	571020	903242	505910	244256	$C_4H_7O_2^+ - CH_3CHO$	Main $O_2^+$ ionization product expected especially for butanedione [62], but signal very large
44.02	$^{13}C^{12}CH_3O^+$	187	1492	6830	12137	19359	10716	5481		Isotope ratio stable around 2.2%

These traces as well as their ratios shown in Fig. 48(a) have been verified within the  $^{13}C$  experiment. As there are quite a number of possible  $C_4H_6O_2$  structural isomers, detailed analysis is necessary for clear identification. Unfortunately, only ionization data available os for 2,3-butanedione [62]. Even though the  $C_2H_3O^+$  fragment was not reported in that SIFT study [62], we can safely assume it comes from easy acetaldehyde dissociation after  $H_3O^+$  ionization under given conditions. Due to the large protonation signal and missing  $C_4H_6O_2^+$  peak we can exclude the possibility of  $O_2^+$  ionization pathway.

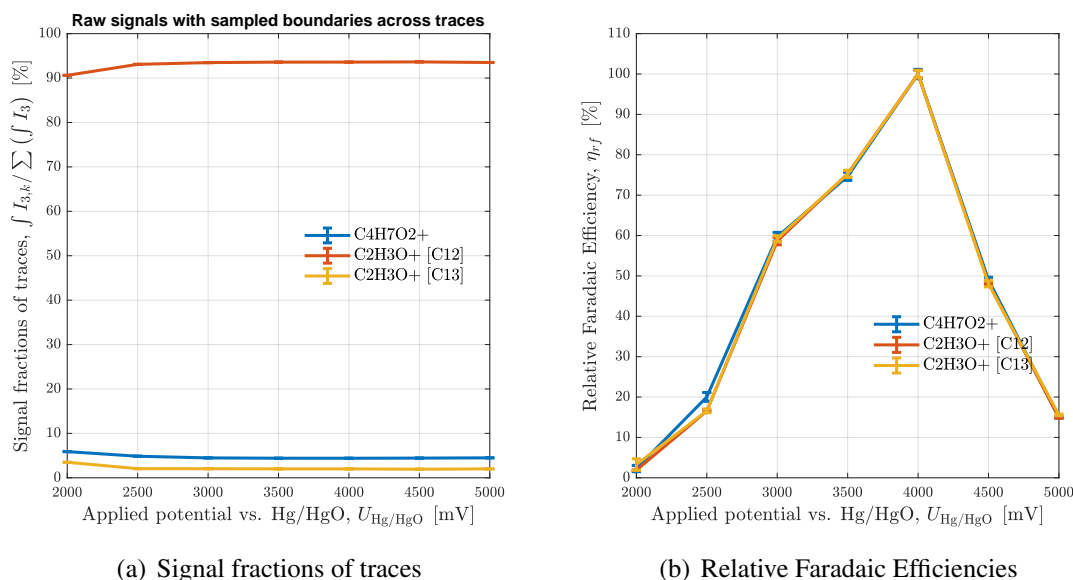


**Figure 48:** Analysis of traces and integrated smoothed intensities within butanedione peak.

We can infer expected ionization products for 1,4-butanediol based on available data on other aldehydes though [63]: easier dissociation of  $H_2O$  would definitely be expected, there-

fore  $C_4H_5O^+$  signal; as well as breaking into more and different fragments. The same applies to some extent for a mixed molecule with a single aldehyde group (keto-butanal). Moreover, the boiling temperatures of these two structural isomers would be considerably higher which makes elution at this time less likely.

Since diols would require a triple bond or two double bonds which is mechanistically unlikely, they can be safely neglected to be produced at this considerable rate. The only remaining group to consider are esters. Based on the fragmentation patterns expected for an ester [64], only vinyl acetate comes into question which also exhibits a boiling point slightly smaller than butanone. Considering the single ester that we unambiguously identify in this study (ethyl acetate, see appendix D.15) though, we would expect overall less fragmentation and a wider range of fragments (e.g., double-oxygenated  $C_2$  fragment). For this reason, the detected signals summarized in Fig. 48 are identified as 2,3-butanedione (diacetyl).

In Fig. 48 the relative Faradaic Efficiencies calculated for the traces related to butanedione are lining up very neatly in this case which indicates that there are no isomers with a slightly different mechanism or product distribution. Faradaic Efficiency for butanedione is seen to exhibit a sharp peak at  $U_{Hg/HgO} = 4.0 V$ .

## D.14 C4H8O isomers

Around  $t = 1310s$  to  $1320s$  a large signal of  $C_4H_9O^+$  suggests the existence of  $C_4H_8O$  species. A second trace of  $C_4H_7^+$  is also recorded, see Tab. 30.

**Table 30:** All detected traces that are peaking with butanal/butanone.

Retention time		Applied potential vs. Hg/HgO in mV								
		2000	2500	3000	3500	4000	4500	5000		
Peak time in s		1311	1318	1316	1320	1321	1314	1312		
Start time in s		1245	1250	1259	1262	1258	1256	1252		
End time in s		1365	1370	1379	1382	1378	1376	1372		
$m/z$	Ion assumed	Integrated smoothed intensity (Normalized counts)							Origin	Comments
73.07	$C_4H_9O^+$	8633	31150	59063	92019	75827	47803	25554	$C_4H_8O^+ + H_3O^+$	Main protonation product of n-butanal according to [63]
55.06	$C_4H_7^+$	791	4162	4221	2490	1578	777	590	$C_4H_9O^+ - H_2O$	Dissociation of water; minor protonation product of n-butanal according to [63]

When comparing the two traces, it becomes apparent that there is a time shift of  $\approx 15s$  between the two: while  $C_4H_9O^+$  is the dominant trace with a bell-shaped peak at a distinct time,  $C_4H_7^+$  exhibits a flatter shape with either a single peak a few seconds earlier or a double peak where the second one coincides with  $C_4H_9O^+$ . This is illustrated in Fig. 49(a) through Fig. 49(c) where peak locations of the two traces are indicated by dashed lines. The signal fractions shown in Fig. 49(d) are not stable and seen to decrease substantially over time which suggests that more than one  $C_4H_8O$  molecule is present. The two traces as well as the time shift has been verified within the  $^{13}C$  experiment.

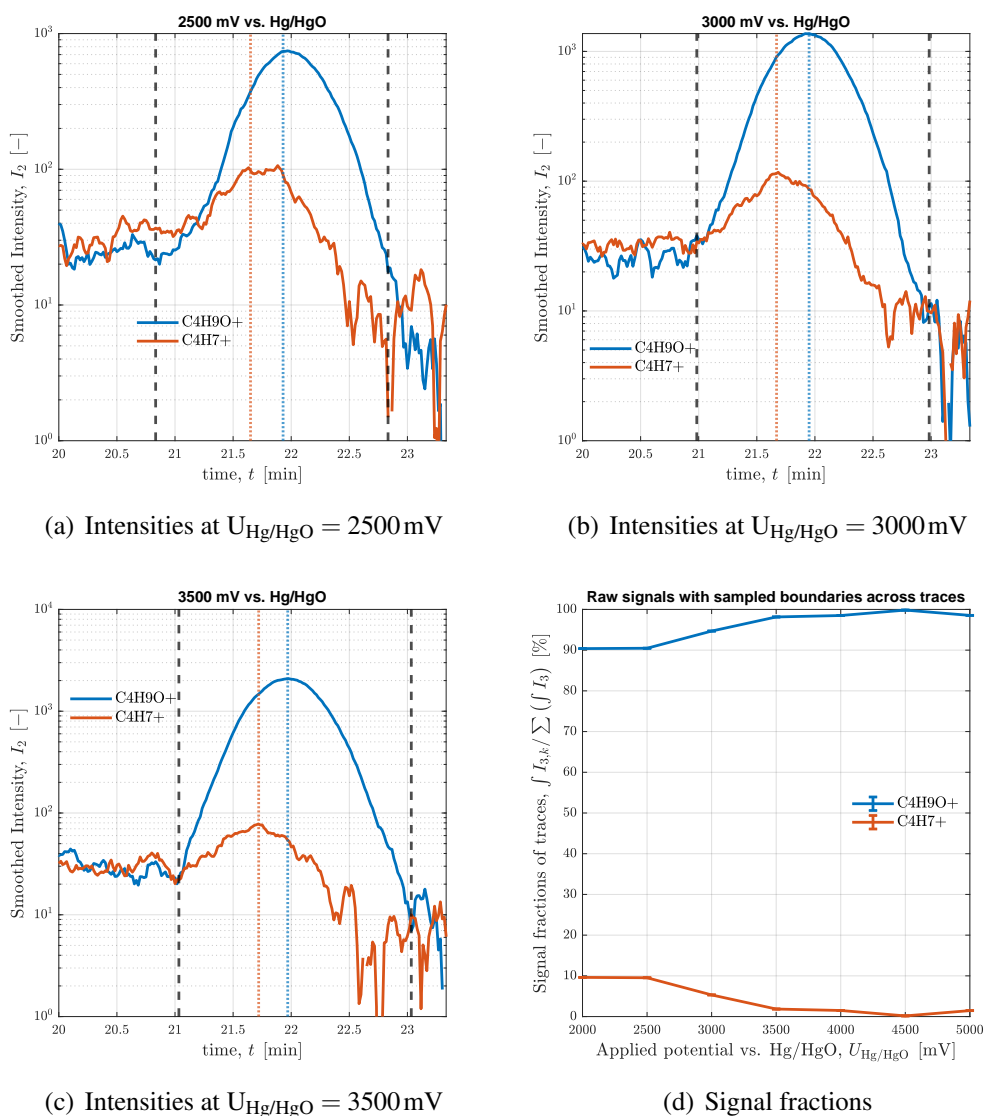


**Figure 49:** Intensities of traces related to  $\text{C}_4\text{H}_8\text{O}$  across different applied potentials.

In order to identify the different  $\text{C}_4\text{H}_8\text{O}$  species, the analogy to identified  $\text{C}_3\text{H}_6\text{O}$  isomers can be used. These  $\text{C}_3\text{H}_6\text{O}$  molecules are listed in Tab. 31 with PTR product and fragment ratios as well as other transferable information. Based on this, we can discuss the three possible analogous  $\text{C}_4$  species: Butanal, butanone and butenol (crotyl alcohol). Unfortunately, none of the (more discriminating)  $\text{O}_2^+$  products were found.

Molecule	Time	$\text{C}_3\text{H}_7\text{O}^+ / \text{C}_3\text{H}_5^+$	$U_{\text{Hg}/\text{HgO}} (\eta_{rf} = 1)$
propanal	$\approx 870 \text{ s}$	$\approx 1\%$	2500 mV
acetone	$\approx 920 \text{ s}$	$\approx 5\%$	4000 mV
allyl alcohol	$\approx 990 \text{ s}$	$\approx 500\%$	4500 mV

**Table 31:** Comparison of identified  $\text{C}_3\text{H}_6\text{O}$  species for  $\text{C}_4\text{H}_8\text{O}$  assignment.

Since we see a similar shift between  $\text{C}_3\text{H}_7\text{O}^+$  to  $\text{C}_3\text{H}_5^+$  in D.11, indicating the barely separated propanal and acetone, it can be speculated that the shifted  $\text{C}_4\text{H}_9\text{O}^+$  and  $\text{C}_4\text{H}_7^+$  peak indicate barely separated butanal and butanone. This is supported by similar differences in boiling points for the  $\text{C}_4\text{H}_8\text{O}$  species, which leads us to expect butanone to elute shortly after butanal. Crotyl alcohol would be expected to elute significantly later and is apparently not observed.

One remaining issue is the fact that we would not ascribe any  $\text{C}_4\text{H}_7^+$  to butanone while acetone even has a larger  $\text{C}_3\text{H}_5^+$  to  $\text{C}_3\text{H}_7\text{O}^+$  ratio than propanal. But as explained in D.11, this fragment is in acetone's case not created by water dissociation but rather subsequent dissociation of atomic oxygen and hydrogen. In a verification experiment with pure butanone we were able to confirm no  $\text{C}_4\text{H}_7^+$  and almost pure  $\text{C}_4\text{H}_9\text{O}^+$  as result of its protonation.

As the two species are overlapping this much, signals cannot be separated in a meaningful way. For this reason, we assign the  $\text{C}_4\text{H}_7^+$  signal completely to butanal and  $\text{C}_4\text{H}_9\text{O}^+$  completely to butanone as we are not interested in absolute concentration but only relative trends. The butanal selectivity trend will be completely accurate but the butanone trend will be skewed towards butanal.

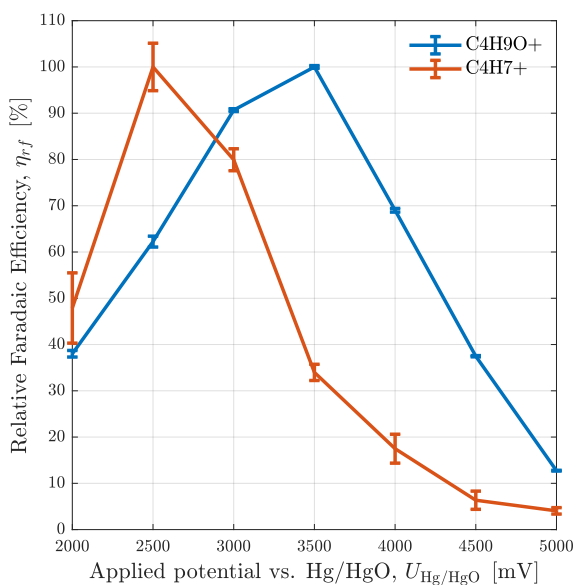


**Figure 50:** Relative Faradaic Efficiency of traces representing *n*-butanal and butanone.

**Butanal** is represented by the  $\text{C}_4\text{H}_7^+$  trace for further analysis which has been reported as minor protonation product also in SIFT studies [56] [63]. Two isomers are technically possible: *n*-butanal (butyraldehyde) and *i*-butanal (2-methyl-propanal). According to [63], only *n*-butanal leads to a small fraction of  $\text{C}_4\text{H}_7^+$ . As the signal fraction for smaller applied potentials (where we expect aldehyde production to dominate over ketone production, see main text) is close to the expected 5% we suggest *n*-butanal as the only  $\text{C}_4\text{H}_8\text{O}$  isomer produced as *i*-butanal would also be mechanistically unlikely.

Fig. 50 shows butanal’s Faradaic Efficiency (represented by  $C_4H_7^+$  trace) peaking at relatively small applied potential, declining rapidly at increasing potentials. This trend is very similar to propanal which reaches its peak Faradaic Efficiency at the same applied potential.

**Butanone** protonation is not well-documented but our verification experiment confirmed the dominance of  $C_4H_9O^+$  and complete absence of  $C_4H_7^+$ . Its relative Faradaic Efficiency represented by the  $C_4H_9O^+$  trace shown in Fig. 50 indicates peak selectivities shifted towards slightly larger potentials than butanal. A similar trend is seen for acetone and propanal but is more pronounced with Faradaic Efficiency peaking for even larger potentials. This can be explained by the partial attribution of  $C_4H_9O^+$  trace to butanal, skewing the results a bit.

## D.15 Ethyl Acetate

Even though, according to documented relative retention times it would be expected a few minutes earlier, the traces found with a distinct peak at  $t = 1319$ s to  $1414$ s all point towards ethyl acetate.

**Table 32:** All detected traces that are peaking with ethyl acetate.

Retention time	Applied potential vs. Hg/HgO in mV							
	2000	2500	3000	3500	4000	4500	5000	
Peak time in s	1397	1398	1396	1398	1403	1392	1395	
Start time in s	1332	1331	1338	1331	1332	1329	1327	
End time in s	1462	1461	1468	1461	1462	1459	1457	

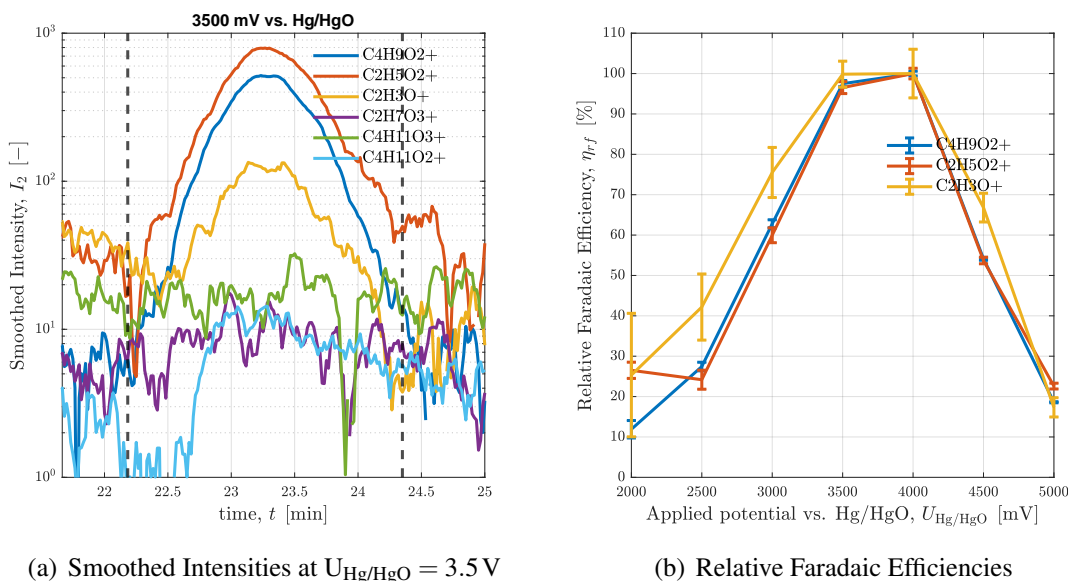
  

$m/z$	Ion assumed	Integrated smoothed intensity (Normalized counts)							Origin	Comments
89.06	$C_4H_9O_2^+$	880	3873	11316	24635	30367	18980	10285	$CH_3COOC_2H_5 + H_3O^+$	Only SIFT product according to [64]
61.03	$C_2H_5O_2^+$	2584	4603	16715	37464	46884	29969	18705	$C_4H_9O_2^+ - C_2H_4$	Most prominent PTR fragment according to [61]
43.02	$C_2H_3O^+$	474	1155	3196	5824	7170	5657	2028	$C_2H_5O_2^+ - H_2O$	Second fragment according to [61]
107.07	$C_4H_{11}O_3^+$	Signal-to-noise ratio so low, that it cannot be properly quantified							$CH_3COOC_2H_5 \cdot H_3O^+$	
91.08	$C_4H_{11}O_2^+$	166	165	181	501	1242	1267	777	$C_4H_{11}O_3^+ - O$	Dissociation of oxygen radical ethylene dissociation
79.04	$C_2H_7O_3^+$	56	8	79	206	468	423	253	$C_4H_{11}O_3^+ - C_2H_4$	

Signals recorded correspond very well with masses documented by Baasandorj et al. [61]: the main traces of protonated ethyl acetate ( $C_4H_9O_2^+$ ), fragments after subsequent dissociation of ethylene ( $C_2H_5O_2^+$ ) and water ( $C_2H_3O^+$ ), as well as the equivalents of the first two clustered with one water molecule ( $C_4H_{11}O_3^+$  and  $C_2H_7O_3^+$ ) are documented. The first three main traces were also verified with the  $^{13}C$  experiment. We interpret the ones with additional water to stem from clustering with hydronium rather than residual humidity due to the GC separation though, see appendix E.3.8. This does not make a difference effectively as trace intensities also fit quantitatively: around 35%  $C_4H_9O_2^+$ , 50%  $C_2H_5O_2^+$  and 15%  $C_2H_3O^+$  correspond well with what was measured for  $E/N \approx 114$ Td at lowest relative humidity.

The ions clustered with water show relatively small signal-to-noise ratio which is why they are not really suitable for quantitative statements, see Fig. 51(a). One of the traces found,  $C_4H_{11}O_2^+$ , is indeed not documented in the literature - even though it shows higher intensities for some of the applied potentials than  $C_4H_{11}O_3^+$ , which we assume to be the

predecessor. The dissociation of an oxygen radical that has been hypothesized for multiple PTR reaction mechanisms in this work, seems to be quite fast.



**Figure 51:** Intensities of traces related to ethyl acetate across different applied potentials.

As the recorded signals fit the literature for ethyl acetate very well, identification is unambiguous. For any other type  $\text{C}_4\text{H}_8\text{O}_2$  isomer, different traces would be expected (for example water dissociation for aldehydes). The other possible ester, methyl propionate, can also be safely discarded as no  $\text{C}_3\text{H}_5\text{O}^+$  is observed [64]. For the first time, an ester has been identified as eCO<sub>2</sub>R product as formation via a subsequent bulk reaction also seems unlikely. Fischer esterification requires acidic acid and is accelerated by acid catalysis, which is contradicted by our large pH. Tishchenko reaction of two acetaldehydes might seem possible due to alkaline milieu and large acetaldehyde signal, but selectivity trends are clearly different as seen in Fig. 51(b): While Faradaic Efficiency of acetaldehyde peaks at  $U_{\text{Hg}/\text{HgO}} = 3.0 \text{ V}$ , ethyl acetate shows largest FE at  $U_{\text{Hg}/\text{HgO}} = 4.0 \text{ V}$ .

## D.16 Pentanedione

Around  $t = 2100 \text{ s}$  to  $2500 \text{ s}$  we observe peaks of a traces that strongly suggest  $\text{C}_5\text{H}_8\text{O}_2$  as the source. The key trace,  $\text{C}_5\text{H}_9\text{O}_2^+$ , is accompanied by a fragment,  $\text{C}_2\text{H}_3\text{O}^+$  for both of the two distinct peaks observed. Analogous to D.13, this points towards pentanedione or pentanedial. As we can see in Fig. 52, the first peak is much smaller and somewhat overlapped by the larger peak following it.

Both of these traces as well as their rough intensity ratios were verified within the  $^{13}\text{C}$  experiment. Regarding the species identification, we can argue analogous to butanedione in D.13. Again, esters are unlikely as no double-oxygenated fragments can be found. The two esters in question would be allyl acetate and isopropenyl acetate but their boiling points are so similar that they might not be separated at all.

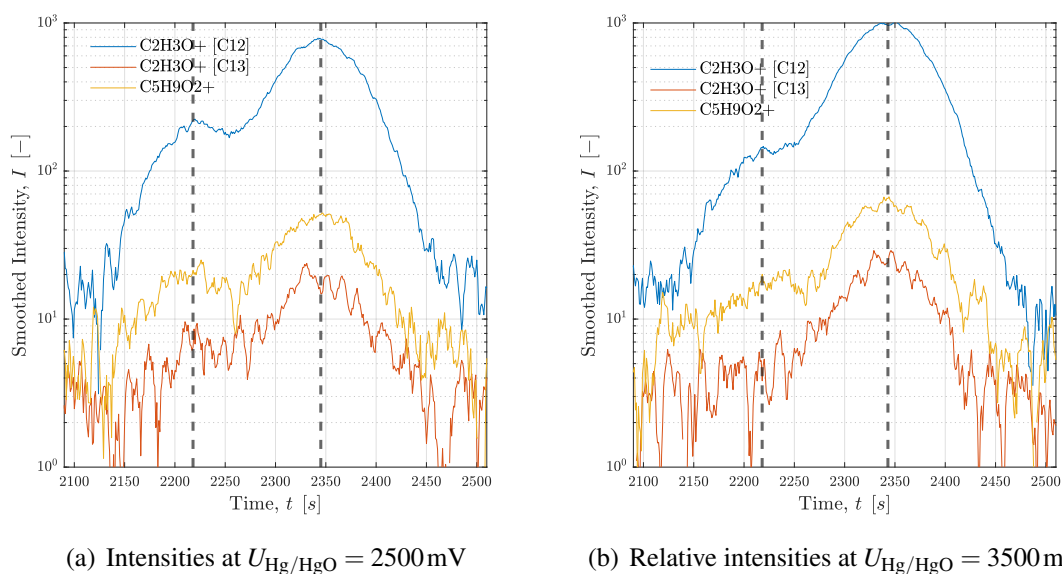


**Figure 52:** Intensities of traces peaking around  $t \approx 2100$  s to 2500 s for different applied potentials.

The documented protonation products of pentanedial include 30%  $C_5H_7O^+$  [56] which we do not observe here. We do observe the fragment possibly caused by acetaldehyde dissociation though,  $C_2H_3O^+$ , albeit at a much larger fraction than the suggested 20%. While different fractions were observed for many of the  $C_{3+}$  hydrocabons and might be caused by increased electric fields, we would nonetheless expect to observe at least some water dissociation (and therefore  $C_5H_7O^+$ ) for aldehydes and especially dialdehydes.

As mentioned, we do observe a large amount of  $C_2H_3O^+$ , which is reported as third  $H_3O^+$  ionization product for dial [56]. For the dione it is only reported as an  $O_2^+$  ionization product [62], but similar to the butanedione discussion (see appendix D.13) we probably see this fragmentation also via  $H_3O^+$  with our specific PTR setup and parameters. Based on molecule geometry we would expect this fragmentation to occur twice as often for 2,4-pentanedione than for 2,3-pentanedione (which is equally likely to produce  $C_3H_5O^+$ ).

In fact, we do see a significant difference in intensities of the fragment relative to the protonated pentanedione. We therefore ascribe the two peaks to pentanedione isomers:

1. The peak around  $t \approx 2200$  s is propably 2,3-pentanedione as fragment (by propanal dissociation on one side) signal is approximately ten times larger than protonated pentanedione signal. Fragmentation could technically also produce  $C_3H_5O^+$  fragment (by acetaldehyde dissociation on the other side), but could not be verified.
2. The second peak around  $t \approx 2350$  s is probably 2,4-pentanedione as fragment (by acetone dissociation on either side) signal is approximately twenty times larger than protonated pentanedione signal.

This is supported by the elution sequence matching expectations based on boiling points.

**2,3-pentanedione** is detected at  $t = 2196$  s to 2222 s, signals are listed in Tab. 33.

**Table 33:** All detected traces that are peaking with 2,3-pentanedione.

Retention time		Applied potential vs. Hg/HgO in mV							Origin	Comments
		2000	2500	3000	3500	4000	4500	5000		
Peak time in s		2219	2218	2213	2218	2205	-	-		
Start time in s		2150	2139	2128	2142	2145	-	-		
End time in s		2270	2259	2248	2262	2265	-	-		
$m/z$	Ion assumed	Integrated smoothed intensity (Normalized counts)								
101.06	$C_5H_9O_2^+$	504	1222	358	346	328	0	0	$C_5H_8O_2 + H_3O^+$	Main protonation product according to [62]
43.02	$^{12}C_2H_3O^+$	3053	7580	4495	2594	2057	0	0	$C_5H_9O_2^+ - C_2H_5CHO$	Consistently around 85% - 90% of the signal
44.02	$^{13}C^{12}CH_3O^+$	Signal-to-noise ratio so low, that it cannot be properly quantified								Where detected, isotope ratio around 2.5%

As shown in Fig. 53, Faradaic Efficiency of 2,3-pentanedione production seems to be highest for small applied potentials ( $U_{Hg/HgO} = 2500$  mV specifically) and is decreasing sharply with larger potentials.

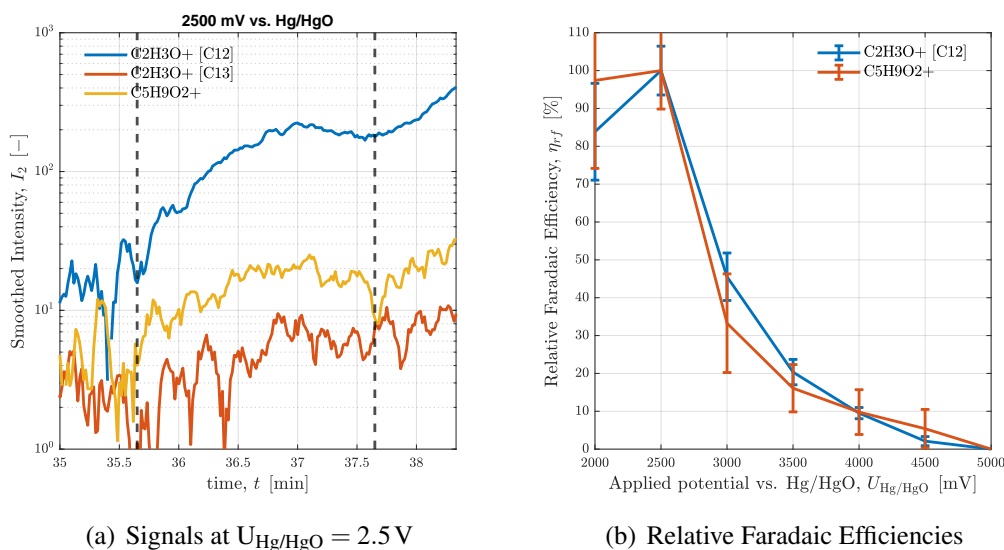


**Figure 53:** Analysis of traces within 2,3-pentanedione peak.

**2,4-pentanedione** is detected at  $t = 2320$  s to 2389 s, signals are listed in Tab. 34.

**Table 34:** All detected traces that are peaking with 2,4-pentanedione.

Retention time		Applied potential vs. Hg/HgO in mV							Origin	Comments
		2000	2500	3000	3500	4000	4500	5000		
Peak time in s		2338	2345	2344	2343	2345	2339	2339		
Start time in s		2268	2269	2262	2261	2268	2270	2271		
End time in s		2448	2449	2442	2441	2448	2450	2451		
$m/z$	Ion assumed	Integrated smoothed intensity (Normalized counts)								
101.06	$C_5H_9O_2^+$	304	3585	5584	4490	1507	952	606	$C_5H_8O_2 + H_3O^+$	Direct protonation product
43.02	$^{12}C_2H_3O^+$	9866	60060	90550	81659	28225	12789	7376	$C_5H_9O_2^+ - C_2H_5CHO$	Consistently around 95% of the signal
44.02	$^{13}C^{12}CH_3O^+$	-107	1248	2186	1673	424	546	46		Isotope ratio around 2.2%

As shown in Fig. 54, the selectivity trend for 2,4-pentanedione deviates from that of its isomer. Its Faradaic Efficiency peaks for medium applied potentials ( $U_{\text{Hg}/\text{HgO}} = 3000 \text{ mV}$  specifically) and is decreasing again with larger potentials.

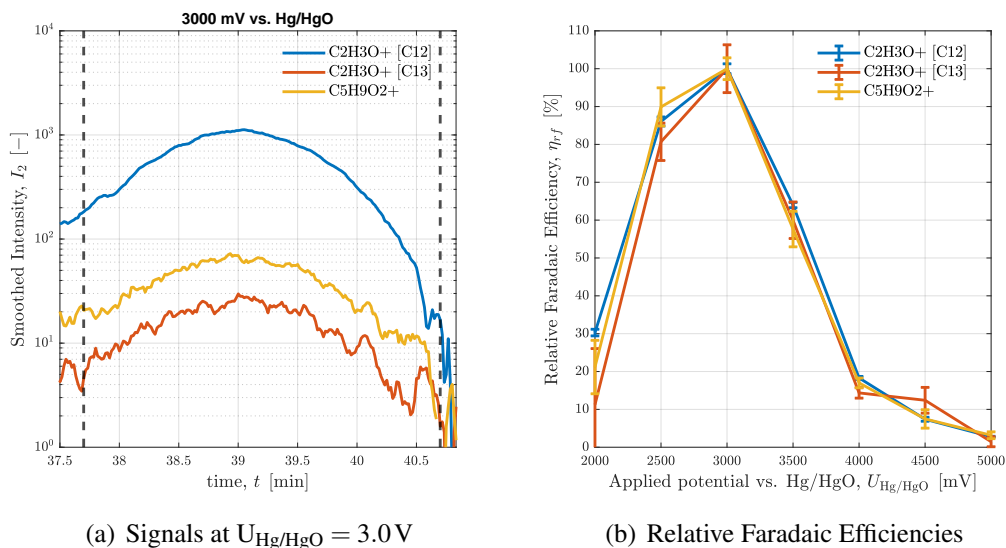


**Figure 54:** Analysis of traces within 2,4-pentanedione peak.

## D.17 Overview of detected species

All detected carbon-containing species are listed with properties of interest in Tab. 35.

**Table 35:** Overview of all detected carbon-containing species. Information on species makeup is given as reduction state  $R$ , number of carbon and oxygen atoms,  $C$  and  $O$ . The observed retention time  $t_{\text{ret}}$  is given alongside an indicator of certainty for this product. For the calculated relative FE the selected representative trace is given with a measure for the applied potential vs. RHE at which the FE is expected at a maximum,  $U_{\text{RHE}}^{\text{max}}$ .

species	makeup			identification		(relative) Faradaic Efficiency $\eta_{rf}$		comment
	$R$	$C$	$O$	confirmed?	$t_{\text{ret}}$ [s]	trace	$U_{\text{RHE}}^{\text{max}}$ [mV]	
carbon dioxide	0	1	2	educt	232	$\text{CO}_2\text{H}^+$		
carbonic acid	0	1	3	educt	230	$\text{H}_2\text{CO}_3\text{H}^+$		
carbon monoxide	2	1	1	known	134	$\text{CO}\cdot\text{H}_3\text{O}^+$	$> -700$	
formaldehyde	4	1	1	known	431	$\text{CH}_3\text{O}^+$	$> -700$	
methanol	6	1	1	known	426	$\text{CH}_5\text{O}^+$	$> -700$	
methane	8	1	0	known	174	$\text{CH}_5\text{O}^+$	$\leq -1500$	$\text{O}_2^+$ product used
acetaldehyde	10	2	1	known	630	$\text{C}_2\text{H}_7\text{O}_2^+$	$-1000$ to $-900$	partial PI depletion
ethylene	12	2	0	known	339	$\text{C}_2\text{H}_5^+$	$-1000$ to $-800$	partial PI depletion
ethanol	12	2	1	known	718	$\text{C}_2\text{H}_7\text{O}^+$	$-1500$ to $-1300$	
propanal	16	3	1	known	872	$\text{C}_3\text{H}_9\text{O}_2^+$	$-850$ to $-750$	traces chosen to reduce overlap (no $\text{C}_3\text{H}_7\text{O}^+$ )
acetone	16	3	1	known	925	$\text{C}_3\text{H}_7^+$	$\approx -1300$	
allyl alcohol	16	3	1	known	990	$\text{C}_3\text{H}_5^+$	$-1500$ to $-1300$	
propylene	18	3	0	known	550	$\text{C}_3\text{H}_4^+$	$\approx -750$	$\text{O}_2^+$ product used
cyclopropane	18	3	0	unconfirmed	787	$\text{C}_3\text{H}_6^+$	$\approx -750$	$\text{O}_2^+$ product used
1-propanol	18	3	1	known	1029	$\text{C}_3\text{H}_7^+$	$-1200$ to $-1100$	not separable
2-propanol	18	3	1	unconfirmed	1029	$\text{C}_3\text{H}_7^+$		
butanedione	18	4	2	confirmed	1232	$\text{C}_2\text{H}_3\text{O}^+$	$\approx -1300$	verified by $\text{C}_4\text{H}_7\text{O}_2^+$
ethyl acetate	20	4	2	confirmed	1398	$\text{C}_4\text{H}_9\text{O}_2^+$	$-1300$ to $-1100$	
butadiene	22	4	0	confirmed	729	$\text{C}_4\text{H}_7^+$	$-850$ to $-750$	
butanal	22	4	1	confirmed	1320	$\text{C}_4\text{H}_7^+$	$-850$ to $-750$	influenced by butanal
butanone	22	4	1	confirmed	1310	$\text{C}_4\text{H}_9\text{O}^+$	$-1200$ to $-1100$	
1-butene	24	4	0	confirmed	723	$\text{C}_4\text{H}_9^+$	$< -1500$	
2-cis-butene	24	4	0	confirmed	762	$\text{C}_4\text{H}_9^+$	$-850$ to $-750$	
2-trans-butene	24	4	0	confirmed	746	$\text{C}_4\text{H}_9^+$	$> -700$	
2,3-pentanedione	24	5	2	confirmed	2218	$\text{C}_2\text{H}_3\text{O}^+$	$-850$ to $-750$	verified by $\text{C}_5\text{H}_9\text{O}_2^+$
2,4-pentanedione	24	5	2	confirmed	2343	$\text{C}_2\text{H}_3\text{O}^+$	$-1000$ to $-800$	
1-pentene	30	5	0	confirmed	1027	$\text{C}_5\text{H}_{11}^+$	$< -1500$	not separable
2-pentene	30	5	0	unconfirmed	1023	$\text{C}_5\text{H}_{11}^+$	signal too small	

Observed retention times in this table are given in seconds rather than minutes to better distinguish species eluting only seconds apart from each other. For the sake of simplicity, only a single time is mentioned (observed for the experiment with  $U_{\text{Hg}/\text{HgO}} = 3.5\text{ V}$ ) as the small variations between experiments are self-consistent and thus not meaningful for this analysis.

In order to discuss the mechanistic implications of the described experiments, it is important to keep in mind the reduction state  $R$  of each species. This measure gives the number of reduction steps (i.e. electrons transferred) necessary to produce this compound from one or multiple carbon dioxide molecules. Based on observed trends in relative Faradaic Efficiencies and Kinetic Isotope Effect, hypotheses regarding common reaction paths can be formulated. To calculate these values, representing traces were chosen based on signal strength, overlaps, and possible saturation effects.

## E Proton-Transfer Reaction Mechanisms

We look at three different types of protons even though we only used hydroxonium as primary ion in our studies. According to the device manufacturer the ions generated are 97.56%  $\text{H}_3\text{O}^+$  with contaminations of 1.95%  $\text{O}_2^+$  and 0.49%  $\text{NO}^+$ . [54]. Proton transfer via  $\text{H}_3\text{O}^+$  is still the dominating mechanism of course and ionization via  $\text{NO}^+$  was not considered in this study since it has the lowest concentration and would not provide additional insight for any of the documented species listed in E.1.2.

### E.1 Literature Data

There is a large body of data available on reaction rates and product ratios for ionizing small organic molecules via  $\text{H}_3\text{O}^+$ ,  $\text{O}_2^+$ , and  $\text{NO}^+$ . The underlying studies were for the most part carried out within a selected-ion flow-tube (SIFT) mass spectrometer with a quadrupole analyser and not in a PTR-MS with time of flight analyser (TOF) as used in this study. For this reason, reaction rate constants calculated in these studies cannot be directly applied which makes direct quantitative calculations and comparisons were costly. In this study we therefore do not report concentrations but compare signal trends qualitatively - between different traces originating from the same species and between experiments of different applied potentials within the same trace. Moreover, if we have a vague idea of reaction rate constants (within reactions of a single product) we can compare orders of magnitude - for example between  $\text{H}_3\text{O}^+$  and  $\text{O}_2^+$  reaction of a species under consideration of the primary ion concentration and contamination.

#### E.1.1 Comparability with SIFT data

As mentioned above, a few important caveats apply to the applicability of data gathered from SIFT studies:

- It is specific to the reduced field strength  $E/N$  (in our case:  $E/N = 114\text{Td}$  auto-calculated from drift tube temperature, voltage and pressure [54]). For example, fragmentation depends heavily on it [61].
- Measurements done by PTR-MS and SIFT-MS are not directly comparable. For example, less clusters with water are observed for PTR-MS [36].
- Following the drift chamber our setup includes a funnel and a lens leading to the TOF sensor. Additional reactions of ions and fragmentation might take place there, see E.3.
- Since we do not dilute the analyte, some of the species have very large concentrations outside the dynamic range of the PTR-MS. This leads to saturation effects described in E.2.

## E.1.2 SIFT mechanism data

Tab. 36 lists all small organic compounds for which SIFT reaction data was available and have therefore been taken into account for species identification.

**Table 36:** List of different species with publically available data on ionization products.

species chemical formula sum	species chemical formula structure	species name	reference	comment
H <sub>2</sub> O		water	[65]	
CH <sub>4</sub>	CH <sub>4</sub>	methane	[57]	No reaction with H <sub>3</sub> O <sup>+</sup> observed
C <sub>2</sub> H <sub>6</sub>	C <sub>2</sub> H <sub>6</sub>	ethane	[57]	No reaction with H <sub>3</sub> O <sup>+</sup> observed
C <sub>3</sub> H <sub>8</sub>	C <sub>3</sub> H <sub>8</sub>	propane	[57]	No reaction with H <sub>3</sub> O <sup>+</sup> observed
C <sub>4</sub> H <sub>10</sub>	n-C <sub>4</sub> H <sub>10</sub>	butane	[60] [57]	No reaction with H <sub>3</sub> O <sup>+</sup> observed Reaction with very small rate observed
C <sub>4</sub> H <sub>10</sub>	i-C <sub>4</sub> H <sub>10</sub>	isobutane	[60] [57]	No reaction with H <sub>3</sub> O <sup>+</sup> observed Reaction with very small rate observed
C <sub>5</sub> H <sub>12</sub>	n-C <sub>5</sub> H <sub>12</sub>	pentane	[60]	No reaction with H <sub>3</sub> O <sup>+</sup> observed
C <sub>5</sub> H <sub>12</sub>	i-C <sub>5</sub> H <sub>12</sub>	isopentane	[60]	No reaction with H <sub>3</sub> O <sup>+</sup> observed
C <sub>6</sub> H <sub>14</sub>	n-C <sub>6</sub> H <sub>14</sub>	hexane	[60]	
C <sub>8</sub> H <sub>18</sub> O	n-C <sub>8</sub> H <sub>18</sub> O	octane	[60]	
C <sub>10</sub> H <sub>22</sub>	n-C <sub>10</sub> H <sub>22</sub>	decane	[60]	
C <sub>3</sub> H <sub>6</sub>	c-C <sub>3</sub> H <sub>6</sub>	cyclopropane	[57]	
C <sub>2</sub> H <sub>4</sub>	C <sub>2</sub> H <sub>4</sub>	ethylene	[57]	
C <sub>3</sub> H <sub>6</sub>	C <sub>3</sub> H <sub>6</sub>	propylene	[57]	
C <sub>4</sub> H <sub>8</sub>	CH <sub>3</sub> CHCHCH <sub>3</sub>	2-butene	[57]	
C <sub>5</sub> H <sub>10</sub>	CH <sub>2</sub> CHC <sub>3</sub> H <sub>7</sub>	1-pentene	[60]	
C <sub>5</sub> H <sub>10</sub>	(CH <sub>3</sub> ) <sub>2</sub> CCHCH <sub>3</sub>	2-methyl-2-butene	[60]	
C <sub>3</sub> H <sub>4</sub>	C <sub>3</sub> H <sub>4</sub>	allene	[57]	
C <sub>5</sub> H <sub>8</sub>	CH <sub>2</sub> CCHCH <sub>2</sub>	isoprene	[60]	
C <sub>2</sub> H <sub>2</sub>	C <sub>2</sub> H <sub>2</sub>	acetylene	[57]	
C <sub>3</sub> H <sub>4</sub>	C <sub>3</sub> H <sub>4</sub>	propyne	[57]	
C <sub>4</sub> H <sub>2</sub>	C <sub>4</sub> H <sub>2</sub>	diacetylene	[57]	
CH <sub>4</sub> O	CH <sub>3</sub> OH	methanol	[59] [65]	products for different humidities
C <sub>2</sub> H <sub>6</sub> O	C <sub>2</sub> H <sub>5</sub> OH	ethanol	[59] [65] [61]	products for different humidities products for different field strengths
C <sub>3</sub> H <sub>8</sub> O	C <sub>3</sub> H <sub>7</sub> OH	1-propanol	[59] [65]	products for different humidities
C <sub>3</sub> H <sub>8</sub> O	CH <sub>3</sub> CH <sub>2</sub> OHCH <sub>3</sub>	2-propanol	[59] [61]	products for different field strengths
C <sub>4</sub> H <sub>10</sub> O	n-C <sub>4</sub> H <sub>9</sub> OH	1-butanol	[59] [65]	products for different humidities
C <sub>4</sub> H <sub>10</sub> O	i-C <sub>4</sub> H <sub>9</sub> OH	2-methyl-1-propanol	[59]	
C <sub>4</sub> H <sub>10</sub> O	CH <sub>3</sub> CH <sub>2</sub> OHC <sub>2</sub> H <sub>5</sub>	2-butanol	[59]	
C <sub>4</sub> H <sub>10</sub> O	t-C <sub>4</sub> H <sub>9</sub> OH	2-met-2-propanol	[59]	
C <sub>5</sub> H <sub>12</sub> O	C <sub>5</sub> H <sub>11</sub> OH	1-pentanol	[59] [65]	products for different humidities
C <sub>5</sub> H <sub>12</sub> O	i-C <sub>5</sub> H <sub>11</sub> OH	3-met-1-butanol	[59]	
C <sub>5</sub> H <sub>12</sub> O	C <sub>2</sub> H <sub>5</sub> CH <sub>2</sub> OHC <sub>2</sub> H <sub>5</sub>	3-pentanol	[59]	
C <sub>5</sub> H <sub>12</sub> O	t-C <sub>5</sub> H <sub>11</sub> OH	2-met-2-butanol	[59]	
C <sub>6</sub> H <sub>14</sub> O	C <sub>6</sub> H <sub>13</sub> OH	1-hexanol	[59] [65]	products for different humidities
C <sub>8</sub> H <sub>18</sub> O	C <sub>8</sub> H <sub>17</sub> OH	1-octanol	[59]	
C <sub>8</sub> H <sub>18</sub> O	CH <sub>3</sub> CH <sub>2</sub> OHC <sub>6</sub> H <sub>13</sub>	2-octanol	[59]	
C <sub>6</sub> H <sub>6</sub> O	C <sub>6</sub> H <sub>5</sub> OH	phenol	[59]	
C <sub>2</sub> H <sub>6</sub> O <sub>2</sub>	CH <sub>2</sub> OHCH <sub>2</sub> OH	1,2-ethanediol	[66]	
C <sub>3</sub> H <sub>8</sub> O <sub>2</sub>	CH <sub>2</sub> OHCHOHCH <sub>3</sub>	1,2-propanediol	[66]	
C <sub>3</sub> H <sub>8</sub> O <sub>2</sub>	CH <sub>2</sub> OHCH <sub>2</sub> CH <sub>2</sub> OH	1,3-propanediol	[66]	
C <sub>4</sub> H <sub>10</sub> O <sub>2</sub>	CH <sub>2</sub> OHCHOHC <sub>2</sub> H <sub>5</sub>	1,2-butanediol	[66]	
C <sub>4</sub> H <sub>10</sub> O <sub>2</sub>	CH <sub>2</sub> OHCH <sub>2</sub> CHOHCH <sub>3</sub>	1,3-butanediol	[66]	
C <sub>4</sub> H <sub>10</sub> O <sub>2</sub>	CH <sub>2</sub> OHC <sub>2</sub> H <sub>4</sub> CH <sub>2</sub> OH	1,4-butanediol	[66]	
C <sub>5</sub> H <sub>12</sub> O <sub>2</sub>	CH <sub>2</sub> OHC <sub>3</sub> H <sub>6</sub> CH <sub>2</sub> OH	1,5-pentanediol	[66]	

C <sub>5</sub> H <sub>10</sub> O <sub>2</sub>	c-CHOHCHOHC <sub>3</sub> H <sub>6</sub>	1,2-cyclopentanediol	[66]	
CH <sub>2</sub> O	HCHO	formaldehyde	[56]	
C <sub>2</sub> H <sub>4</sub> O	CH <sub>3</sub> CHO	acetaldehyde	[56]	
C <sub>3</sub> H <sub>6</sub> O	C <sub>2</sub> H <sub>5</sub> CHO	propanal	[56]	
C <sub>4</sub> H <sub>8</sub> O	C <sub>3</sub> H <sub>7</sub> CHO	butanal	[56] [63]	in agreement with earlier study
C <sub>4</sub> H <sub>8</sub> O	(CH <sub>3</sub> ) <sub>2</sub> CHCHO	isobutanal	[63]	
C <sub>5</sub> H <sub>10</sub> O	C <sub>4</sub> H <sub>9</sub> CHO	pentanal	[56]	
C <sub>5</sub> H <sub>10</sub> O	(CH <sub>3</sub> ) <sub>2</sub> CHCH <sub>2</sub> CHO	isopentanal	[63]	
C <sub>6</sub> H <sub>12</sub> O	C <sub>5</sub> H <sub>11</sub> CHO	hexanal	[56]	
C <sub>7</sub> H <sub>14</sub> O	C <sub>6</sub> H <sub>13</sub> CHO	heptanal	[63]	
C <sub>9</sub> H <sub>18</sub> O	C <sub>8</sub> H <sub>17</sub> CHO	octanal	[63]	
C <sub>10</sub> H <sub>20</sub> O	C <sub>9</sub> H <sub>19</sub> CHO	decanal	[63]	
C <sub>7</sub> H <sub>6</sub> O	C <sub>6</sub> H <sub>5</sub> CHO	benzaldehyde	[56]	
C <sub>3</sub> H <sub>4</sub> O	CH <sub>2</sub> CHCHO	propenal	[56]	
C <sub>4</sub> H <sub>6</sub> O	CH <sub>3</sub> CHCHCHO	2-butenal	[63]	
C <sub>5</sub> H <sub>8</sub> O	t-C <sub>2</sub> H <sub>5</sub> CHCHCHO	trans-2-pentenal	[63]	
C <sub>5</sub> H <sub>8</sub> O	t-C <sub>3</sub> H <sub>7</sub> CH(CH <sub>3</sub> )(CHO)	trans-2-methyl-2-butenal	[63]	
C <sub>6</sub> H <sub>10</sub> O	C <sub>3</sub> H <sub>7</sub> CHCHCHO	trans-2-hexenal	[56]	
C <sub>6</sub> H <sub>10</sub> O	C <sub>2</sub> H <sub>5</sub> CHCHCH <sub>2</sub> CHO	cis-3-hexenal	[56]	
C <sub>7</sub> H <sub>12</sub> O	t-C <sub>4</sub> H <sub>9</sub> CHCHCHO	trans-2-heptenal	[63]	
C <sub>8</sub> H <sub>14</sub> O	t-C <sub>5</sub> H <sub>11</sub> CHCHCHO	trans-2-octenal	[63]	
C <sub>9</sub> H <sub>16</sub> O	t-C <sub>6</sub> H <sub>13</sub> CHCHCHO	trans-2-nonenal	[63]	
C <sub>5</sub> H <sub>8</sub> O <sub>2</sub>	CHOC <sub>3</sub> H <sub>6</sub> CHO	1,5-pentanedial	[56]	
C <sub>2</sub> H <sub>4</sub> O <sub>2</sub>	CH <sub>2</sub> OHCHO	glycoaldehyde	[61]	products for different field strengths
C <sub>3</sub> H <sub>6</sub> O	CH <sub>3</sub> COCH <sub>3</sub>	acetone	[56] [62]	products for different humidities
C <sub>4</sub> H <sub>8</sub> O	CH <sub>3</sub> COC <sub>2</sub> H <sub>5</sub>	2-butanone	[56] [62]	products for different humidities
C <sub>5</sub> H <sub>10</sub> O	CH <sub>3</sub> COC <sub>3</sub> H <sub>7</sub>	2-pentanone	[56] [62]	products for different humidities
C <sub>5</sub> H <sub>10</sub> O	C <sub>2</sub> H <sub>5</sub> COC <sub>2</sub> H <sub>5</sub>	3-pentanone	[56]	
C <sub>5</sub> H <sub>10</sub> O	(CH <sub>3</sub> ) <sub>2</sub> CHCOCH <sub>3</sub>	3-methyl-2-butanone	[62]	products for different humidities
C <sub>6</sub> H <sub>12</sub> O	CH <sub>3</sub> COC <sub>4</sub> H <sub>9</sub>	2-hexanone	[56] [62]	products for different humidities
C <sub>6</sub> H <sub>12</sub> O	C <sub>2</sub> H <sub>5</sub> COC <sub>3</sub> H <sub>7</sub>	3-hexanone	[56] [62]	products for different humidities
C <sub>6</sub> H <sub>12</sub> O	CH <sub>3</sub> COCH(CH <sub>3</sub> )(C <sub>2</sub> H <sub>5</sub> )	3-methyl-2-pentanone	[62]	products for different humidities
C <sub>6</sub> H <sub>12</sub> O	(CH <sub>3</sub> ) <sub>2</sub> CHCH <sub>2</sub> CCH <sub>3</sub>	4-methyl-2-pentanone	[62]	products for different humidities
C <sub>7</sub> H <sub>14</sub> O	CH <sub>3</sub> COC <sub>5</sub> H <sub>11</sub>	2-heptanone	[62]	products for different humidities
C <sub>7</sub> H <sub>14</sub> O	C <sub>2</sub> H <sub>5</sub> COC <sub>4</sub> H <sub>9</sub>	3-heptanone	[62]	products for different humidities
C <sub>8</sub> H <sub>16</sub> O	C <sub>2</sub> H <sub>5</sub> COC <sub>5</sub> H <sub>11</sub>	3-octanone	[62]	products for different humidities
C <sub>9</sub> H <sub>18</sub> O	CH <sub>3</sub> COC <sub>7</sub> H <sub>15</sub>	2-nonanone	[62]	products for different humidities
C <sub>10</sub> H <sub>20</sub> O	CH <sub>3</sub> COC <sub>8</sub> H <sub>17</sub>	2-decanone	[62]	products for different humidities
C <sub>4</sub> H <sub>6</sub> O <sub>2</sub>	CH <sub>3</sub> COCOCH <sub>3</sub>	2,3-butanedione	[56] [62]	products for different humidities
C <sub>5</sub> H <sub>8</sub> O <sub>2</sub>	CH <sub>3</sub> COCOC <sub>2</sub> H <sub>5</sub>	2,3-pentanedione	[62]	products for different humidities
C <sub>6</sub> H <sub>10</sub> O <sub>2</sub>	CH <sub>3</sub> COCOC <sub>3</sub> H <sub>7</sub>	2,3-hexanedione	[62]	products for different humidities
C <sub>4</sub> H <sub>6</sub> O	CH <sub>3</sub> COC <sub>2</sub> H <sub>3</sub>	3-buten-2-one	[62]	products for different humidities
C <sub>5</sub> H <sub>8</sub> O	CH <sub>3</sub> C(CH <sub>2</sub> )(COCH <sub>3</sub> )	3-methyl-3-buten-2-one	[62]	products for different humidities
C <sub>6</sub> H <sub>10</sub> O	C <sub>2</sub> H <sub>4</sub> C(CH <sub>3</sub> )(COCH <sub>3</sub> )	3-methyl-3-penten-2-one	[62]	products for different humidities
C <sub>6</sub> H <sub>10</sub> O	(CH <sub>3</sub> ) <sub>2</sub> CCHCOCH <sub>3</sub>	4-methyl-3-penten-2-one	[62]	products for different humidities
C <sub>8</sub> H <sub>8</sub> O	C <sub>6</sub> H <sub>5</sub> COCH <sub>3</sub>	acetophenone	[62]	products for different humidities
C <sub>8</sub> H <sub>8</sub> O	C <sub>6</sub> H <sub>5</sub> COCH <sub>3</sub>	1-phenylethanone	[56]	
C <sub>2</sub> H <sub>4</sub> O <sub>2</sub>	HCOOCH <sub>3</sub>	methyl formate	[64]	
C <sub>3</sub> H <sub>6</sub> O <sub>2</sub>	HCOOC <sub>2</sub> H <sub>5</sub>	ethyl formate	[64]	
C <sub>3</sub> H <sub>6</sub> O <sub>2</sub>	CH <sub>3</sub> COOCH <sub>3</sub>	methyl acetate	[64]	
C <sub>4</sub> H <sub>8</sub> O <sub>2</sub>	CH <sub>3</sub> COOC <sub>2</sub> H <sub>5</sub>	ethyl acetate	[64] [61]	products for different field strengths
C <sub>4</sub> H <sub>8</sub> O <sub>2</sub>	C <sub>2</sub> H <sub>5</sub> COOCH <sub>3</sub>	methyl propionate	[64]	
C <sub>4</sub> H <sub>8</sub> O <sub>2</sub>	C <sub>2</sub> H <sub>5</sub> COOC <sub>2</sub> H <sub>5</sub>	ethyl propionate	[64]	
C <sub>5</sub> H <sub>10</sub> O <sub>2</sub>	C <sub>3</sub> H <sub>7</sub> COOCH <sub>3</sub>	methyl butanoate	[64]	
C <sub>8</sub> H <sub>8</sub> O <sub>2</sub>	C <sub>6</sub> H <sub>5</sub> COOCH <sub>3</sub>	methyl benzoate	[64]	
C <sub>4</sub> H <sub>10</sub> O	C <sub>2</sub> H <sub>5</sub> OC <sub>2</sub> H <sub>5</sub>	diethyl ether	[58]	
C <sub>5</sub> H <sub>10</sub> O	C <sub>3</sub> H <sub>5</sub> OC <sub>2</sub> H <sub>5</sub>	allyl ethyl ether	[58]	

C <sub>5</sub> H <sub>12</sub> O	C <sub>4</sub> H <sub>9</sub> OCH <sub>3</sub>	butyl methyl ether	[58]	
C <sub>6</sub> H <sub>14</sub> O	C <sub>2</sub> H <sub>5</sub> C(CH <sub>3</sub> ) <sub>2</sub> OCH <sub>3</sub>	tertiary pentyl methyl ether	[58]	
C <sub>6</sub> H <sub>14</sub> O	C(CH <sub>3</sub> ) <sub>3</sub> OC <sub>2</sub> H <sub>5</sub>	butyl ethyl ether	[58]	
C <sub>6</sub> H <sub>14</sub> O	C <sub>3</sub> H <sub>7</sub> OC <sub>3</sub> H <sub>7</sub>	dipropyl ether	[58]	
C <sub>6</sub> H <sub>14</sub> O	(CH <sub>3</sub> ) <sub>2</sub> CHOCH(CH <sub>3</sub> ) <sub>2</sub>	diisopropyl ether	[58]	
C <sub>4</sub> H <sub>10</sub> O <sub>2</sub>	CH <sub>3</sub> OC <sub>2</sub> H <sub>4</sub> OCH <sub>3</sub>	ethylene glycol dimethyl ether	[58]	
C <sub>4</sub> H <sub>8</sub> O		tetrahydrofuran	[58]	
C <sub>7</sub> H <sub>8</sub> O	C <sub>6</sub> H <sub>5</sub> OCH <sub>3</sub>	anisole	[58]	
CH <sub>2</sub> O <sub>2</sub>	HCOOH	formic acid	[64] [61]	products for different field strengths
C <sub>2</sub> H <sub>4</sub> O <sub>2</sub>	CH <sub>3</sub> COOH	acetic acid	[64] [61]	products for different field strengths
C <sub>3</sub> H <sub>6</sub> O <sub>2</sub>	C <sub>2</sub> H <sub>5</sub> COOH	propionic acid	[64]	
C <sub>4</sub> H <sub>8</sub> O <sub>2</sub>	C <sub>3</sub> H <sub>7</sub> COOH	n-butyric acid	[64]	
C <sub>4</sub> H <sub>8</sub> O <sub>2</sub>	(CH <sub>3</sub> ) <sub>2</sub> CHCOOH	iso-butyric acid	[64]	
C <sub>5</sub> H <sub>10</sub> O <sub>2</sub>	C <sub>4</sub> H <sub>9</sub> COOH	valeric acid	[64]	
C <sub>5</sub> H <sub>10</sub> O <sub>2</sub>	(CH <sub>3</sub> ) <sub>3</sub> CCOOH	trimethylacetic acid	[64]	
C <sub>3</sub> H <sub>4</sub> O <sub>2</sub>	CH <sub>2</sub> CHCOOH	acrylic acid	[64]	
C <sub>3</sub> H <sub>6</sub> O <sub>3</sub>	CH <sub>3</sub> CHOHCOOH	lactic acid	[64]	
C <sub>6</sub> H <sub>6</sub>	C <sub>6</sub> H <sub>6</sub>	benzene	[60]	
C <sub>7</sub> H <sub>8</sub>	C <sub>6</sub> H <sub>5</sub> CH <sub>3</sub>	toluene	[60]	
C <sub>8</sub> H <sub>10</sub>	C <sub>6</sub> H <sub>5</sub> C <sub>2</sub> H <sub>5</sub>	ethylbenzene	[60]	
C <sub>8</sub> H <sub>10</sub>	o-C <sub>6</sub> H <sub>5</sub> CH <sub>3</sub> CH <sub>3</sub>	ortho-xylene	[60]	
C <sub>8</sub> H <sub>10</sub>	m-C <sub>6</sub> H <sub>5</sub> CH <sub>3</sub> CH <sub>3</sub>	meta-xylene	[60]	
C <sub>8</sub> H <sub>10</sub>	p-C <sub>6</sub> H <sub>5</sub> CH <sub>3</sub> CH <sub>3</sub>	para-xylene	[60]	

### E.1.3 Proton Affinities

For species without SIFT data available or where ionization via H<sub>3</sub>O<sup>+</sup> is not reported, assessing the proton affinity can be helpful. It is defined as the negative enthalpy change at protonation and in comparison to the proton affinity of water is a measure of how likely a proton transfer from H<sub>3</sub>O<sup>+</sup> is. A proton affinity smaller than water does not necessarily mean that there is no ionization via H<sub>3</sub>O<sup>+</sup> at all though: Firstly, protonation can still occur - as it is just a matter of probability - if the proton affinity is not much smaller and the analyte is present in substantial concentration. Secondly, cluster forming via H<sub>3</sub>O<sup>+</sup> is possible as was observed for multiple species and documented in E.3.

**Table 37:** Proton affinities (PA) at room temperature ( $T = 300\text{ K}$ ) and mean edobserved elution times (ET) of described species. Water is used as a reference, all values below are highlighted in red and values only slightly above are highlighted in yellow.

Observed species	PA [kJ mol <sup>-1</sup> ]	ET [min]	Comment
water	691		from [67]
carbon monoxide	594	2.2	from [67]
methane	552	2.9	from [67]
carbonic acid	741	3.8	from [68]
carbon dioxide	541	3.9	from [67]
ethylene	681	5.6	from [67]
methanol	725	7.1	from [67]
formaldehyde	712	7.2	from [67]
propylene	752	9.1	from [67]

acetaldehyde	769	10.5	from [67]
ethanol	776	11.9	from [67]
1-butene	802	12.0	from [67]
butadiene	783	12.2	from [67]
trans-butene	747	12.4	from [67]
cis-butene	≈ 747	12.7	assumed similar to diastereomer
cyclopropane	750	13.1?	from [67]
propanal	786	14.5	from [67]
acetone	812	15.3	from [67]
allyl-alcohol	750 to 850	16.5	assumed similar to structural isomers
1-pentene	≈ 809	16.9	assumed similar to positional isomer
propanol	787	17.2	from [67]
2-pentene	809	17.3?	from [67]
butanedione	802	20.5	from [67]
crotyl alcohol	750 to 850	20.8?	assumed similar to structural isomers
butanone	827	21.6?	from [67]
butanal	793	21.9	from [67]
ethyl-acetate	836	23.3	from [67]
2,3-pentanedione	≈ 874	36.9	assumed similar to positional isomer
2,4-pentanedione	874	39.0	from [67]

## E.2 Saturation Effects

If some species have a very large concentration (outside of the dynamic range of the instrument), specific effects start to occur. It is important to identify these effects and assess their severity so they can be handled accordingly. For all species affected, it is included in the discussion in [D](#) accordingly.

### E.2.1 Primary Ion depletion

If the ionization rate of a species via a specific primary ion is very large - due to large concentration of the species and/or high reaction rate constant (RRC) - the primary ion concentration can drop noticeably and is no longer orders of magnitude greater than any secondary ion detected. This has two direct consequences:

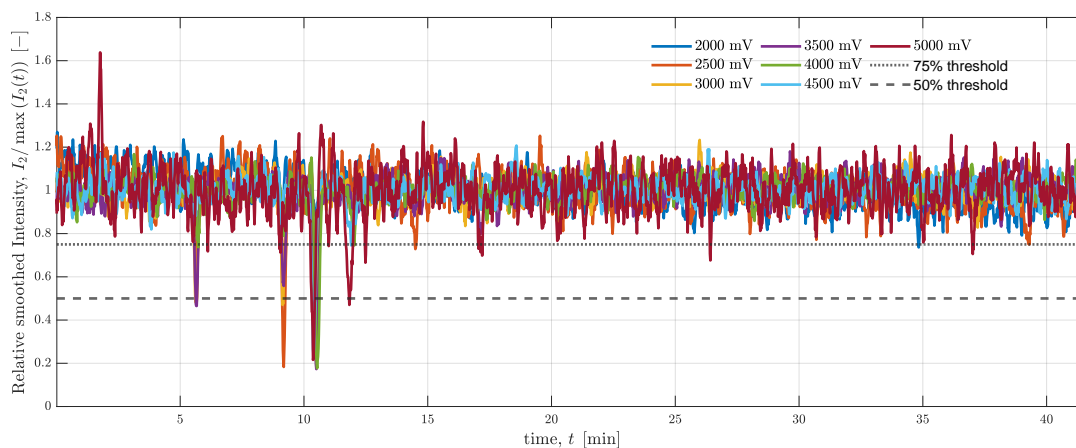
1. The concentration of primary ions can no longer be assumed to be constant. Considering the rate equation  $\frac{d[\text{MH}^+]}{dt} = k_C [\text{M}] [\text{H}_3\text{O}^+]$  for protonation  $\text{M} + \text{H}_3\text{O}^+ \longrightarrow \text{MH}^+ + \text{H}_2\text{O}$ , even if the RRC  $k_C$  is constant, the reaction rate (aka counts per second) is no longer a direct measure for analyte concentration  $[\text{M}]$ . Relative Faradaic Efficiencies calculated for these data points are therefore skewed.
2. Now, secondary ions (aka protonated species) are at similar or even higher concentrations as primary ions ( $[\text{MH}^+] \approx [\text{H}_3\text{O}^+]$ ). Thus, they are now likely to hit unionized species to form large clusters at an observable rate, see [E.2.2](#).

For these reasons, substantial drops in PI concentration were identified and applied to species via their observed elution times. Tab. 38 lists all species for which primary ion depletion of either  $\text{H}_3\text{O}^+$  or  $\text{O}_2^+$  was verified, details shown further below. To circumvent or reduce the effects of PI depletion listed above, for these species the products of ionization via residual  $\text{O}_2^+$  should be analysed in detail. Alternatively, trends of cluster-forming can be roughly quantified as discussed in E.2.2.

**Table 38:** Detected species that verifiably caused depletion of primary ions in some of the experiments.

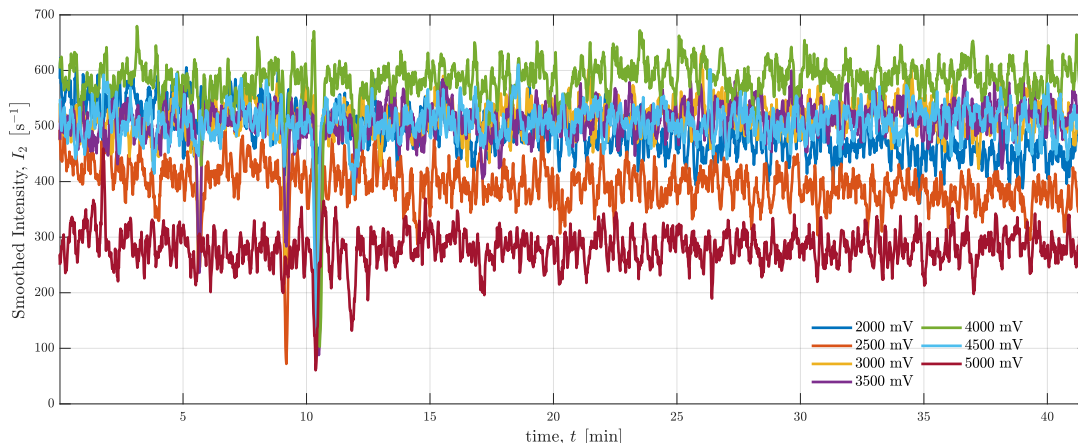
Species	Ionization PI	Applied potential $U_{\text{Hg}/\text{HgO}}$ [mV]						
		2000	2500	3000	3500	4000	4500	5000
Ethylene	$\text{O}_2^+$		full	full	full	full	full	full
	$\text{H}_3\text{O}^+$		partial	full	full	partial		
Propylene	$\text{H}_3\text{O}^+$		full	full	partial			
Acetaldehyde	$\text{H}_3\text{O}^+$		full	full	full	full	full	full
Ethanol	$\text{H}_3\text{O}^+$					partial	partial	partial
Propanal	$\text{H}_3\text{O}^+$		partial					

**Drop in hydronium ions** was analysed via Fig. 55. Unfortunately, the trace representing  $\text{H}_3^{16}\text{O}^+$  ( $m/z = 19.05\text{Da}$ ) cannot be used for assessment of PI depletion since the detector is saturated (see E.2.3). We therefore used  $m/z = 21.02\text{Da}$  which is corresponding with low-abundance oxygen isotope  $\text{H}_3^{18}\text{O}^+$ . Fig. 56(a) shows somewhat varying baseline signals for the different measurements. For this reason, depletion was assessed via signals normalized to the median intensity throughout the course of an experiment, see Fig. 55(a). The usual noise levels can be seen around 15% to 20%, so the threshold for partial PI depletion was set to 25% deviation from the median.



(a) Smoothed signal relative to median

**Figure 55**

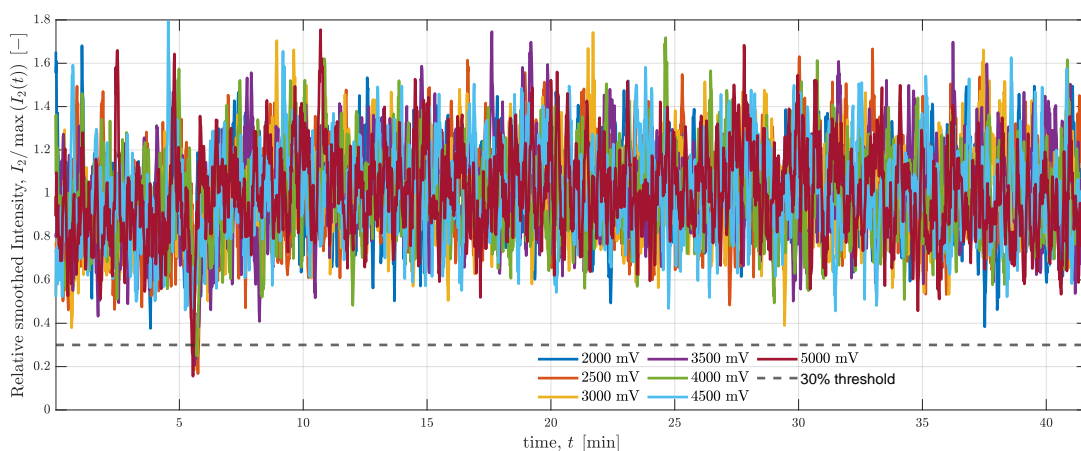


(a) Smoothed signal

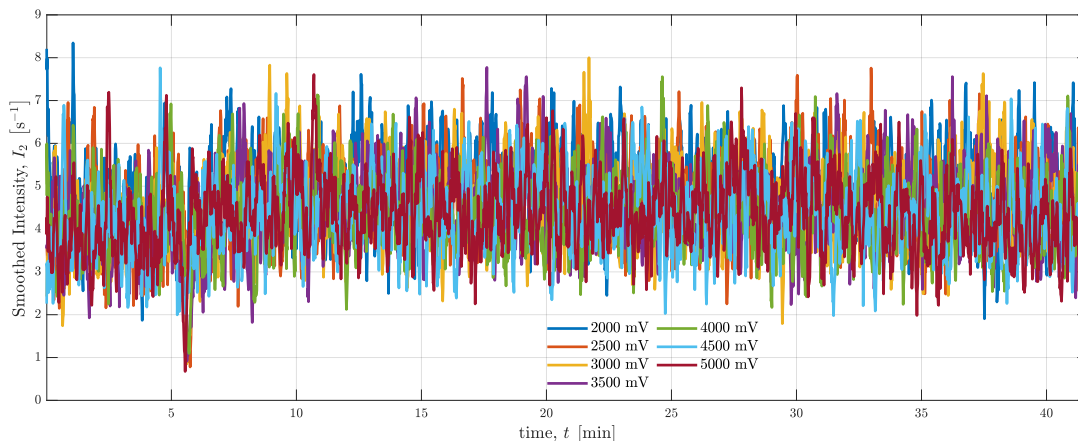
**Figure 55:** Signals of  $\text{H}_3^{18}\text{O}^+$  trace.

As a few species cause such an extreme drop in PI concentration that we must assume no further protonation via PI at this point, full depletion was defined for drop below 50% of the median. Since the average signal of the experiment at  $U_{\text{Hg}/\text{HgO}} = 5\text{ V}$  is considerably smaller, similar absolute standard deviations account for significantly larger relative noise levels. For this reason, a drop below the according threshold in this experiment was only considered as partial or full depletion in Tab. 38 if it fit the trend of production rates at this retention time.

**Drop in oxygen ions** was analysed via Fig. 55. Analogous to  $\text{H}_3\text{O}^+$ , the low-abundance oxygen isotope  $^{16}\text{O}^{18}\text{O}^+$  ( $m/z = 33.99\text{ Da}$ ) was used instead of  $^{16}\text{O}_2^+$  for PI depletion assessment. As the signals depicted in Fig. 56(c) are quite small, relative noise levels are quite large and only substantial drops of intensity levels were considered. Again, the signal was normalized by the median but as intensity levels are similar here throughout experiments, this does not change the picture much in Fig. 56(b): Full PI depletion was now defined for any signal dropping below 30% of the median.



(b) Smoothed signal relative to median



(c) Smoothed signal

**Figure 55:** Signals of  $^{16}\text{O}^{18}\text{O}^+$  trace.

## E.2.2 Cluster forming

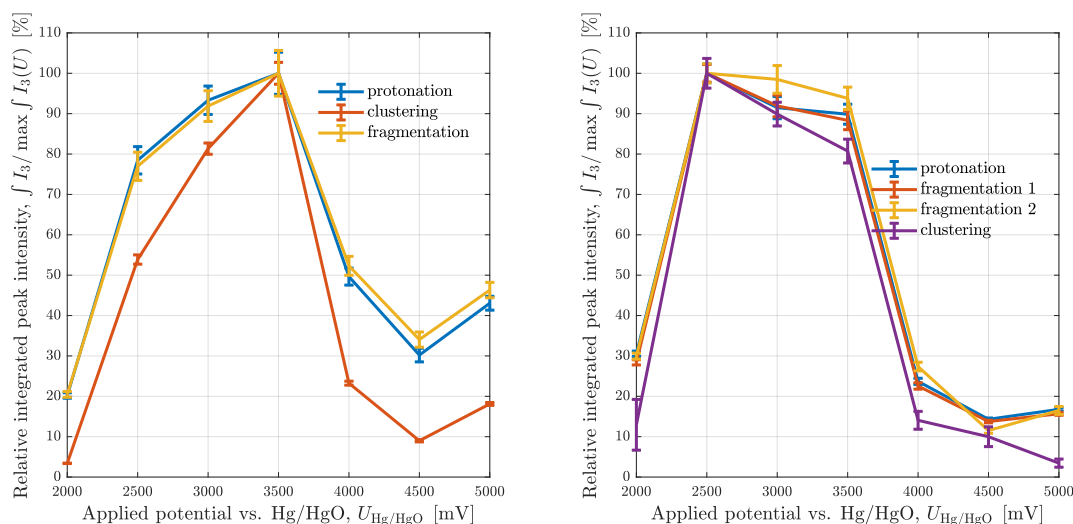
As a direct consequence of (partial or full) PI depletion, PTR mechanisms might change and therefore products and product fractions. For example, detected fragmentation can be reduced as fragments themselves act as proton donors in secondary proton transfer reactions or temperature conditions change. [69] This would mean that product ratios change towards fewer fragments in favour of directly protonated species. Comparing relative integrated intensities of  $\text{MH}^+$  with fragments such as  $\text{MH}^+ - \text{CH}_4$ , this effect would show up as broadened curves for the fragment - flatter around the peak as its product ratio is smallest for peak production.

Caused by the same fact of more collisions between unionized species with secondary products, we mostly observe a different effect in this study: Clusters between unionized species and either protonated species or fragments thereof are forming and are stable enough to be detected as large ions, see E.3. The larger these clusters get, they will be subject to increased fragmentation which leads to signals for a multitude of traces/masses. These effects have been identified as a problem in the analysis of alcoholic compounds where PI depletion via ethanol protonation, cluster forming and subsequent fragmentation precludes monitoring of some minor species that should appear at the same masses. [38] This is one of the reasons why product separation via GC column was done in this study.

The observed clustering should increase with concentration of the respective species and can therefore help with identification and quantification [69]. Relative integrated intensities of traces representing clusters should show steeper curves than those representing simply protonated species. Relative to a sharp peak, the relative integrated intensities should be smaller for all other applied potentials as its product ratio is smallest for the lowest production rate.

We can explore the relative trends mentioned above by comparing secondary ions detected for species that cause PI depletion as in Fig. 56. In Fig. 56(d) we compare the relative integrated intensities of the main secondary ion via PTR  $\text{C}_2\text{H}_4 + \text{H}_3\text{O}^+ \longrightarrow \text{C}_2\text{H}_5^+ + \text{H}_2\text{O}$  with its directly related tertiary ions via fragmentation  $\text{C}_2\text{H}_5^+ - \text{H}_2 \longrightarrow \text{C}_2\text{H}_3^+$  and clus-

tering  $\text{C}_2\text{H}_5^+ + \text{C}_2\text{H}_4 \longrightarrow \text{C}_4\text{H}_9^+$  (full mechanism see E.3.2). As expected, the curve representing the signal from the cluster has a much sharper curve that is below the secondary ion. Meanwhile, the curve representing the signal of the fragment coincides with that of the secondary ion within one standard deviation for  $U_{\text{Hg}/\text{HgO}} \leq 3.5 \text{ V}$ . For bigger applied potentials, it is slightly above - indicating a flatter shape as expected through secondary proton transfers. Overall, this effect seems to be less pronounced for the conditions used in our experiments: in Fig. 56(e) the “fragmentation 2” curve is also only slightly above or on the curve of the secondary ion within one standard deviation. Here we compare the main secondary ion of propylene via PTR  $\text{C}_3\text{H}_6 + \text{H}_3\text{O}^+ \longrightarrow \text{C}_3\text{H}_7^+$  and its direct tertiary ion via fragmentation  $\text{C}_3\text{H}_7^+ - \text{H}_2^+ \longrightarrow \text{C}_3\text{H}_5^+$  (as “fragmentation 1”) with the secondary ion’s direct tertiary ions via clustering  $\text{C}_3\text{H}_5^+ + \text{C}_3\text{H}_6 \longrightarrow \text{C}_6\text{H}_{11}^+$  and fragmentation  $\text{C}_3\text{H}_5^+ - \text{H}_2 \longrightarrow \text{C}_3\text{H}_3^+$  (as “fragmentation 2”). For the full mechanism, see 60.



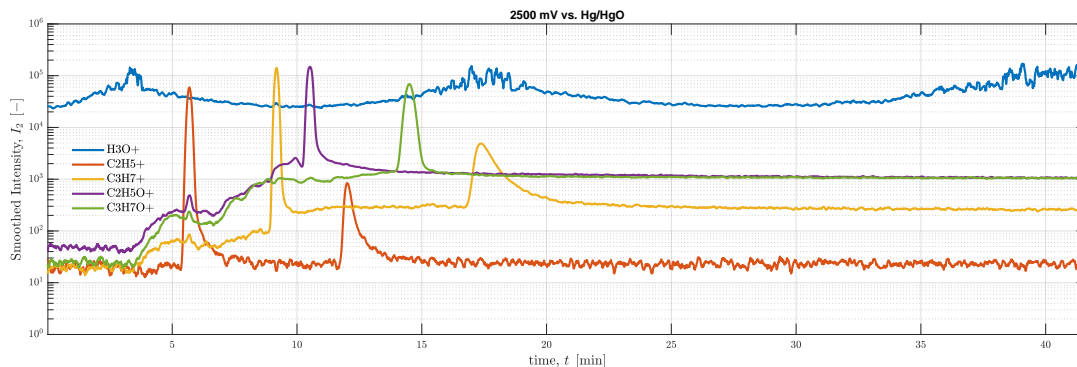
(d) Ethylene: protonated species  $\text{C}_2\text{H}_5^+$  vs. directly related fragment  $\text{C}_2\text{H}_3^+$  and cluster  $\text{C}_4\text{H}_9^+$  (e) Propylene: protonated species  $\text{C}_3\text{H}_7^+$  and its direct fragment 1  $\text{C}_3\text{H}_5^+$  vs. derived cluster  $\text{C}_6\text{H}_{11}^+$  fragment 2  $\text{C}_3\text{H}_3^+$

**Figure 56:** Relative intensities of traces related to products that cause primary ion depletion. Comparison of trends between protonated species, fragments, and clusters.

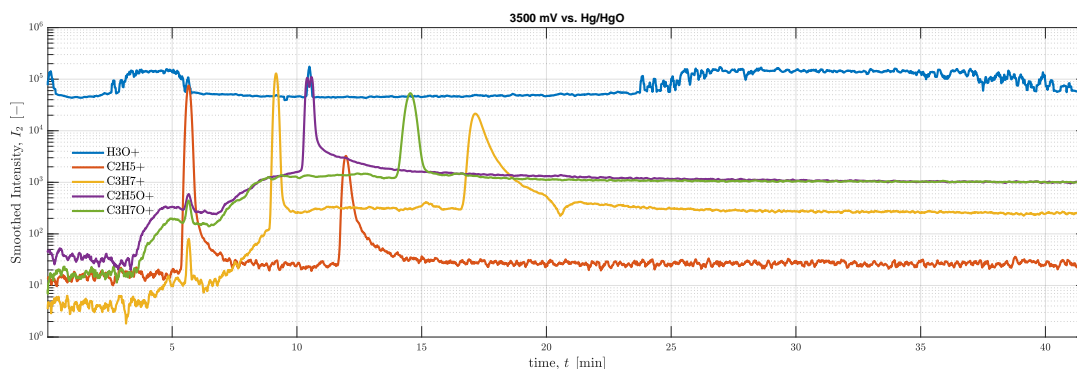
### E.2.3 Detector saturation

The TOF analyser has a detection limit of counts per second that seems to be  $\approx 1 \times 10^5 \text{ s}^{-1}$  as this is the maximum intensity detected for the primary ion  $\text{H}_3\text{O}^+$ . We know the actual concentration to be larger as the  $\text{H}_3^{18}\text{O}^+$  signal is around  $500 \text{ s}^{-1}$  on average which represents an isotope of 0.2% natural abundance which would warrant a  $\text{H}_3^{16}\text{O}^+$  signal of up to  $3 \times 10^5 \text{ s}^{-1}$ . This postulated detection limit is not constantly reached by the primary ion as it largely depends on the curve fit over  $m/z$  dimension: baselines vary

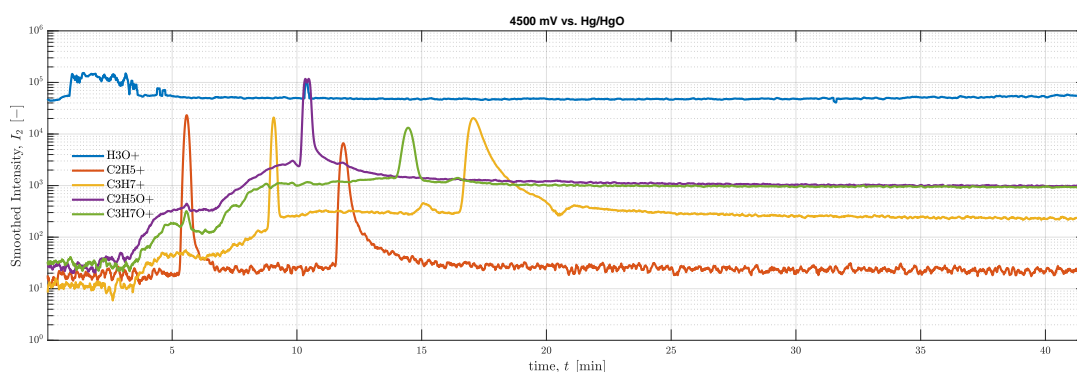
across measurements and also change within the same measurement. Because of this, an even larger signal of  $\text{H}_3\text{O}^+$  might be detected at times of PI depletion since changing curve shapes can change the fitting parameters - this is the reason we need to look at the signals of less-abundant isotopes to assess PI depletion.



(a)  $U_{\text{Hg}/\text{HgO}} = 2500 \text{ mV}$



(b)  $U_{\text{Hg}/\text{HgO}} = 3500 \text{ mV}$



(c)  $U_{\text{Hg}/\text{HgO}} = 4500 \text{ mV}$

**Figure 57:** Comparison of the traces with the largest signals for different applied potentials in order to check for detector saturation.

In order to check for detector saturation for any of the other masses used for product analysis analysis, the four traces with the largest peak signals were compared to the primary ion in Fig. 57. All of these traces at some point have signals larger than the primary ion -

namely for ethylene, propylene, acetaldehyde and propanal. Intensities larger than that of the primary ion trace do not necessarily mean detector saturation was reached, but it is a strong indicator. Additionally, in some instances (e.g.  $C_2H_5O^+$  at  $t_{CH_3CHO} = 10.5$  min for  $U_{Hg/HgO} = 3.5$  V) a signal drop in the middle of the peak can be seen - a clear sign that the detector could no longer count the corresponding masses hitting the sensor.

The qualitative trends of masses represented by traces with potential detector saturation need to be measured by some alternative trace representing another mass connected to the same product under assessment. Ideally, we just use the corresponding  $^{13}C$  isotopes as other traces might show different trends as explained in E.2.2. In some cases we might even be able to use oxygen isotopes  $^{18}O$  as we did for PI depletion assessment in E.2.1.

### E.3 New reactions and fragments

There are three types of additional reactions found:

1. Clustering with unionized version (for large concentrations, see E.2.2)
2. Cluster with hydronium as additional protonation product: In the literature this is rather often interaction with humidity but our device is designed in a way to minimize this and we have good separation of water (except for D.3 and D.5). Forming of hydronium clusters
3. Dissociation of (usually stable) species

In the following, PTR mechanisms of species with a number of newly found reactions and fragments are sketched out. Blue reaction arrows represent high certainty while orange means some uncertainties are remaining.

#### E.3.1 Methane

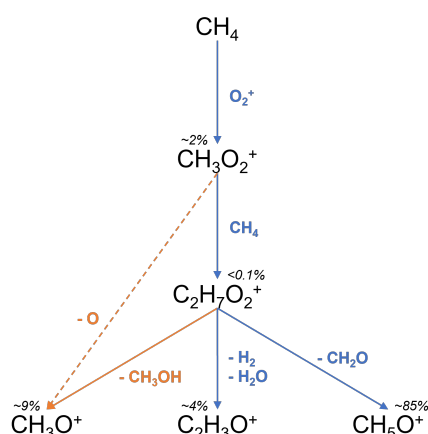


**Figure 58:** Suggested PTR mechanism for methane.

The mechanism in Fig. 58 shows confirmation of exclusive  $O_2^+$  ionization due to the small proton affinity of methane. Other than in SIFT-MS studies [57], we observed substantial fragmentation of the formed  $CH_3 \cdot O_2^+$  cluster.

### E.3.2 Ethylene

For very large ethylene concentrations, a majority of  $C_2H_4$  molecules is not ionized, we can see a drop in both primary ions as well (see E.2.1). At this point, protonated ethylene reacts further with unprotonated ethylene via the mechanism described in Fig. 59.

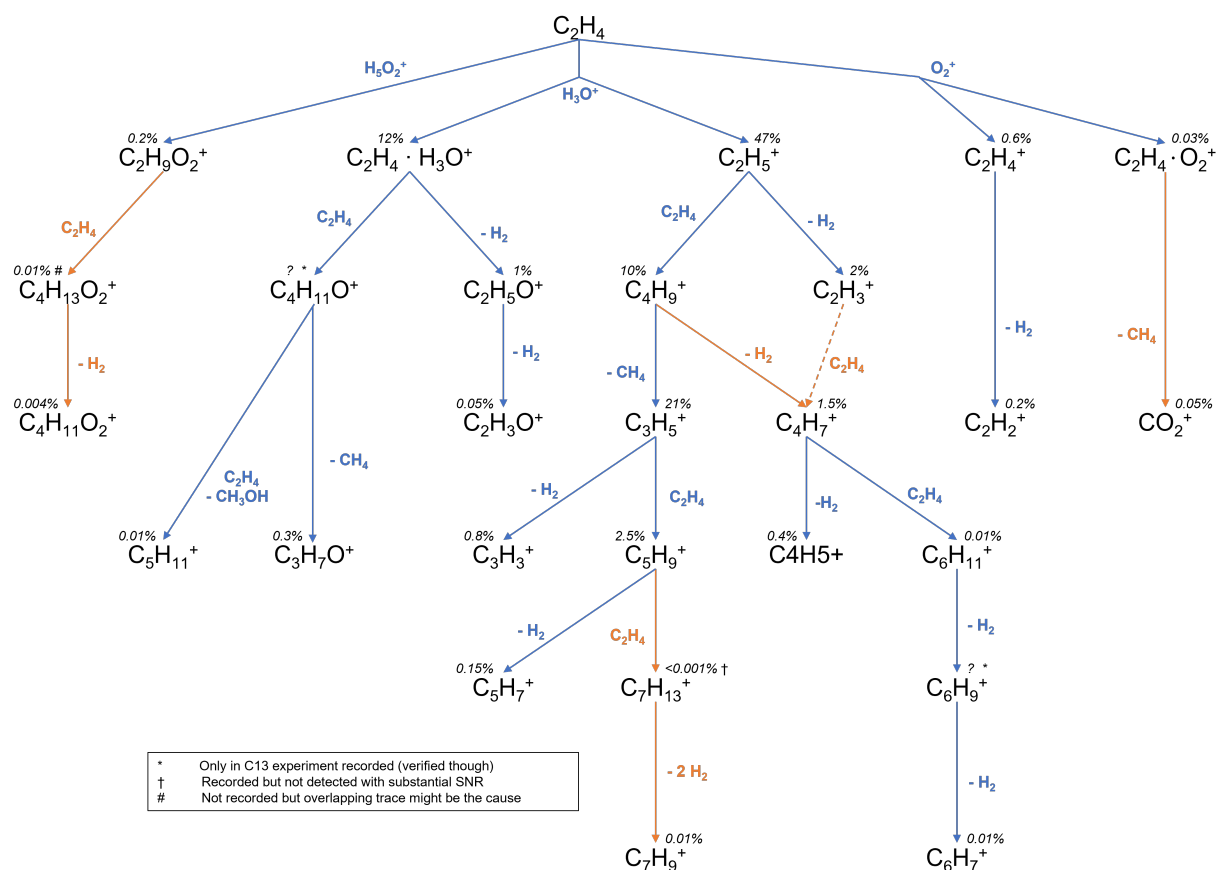


**Figure 59:** Suggested PTR mechanism for ethylene.

In Fig. 59 we see all the documented PTR reactions as per SIFT-MS studies [57] as well as all newly observed secondary reactions leading to tertiary ions etc. but even additional secondary ions  $C_2H_4 \cdot H_5O_2^+$  and  $C_2H_4 \cdot O_2^+$ . Signal fractions are calculated via sampling (as described in C.3.2) and the values shown are estimated averages across applied potentials. It has to be noted though that since many of these ions depend on significant PI depletion and therefore ethylene concentration, variance can be large.

### E.3.3 Propylene

In Fig. 60 we see very similar effects for propylene ionization as for the ethylene described in E.3.2: Additional secondary ion via  $C_3H_6 + H_3O^+ \longrightarrow C_3H_9O^+$  has been established along with a range of tertiary ions caused by fragmentation (partially dependent on reduced field in drift chamber) and clustering (mostly due to large propylene concentration and PI depletion).

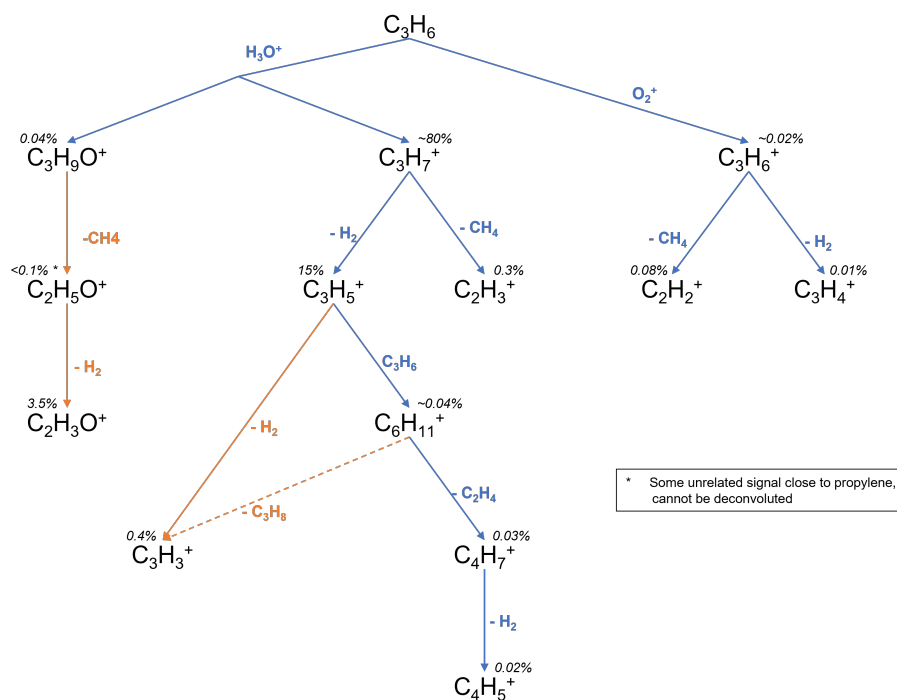


**Figure 60:** Suggested PTR mechanism for propylene.

The mechanism towards a few of the detected species remains unclear - especially if signals are very small (which makes it hard to compare trends as uncertainties are large) or if their signals are much larger than supposed “upstream” species. The latter case occurs for example with large signal of  $C_2H_3O^+$  compared to small  $C_3H_9O^+$  and barely detectable  $C_2H_5O^+$  signal. This can be explained though if secondary and tertiary ions are unstable and e.g. fragmentation has a larger reaction rate constant than initial ionization.

### E.3.4 Acetaldehyde

Fig. 61 shows the compiled mechanism of acetaldehyde ionization witnessed in the PTR-MS experiments conducted. Again there is an additional secondary ion via  $H_3O^+$  cluster forming and a few other tertiary ions but it is interesting to note that even though it is probably the species that leads to the most protonation (see PI depletion in E.2.1), we do not see much clustering with existing acetaldehyde as we do for ethylene in 59. The reason is probably that  $C_2H_5O^+$  does not protonate nearly as well as hydronium ions (condition for significant rate of secondary reactions is  $[MH^+] \gtrsim k_1/k_2 [H_3O^+]$  where  $k_1$  is RRC for

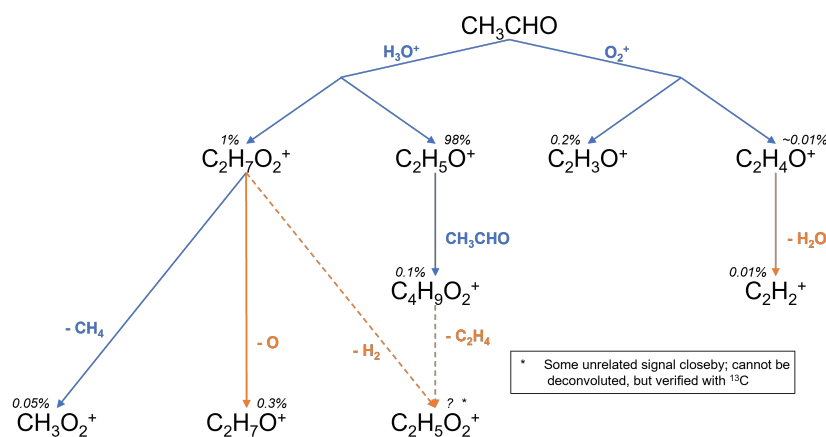
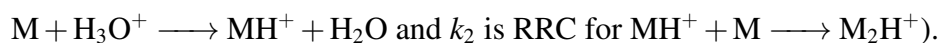


**Figure 61:** Suggested PTR mechanism for acetaldehyde.

The  $C_2H_5O_2^+$  signal seems to be an artifact at first glance but is ultimately verified as acetaldehyde ionization product, see discussion in D.7. The exact mechanism remains unclear due to lack of comparability.

### E.3.5 Ethanol

Fig. 62 shows the mechanism of ethanol ionization witnessed. Compared to a study analysing alcoholic beverages via PTR-MS [38] we see the same main responses: secondary ion  $C_2H_7O^+$  and tertiary ion  $C_2H_5^+$  making up a slightly higher percentage than in the literature. Also,  $C_2H_9O_2^+$  is observed with a significantly larger signal fraction which is probably caused by different origins - while the humidity in the literature experiment causes clustering of secondary ion with water, the larger field strength in our experiment makes this another secondary ion.

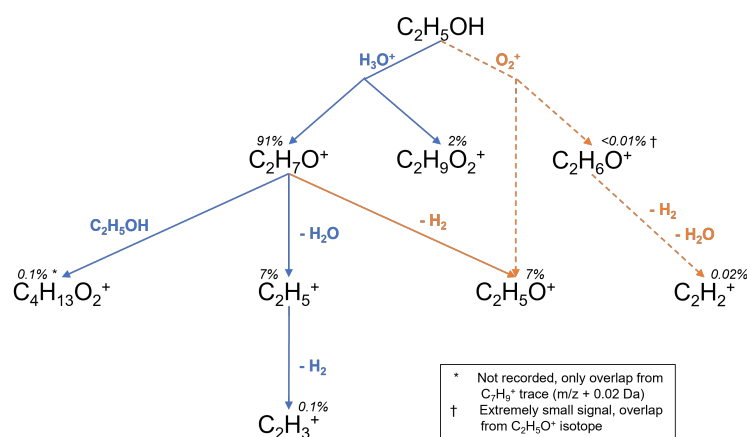


**Figure 62:** Suggested PTR mechanism for ethanol.

Clustering with unionized species to form  $C_4H_{13}O_2^+$  is observed in our experiments at a much smaller scale as ethanol concentration is definitely smaller than the 10 vol-% in the literature [38]. The mentioned study does not report any of the other fragments reported at signal fractions smaller than 1% here. Furthermore, no  $C_2H_5O^+$  is reported. This could be interpreted as evidence for  $O_2^+$  origin (since residual primary ion ratios would have differed) but could also plainly be caused by the smaller reduced field strength leading to less fragmentation.

### E.3.6 Propanol

The documented main  $O_2^+$  product  $CH_3O^+$  [59] was not detected - most likely due to overlap with the primary ion. The two documented protonation products  $C_3H_7^+$  and  $C_3H_9O^+$  [59] were found but in a different ratio as the  $C_3H_7^+$  signal is multiple orders of magnitude larger. This is consistent with increased fragmentation experienced in our system compared to most of the referenced SIFT studies. For this reason, a few traces resulting from even further fragmentation were found - one of them ( $C_3H_5^+$ ) with a significant signal strength. Moreover, a  $H_3O^+$  cluster was found.

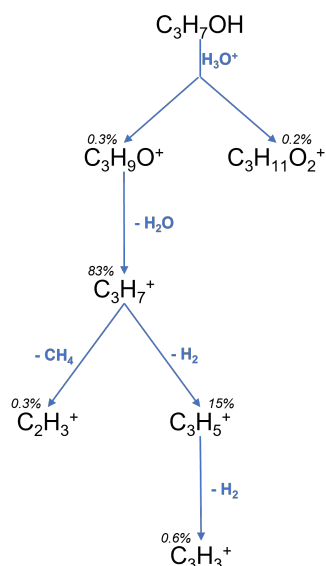


**Figure 63:** Suggested PTR mechanism for propanol.

### E.3.7 Propanal

For propanal, none of the reported  $O_2^+$  products [56] were detected - concentrations were probably too small to lead to any significant protonation by small amounts of residual oxygen primary ions. A few other protonation products apart from the reported  $C_3H_7O^+$  [56]: again, a cluster with  $H_3O^+$  was found as well as a few fragments due to dissociation from the secondary ions.

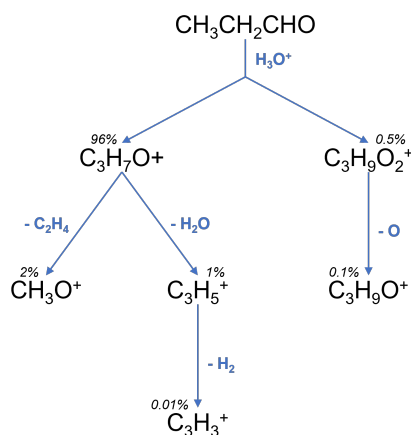


**Figure 64:** Suggested PTR mechanism for propanal.

As the very small signal at  $m/z \approx 64$  Da could not be assigned with a reasonable degree of certainty as documented in D.11, it is not shown here.

### E.3.8 Ethyl acetate

For acetaldehyde our observations lined up very closely with a previous PTR-MS study reporting secondary ions and their ratios for different reduced field strengths [61]. The signal ratios of the major ions  $\text{C}_4\text{H}_9\text{O}_2^+$ ,  $\text{C}_2\text{H}_5\text{O}_2^+$ , and  $\text{C}_2\text{H}_3\text{O}^+$  were very close to the ratios reported for  $E/N \approx 113$  Td at the smallest relative humidity. Extrapolating the data to even smaller humidities, the values come even closer to what was observed in this study. Moreover, the only minor secondary ion reported independent of humidity,  $\text{C}_4\text{H}_{11}\text{O}_3^+$  was also observed along with two of its unreported fragments,  $\text{C}_2\text{H}_7\text{O}_3^+$  and  $\text{C}_4\text{H}_{11}\text{O}_2^+$ .

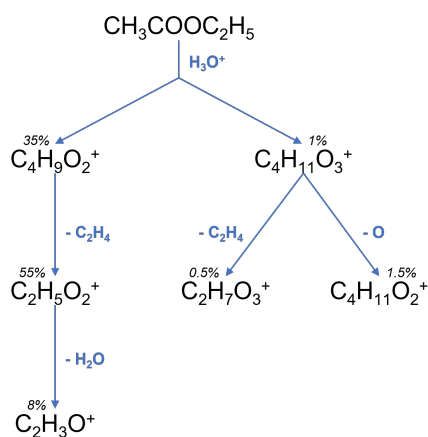


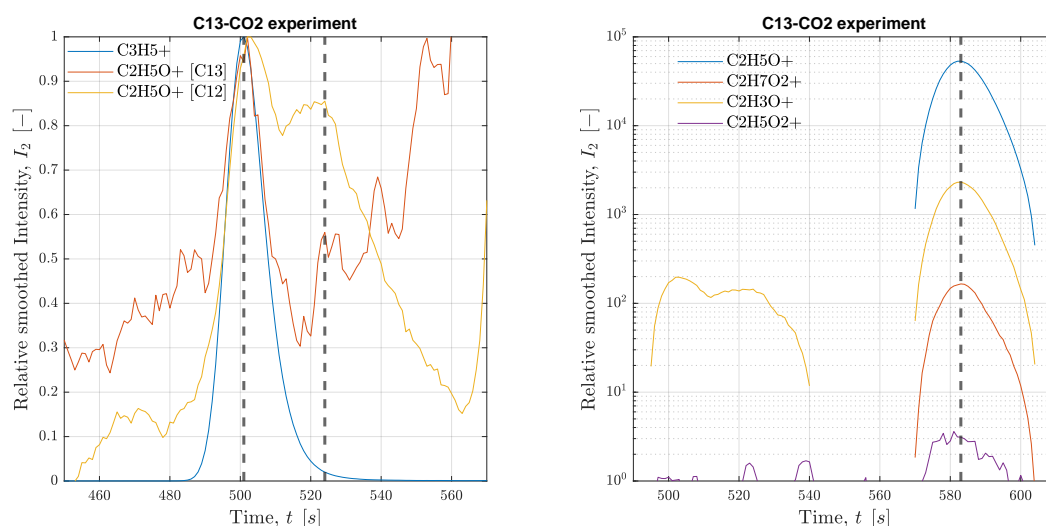
**Figure 65:** Suggested PTR mechanism for ethyl acetate.

## F C13 verification of specific traces

The single run with  $^{13}\text{CO}_2$  was performed at a constant current density of  $1.5\text{ A cm}^{-2}$ . It was carried out and measured analogous to the other experiments described. Additional traces were extracted to verify specific compounds as mentioned in appendix D. Only the species for which we relied on this experiment for verification and actually expected a signal are shown below.

### F.1 Assessment of potential artefacts

The  $\text{C}_2\text{H}_5\text{O}^+$  trace which appeared shifted against the rest of the propylene signal in appendix D.6 coincides perfectly with the main ion responses as shown in Fig. 66(b).



(a)  $\text{C}_2\text{H}_5\text{O}^+$  compared to propylene signals

(b)  $\text{C}_2\text{H}_5\text{O}_2^+$  compared to acetaldehyde signals

**Figure 66:** Analysis of traces suspected to be connected to artefacts.

The  $\text{C}_2\text{H}_5\text{O}_2^+$  trace which appeared shifted against the rest of the acetaldehyde signal in appendix D.6 coincides perfectly with the main ion responses as shown in Fig. 66(a). A shifted peak of the  $^{12}\text{C}$  isotope is still observed though, clearly distinct from  $^{13}\text{C}_2\text{H}_3\text{O}^+$ . This indicates overlapping signals of a systematic artifact and actual product of acetaldehyde ionization.

### F.2 Butene isomers and butadiene

For verification of the different  $\text{C}_4$  hydrocarbons reported in appendix D.9, corresponding secondary ions are shown in Fig. 67. All three reported butene isomers were found in this experiment too, while butadiene could not be confirmed. This is most likely caused by the large current at which butadiene selectivity is very small.

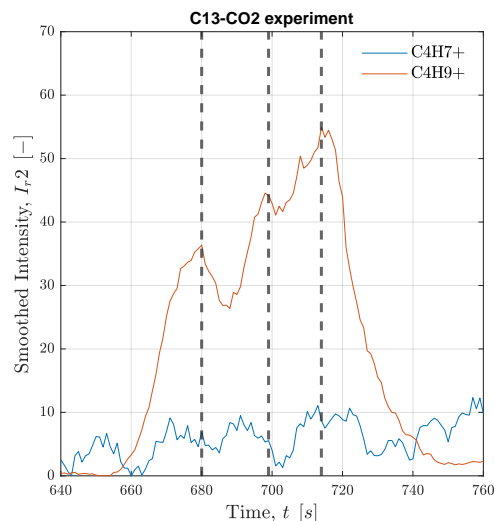


**Figure 67:** Signals of main ion responses associated with butene and butadiene

### F.3 Cyclopropane confirmation

Cyclopropane hypothesized in appendix D.10 could not be confirmed with sufficient certainty. In Fig. 68 the corresponding signal is shown with a small peak at the expected retention time but the SNR is too small for unambiguous identification.

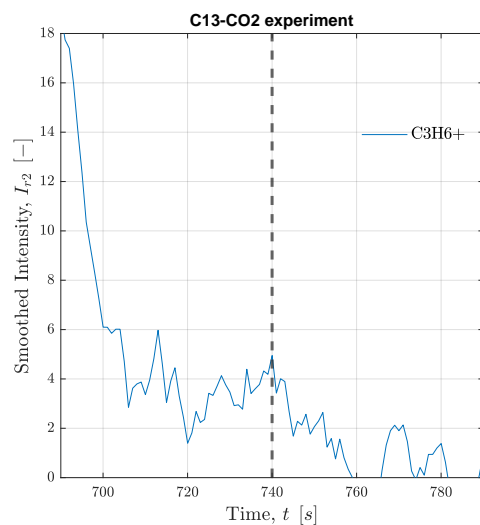


**Figure 68:** Signal of ion response associated with cyclopropane.

### F.4 C<sub>3</sub>H<sub>6</sub>O isomers

For verification of the different  $C_3H_6O$  isomers reported in appendix D.11, corresponding secondary ions are shown in Fig. 69. All three reported isomers were found in this exper-

iment too, the acetone signal is expectedly small in comparison with propanal and allyl alcohol.

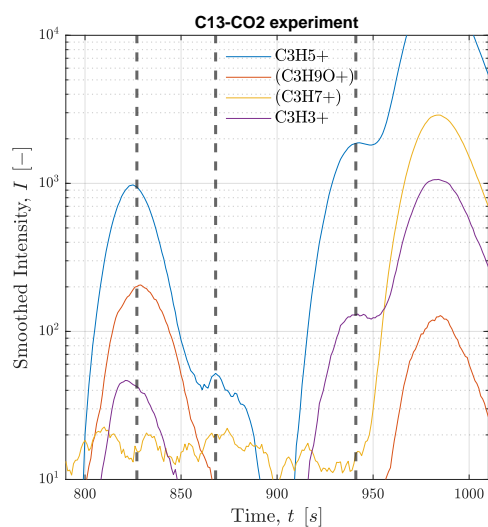


**Figure 69:** Signal of ion response associated with propanal, acetone, and allyl alcohol. The traces shown in brackets are represented by a slightly different mass.

As expected, propanal peak includes  $C_3H_5^+$ ,  $C_3H_9O^+$ , and  $C_3H_3^+$ . Acetone peak includes  $C_3H_5^+$  and  $C_3H_7^+$ . Allyl alcohol peak includes  $C_3H_5^+$  and  $C_3H_3^+$

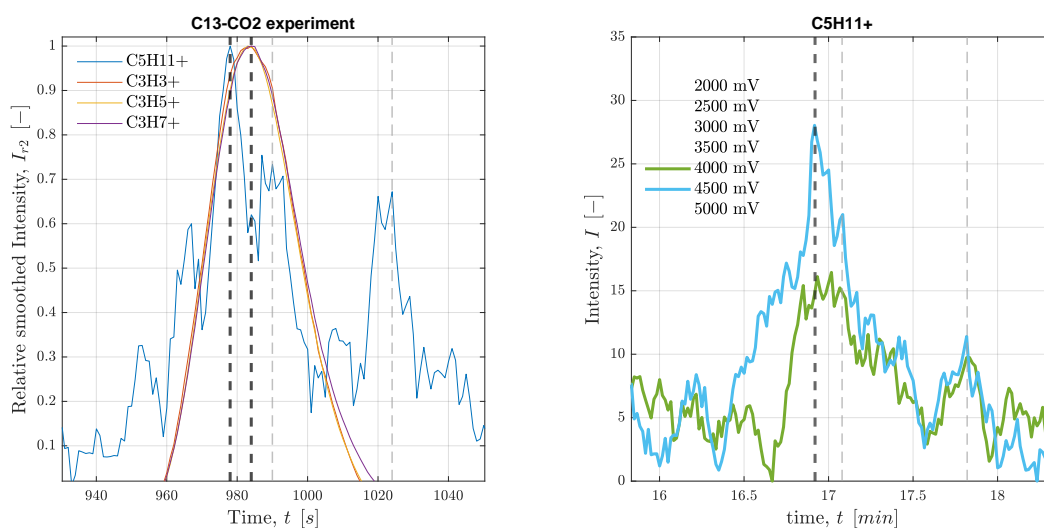
## F.5 Pentene confirmation

To confirm the observed pentene signal overlapping with propanol signal discussed in appendix D.12, corresponding secondary ions are shown in Fig. 70(a). The relative signals show a peak of  $C_5H_{11}^+$  a few seconds before the propanol-related  $C_3$  traces are peaking as indicated by the thick black dashed lines. As 1-pentene production is not very large even at this applied potential, the absolute intensities are much smaller than for propanol. What can be observed though are two additional peaks in the minute after 1-pentene elution that might indicate additional isomers - most likely 2-pentene stereoisomers analogous to butene observations in appendix D.9. These are indicated by thin gray dashed lines.

The additional peaks found correspond well with those observed in the  $^{12}C$  experiments at some of the applied potentials as shown in Fig. 70(b): the second peak appears  $\approx 10$ s and the third  $\approx 50$ s after the initial one.

## F.6 Butanedione confirmation

Butanedione was confirmed in this experiment as shown in Fig. 71. Both secondary ions reported in appendix D.13 were observed and even an isotope of the main ion response,  $^{13}C^{12}CH_3O^+$ , which based on the small  $^{12}C$  impurities of the  $CO_2$  used, was identified.



(a) Signal of ion response associated with pentene and propanol. (b)  $C_5H_{11}^+$  signal of pentene in  $^{12}C$  experiment.

**Figure 70:** Analysis of signals associated with pentene compared to propanol and  $^{12}C$  experiment.

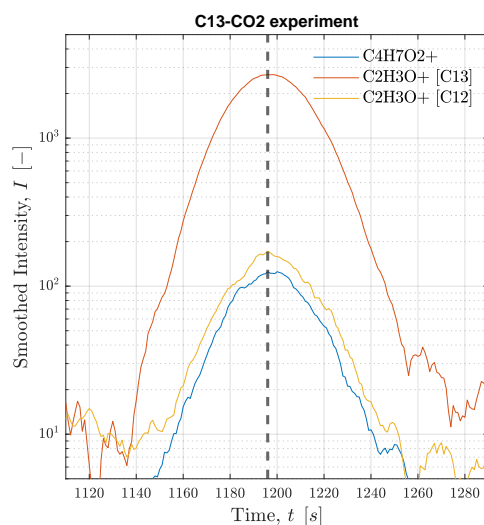


**Figure 71:** Signal of ion response associated with butanedione.

## F.7 C4H8O isomers

For verification of the two  $C_4H_8O$  isomers reported in appendix D.14, corresponding secondary ions are shown in Fig. 72. The shift between peaks of  $C_4H_9O^+$  and  $C_4H_7^+$  trace of  $\approx 15$  s was observed again, confirming the suspicion of separate butanal and butanone identification analogous to  $C_3H_6O$  isomers.

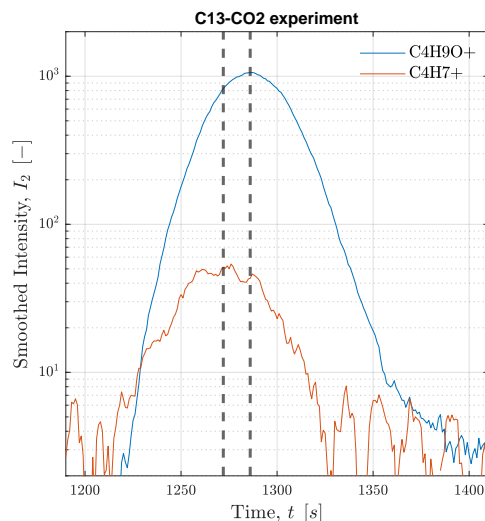


**Figure 72:** Signal of ion response associated with butanal and butanone.

## F.8 Ethyl acetate confirmation

Ethyl acetate was confirmed in this experiment as shown in Fig. 73.

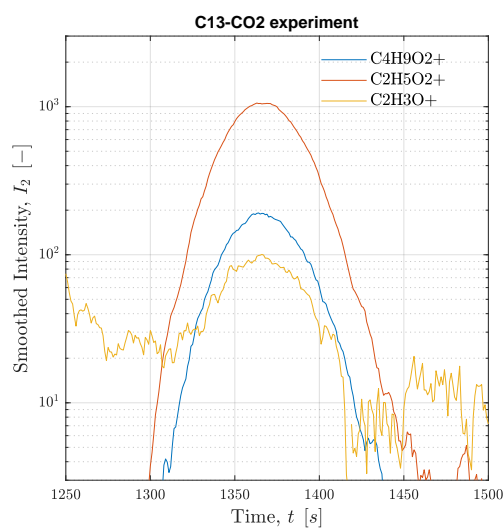


**Figure 73:** Signal of ion response associated with ethyl acetate.

The three main ion responses reported in appendix D.15 were observed at the expected retention time.

## F.9 Pentanedione confirmation

Both pentanedione isomers were confirmed in this experiment as shown in Fig. 74. Tracking the relevant traces, two peaks can be observed: a smaller first one and a much larger

second one  $\approx 140$  s later.

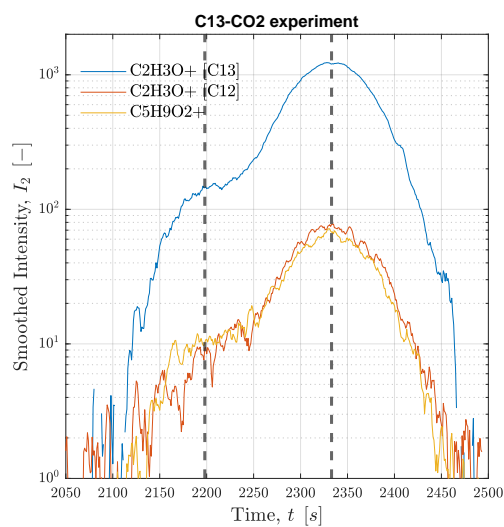


**Figure 74:** Signal of ion response associated with pentanedione.

Both secondary ions reported in appendix D.16 were observed and even an isotope of the main ion response,  $^{13}\text{C}^{12}\text{CH}_3\text{O}^+$ , which based on the small  $^{12}\text{C}$  impurities of the  $\text{CO}_2$  used, was identified.

## G Quantification of abundance

Absolute quantification of species concentrations is not possible within acceptable errors due to a number of factors: First of all, RRCs are only reported for SIFT-MS. Even if these can be adopted unaltered for PTR-MS, high species abundance will cause them to not be constant anymore as discussed in appendix E.2. Furthermore, we only analyse the gas outlet, liquid products are therefore only present based on their vapour-liquid-equilibrium (VLE). To compensate for this effect, Henry's law can be used - but it is technically only applicable for infinite dilution and values are only available for binary systems with water. Lastly, volume fluxes needed for determination of absolute concentrations are ambiguous, therefore the PTR-MS would have to be calibrated for each identified product individually.

We still can try to correct for RRC and VLE with the values that are available and compare orders of magnitude expected for absolute Faradaic Efficiencies. A corrected and compensated signal as indirect measure for absolute FE can be calculated via

$$c_{r,i}(\text{U}_{\text{Hg}/\text{HgO}}) = \int_j I_3(\text{U}_{\text{Hg}/\text{HgO}}) / k_c / x_{\text{PI}} \times H^{cp} / J_{\text{total}} \times n_{e^-}, \quad (\text{G.1})$$

where  $\int_j I_3(\text{U}_{\text{Hg}/\text{HgO}})$  is the sum of all integrated signals originating from the same primary ion ionizing a species. The fraction of the primary ion used is given by  $x_{\text{PI}}$  and the number of electrons transferred to form the product in question. The constant of Henry's law for mixtures with water is given by  $H^{cp}$  but only applied in Eq. (G.1) for liquid products under the given conditions.

The parameters needed for correcting and compensating signals as well as the final values are given in Tab. 39. Reaction rate coefficients are taken from SIFT publications given in appendix E.1.2. If the value is orange, no value was available and is therefore estimated. Henry's law constants for water as solvent from [70].

Furthermore, some secondary ions could not be unambiguously assigned to a primary ion, creating uncertainties. The primary ions for the corresponding species are given in orange. Lastly, total signal could not be assigned confidently to a handful of species as they showed significant overlap with another species. The total signal strength as well as compensated values are therefore highlighted yellow. As expected, the absolute quantification is not very precise, especially when  $\text{O}_2^+$  and  $\text{H}_3\text{O}^+$  values differ a lot and for liquid products. Comparison of gaseous products at least seems to be correct in orders of magnitude.

**Table 39: Total signal strength for each product and compensation for VLE as well as RRC.**

name	product	$n_e$	$H^{FP}$ [ $\frac{\text{mol}}{\text{m}^3 \cdot \text{Pa}}$ ]	type	$k_e$	Primary Ion [ $\frac{10^{-9} \text{ cm}^3}{\text{s}}$ ]	purity	sum of raw integrated signals $\sum_i J_{f_3}(\text{U}_{\text{HighIGO}})$							corrected and compensated signals $c_{r_i}(\text{U}_{\text{HighIGO}})$							
								2000 mV	2500 mV	3000 mV	3500 mV	4000 mV	4500 mV	5000 mV	2000 mV	2500 mV	3000 mV	3500 mV	4000 mV	4500 mV	5000 mV	
carbon monoxide		2	$9.70 \times 10^{-6}$	$\text{H}_3\text{O}^+$	0.001	97.56%	$2.5 \times 10^2$	$3.2 \times 10^2$	$2.2 \times 10^2$	$1.8 \times 10^2$	$1.8 \times 10^2$	0.0	0.0	$2.7 \times 10^6$	$1.6 \times 10^6$	$8.4 \times 10^5$	$4.8 \times 10^5$	$4.0 \times 10^5$	0.0	0.0	5000 mV	
methane		8	$1.40 \times 10^{-5}$	$\text{O}_2^+$	0.005	1.95%	0.0	0.0	$2.5 \times 10^3$	$5.6 \times 10^3$	$1.1 \times 10^4$	$1.1 \times 10^4$	$1.2 \times 10^4$	0.0	0.0	$3.7 \times 10^8$	$6.1 \times 10^8$	$1.7 \times 10^8$	$1.0 \times 10^8$	$1.0 \times 10^8$	$8.7 \times 10^8$	$6.2 \times 10^8$
ethylene		12	$5.90 \times 10^{-5}$	$\text{H}_3\text{O}^+$	0.063	97.56%	$2.5 \times 10^3$	$1.3 \times 10^6$	$1.7 \times 10^6$	$1.9 \times 10^6$	$7.3 \times 10^5$	$4.1 \times 10^5$	$6.2 \times 10^5$	$2.6 \times 10^8$	$6.1 \times 10^8$	$6.0 \times 10^8$	$4.9 \times 10^8$	$1.6 \times 10^8$	$1.6 \times 10^8$	$7.6 \times 10^7$	$7.3 \times 10^7$	$3.2 \times 10^6$
formaldehyde		4	$3.20 \times 10^{-1}$	$\text{H}_3\text{O}^+$	3.4	97.56%	$2.1 \times 10^4$	$2.0 \times 10^4$	$2.6 \times 10^4$	$3.1 \times 10^4$	$3.5 \times 10^4$	$3.3 \times 10^4$	$3.9 \times 10^4$	$4.3 \times 10^6$	$1.9 \times 10^6$	$1.9 \times 10^6$	$1.6 \times 10^6$	$1.5 \times 10^6$	$1.5 \times 10^6$	$1.2 \times 10^6$	$9.2 \times 10^5$	$9.2 \times 10^5$
methanol		6	2.20	$\text{H}_3\text{O}^+$	2.7	97.56%	$3.7 \times 10^3$	$3.5 \times 10^3$	$4.0 \times 10^3$	$4.2 \times 10^3$	$4.4 \times 10^3$	$4.7 \times 10^3$	$4.6 \times 10^3$	$9.8 \times 10^4$	$4.2 \times 10^4$	$3.7 \times 10^4$	$2.6 \times 10^4$	$2.3 \times 10^4$	$2.1 \times 10^4$	$2.1 \times 10^4$	$1.4 \times 10^4$	$1.4 \times 10^4$
propylene		18	$4.70 \times 10^{-5}$	$\text{H}_3\text{O}^+$	1.3	97.56%	$5.5 \times 10^5$	$1.8 \times 10^6$	$1.7 \times 10^6$	$4.3 \times 10^5$	$2.6 \times 10^5$	$3.1 \times 10^5$	$3.1 \times 10^5$	$4.2 \times 10^7$	$6.3 \times 10^7$	$4.5 \times 10^7$	$3.1 \times 10^7$	$6.8 \times 10^6$	$3.5 \times 10^6$	$3.5 \times 10^6$	$2.6 \times 10^6$	$2.6 \times 10^6$
acetaldehyde		10	$1.30 \times 10^{-1}$	$\text{H}_3\text{O}^+$	3.7	97.56%	$6.0 \times 10^5$	$2.2 \times 10^6$	$2.1 \times 10^6$	$2.0 \times 10^6$	$2.2 \times 10^6$	$2.0 \times 10^6$	$2.0 \times 10^6$	$8.7 \times 10^6$	$1.5 \times 10^7$	$1.1 \times 10^7$	$7.5 \times 10^6$	$6.2 \times 10^6$	$5.7 \times 10^6$	$5.7 \times 10^6$	$3.4 \times 10^6$	$3.4 \times 10^6$
ethanol		12	1.90	$\text{H}_3\text{O}^+$	2.7	97.56%	$1.9 \times 10^5$	$2.3 \times 10^5$	$4.4 \times 10^5$	$7.8 \times 10^5$	$1.4 \times 10^6$	$1.6 \times 10^6$	$1.6 \times 10^6$	$8.9 \times 10^6$	$4.8 \times 10^6$	$7.0 \times 10^6$	$8.9 \times 10^6$	$8.9 \times 10^6$	$1.3 \times 10^7$	$1.3 \times 10^7$	$8.5 \times 10^6$	$8.5 \times 10^6$
1-butene		24	$3.90 \times 10^{-5}$	$\text{H}_3\text{O}^+$	1.6	97.56%	$3.9 \times 10^3$	$5.2 \times 10^3$	$8.9 \times 10^3$	$1.1 \times 10^4$	$1.3 \times 10^4$	$1.0 \times 10^4$	$1.0 \times 10^4$	$1.1 \times 10^7$	$6.4 \times 10^6$	$8.4 \times 10^6$	$7.5 \times 10^6$	$7.5 \times 10^6$	$6.3 \times 10^6$	$6.3 \times 10^6$	$3.2 \times 10^6$	$3.2 \times 10^6$
butadiene		22	$1.00 \times 10^{-4}$	$\text{H}_3\text{O}^+$	1.6	97.56%	$2.9 \times 10^2$	$1.9 \times 10^3$	$7.4 \times 10^2$	$4.5 \times 10^2$	$9.8 \times 10^1$	$1.4 \times 10^2$	$7.3 \times 10^1$	$5.4 \times 10^4$	$2.1 \times 10^4$	$2.7 \times 10^4$	$3.3 \times 10^4$	$3.2 \times 10^4$	$3.2 \times 10^4$	$5.4 \times 10^4$	$5.1 \times 10^4$	$5.1 \times 10^4$
trans-2-butene		24	$5.00 \times 10^{-5}$	$\text{H}_3\text{O}^+$	1.6	97.56%	$2.0 \times 10^3$	$2.1 \times 10^3$	$1.5 \times 10^3$	$8.4 \times 10^2$	$5.8 \times 10^2$	$4.0 \times 10^2$	$3.9 \times 10^2$	$2.1 \times 10^4$	$6.3 \times 10^4$	$1.9 \times 10^4$	$8.3 \times 10^3$	$1.5 \times 10^3$	$1.9 \times 10^3$	$1.9 \times 10^3$	$6.3 \times 10^2$	$6.3 \times 10^2$
cis-2-butene		24	$5.00 \times 10^{-5}$	$\text{H}_3\text{O}^+$	1.6	97.56%	$5.6 \times 10^2$	$3.1 \times 10^3$	$2.6 \times 10^3$	$1.6 \times 10^3$	$7.4 \times 10^2$	$6.0 \times 10^2$	$9.1 \times 10^2$	$4.5 \times 10^4$	$1.2 \times 10^5$	$7.4 \times 10^4$	$3.3 \times 10^4$	$1.3 \times 10^4$	$8.8 \times 10^3$	$8.8 \times 10^3$	$8.5 \times 10^3$	$8.5 \times 10^3$
cyclopropane		18	$1.10 \times 10^{-4}$	$\text{O}_2^+$	1.3	1.95%	$2.3 \times 10^2$	$5.9 \times 10^2$	$3.1 \times 10^2$	$2.6 \times 10^2$	$3.4 \times 10^2$	$1.3 \times 10^2$	$3.1 \times 10^2$	$8.5 \times 10^5$	$1.0 \times 10^6$	$4.0 \times 10^5$	$2.5 \times 10^5$	$2.7 \times 10^5$	$2.7 \times 10^5$	$8.9 \times 10^4$	$1.3 \times 10^4$	$1.3 \times 10^4$
propanal		16	$9.90 \times 10^{-2}$	$\text{H}_3\text{O}^+$	3.6	97.56%	$5.5 \times 10^5$	$1.7 \times 10^6$	$1.6 \times 10^6$	$1.4 \times 10^6$	$6.3 \times 10^5$	$3.2 \times 10^5$	$1.9 \times 10^5$	$1.3 \times 10^7$	$1.8 \times 10^7$	$1.3 \times 10^7$	$8.1 \times 10^6$	$3.4 \times 10^6$	$1.4 \times 10^6$	$5.3 \times 10^5$	$5.3 \times 10^5$	$5.3 \times 10^5$
acetone		16	$2.70 \times 10^{-1}$	$\text{H}_3\text{O}^+$	3.9	97.56%	$1.8 \times 10^3$	$6.5 \times 10^3$	$1.6 \times 10^3$	$3.2 \times 10^3$	$5.0 \times 10^3$	$4.9 \times 10^3$	$5.2 \times 10^3$	$4.1 \times 10^4$	$6.6 \times 10^3$	$1.3 \times 10^4$	$1.7 \times 10^4$	$2.3 \times 10^4$	$2.3 \times 10^4$	$1.9 \times 10^4$	$1.3 \times 10^4$	$1.3 \times 10^4$
allyl alcohol		16	2.00	$\text{H}_3\text{O}^+$	2	97.56%	$7.9 \times 10^3$	$9.0 \times 10^3$	$1.4 \times 10^4$	$2.4 \times 10^4$	$3.5 \times 10^4$	$3.8 \times 10^4$	$6.9 \times 10^5$	$6.9 \times 10^5$	$3.6 \times 10^5$	$4.4 \times 10^5$	$5.1 \times 10^5$	$6.3 \times 10^5$	$6.3 \times 10^5$	$3.7 \times 10^5$	$3.7 \times 10^5$	
pentene		30	$2.50 \times 10^{-5}$	$\text{H}_3\text{O}^+$	1.9	97.56%	$6.2 \times 10^2$	$4.5 \times 10^2$	$2.0 \times 10^3$	$3.5 \times 10^3$	$3.3 \times 10^3$	$3.4 \times 10^3$	$3.4 \times 10^3$	$5.3 \times 10^4$	$1.8 \times 10^4$	$6.0 \times 10^4$	$7.4 \times 10^4$	$5.9 \times 10^4$	$4.8 \times 10^4$	$4.8 \times 10^4$	$3.3 \times 10^4$	$3.3 \times 10^4$
propanol		18	1.40	$\text{H}_3\text{O}^+$	2.7	97.56%	$9.6 \times 10^4$	$2.1 \times 10^5$	$5.8 \times 10^5$	$8.7 \times 10^5$	$1.0 \times 10^6$	$7.3 \times 10^5$	$4.9 \times 10^6$	$4.9 \times 10^6$	$5.0 \times 10^6$	$1.0 \times 10^7$	$1.1 \times 10^7$	$1.1 \times 10^7$	$7.5 \times 10^6$	$7.5 \times 10^6$	$4.2 \times 10^6$	$4.2 \times 10^6$
butanediol		18	$7.30 \times 10^{-1}$	$\text{H}_3\text{O}^+$	1.7	97.56%	$4.0 \times 10^3$	$7.4 \times 10^3$	$3.4 \times 10^3$	$6.1 \times 10^3$	$9.7 \times 10^3$	$2.6 \times 10^3$	$2.3 \times 10^5$	$2.3 \times 10^5$	$1.9 \times 10^6$	$6.8 \times 10^6$	$8.7 \times 10^6$	$1.2 \times 10^7$	$1.2 \times 10^7$	$1.7 \times 10^6$	$1.7 \times 10^6$	$1.7 \times 10^6$
butanone		22	$2.00 \times 10^{-1}$	$\text{H}_3\text{O}^+$	3.9	97.56%	$8.6 \times 10^3$	$3.1 \times 10^4$	$5.9 \times 10^4$	$9.2 \times 10^4$	$7.6 \times 10^4$	$4.8 \times 10^4$	$2.6 \times 10^4$	$2.6 \times 10^5$	$4.4 \times 10^5$	$6.3 \times 10^5$	$7.0 \times 10^5$	$4.8 \times 10^5$	$4.8 \times 10^5$	$2.6 \times 10^5$	$8.9 \times 10^4$	$8.9 \times 10^4$
butanal		22	$9.50 \times 10^{-2}$	$\text{H}_3\text{O}^+$	3.8	97.56%	$7.9 \times 10^2$	$4.2 \times 10^3$	$2.5 \times 10^3$	$1.6 \times 10^3$	$7.8 \times 10^2$	$5.9 \times 10^2$	$5.9 \times 10^2$	$2.5 \times 10^4$	$6.0 \times 10^4$	$4.6 \times 10^4$	$1.9 \times 10^4$	$1.9 \times 10^4$	$1.0 \times 10^4$	$4.4 \times 10^3$	$2.1 \times 10^3$	$2.1 \times 10^3$
ethyl acetate		20	$5.90 \times 10^{-2}$	$\text{H}_3\text{O}^+$	2.9	97.56%	$4.6 \times 10^3$	$1.0 \times 10^4$	$3.2 \times 10^4$	$6.9 \times 10^4$	$8.7 \times 10^4$	$3.2 \times 10^4$	$3.2 \times 10^4$	$1.7 \times 10^5$	$1.7 \times 10^5$	$4.2 \times 10^5$	$6.4 \times 10^5$	$6.7 \times 10^5$	$3.8 \times 10^5$	$3.8 \times 10^5$	$1.4 \times 10^5$	$1.4 \times 10^5$
2,3-pentanedione		30	$3.77 \times 10^1$	$\text{H}_3\text{O}^+$	1.88	97.56%	$3.7 \times 10^3$	$9.0 \times 10^3$	$5.1 \times 10^3$	$3.0 \times 10^3$	$2.4 \times 10^3$	0.0	0.0	$1.2 \times 10^7$	$1.3 \times 10^7$	$5.8 \times 10^6$	$2.4 \times 10^6$	$1.7 \times 10^6$	0.0	0.0	0.0	0.0
2,4-pentanedione		30	4.30	$\text{H}_3\text{O}^+$	1.88	97.56%	$1.0 \times 10^4$	$6.5 \times 10^4$	$9.8 \times 10^4$	$8.8 \times 10^4$	$3.0 \times 10^4$	$1.4 \times 10^4$	$8.0 \times 10^3$	$3.8 \times 10^6$	$1.1 \times 10^7$	$1.3 \times 10^7$	$8.1 \times 10^6$	$2.3 \times 10^6$	$2.3 \times 10^6$	$9.5 \times 10^5$	$3.4 \times 10^5$	$3.4 \times 10^5$

## H Kinetic Isotope Effect

### H.1 Calculation of shift

Usually the shift is calculated as follows:

$$\delta^{13}\text{C}(\text{‰}) = \left[ \frac{\left(\frac{^{13}\text{C}}{^{12}\text{C}}\right)_{\text{sample}}}{\left(\frac{^{13}\text{C}}{^{12}\text{C}}\right)_{\text{CO}_2}} \right] \times 1000 \text{ where } \left(\frac{^{13}\text{C}}{^{12}\text{C}}\right)_{\text{sample}} = \frac{I(^{13}\text{C})_{\text{species}}}{I(^{12}\text{C})_{\text{species}} \times n(\text{C})_{\text{species}}} \quad (\text{H.1})$$

This yields the more fundamental version of

$$\delta^{13}\text{C}(\text{‰}) = \left[ \frac{\frac{I(^{13}\text{C})_{\text{sample}}}{I(^{12}\text{C})_{\text{sample}} \times n(\text{C})_{\text{sample}}}}{\frac{I(^{13}\text{C})_{\text{CO}_2}}{I(^{12}\text{C})_{\text{CO}_2} \times n(\text{C})_{\text{CO}_2}}} - 1 \right] \times 1000 \quad (\text{H.2})$$

We can see that this is only a specific case of the more widely applicable

$$\delta^{13}\text{C}(\text{‰}) = \left[ \frac{\frac{I(^{13}\text{C}_x \text{ } ^{12}\text{C}_{n-x})_{\text{sample}}}{I(^{12}\text{C}_n)_{\text{sample}}}}{\frac{I(^{13}\text{CO}_2)}{I(^{12}\text{CO}_2)} \times \binom{n}{x}} - 1 \right] \times 1000 \quad \text{with} \quad n = n(\text{C})_{\text{species}} \quad (\text{H.3})$$

The commonly used version in Eq. H.1 is therefore only a more specific version of Eq. H.3  $x = 1$  which makes sense since most of the time only the single-isotope version is found. For larger hydrocarbon chains multi-isotope versions become more probable though and can be used to verify the  $^{13}\text{C}$  shift and distinguish traces.

For an intermediate or product ( $\text{H}_x\text{C}_y\text{O}_z^+$  at a given  $m/z$ ), its isotope peak ( $m/z + 1.003$ ) not only contains  $^1\text{H}_x \text{ } ^{12}\text{C}_{y-1} \text{ } ^{16}\text{O}_z \text{ } ^{13}\text{C}^+$  but also other isotopologues, such as  $^1\text{H}_{x-1} \text{ } ^{12}\text{C}_y \text{ } ^{16}\text{O}_z \text{ } ^2\text{H}^+$  and  $^1\text{H}_x \text{ } ^{12}\text{C}_y \text{ } ^{16}\text{O}_{z-1} \text{ } ^{18}\text{O}^+$ , due to the isotopic natural abundance in reactants. Therefore, a small correction for this effect is necessary and is performed in the present work using IsoCor v2 (implemented in Python 3) [71].

Choice of ion can skew the calculated shift if we choose a fragment or cluster where a carbon was added or removed from the original secondary ion. This can happen for two reasons:

1. Increased selectivity towards  $^{12}\text{C}$  over  $^{13}\text{C}$  in CO2R specific to asymmetrical steps. This means that the carbon atoms have different probabilities to be one isotope or the other. For this reason, after dissociation of a carbon-containing species (which is specific to the carbon depending on its structure), the  $\delta^{13}\text{C}$  will be different than before.
2. The fragmentation or clustering reaction in the drift tube itself discriminates between carbon isotopes.

## H.2 Individual species

Recently, the tracking of  $^{13}\text{C}$  isotopes of protonated analyte has been suggested as a means for CO<sub>2</sub>R product analysis. [34] Analogous to other carbon-conversion processes, a kinetic isotope effect can be observed as the ratio of  $^{13}\text{C}$  isotopes drops below levels of natural abundance due to increased selectivity for  $^{12}\text{C}$  isotopes as reactant. Wherever possible, we calculated  $\delta^{13}\text{C}$  as a measure for this shift of isotope ratios.

For most of the products detected this was not possible with sufficient accuracy as the system was designed rather for species identification than very accurate signal quantification. Especially the low dilution level leads to such high concentrations for the most abundant species that effects described in section E.2 take effect and skew results. On the other hand, most less-abundant species are still observed at concentrations too small for accurate determination of the effect as  $^{13}\text{C}$  isotope traces are observed only with very small signal-to-noise ratios. The only products for which the Kinetic Isotope Effect could be calculated and discussed with sufficient confidence are the C<sub>3</sub> species propylene, propanol, and propanal shown in Fig. 75.

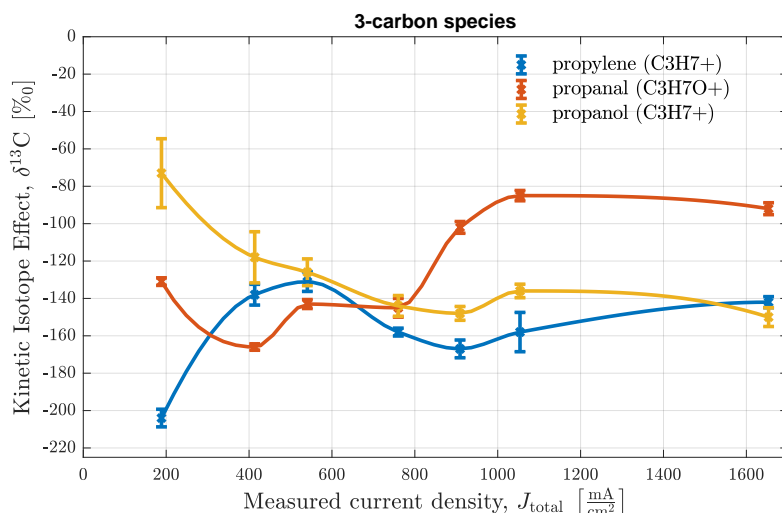


**Figure 75:** Kinetic Isotope Effect of selected traces representing C<sub>3</sub> products across the range of applied potential.

The initial value at  $J \approx 200 \text{ A cm}^{-2}$  for propanal is similar to the benchmark [34] as is the trend towards bigger shifts with larger currents - including the indicated inflection point towards slightly smaller shifts again around  $J \approx 500 \text{ A cm}^{-2}$ . For propanol and propylene, initial values deviate a lot from the benchmark but their average is close to the reported value (as the two are not distinguished in [34]). The trend of propanol for bigger shifts with larger currents corresponds to the initial trend reported and the trend of propylene towards smaller shifts corresponds to the later trend around  $J > 400 \text{ A cm}^{-2}$ . A noteworthy observation is that the alcohol shows a smaller shift towards  $^{12}\text{C}$  than the alkene for smaller currents, but this gets inverted at a medium current density due to increasing shift for the alcohol and decreasing shift for the alkene.

## References

- [1] Samantha Eleanor Tanzer and Andrea Ramírez. When are negative emissions negative emissions? *Energy and Environmental Science*, 12(4):1210–1218, 2019. ISSN 17545706. doi:10.1039/c8ee03338b.
- [2] Kendra P. Kuhl, Etosha R. Cave, David N. Abram, and Thomas F. Jaramillo. New insights into the electrochemical reduction of carbon dioxide on metallic copper surfaces. *Energy and Environmental Science*, 5(5):7050–7059, 2012. ISSN 17545692. doi:10.1039/c2ee21234j.
- [3] Stephanie Nitopi, Erlend Bertheussen, Soren B. Scott, Xinyan Liu, Albert K. Engstfeld, Sebastian Horch, Brian Seger, Ifan E.L. Stephens, Karen Chan, Christopher Hahn, Jens K. Nørskov, Thomas F. Jaramillo, and Ib Chorkendorff. Progress and Perspectives of Electrochemical CO<sub>2</sub> Reduction on Copper in Aqueous Electrolyte. *Chemical Reviews*, 119(12):7610–7672, 2019. ISSN 15206890. doi:10.1021/acs.chemrev.8b00705.
- [4] Alejandro J. Garza, Alexis T. Bell, and Martin Head-Gordon. Mechanism of CO<sub>2</sub> Reduction at Copper Surfaces: Pathways to C<sub>2</sub> Products. *ACS Catalysis*, 8(2):1490–1499, 2018. ISSN 21555435. doi:10.1021/acscatal.7b03477.
- [5] Youngkook Kwon, Yanwei Lum, Ezra L. Clark, Joel W. Ager, and Alexis T. Bell. CO<sub>2</sub> Electroreduction with Enhanced Ethylene and Ethanol Selectivity by Nanostructuring Polycrystalline Copper. *ChemElectroChem*, 3(6):1012–1019, 2016. ISSN 21960216. doi:10.1002/celec.201600068.
- [6] Recep Kas, Ruud Kortlever, Hasan Yilmaz, Marc T.M. Koper, and Guido Mul. Manipulating the Hydrocarbon Selectivity of Copper Nanoparticles in CO<sub>2</sub> Electroreduction by Process Conditions. *ChemElectroChem*, 2(3):354–358, 2015. ISSN 21960216. doi:10.1002/celec.201402373.
- [7] Klaas Jan P. Schouten, Zisheng Qin, Elena Pérez Gallent, and Marc T.M. Koper. Two pathways for the formation of ethylene in CO reduction on single-crystal copper electrodes. *Journal of the American Chemical Society*, 134(24):9864–9867, 2012. ISSN 00027863. doi:10.1021/ja302668n.
- [8] F. Pelayo García de Arquer, Cao Thang Dinh, Adnan Ozden, Joshua Wicks, Christopher McCallum, Ahmad R. Kirmani, Dae Hyun Nam, Christine Gabardo, Ali Seifitokaldani, Xue Wang, Yuguang C. Li, Fengwang Li, Jonathan Edwards, Lee J. Richter, Steven J. Thorpe, David Sinton, and Edward H. Sargent. CO<sub>2</sub> electrolysis to multicarbon products at activities greater than 1 A cm<sup>-2</sup>. *Science*, 367(6478):661–666, 2020. ISSN 10959203. doi:10.1126/science.aay4217.
- [9] Cao Thang Dinh, Thomas Burdyny, Golam Kibria, Ali Seifitokaldani, Christine M. Gabardo, F. Pelayo García De Arquer, Amirreza Kiani, Jonathan P. Edwards, Phil De Luna, Oleksandr S. Bushuyev, Chengqin Zou, Rafael Quintero-Bermudez, Yuanjie Pang, David Sinton, and Edward H. Sargent. CO<sub>2</sub> electroreduction to ethylene via hydroxide-mediated copper catalysis at an abrupt interface. *Science*, 360(6390):783–787, 2018. ISSN 10959203. doi:10.1126/science.aas9100.

- [10] Gastón O. Larrazábal, Valery Okatenko, Ib Chorkendorff, Raffaella Buonsanti, and Brian Seger. Investigation of Ethylene and Propylene Production from CO<sub>2</sub> Reduction over Copper Nanocubes in an MEA-Type Electrolyzer. *ACS Applied Materials and Interfaces*, 14(6):7779–7787, 2022. ISSN 19448252. doi:10.1021/acsami.1c18856.
- [11] Zhuang Zhuang Niu, Li Ping Chi, Ren Liu, Zhi Chen, and Min Rui Gao. Rigorous assessment of CO<sub>2</sub> electroreduction products in a flow cell. *Energy and Environmental Science*, 14(8):4169–4176, 2021. ISSN 17545706. doi:10.1039/d1ee01664d.
- [12] Magda H. Barecka, Joel W. Ager, and Alexei A. Lapkin. Economically viable CO<sub>2</sub> electroreduction embedded within ethylene oxide manufacturing. *Energy and Environmental Science*, 14(3):1530–1543, 2021. ISSN 17545706. doi:10.1039/d0ee03310c.
- [13] Xinyan Liu, Jianping Xiao, Hongjie Peng, Xin Hong, Karen Chan, and Jens K. Nørskov. Understanding trends in electrochemical carbon dioxide reduction rates. *Nature Communications*, 8(May):1–7, 2017. ISSN 20411723. doi:10.1038/ncomms15438.
- [14] Xiaowa Nie, Wenjia Luo, Michael J. Janik, and Aravind Asthagiri. Reaction mechanisms of CO<sub>2</sub> electrochemical reduction on Cu(1 1 1) determined with density functional theory. *Journal of Catalysis*, 312:108–122, 2014. ISSN 00219517. doi:10.1016/j.jcat.2014.01.013.
- [15] Ruud Kortlever, Jing Shen, Klaas Jan P. Schouten, Federico Calle-Vallejo, and Marc T.M. Koper. Catalysts and Reaction Pathways for the Electrochemical Reduction of Carbon Dioxide. *Journal of Physical Chemistry Letters*, 6(20):4073–4082, 2015. ISSN 19487185. doi:10.1021/acs.jpcclett.5b01559.
- [16] Xinyan Liu, Philomena Schlexer, Jianping Xiao, Yongfei Ji, Lei Wang, Robert B. Sandberg, Michael Tang, Kristopher S. Brown, Hongjie Peng, Stefan Ringe, Christopher Hahn, Thomas F. Jaramillo, Jens K. Nørskov, and Karen Chan. pH effects on the electrochemical reduction of CO<sub>2</sub> towards C<sub>2</sub> products on stepped copper. *Nature Communications*, 10(1):1–10, 2019. ISSN 20411723. doi:10.1038/s41467-018-07970-9.
- [17] Jason D. Goodpaster, Alexis T. Bell, and Martin Head-Gordon. Identification of Possible Pathways for C-C Bond Formation during Electrochemical Reduction of CO<sub>2</sub>: New Theoretical Insights from an Improved Electrochemical Model. *Journal of Physical Chemistry Letters*, 7(8):1471–1477, 2016. ISSN 19487185. doi:10.1021/acs.jpcclett.6b00358.
- [18] Wenjia Luo, Xiaowa Nie, Michael J. Janik, and Aravind Asthagiri. Facet Dependence of CO<sub>2</sub> Reduction Paths on Cu Electrodes. *ACS Catalysis*, 6(1):219–229, 2016. ISSN 21555435. doi:10.1021/acscatal.5b01967.
- [19] Anna Wuttig, Can Liu, Qiling Peng, Momo Yaguchi, Christopher H. Hendon, Kenta Motobayashi, Shen Ye, Masatoshi Osawa, and Yogesh Surendranath. Tracking a

- common surface-bound intermediate during CO<sub>2</sub>-to- fuels catalysis. *ACS Central Science*, 2(8):522–528, 2016. ISSN 23747951. doi:10.1021/acscentsci.6b00155.
- [20] Elena Pérez-Gallent, Marta C. Figueiredo, Federico Calle-Vallejo, and Marc T.M. Koper. Spectroscopic Observation of a Hydrogenated CO Dimer Intermediate During CO Reduction on Cu(100) Electrodes. *Angewandte Chemie - International Edition*, 56(13):3621–3624, 2017. ISSN 15213773. doi:10.1002/anie.201700580.
- [21] Klaas Jan P. Schouten, Youngkook Kwon, C. J.M. Van Der Ham, Z. Qin, and Marc T.M. Koper. A new mechanism for the selectivity to C1 and C2 species in the electrochemical reduction of carbon dioxide on copper electrodes. *Chemical Science*, 2(10):1902–1909, 2011. ISSN 20416520. doi:10.1039/c1sc00277e.
- [22] Tao Cheng, Hai Xiao, and William A. Goddard. Full atomistic reaction mechanism with kinetics for CO reduction on Cu(100) from ab initio molecular dynamics free-energy calculations at 298 K. *Proceedings of the National Academy of Sciences of the United States of America*, 114(8):1795–1800, 2017. ISSN 10916490. doi:10.1073/pnas.1612106114.
- [23] Aamir Hassan Shah, Yanjie Wang, Abebe Reda Woldu, Lin Lin, Muzaffar Iqbal, David Cahen, and Tao He. Revisiting Electrochemical Reduction of CO<sub>2</sub> on Cu Electrode: Where Do We Stand about the Intermediates? *Journal of Physical Chemistry C*, 122(32):18528–18536, 2018. ISSN 19327455. doi:10.1021/acs.jpcc.8b05348.
- [24] Erlend Bertheussen, Arnau Verdaguer-Casadevall, Davide Ravasio, Joseph H. Montoya, Daniel B. Trimarco, Claudie Roy, Sebastian Meier, Jürgen Wendland, Jens K. Nørskov, Ifan E.L. Stephens, and I. Chorkendorff. Acetaldehyde as an Intermediate in the Electroreduction of Carbon Monoxide to Ethanol on Oxide-Derived Copper. *Angewandte Chemie - International Edition*, 55(4):1450–1454, 2016. ISSN 15213773. doi:10.1002/anie.201508851.
- [25] Yoshio Hori, Ryutaro Takahashi, Yuzuru Yoshinami, and Akira Murata. Electrochemical reduction of CO at a copper electrode. *Journal of Physical Chemistry B*, 101(36):7075–7081, 1997. ISSN 15206106. doi:10.1021/jp970284i.
- [26] Mikhail K. Kovalev, Hangjuan Ren, Marsha Zakir Muhamad, Joel W. Ager, and Alexei A. Lapkin. Minor Product Polymerization Causes Failure of High-Current CO<sub>2</sub>-to-Ethylene Electrolyzers. *ACS Energy Letters*, 7(2):599–601, 2022. ISSN 23808195. doi:10.1021/acsenergylett.1c02450.
- [27] Simon D. Rihm, Jethro Akroyd, and Markus Kraft. Modelling a detailed kinetic mechanism for electrocatalytic reduction of CO<sub>2</sub>. *Proceedings of the Combustion Institute*, 000:1–9, 2022. ISSN 15407489. doi:10.1016/j.proci.2022.07.096.
- [28] Zhijiang Wang, Lina Wu, Kun Sun, Ting Chen, Zhaohua Jiang, Tao Cheng, and William A. Goddard. Surface Ligand Promotion of Carbon Dioxide Reduction through Stabilizing Chemisorbed Reactive Intermediates. *Journal of Physical Chemistry Letters*, 9(11):3057–3061, 2018. ISSN 19487185. doi:10.1021/acs.jpcllett.8b00959.

- [29] Jan Philipp Grote, Aleksandar R. Zeradjanin, Serhiy Cherevko, and Karl J.J. Mayrhofer. Coupling of a scanning flow cell with online electrochemical mass spectrometry for screening of reaction selectivity. *Review of Scientific Instruments*, 85 (10), 2014. ISSN 10897623. doi:10.1063/1.4896755.
- [30] Ezra L. Clark, Meenesh R. Singh, Youngkook Kwon, and Alexis T. Bell. Differential Electrochemical Mass Spectrometer Cell Design for Online Quantification of Products Produced during Electrochemical Reduction of CO<sub>2</sub>. *Analytical Chemistry*, 87 (15):8013–8020, 2015. ISSN 15206882. doi:10.1021/acs.analchem.5b02080.
- [31] Thomas De Vijlder, Dirk Valkenburg, Filip Lemière, Edwin P. Romijn, Kris Laukens, and Filip Cuyckens. A tutorial in small molecule identification via electrospray ionization-mass spectrometry: The practical art of structural elucidation. *Mass Spectrometry Reviews*, 37(5):607–629, 2018. ISSN 10982787. doi:10.1002/mas.21551.
- [32] Mario Löffler, Karl J.J. Mayrhofer, and Ioannis Katsounaros. Oxide Reduction Precedes Carbon Dioxide Reduction on Oxide-Derived Copper Electrodes. *Journal of Physical Chemistry C*, 2021. ISSN 19327455. doi:10.1021/acs.jpcc.0c09107.
- [33] Mario Löffler, Peyman Khanipour, Nadiia Kulyk, Karl J.J. Mayrhofer, and Ioannis Katsounaros. Insights into Liquid Product Formation during Carbon Dioxide Reduction on Copper and Oxide-Derived Copper from Quantitative Real-Time Measurements. *ACS Catalysis*, 10(12):6735–6740, 2020. ISSN 21555435. doi:10.1021/acscatal.0c01388.
- [34] Hangjuan Ren, Mikhail K. Kovalev, Zhaoyue Weng, Marsha Zakir Muhamad, Yuan Sheng, Libo Sun, Jingjing Wang, Simon D. Rihm, Hongyang Ma, Wanfeng Yang, Alexei A. Lapkin, and Joel W. Ager. Operando Proton Transfer Reaction-Time of Flight-Mass Spectrometry of Carbon Dioxide Reduction Electrocatalysis. Accepted for publication., 2022.
- [35] Thomas Burdyny and Wilson A. Smith. CO<sub>2</sub> reduction on gas-diffusion electrodes and why catalytic performance must be assessed at commercially-relevant conditions. *Energy and Environmental Science*, 12(5):1442–1453, 2019. ISSN 17545706. doi:10.1039/c8ee03134g.
- [36] David Smith and Patrik Španěl. Direct, rapid quantitative analyses of BVOCs using SIFT-MS and PTR-MS obviating sample collection. *TrAC - Trends in Analytical Chemistry*, 30(7):945–959, 2011. ISSN 01659936. doi:10.1016/j.trac.2011.05.001.
- [37] A. Jordan, S. Haidacher, G. Hanel, E. Hartungen, J. Herbig, L. Märk, R. Schotzkowsky, H. Seehauser, P. Sulzer, and T. D. Märk. An online ultra-high sensitivity Proton-transfer-reaction mass-spectrometer combined with switchable reagent ion capability (PTR + SRI - MS). *International Journal of Mass Spectrometry*, 286(1): 32–38, 2009. ISSN 13873806. doi:10.1016/j.ijms.2009.06.006.
- [38] Etienne Sémon, Gaëlle Arvisenet, Elisabeth Guichard, and Jean Luc Le Quéré. Modified proton transfer reaction mass spectrometry (PTR-MS) operating conditions for

in vitro and in vivo analysis of wine aroma. *Journal of Mass Spectrometry*, 53(1): 65–77, 2018. ISSN 10969888. doi:10.1002/jms.4036.

- [39] Yoshio Hori, Ichiro Takahashi, O. Koga, and Nagahiro Hoshi. Electrochemical reduction of carbon dioxide at various series of copper single crystal electrodes. *Journal of Molecular Catalysis A: Chemical*, 199(1-2):39–47, 2003. ISSN 13811169. doi:10.1016/S1381-1169(03)00016-5.
- [40] Lily Mandal, Ke R. Yang, Mallikarjuna Rao Motapothula, Dan Ren, Peter Lobaccaro, Abhijeet Patra, Matthew Sherburne, Victor S. Batista, Boon Siang Yeo, Joel W. Ager, Jens Martin, and T. Venkatesan. Investigating the Role of Copper Oxide in Electrochemical CO<sub>2</sub> Reduction in Real Time. *ACS Applied Materials and Interfaces*, 10(10):8574–8584, 2018. ISSN 19448252. doi:10.1021/acsami.7b15418.
- [41] Karin U.D. Calvino, Anders B. Laursen, Kyra M.K. Yap, Timothy A. Goetjen, Shinjae Hwang, Nagarajan Murali, Bryan Mejia-Sosa, Alexander Lubarski, Krishani M. Teeluck, Eugene S. Hall, Eric Garfunkel, Martha Greenblatt, and G. Charles Dismukes. Selective CO<sub>2</sub> reduction to C<sub>3</sub> and C<sub>4</sub> oxyhydrocarbons on nickel phosphides at overpotentials as low as 10 mV. *Energy and Environmental Science*, 11(9):2550–2559, 2018. ISSN 17545706. doi:10.1039/c8ee00936h.
- [42] Hai Xiao, Tao Cheng, William A. Goddard, and Ravishankar Sundararaman. Mechanistic Explanation of the pH Dependence and Onset Potentials for Hydrocarbon Products from Electrochemical Reduction of CO on Cu (111). *Journal of the American Chemical Society*, 138(2):483–486, 2016. ISSN 15205126. doi:10.1021/jacs.5b11390.
- [43] Yanwei Lum, Tao Cheng, William A. Goddard, and Joel W. Ager. Electrochemical CO Reduction Builds Solvent Water into Oxygenate Products. *Journal of the American Chemical Society*, 140(30):9337–9340, 2018. ISSN 15205126. doi:10.1021/jacs.8b03986.
- [44] Andrew A. Peterson, Frank Abild-Pedersen, Felix Studt, Jan Rossmeisl, and Jens K. Nørskov. How copper catalyzes the electroreduction of carbon dioxide into hydrocarbon fuels. *Energy and Environmental Science*, 3(9):1311–1315, 2010. ISSN 17545692. doi:10.1039/c0ee00071j.
- [45] Federico Calle-Vallejo and Marc T.M. Koper. Theoretical considerations on the electroreduction of CO to C<sub>2</sub> Species on Cu(100) electrodes. *Angewandte Chemie - International Edition*, 52(28):7282–7285, 2013. ISSN 14337851. doi:10.1002/anie.201301470.
- [46] Xiaowa Nie, Monica R. Esopi, Michael J. Janik, and Aravind Asthagiri. Selectivity of CO<sub>2</sub> Reduction on Copper Electrodes: The Role of the Kinetics of Elementary Steps. *Angewandte Chemie*, 125(9):2519–2522, 2013. ISSN 1521-3757. doi:10.1002/ange.201208320.

- [47] Yuvraj Y. Birdja, Elena Pérez-Gallent, Marta C. Figueiredo, Adrien J. Göttle, Federico Calle-Vallejo, and Marc T.M. Koper. Advances and challenges in understanding the electrocatalytic conversion of carbon dioxide to fuels. *Nature Energy*, 4(9): 732–745, 2019. ISSN 20587546. doi:10.1038/s41560-019-0450-y.
- [48] William J. Durand, Andrew A. Peterson, Felix Studt, Frank Abild-Pedersen, and Jens K. Nørskov. Structure effects on the energetics of the electrochemical reduction of CO<sub>2</sub> by copper surfaces. *Surface Science*, 605(15-16):1354–1359, 2011. ISSN 00396028. doi:10.1016/j.susc.2011.04.028.
- [49] Xue Wang, Ziyun Wang, Tao Tao Zhuang, Cao Thang Dinh, Jun Li, Dae Hyun Nam, Fengwang Li, Chun Wei Huang, Chih Shan Tan, Zitao Chen, Miaofang Chi, Christine M. Gabardo, Ali Seifitokaldani, Petar Todorović, Andrew Proppe, Yuanjie Pang, Ahmad R. Kirmani, Yuhang Wang, Alexander H. Ip, Lee J. Richter, Benjamin Scheffel, Aoni Xu, Shen Chuan Lo, Shana O. Kelley, David Sinton, and Edward H. Sargent. Efficient upgrading of CO to C<sub>3</sub> fuel using asymmetric C-C coupling active sites. *Nature Communications*, 10(1):1–7, 2019. ISSN 20411723. doi:10.1038/s41467-019-13190-6.
- [50] Valco Instruments Company Inc. Retention Index Comparison Table - Hayesep D Order, . URL <https://www.vici.com/columns/r-index-d.php>.
- [51] Valco Instruments Company Inc. Relative Retention Times - HayeSep Porous Polymers, . URL <https://www.vici.com/hayesep/reftimes.php>.
- [52] Valco Instruments Company Inc. Trace unsaturates C<sub>2</sub> - C<sub>6</sub> - HayeSep D, 100/120 mesh, . URL <https://www.vici.com/hayesep/hsd{ }c11.php>.
- [53] Valco Instruments Company Inc. Test Gas Mixture - ValcoPLOT HayeSep D Column, . URL <https://www.vici.com/columns/d-mix.php>.
- [54] PTR-MS Viewer, 2018.
- [55] Adam J. Fleisher, Hongming Yi, Abneesh Srivastava, Oleg L. Polyansky, Nikolai F. Zobov, and Joseph T. Hodges. Absolute <sup>13</sup>C/<sup>12</sup>C isotope amount ratio for Vienna PeeDee Belemnite from infrared absorption spectroscopy. *Nature Physics*, 17(8): 889–893, 2021. ISSN 17452481. doi:10.1038/s41567-021-01226-y.
- [56] Patrik Španěl, Yufeng Ji, and David Smith. SIFT studies of the reactions of H<sub>3</sub>O<sup>+</sup>, NO<sup>+</sup> and O<sub>2</sub><sup>+</sup> with a series of aldehydes and ketones. *International Journal of Mass Spectrometry and Ion Processes*, 165-166:25–37, 1997. ISSN 01681176. doi:10.1016/s0168-1176(97)00166-3.
- [57] Paul F. Wilson, Colin G. Freeman, and Murray J. McEwan. Reactions of small hydrocarbons with H<sub>3</sub>O<sup>+</sup>, O<sub>2</sub><sup>+</sup> and NO<sup>+</sup> ions. *International Journal of Mass Spectrometry*, 229(3):143–149, 2003. ISSN 13873806. doi:10.1016/S1387-3806(03)00290-2.

- [58] Patrik Španěl, David Smith, and Jiří Hněvovský. Mass Spectrometry SIFT studies of the reactions of H<sub>3</sub>O<sup>+</sup>, NO<sup>+</sup> and O<sub>2</sub><sup>+</sup> with several ethers. *International Journal of Mass Spectrometry and Ion Processes*, 172:247, 1998. doi:10.1016/S0168-1176(97)00277-2.
- [59] Patrik Španěl and David Smith. SIFT studies of the reactions of H<sub>3</sub>O<sup>+</sup>, NO<sup>+</sup> and O<sub>2</sub><sup>+</sup> with a series of alcohols. *International Journal of Mass Spectrometry and Ion Processes*, 167-168:375–388, 1997. ISSN 01681176. doi:10.1016/s0168-1176(97)00085-2.
- [60] Patrik Španěl and David Smith. Selected ion flow tube studies of the reactions of H<sub>3</sub>O<sup>+</sup>, NO<sup>+</sup>, and O<sub>2</sub><sup>+</sup> with several aromatic and aliphatic monosubstituted halocarbons. *International Journal of Mass Spectrometry*, 189(2-3):213–223, 1999. ISSN 13873806. doi:10.1016/s1387-3806(99)00103-7.
- [61] M. Baasandorj, D. B. Millet, L. Hu, D. Mitroo, and B. J. Williams. Measuring acetic and formic acid by proton-transfer-reaction mass spectrometry: Sensitivity, humidity dependence, and quantifying interferences. *Atmospheric Measurement Techniques*, 8(3):1303–1321, 2015. ISSN 18678548. doi:10.5194/amt-8-1303-2015.
- [62] David Smith, Patrik Španěl, and Kseniya Dryahina. H<sub>3</sub>O<sup>+</sup>, NO<sup>+</sup> and O<sub>2</sub><sup>+</sup>[rad] reactions with saturated and unsaturated monoketones and diones; focus on hydration of product ions. *International Journal of Mass Spectrometry*, 435:173–180, 2019. ISSN 13873806. doi:10.1016/j.ijms.2018.10.027.
- [63] Patrik Španěl, Jane M. Van Doren, and David Smith. A selected ion flow tube study of the reactions of H<sub>3</sub>O<sup>+</sup>, NO<sup>+</sup>, and O<sub>2</sub><sup>+</sup> with saturated and unsaturated aldehydes and subsequent hydration of the product ions. *International Journal of Mass Spectrometry*, 213(2-3):163–176, 2002. ISSN 13873806. doi:10.1016/S1387-3806(01)00531-0.
- [64] Patrik Španěl and David Smith. SIFT studies of the reactions of H<sub>3</sub>O<sup>+</sup>, NO<sup>+</sup> and O<sub>2</sub><sup>+</sup> with a series of volatile carboxylic acids and esters. *International Journal of Mass Spectrometry and Ion Processes*, 172(1-2):137–147, 1998. ISSN 01681176. doi:10.1016/s0168-1176(97)00246-2.
- [65] Patrik Španěl, Jan Žabka, Illia Zymak, and David Smith. Selected ion flow tube study of the reactions of H<sub>3</sub>O<sup>+</sup> and NO<sup>+</sup> with a series of primary alcohols in the presence of water vapour in support of selected ion flow tube mass spectrometry. *Rapid Communications in Mass Spectrometry*, 31(5):437–446, 2017. ISSN 10970231. doi:10.1002/rcm.7811.
- [66] Patrik Španěl, Tianshu Wang, and David Smith. A selected ion flow tube, SIFT, study of the reactions of H<sub>3</sub>O<sup>+</sup>, NO<sup>+</sup> and O<sub>2</sub><sup>+</sup> ions with a series of diols. *International Journal of Mass Spectrometry*, 218(3):227–236, 2002. ISSN 13873806. doi:10.1016/S1387-3806(02)00724-8.
- [67] Sharon G. Lias, Joel F. Liebman, and Rhoda D. Levin. Evaluated Gas Phase Basicities and Proton Affinities of Molecules; Heats of Formation of Protonated

- Molecules. *Journal of Physical and Chemical Reference Data*, 13(3):695–808, 1984. ISSN 15297845. doi:10.1063/1.555719.
- [68] Pascal Gerboux and František Tureček. Protonated carbonic acid and the trihydroxymethyl radical in the gas phase. A neutralization-reionization mass spectrometric and ab initio/RRKM study. *Journal of Physical Chemistry A*, 106(24):5938–5950, 2002. ISSN 10895639. doi:10.1021/jp020162c.
- [69] Erna Schuhfried, Tilmann D. Märk, and Franco Biasoli. Primary Ion Depletion Kinetics (PIDK) Studies as a New Tool for Investigating Chemical Ionization Fragmentation Reactions with PTR-MS. *PLoS ONE*, 8(6):1–10, 2013. ISSN 19326203. doi:10.1371/journal.pone.0066925.
- [70] R. Sander. Compilation of Henry’s law constants (version 4.0) for water as solvent. *Atmospheric Chemistry and Physics*, 15(8):4399–4981, 2015. ISSN 16807324. doi:10.5194/acp-15-4399-2015.
- [71] Pierre Millard, Baudoin Delépine, Matthieu Guionnet, Maud Heuillet, Floriant Belvert, and Fabien Létisse. IsoCor: Isotope correction for high-resolution MS labeling experiments. *Bioinformatics*, 35(21):4484–4487, 2019. ISSN 14602059. doi:10.1093/bioinformatics/btz209.